ISSN 1349-0087
SPring-8 Document D2010-007

SPring-8 Research Frontiers

2009

SPring-8 Research Frontiers 2009

CONTENTS 2009

Preface 7

Scientific Frontiers 9

A Place in the "X-ray" Sun – On the Cutting Edge 10

Life Science: Structural Biology 16

Crystal Structure of the Sodium-Potassium Pump and Its Regulation by Cardiac Glycosides 18
C. Toyoshima and H. Ogawa

Structure of the Connexin 26 Gap Junction Channel at 3.5 Å Resolution 20
S. Maeda and T. Tsukihara

Location and Function of Chloride Ions in Oxygen-Evolving Photosystem II Revealed by X-ray Crystallography 22
J.-R. Shen

Mechanism of Hormone and Effector Recognition by the Gibberellin Receptor 24
Y. Hirano, K. Murase and T. Hakoshima

Structural Basis for Gibberellin Recognition by Its Receptor GID1 26
H. Kato

Structure of Rat Liver Vault at 3.5 Å Resolution 28
K. Kato, H. Tanaka and T. Tsukihara

Conformational Transition of Sec Machinery Inferred from Bacterial SecYE Structures 30
T. Tsukazaki and O. Nureki

Crystallographic Study of the Conserved N-Terminal Domain of the Peroxisomal Matrix-Protein-Import Receptor, Pex14p 32
J.-R. Su, K. Takeda and K. Miki

Insights into the Stator Assembly of the Na^+-Driven *Vibrio* Flagellar Motor from the Crystal Structure of MotY 34
S. Kojima, M. Homma and K. Imada

Stator Assembly and Activation Mechanism of the Flagellar Motor Revealed by the Crystal Structure of the Periplasmic Region of MotB 36
S. Kojima, K. Imada and K. Namba

Life Science: Medical Biology 38

Inner Structure of Cretaceous Fossil Flower Revealed by X-Ray Microtomography 40
M. Takahashi

Revealing Human Brain Circuits by Microtomography 42
R. Mizutani

X-Ray Phase-Contrast Microtomography for Visualizing of Renal Microstructures in Albino-Panda-Albino Hamsters 44
J. Wu, T. Takeda and A. Momose

Three-Dimensional Visualization of a Human Chromosome Using Coherent X-Ray Diffraction 46
K. Maeshima and Y. Nishino

Compact Packing of Lipocalin-Type Prostaglandin D Synthase Induced by Binding of Lipophilic Ligands 48
T. Inui and K. Inoue

Actin Molecule Becomes a Flat Conformation by Polymerization 50
T. Oda

MATERIALS SCIENCE: STRUCTURE 52

Electronic and Magnetic Structures of Spin-Orbit Coupling Induced Mott Insulator Sr_2IrO_4 54
H. Ohsumi, T. Arima and H. Takagi

Tetragonal-Orthorhombic Phase Transition in LaFeAsO – Relevant to High-Temperature Superconductivity 56
T. Nomura and H. Hosono

Fulleride Superconductors are Three-Dimensional Members of the High-T_c Family 58
K. Prassides and M. J. Rosseinsky

Entry of Novel π-Conjugated Molecules into Liquid Crystalline Materials 60
K. Tashiro

Analyses on Crystalline Structures of Carbon Nanowalls by Grazing-Incidence X-Ray Diffraction Using Synchrotron Light Source 62
W. Takeuchi, H. Kondo and M. Hori

Nature of Structural Transformations in the B_2O_3 Glass under High Pressure 64
V. V. Brazhkin, Y. Katayama and K. Trachenko

X-Ray Diffractometry for the Structure Determination of a Submicrometer-Scale Single Powder Grain 66
S. Kimura

Angular Anomaly in the Dynamic Structure Factor of Graphite Close to Bragg Reflections 68
R. Hambach, C. Giorgetti, N. Hiraoka and L. Reining

MATERIALS SCIENCE: ELECTRONIC & MAGNETIC PROPERTIES 70

Looking Deeper into Buried Nanolayers and Complex Materials: Standing-Wave and Angle-Resolved Hard X-Ray Photoemission 72
C. S. Fadley, S. Ueda and K. Kobayashi

Definitive Evidence for Fully Occupied $4f$ Electrons in YbS and Yb Metal 74
M. Matsunami

Fermi Surface Variation Near Quantum Critical Point of $CeRu_2(Si_{1-x}Ge_x)_2$ Studied by Resonant ARPES 76
T. Okane

Dependence of Electronic Properties of Epitaxial Few-Layer Graphene on Number of Layers Investigated by Photoemission Electron Microscopy 78
H. Hibino and Y. Watanabe

Transverse Acoustic Excitations in Simple Liquid 80
S. Hosokawa, M. Inui and Alfred Q. R. Baron

Metal-Insulator Transitions in Complex Oxides Probed by High Resolution X-Ray Compton Scattering 82
B. Barbiellini, A. Koizumi and M. Itou

Energy Domain Mössbauer Spectroscopy Using Synchrotron Radiation 84
M. Seto

High-Magnetic-Field XMCD Using Pulsed Magnet 86
Y. H. Matsuda

CHEMICAL SCIENCE 88

Molecular-Frame Photoelectron Angular Distributions of Gas-Phase Molecules 90
K. Ueda, X. Liu, H. Fukuzawa and N. Saito

Inhomogeneity of Liquid Water – Two Structural Motifs 92
T. Tokushima, Y. Harada, S. Shin and A. Nilsson

Identification of Valence Electronic States of Aqueous Acetic Acid in Acid-Base Equilibrium Using Site-Selective X-Ray Emission Spectroscopy 94
Y. Horikawa, T. Tokushima and S. Shin

Small-Angle X-Ray Scattering from Drug Delivering Nanoparticles in Solutions: Pharmacological Efficiency and Particle-Inner Structures 96
K. Sakurai

Evaluation of Structural Relationship in Hybridized Porous Coordination Polymer Crystals 98
K. Hirai, S. Furukawa, O. Sakata and S. Kitagawa

AgI Nanoparticles : Size-Controlled Stabilization of Superionic Phase to Room Temperature 100
R. Makiura, H. Kitagawa and K. Kato

Synchrotron X-Ray Diffraction Study of Fe-1111 Type Superconductor *Ae*FeAsF (*Ae* = Ca and Sr): Possibility of Higher T_c 102
S. Matsuishi and H. Hosono

Comprehensive Structural Study of Glassy $BaTi_2O_5$ 104
J. Yu, S. Kohara and A. Masuno

A Novel Form of Topologically Ordered Amorphous Silica obtained from Collapsed Silicalite at High Pressure 106
J. Haines, C. Levelut, A. Isambert, P. Hébert and D. A. Keen

EARTH & PLANETARY SCIENCE 108

Phase Relations of Iron-Nickel Alloys at Multimegabar Pressure: A Study of the Earth's Inner Core Material 110
Y. Kuwayama

Elasticity of MgO to 130 GPa: Implications for Lower Mantle Mineralogy 112
M. Murakami

Mineralogy of the Lower Mantle Investigated Using Sintered Diamond Multianvil Apparatus 114
Y. Tange

Nondestructive Search for Micrometer-Scale Platinum-Group Minerals in Mantle Peridotite with Microbeam X-Ray Fluorescence Analysis 116
T. Kogiso, K. Suzuki and T. Suzuki

Characterization of a Hard X-Ray Telescope 118
Y. Ogasaka

Environmental Science 120

Speciation of Antimony in PET Bottles Produced in Japan and China by X-Ray Absorption Fine Structure Spectroscopy 122
Y. Takahashi

Synchrotron X-Ray Spectroscopic Evidence of Dioxin Formation Mechanism in Solid Waste Incinerator – Direct Chlorination of Carbon by Copper Chloride – 124
M. Takaoka and T. Fujimori

Antimony Interaction with an Abiotic Reducer in Aquatic Environment: Green Rust Compounds 126
S. Mitsunobu and Y. Takahashi

Industrial Applications 128

X-Ray Reflectivity Study on Depth Profile of Acid Generator Distribution in Chemically Amplified Resists 130
T. Kozawa

Stability-Instability Transition of Reaction Fronts in Thermal Silicon Oxidation 132
H. Omi

Direct Observation of Reduced Path Formation in CuO-Based Resistance-Switching Devices 134
R. Yasuhara, H. Kumigashira and M. Oshima

Characterization of Liquid Crystal Alignment on Rubbed Polyimide Film by Grazing-Incidence X-Ray Diffraction 136
T. Koganezawa, I. Hirosawa and H. Ishii

Precise Observation of Dynamic Structural Change of Pd Particles under CO/NO Catalytic Reaction Studied by Dispersive X-Ray Absorption Fine Structure 138
D. Matsumura

Crystal Structure at the Initial Growth Stage of Organic Semiconducting Thin Films Studied by GIXD 140
N. Yoshimoto

Formation of Autoclaved Aerated Concrete Studied by *In Situ* X-Ray Diffraction under Hydrothermal Condition 142
J. Kikuma

Detection of Tooth Enamel Microstructural Transformations during De- and Re-mineralization in the Early Stage of Caries 144
T. Tanaka, Y. Terada and H. Kamasaka

Nuclear Physics 146

Further Evidence for Θ^+ from LEPS 148
T. Nakano

Near-Threshold Photoproduction of $\Lambda(1520)$ from Protons and Deuterons 150
N. Muramatsu

Accelerators & Beamlines Frontiers 152

Beam Performance 153

Developments and Upgrades of Storage Ring and Booster Synchrotron 153

Developments and Upgrades of Linac 164

New Apparatus & Upgrades 165

A Beamline Dedicated to Soft Matter Research has been Now Launched at BL03XU 165

The University of Tokyo Soft X-Ray Materials Science Beamline 167

New Microbeam Beamline Dedicated to Protein Microcrystallography 169

TOYOTA Beamline BL33XU 170

Development of the High-Throughput and High-Accuracy Measurement System for Powder Diffraction 171

Development of a Differential Pumping System of Soft X-Ray Beamline for Windowless Experiments under Normal Atmospheric Conditions 172

Facility Status 174

Introduction 175

Machine Operation 176

Beamlines 177

User Program and Statistics 180

Budget and Personnel 184

Research Complex 185

Users Societies, Conferences and Other Activities 187

Project XFEL 189

Progress of the XFEL Project 190

NewSUBARU 194

EUV Interference Lithography at BL9 Beamline in NewSUBARU 195

Note: The principal publication(s) concerning each article is indicated with all author's names in italics in the list of references.

Preface

When I came back to the SPring-8 campus about a year ago to succeed Dr. Kira, the former president of JASRI, I was very much delighted to see the big progress SPring-8 has accomplished so far in the field of synchrotron radiation science and technology.

I personally recall back in the 1990's witnessing day by day the progress of SPring-8 under construction as the director of the Planning and Research Division of JASRI, although at that time it was just too early to establish concrete prospects upon how best SPring-8 could contribute to synchrotron radiation science and technology.

Since then, SPring-8 has been rapidly increasing its importance not only in academia but in industry and is now regarded as an indispensable research infrastructure for promoting science and technology in Japan.

- On June 5, 2009, the number of total user visits to SPring-8 reached 100,000.
- Construction of new beamlines is still going on to reach 55 beamlines operational toward the end of March 2011.
- Remarkable scientific achievements in synchrotron radiation are continuously being obtained at SPring-8 and have been reported in prestigious scientific journals, such as Nature and Science.
- The XFEL project in the SPring-8 campus is going well and construction is expected to be completed by March 2010.

These are the major developments that are covered in SPring-8 Research Frontiers 2009, which I sincerely hope will provide useful and timely information about SPring-8 for all its readers both in Japan and abroad.

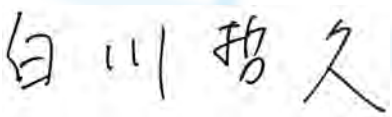

Tetsuhisa Shirakawa
President
SPring-8 / JASRI

Editor's Note

SPring-8 Research Frontiers 2009 covers advances achieved during the last two consecutive research periods, the second half of 2008 (2008B) and the first half of 2009 (2009A). It describes the remarkable scientific achievements obtained at SPring-8 in various fields of basic and applied sciences including industrial applications, as well as the development of accelerators, beamlines and experimental apparatus, and the present status of the SPring-8 facility. The progress of the XFEL project at SPring-8 toward completion in FY2010 is also reported. In addition, activities using NewSUBARU, which forms an integral part of the research complex, are introduced.

Last winter, SPring-8 was in a great uproar about the drastic budget cuts recommended by the government revitalization unit. Under retrenchment circumstances, SPring-8 is required to curtail extra expenses in all departments. The publication business, although considered important, is not an exception. Therefore, the editorial board decided to reduce the total number of pages of SPring-8 Research Frontiers by about fifteen percent while keeping the qualities of the contents high .

Until the last issue, the research reports were categorized into ten research fields. However, this time, the "Instrumentation & Methodology" category is omitted and the reports that belong to this category are incorporated into closely related research fields or into the "New Apparatus and Upgrades" section, because it will be more suitable in light of the present state of the facility.

Copies of SPring-8 Research Frontiers will be sent on request. Its full text is also available on the SPring-8 website (http://www.spring8.or.jp/). For the list of publications produced by SPring-8 users and staff, please visit the publication database at https:///user.spring8.or.jp/uisearch/publication/en.

We extend our appreciation to those who have recommended excellent research results suitable for publication in SPring-8 Research Frontiers. We would also like to express our sincere gratitude to the users and staff of SPring-8 for contributing their reports to this issue.

Editorial Board

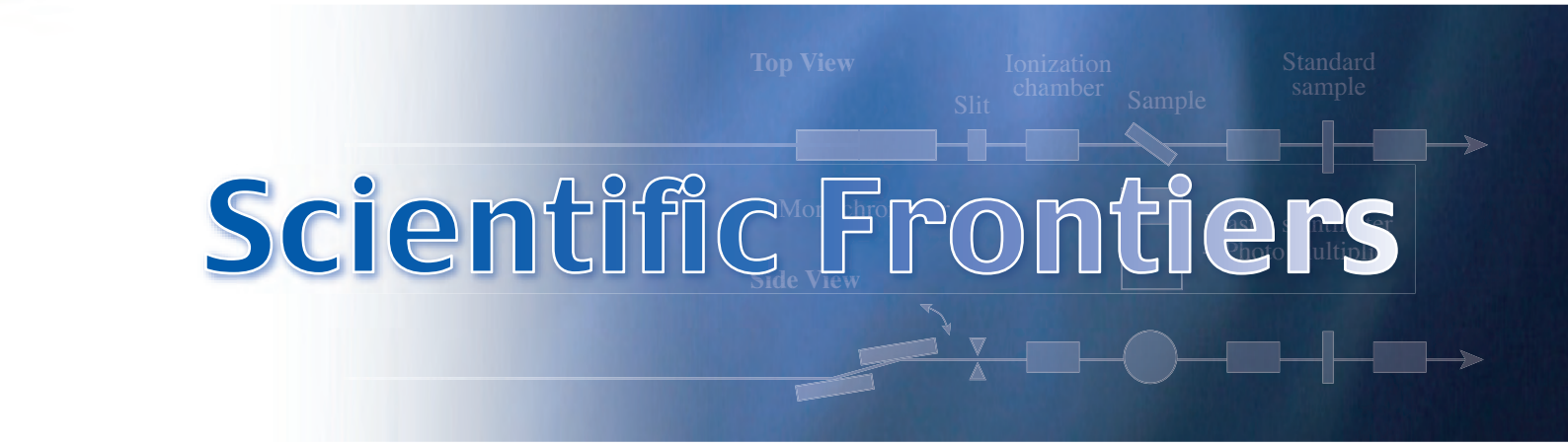

Scientific Frontiers

A Place in the "X-ray" Sun

On the Cutting Edge

Since the inception of the SPring-8 utilization in 1997, more than 100,000 users have visited SPring-8 and carried out experiments to uncover mysteries in science. Described here are a lineup of the nine pioneers in Life Science, Materials Science, Chemical Science, Earth & Planetary Science, and Light Source Technology from SPring-8.

1. A Scenario Writer of Interplay between Protein and Ion in Membrane Transport
Chikashi TOYOSHIMA

Noted for his distinguished achievements for the calcium ion pump (Sarco- (Endo-) plasmic reticulum Calcium ATPase 1, SERCA1) in structural biology, Chikashi Toyoshima has been one of the top international biophysicists in the highly competitive world of life science. He is a professor of Molecular and Cellular Biosciences at the University of Tokyo.

He started his scientific career as an electron microscopist and worked on muscle filaments and ion channels. Drawing on all of his expertise in the fields of mathematics, physics and biology, he has uncovered the atomic structures of biomolecular complexes that could never be studied before. From 1986-1988, he worked on the acetylcholine receptor and a motility assay for motor proteins as a Postdoctoral Fellow with Drs. Nigel Unwin and James Spudich at Stanford University, in the USA. He then moved to the MRC Laboratory of Molecular Biology in Cambridge in the UK to continue his work with Dr. Unwin on the electron crystallography of 2D and tubular crystals of membrane proteins. During this

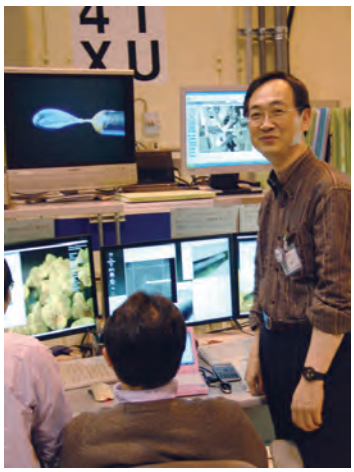

Chikashi Toyoshima
Leading his research team even at midnight at SPring-8

period, he initiated collaboration on SERCA1a with Dr. David Stokes. Toyoshima was a major contributor to the development of cryo-electron microscopy and computer programs that permit 3D structures to be reconstructed from tubular crystals. He used these methods to obtain the first images of the nicotinic acetylcholine receptor in its native membrane and an 8 Å structure of SERCA1a.

After that, Toyoshima determined the structure of the calcium pump in different phases of the reaction cycle by X-ray crystallography. The work provided a magnificent result for the structural elucidation of the mechanism of the action of P-type ATPases: cation pumps that become phosphorylated during the reaction cycle and are responsible for maintaining cation gradients across membranes. The questions that he has successfully addressed using SERCA1a as a model are as follows: How are cation binding sites created and destroyed in the transmembrane domain following chemical events at the phosphorylation site 50 Å away? How is the chemical energy in ATP converted to transfer ions against a concentration gradient? What is the role of phosphorylation? Why is countertransport necessary, despite the fact that the countertransported ions return to the original side through ion channels? He has provided answers to these fundamental questions by combining X-ray crystallography, electron microscopy and molecular dynamics simulations and, therefore, "revolutionized how researchers are able to study the structure of proteins" (Hitchcock Lectures citation at the University of California, Berkeley, 2008). His research produced the first images of an ion pump at work in atomic detail and explained well the mechanism of the reaction scheme.

Toyoshima has also collaborated with Dr. MacLennan to provide an explanation at molecular and atomic levels for the mechanism of regulation of SERCA by phospholamban and sarcolipin in cardiac tissues. He showed thapsigargin (TG) and two other inhibitors prevent the movements of transmembrane helices in SERCA, and a complementary protein surface is enough to confer a picomolar dissociation constant for TG. These are the first studies for the structural elucidation of inhibitors that bind to a transmembrane region.

On the basis of his crystal structures and proposals, a new generation of experimental studies, including mutagenesis, spectroscopy, and electrophysiology, and theoretical studies have been conducted. For instance, by analyzing his crystal structures, an even more potent derivative of TG was developed by an American/Danish group and its application to prostate cancer therapy is advancing. His work is thus widely influential and has been included in textbooks of biochemistry and even statistical physics. There is no doubt that SPring-8 has played a crucial role in his achievements in Structural Biology. His paper in this scientific highlights is shown on page 18 .

Cover Picture of Nature in 2000

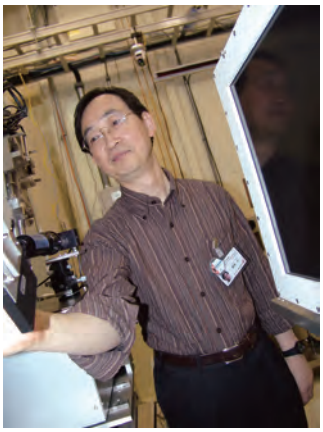

Toyoshima is always leading off his experiment

2. A Pathfinder in Materials Science of Correlated Electron System
Hidenori TAKAGI

Hidenori Takagi is a professor at the University of Tokyo and a chief scientist of RIKEN. He has been breaking ground on various advanced hard materials by discovering the self-organization of electrons, superconductivity thermoelectricity, and negative thermal expansion as well as with their applications. In his research, SPring-8 is one of the indispensable tools for unveiling a rich variety of exotic electronic materials.

So far, right after the discovery by Bednorz and Muller of high temperature superconductivity in La- Ba-Cu-O, Takagi verified for the first time the occurrence of superconductivity by magnetization measurement and subsequently identified the layered K_2NiF_4 structure responsible for high temperature superconductivity, by which "two-dimensionality" was

recognized. He then discovered the electron-doped superconductor $(Nd,Ce)_2CuO_4$ and showed that high temperature superconductivity shows up symmetrically by both hole- and electron-doping. This has brought a drastic change in our understanding of high-T_c cuprate superconductors. He found the unusual charge transport (such as resistivity and Hall effect) in the normal state of cuprates, which led to the concept of the pseudo (normal state)-gap, one of the most important key ideas in cuprate physics nowadays. Since then, he has been addressing the mystery of the pseudo-gap phase. To understand the much-discussed hidden electronic order behind the pseudo-gap, he developed a new class of cuprate superconductors $(Ca,Na)_2CuO_2Cl_2$ as a playground, which led to the discovery of a self-organized state of electrons, often called a checkerboard or nanostripe.

He recognized the very rich physics in correlated electrons through those outstanding achievements in cuprate physics. In the mid-90s, he expanded his repertoire from cuprates to transition metal oxides in general. Since then, he has been pioneering work on the novel electronic phases of a variety of complex transition metal oxides, particularly exotic charges and spin liquids produced by geometrical frustration. His discoveries include a frustration-induced heavy fermion state in mixed-valent LiV_2O_4, magnetic-field-induced half-magnetization state in the strongly frustrated S=3/2 anti-ferromagnet $CdCr_2O_4$, three-dimensional quantum spin liquid state in $Na_4Ir_3O_8$ with hyper-kagome lattice, Jahn-Teller driven charge ordering in mixed-valent $LiRh_2O_4$, and spin-orbit complex state in a Mott insulator Sr_2IrO_4. Now, he is trying to open the door to the 5*d* metal magnetism using a newly developed magnetic scattering technique in SPring-8, whose details are described in the section of Materials Science, page 54. His recent discovery of a spin-orbital Mott state in Sr_2IrO_4 shall ignite intensive research on exotic 5*d* metal oxides.

Hidenori Takagi

3. Twosome Players in Fullerene Superconductivity

Kosmas PRASSIDES & Matthew ROSSEINSKY

Kosmas Prassides is professor of Materials Chemistry at the Department of Chemistry, Durham University. Matthew Rosseinsky is professor of Inorganic Chemistry at the University of Liverpool and was elected a Fellow of the Royal Society (FRS) in 2008.

They share a common scientific origin to their careers since both obtained their D. Phil. degrees under the supervision of professor Peter Day FRS. Their research interests are multi-disciplinary and encompass a range of structural, magnetic and electronic problems in advanced materials, straddling the areas of condensed matter physics and chemistry. Their work has been spanning several fields, microporous materials science, mixed valency and transition metal oxide chemistry as well as fullerene science and they have extensive collaborations at SPring-8.

Kosmas Prassides

In the last two decades, Rosseinsky and Prassides have been leading the research on fullerene superconductivity since the discovery of alkali metal fullerides (*Nature* 352 (1991) 787). They have been using core chemical approaches to access unusual structures and electronic, conducting and magnetic ground states and probe the physics in key materials, especially metal fulleride solids. Rosseinsky has been developing synthesis techniques of novel functional materials in a chemically understandable manner. Prassides has unveiled their structure-property relationships. He is a frequent user himself of the SPring-8 facilities and his recent activities have been facilitated by utilization of the BL44B2 & BL10XU beamlines. In the last two years, Prassides and Rosseinsky have developed the metal fullerides into the best model systems for correlated electron high T_c superconductivity (*Nature Materials* 7 (2008) 367; *Science* 323 (2009) 1585; *Nature* 465 (2010) doi:10.1038/nature09120) and have supported their

ideas by structural characterization using high pressure powder diffraction experiments at BL10XU (see page 58). Their work has advanced the understanding of molecular superconductivity and magnetism and the generic problem of the metal-Mott insulator transition to an unprecedentedly high level.

Matthew Rosseinsky

4. The Tailor of Superb Exotic Molecules Takuzo AIDA

Takuzo Aida, Professor; the University of Tokyo/RIKEN is known as one of the most imaginative and productive polymer chemists in the world. His energy and creativity have helped shape polymer chemistry for more than two decades. Aida has achieved seminal and creative chemistry demonstrating novel syntheses and functions of linear, dendritic, and supramolecular polymers as well as tailoring nanoscale functions through precision control of molecular interactions.

In recent years, he has used SPring-8 as a key tool to prove that the molecular structure is conclusively created as he designed it as well as to find a clue to more advanced designs of molecules. His first successful utilization of SPring-8 was the structure confirmation of a new type of nanotube that could also conduct electricity.

Several years ago, Aida aimed to create s new nanotube using a new type of graphene molecule by adding hydrophilic and hydrophobic moieties. The

Takuzo Aida

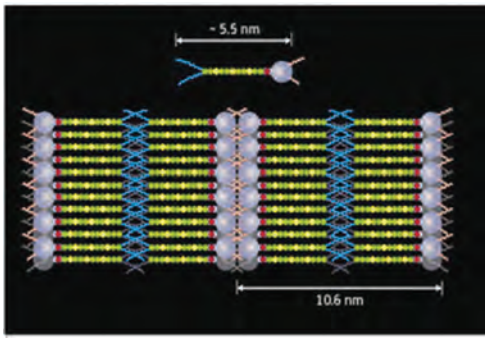

New liquid-crystal molecule (top) designed with fullerene (purple). The oligothiophene chains (yellow/green) self organize. Liquid crystal photovoltaic device (bottom) tailored using hydrophobic/hydrophilic tails represented by blue/red lines, respectively.

molecule "self-organization" combined to form nanotubes of 20 nm diameter with hydrophobic moieties inside.

By the SR scattering experiment, he established solid evidence that graphene molecules bearing hydrophobic and hydrophilic moieties bond together at the hydrophobic moiety, forming molecular pairs that build up in a spiral pattern to creat a tube (*J. Am. Chem. Soc.*, 2008). Consequently, his discovery proved the feasibility of creating a new functional graphite nanotubes by changing the structural design of the original molecules.

Aida has also succeeded in designing liquid crystals phase that flows like a liquid but has a short-range order between molecules that spontaneously assemble to form a donor-acceptor array, which should lead to the development of high-efficiency organic photovoltaic devices (*J. Am. Chem. Soc.*, 2008).

This year, his discovery of "bicontinuous cubic liquid crystalline materials from discotic molecules" led to a photograph of the materials being the cover

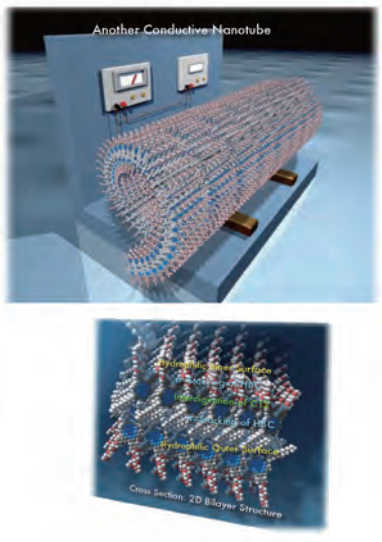

Novel graphite nanotube created by Aida

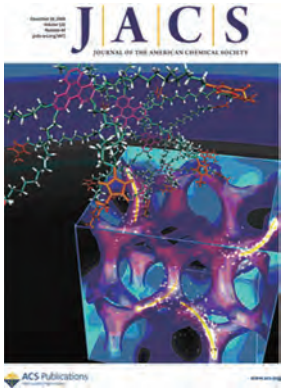

Novel graphite nanotube

picture of the Journal of the American Chemical Society. The details will appear in the section of Chemical Science, page 60. Aida's quest for a new paradigm creation in Chemistry shall attract increasing attention via SPring-8.

5. An Expedition Cartographer in High Pressure Science Tetsuo IRIFUNE

One of the pioneers in Earth Sciences, Tetsuo Irifune, is a professor at Ehime University. He has been leading synchrotron radiation experiments under high pressure using the Kawai-type multianvil apparatus (KMA) at BL04B1 since beamline construction started. He published the very first paper from SPring-8 in *Science* (1998) and has been keeping on top of world-class research activities. One of his representative works is "*Phase transitions in mantle and subducting plate materials*".

Irifune has been conducting systematic experiments on phase transitions and associated density changes in the subducting lithosphere (plate) as well as on surrounding mantle materials using the KMA, combined with synchrotron radiation in addition to SEM, XRD, TEM, etc. His research covers various materials of the Earth's interior, such as pyrolite, harzburgite, basalt, and granite compositions, as well as related minerals with simpler chemical compositions. In the past decade, Irifune's findings have led to new models on the dynamics and circulation of plate-related materials in the mantle. Some breakthroughs in the Earth Sciences began to arise from his discovery of new high-pressure phases, such as the calcium-ferrite type $MgAl_2O_4$, CAS phase,

Tetsuo Irifune

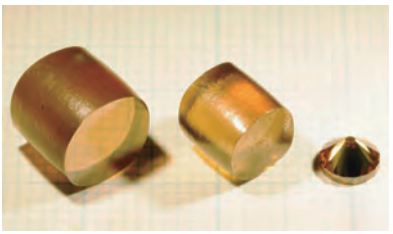

HIME-DIAs

K-hollandite II, and $MgCO_3$ magnesite II (*Nature*, 2004), in which SPring-8 played a major role.

His research and development at SPring-8 have also facilitated various innovations on a higher-pressure generation techniques, which have been applied in order to upgrade the measurement techniques, and allowing for the exploring of even deeper Earth mineralogy at SPring-8. One of his most important contributions is the development of an advanced cell (Ehime cell) for the KMA apparatus, which allows *in situ* X-ray observations of phase transitions under higher pressure and temperature. The first successful application was the precise determination of the spinel-postspinel transition boundary in Mg_2SiO_4 (*Science*, 1998). This high-performance cell has been opened for public use and has widely contributed to the Earth science community at SPring-8.

Very recently, an upgraded form of the Ehime cell generated pressures above 50 GPa and temperatures of ~2500 K. One outcome from such an advanced technique has been published in *Science* (2010) and is described in the section of Earth & Planetary Science in this scientific highlights (see page 114). In the meantime, he applied KMA technology to materials synthesis and succeeded in the first synthesis of a pure nano-polycrystalline diamond (NPD or HIME-DIA = Highly Incompressible and Mechanically Endurable DIAmond) under high pressure (*Nature*, 2003). Irifune is now applying the HIME-DIA for various purposes relevant to high-pressure Earth and Materials Sciences, including those for further higher pressure and temperature generation at SPring-8.

Irifune's Laboratory

6. Trinity Siblings at the Forefront of the XFEL Project

Takahiro Inagaki, Takashi Tanaka & Kazuaki Togawa

One of the three X-ray Free-Electron Laser (XFEL) facilities in the world is nearing completion at the SPring-8 campus. The others are the Linac Coherent Light Source (LCLS, Stanford University, USA) and the European XFEL (DESY, Germany (EU)). Among them, the XFEL in SPring-8 has a unique concept, i.e., SCSS (SPring-8 Compact SASE Source), which will achieve a high-performance XFEL in a compact size. This concept requires accomplishing three technical innovations: a low-emittance injector based on a 500-kV pulsed thermionic gun with a single-crystal cathode, a high-gradient C-band acceleration system, and a short-period in-vacuum undulator. The following three young scientists (RIKEN) have been tackling these challenging tasks.

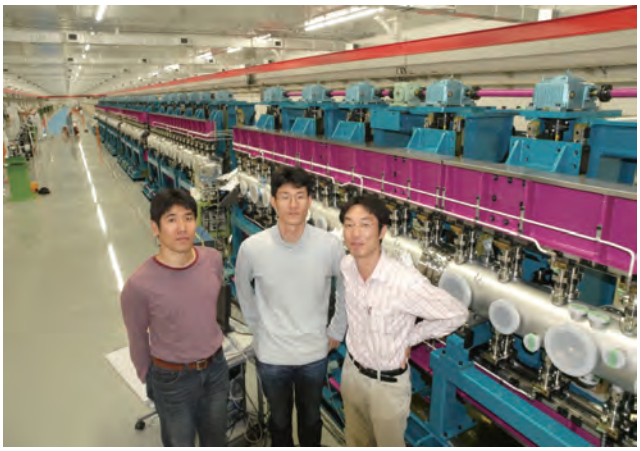

Kazuaki Togawa is a thoughtful achiever, who made a breakthrough in the common assumption of low-emittance injector technology. When the discussion of the SCSS concept design started, most scientists thought that a photocathode RF gun would be the best choice for the XFEL. Thus, our choice, which is a thermionic-gun based system, was thought to be a high-risk challenge. However, his elaborate thermionic-gun system succeeded in achieving the homogeneous and stable low-emittance electron beams required for XFEL and disproved the prejudice. The original system based on a CeB_6 single crystal cathode produced by his deep technical insight and passion for the XFEL project is cornerstone of the achievements of the XFEL project as well as of the EUV FEL in utilization.

Takashi Tanaka is a task leader for the development of the short-period in-vacuum undulator. He has created a specific permanent-magnet formation optimized for the required short period toward the present design limit. He has also developed the world's first *in situ* field measurement system named "SAFALI" (Self Aligned Field Analyzer with Laser Instrumentation), to achieve the strict field quality specification for the XFEL. In addition, he constructed a three-dimensional FEL simulator, SIMPLEX (reverse order of X-ray fEL Practical SIMulator; abbreviation in reverse), which is a powerful tool for figuring out various technical problems, because gimmicks on the performance of the undulator train associated with alignment tolerance, an energy chirp by undulator resistive-wall impedance, and an orbit setting error, among other factors should be removed to achieve the full-power operation of the SASE XFEL. So far, SIMPLEX has provided feasible approaches to solve all the problems we had for the XFEL construction at the SPring-8 site.

Takahiro Inagaki is a key person in the development of the operational acceleration system based on the C-band optimized for the XFEL. Since this system provides a high gradient of 35~40 MV/m, which is twice as high as a conventional gradient of ~20 MV/m, the length of an electron linear accelerator, a main part of the facility, can be reduced by half. Also, he succeeded in developing an ultra-stable klystron modulator power supply to stabilize the RF acceleration phase, which is crucial for the stable operation of the XFEL. His painstaking work, the newly developed C-band system, has achieved the design performance of XFEL, i.e., 39 MV/m at a repetition rate of 60-pps, with the lowest fault rate satisfying a usable level.

by Masaki Takata and Hitoshi Tanaka

Life Science:

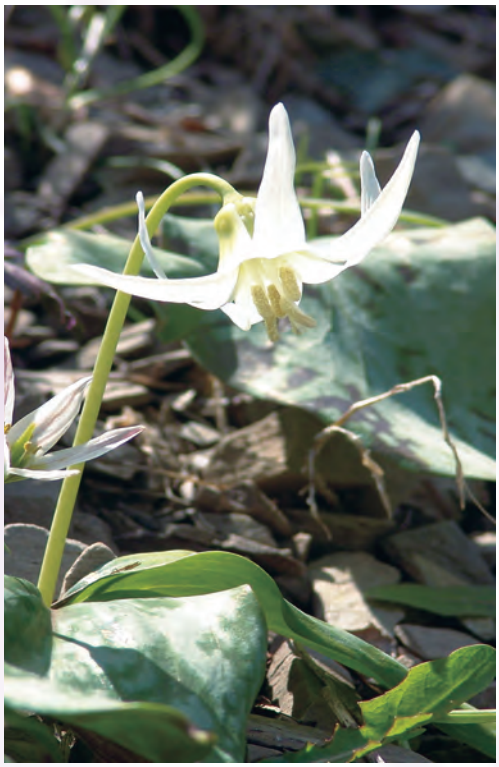

Brilliant synchrotron X-ray is continuously shedding light on the structural aspects of biological macromolecules. As a result of completing the first phase in structural genomics research projects throughout the world, the monotonic increment of the number of determined structures by year was stopped in 2008. However, by last year, the number was recovering. This might be caused by the advancement of the research techniques under the former projects and the start of the next phase of structural genomics research. This affects studies in structural biology not only quantitatively but also qualitatively. Within this background, we select ten topics among the variety of fruitful research conducted in 2009. Their brief summaries are described below.

Ion transport is a key function in signaling and action driven by a concentration gradient. Ca-ATPase works as a pump to recover the ion gradient after muscle contraction. Toyoshima and colleagues successfully determined its structures in the nine reaction steps and revealed its dynamical properties, as briefly summarized in the overview, "A place in the "X-ray" sun." His group also investigated another ion pump protein, Na, K-ATPase, which produces ion gradient for nervous stimuli and so on. The structure revealed the action of a heart stimulant drug, ouabain. In contrast to the pump proteins, channel proteins passively transport molecules using the concentration gradient. Connexin acts as a bridge between the cytoplasm of adjacent cells and controls the permeation of ions

Structural Biology

or small molecules. Its characteristic *tsuzumi*-like structure and gating mechanism were revealed by Tsukihara and colleagues. Its initial model, obtained using electron microscope, was improved using high resolution X-ray diffraction data.

For environmental and agricultural applications, plant biology is an important research. Photosystem II is a large membrane protein and contains a metal ion cluster and chloride ions needed to recycle atmospheric oxygen by water oxidation. Shen and colleagues revealed previously undiscovered but essential chloride binding sites using anomalous signals from substituted bromine and iodine. Gibberrelin is a key hormone in plant growth stimulation. Its discovery and major research progress were accomplished by Japanese researchers. Last year two Japanese groups independently determined its receptor protein structures (Hakoshima *et al*. and Kato *et al*.). The analyses reveal clearly the stimulation mechanism by which the gibberellin binding to the receptor induces a direct interaction with the repressor protein, leading to the degradation of the receptor by ubiquitin ligase.

In supramolecule research, the structure of the largest cytoplasmic protein, vault, was determined by Tsukihara and colleagues. Its rugby-ball-like structure is an assembly of 78 monomers and its long axis reaches 65 nm. A fine and parallel X-ray beam produced from an X-ray undulator enabled data collection from crystals with a large lattice length of 700 Å.

The next topic is protein transport. A cell is not a simple mixture of biological molecules and their subcellular localization is essential to maintain its system. The membrane protein SecYE plays a role in the secretion of proteins produced in cytoplasm to the extracellular region. Its structure, determined by Nureki *et al*., revealed its dynamical open-close conformational change induced by binding SecA protein. Peroxisome is an organelle that participates in fatty-acid metabolism. Its contents are imported from cytosol across the membrane by a protein import machinery. Miki *et al*. determined the structure of the machinery component Pex14p. This result clearly showed the high affinity of Pex14p to a specific motif observed in the machinery components.

Dynamic motion is characteristic of living organisms. Even small bacteria can swim in some species by flagellar rotation with a screwlike motion. This action is achieved by a protein biomotor driven by the energy of an ion gradient. Imada's group recently determined two proteins located in the motor stator, and added new lines to the blueprint of the biomotor.

Takashi Kumasaka

"Matsubaunran" - *Blue Toadflax*

Crystal Structure of the Sodium-Potassium Pump and Its Regulation by Cardiac Glycosides

Sodium-potassium ATPase is an ATP-powered ion pump that establishes concentration gradients for Na^+ and K^+ across the plasma membrane in all animal cells by pumping Na^+ from the cytoplasm and K^+ from the extracellular medium. Such gradients are used for many essential processes, notably for generating action potentials. Na^+,K^+-ATPase is a member of the P-type ATPases that include sarcoplasmic reticulum Ca^{2+}-ATPase, the crystal structures of which have been determined for 9 different intermediates that cover nearly the entire reaction cycle [1]. Crystallography of Na^+, K^+-ATPase is far more difficult, partly because heavily glycosylated β-subunit and a regulatory FXYD protein are integral parts of this ATPase in addition to the catalytic α-subunit. We published the first high resolution crystal structure of this important ion pump from shark rectal gland fixed in a state analogous to $E2{\cdot}2K^+{\cdot}Pi$ (Fig. 1), in which the ATPase has a high affinity to K^+ and still binds Pi [2]. Clearly visualised at 2.4 Å resolution were co-ordination of K^+ and associated water molecules in the transmembrane binding sites and a phosphate analogue (MgF_4^{2-}) in the phosphorylation site. The crystal structure showed that the β-subunit plays a critical role in K^+ binding, by stabilising the kinked part of a transmembrane helix M7 (Fig. 2). This kink is caused by another kink in M5, originating from a Pro that effectively makes a larger space than Gly, the corresponding residue in Ca^{2+}-ATPase, for accommodating K^+. The involvement of the β-subunit explains, at least partially, why the homologous Ca^{2+}-ATPase countertransports H^+ rather than K^+, although the co-ordinating residues are almost identical.

Cardiac glycosides, prescribed for congestive heart failure for more than two centuries, are efficient inhibitors of Na^+,K^+-ATPase. Their therapeutic index is, however, low and structural details on their binding have been keenly sought. In the subsequent paper [3], we reported a 2.8 Å resolution crystal structure of this ATPase with bound ouabain (Fig. 3(a)), a representative cardiac glycoside derived from a plant *Strophanthus gratus*, introduced by soaking the $E2{\cdot}2K^+{\cdot}MgF_4^{2-}$ crystals. Ouabain was deeply inserted into the transmembrane domain with the lactone ring very close to the bound K^+, in marked contrast to previous models (Fig. 3). Due to antagonism between ouabain and K^+, the structure represents a low-affinity ouabain bound state. Yet, most of the mutagenesis data obtained with the high-affinity state are readily explained by the present crystal structure, indicating that the binding site for ouabain is essentially the same and a high affinity is conferred by closure of the binding cavity. All the diffraction data were collected at beamline **BL41XU**.

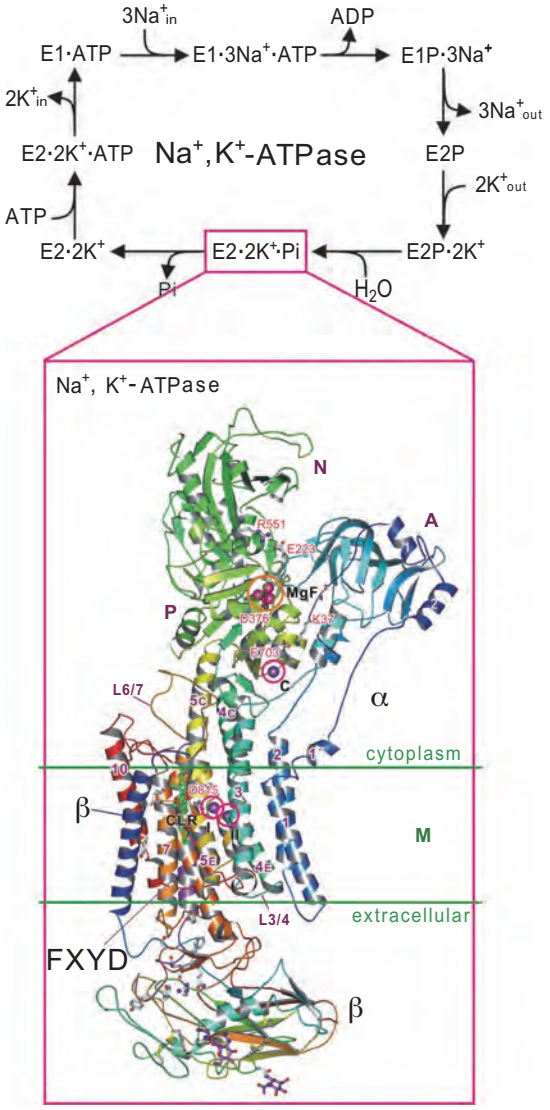

Fig. 1. The reaction cycle and a 2.4 Å resolution crystal structure of Na^+, K^+-ATPase in the $E2{\cdot}2K^+{\cdot}MgF_4^{2-}$ form, representing the $E2{\cdot}2K^+{\cdot}Pi$ state. According to the classical Albers-Post mechanism, the ATPases have a high affinity in the E1 state and a low affinity in E2 for the ion transferred from the cytoplasm across the membrane (i.e., Na^+); the affinity is reversed for the ion countertransported (K^+). During the reaction cycle, the ATPase is autophosphorylated by ATP at an aspartyl residue. Na^+ bound to the transmembrane binding sites are occluded in E1P, and released to the opposite side of the membrane in the E2P ground state, and the binding sites become occupied by the counterions (K^+). Hydrolysis of the aspartylphosphate and transition into the product state ($E2{\cdot}Pi$) closes the extracellular (lumenal) gate and the counterions become occluded. K^+ (purple spheres) and MgF_4^{2-} (orange circle) are shown in space fill.

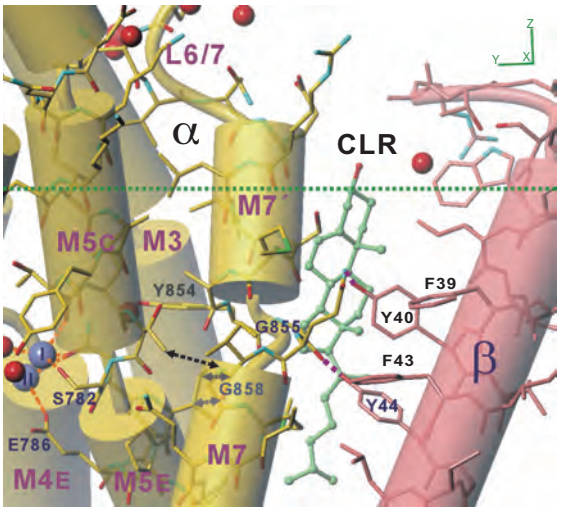

Fig. 2. Details around the unwound part of the M7 helix. Purple spheres represent bound K^+ (I, II). A cholesterol molecule (CLR) is depicted in ball-and-stick. Note that the Gly855 carbonyl is stabilized by a hydrogen bond with Tyr44 of the β-subunit. The horizontal green line shows the approximate boundary of the hydrophobic core of the lipid bilayer.

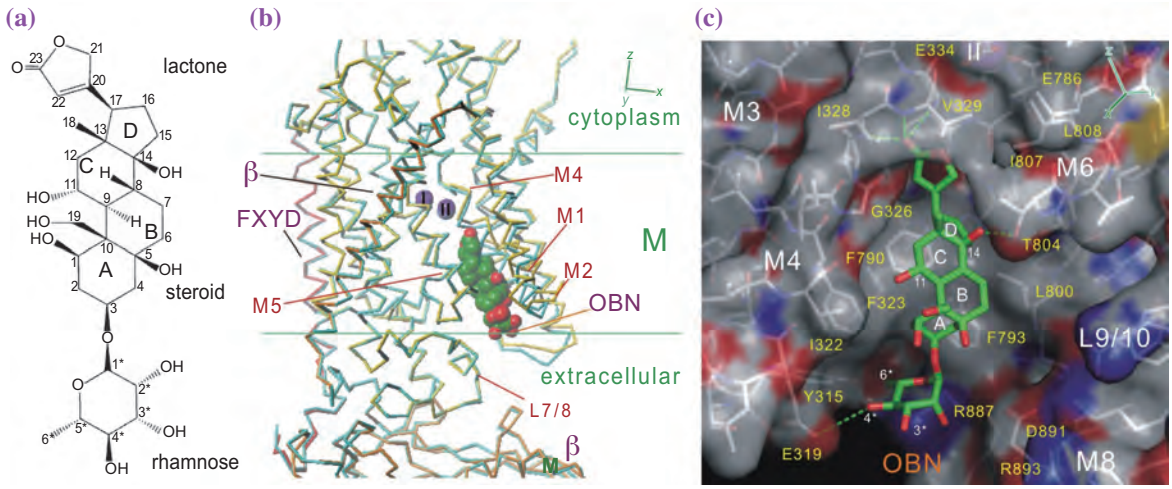

Fig. 3. Crystal structure of Na^+,K^+-ATPase with bound ouabain. **(a)** A diagram of ouabain (OBN). **(b)** Superimposition of Cα traces of Na^+, K^+-ATPase in ouabain bound (yellow) and ouabain unbound (cyan) forms, viewed in the same direction as in Fig. 1. Ouabain (green and red) and K^+ ions (I, II; purple) are shown in space fill. Green horizontal lines indicate the approximate position of lipid bilayer. **(c)** Details of the ouabain binding site viewed parallel to the membrane. Water accessible surface in atom color is superimposed on the atomic model.

Chikashi Toyoshima* and Haruo Ogawa

Institute of Molecular and Cellular Biosciences,
The University of Tokyo

*E-mail: ct@iam.u-tokyo.ac.jp

References

[1] *C. Toyoshima: Biochim. Biophys. Acta* ***1793*** *(2009) 941.*
[2] *T. Shinoda, H. Ogawa, F. Cornelius and C. Toyoshima: Nature* ***459*** *(2009) 446.*
[3] *H. Ogawa, T. Shinoda, F. Cornelius and C. Toyoshima: Proc. Natl. Acad. Sci. USA* ***106*** *(2009) 13742.*

Structure of the Connexin 26 Gap Junction Channel at 3.5 Å Resolution

Intercellular signaling is fundamental to the complex biological functions of multicellular organisms such as neural transmission, immune reaction, or reproductive function. Gap junctions mediate the intercellular signal by connecting the cytoplasms of two neighboring cells [1]. A gap junction contains clusters of intercellular channels called "gap junction channel." End-to-end docking of two hemichannels, also referred to as "connexons," forms a gap junction channel. Each connexon is composed of six connexin subunits surrounding the central pore. There are 21 connexin (Cx) isoforms in human with highly conserved sequences but different physiological properties. They can form heteromeric (more than two different connexins in a connexon) or heterotypic (a gap junction channel with different connexons) channels, conferring further complex diversity. Gap junctions are known to be involved in a wide variety of biological processes such as the cardiovascular system, reproduction system, nervous system and auditory system [2].

The primary method for the three-dimensional structural analysis of the gap junction channel has been electron microscopy (EM) [3,4]. Although EM revealed a great deal of the structure of the gap junction channel, a high resolution structure where each amino acid could be distinguished has been essential for more detailed biochemical and physiological analyses. Here, we have determined the structure of Cx26 at 3.5 Å resolution by X-ray three-dimensional crystallographic analysis. The data sets were collected at beamline **BL44XU**.

The overall structure of the Cx26 gap junction channel is like that of tsuzumi, a traditional Japanese drum (Fig. 1). Since there are no obstructions through the pore, and our crystallization condition generally promotes the channel in its open state, the structure is considered as an open conformation.

The Cx26 monomer has four transmembrane helices (TM1-TM4), two extracellular loops (E1, E2), an N-terminal region (NT), a cytoplasmic loop (CL), and a C-terminal tail (CT) (Fig. 1). NT has an N-terminal helix (NTH) inserted into the pore. The anomalous signals from seleno-methionine derivative crystals definitely reveal the four-helical arrangement. Each connexin protein has three intramolecular disulfide bonds between two extracellular loops, which are essential for the formation of the intercellular channel. The anomalous signals from native sulfur atoms show the locations of the three disulfide bonds in the extracellular region.

Most of the intermonomer interactions are located at the extracellular side of the membrane region (Fig. 2). These residues, and also those of the intramonomer interactions, are conserved among connexin isoforms, suggesting that the manner of folding and oligomerization is conserved in the connexin family, as has been suggested by the similarity in cryoEM structures of two types of connexin (Cx43 and Cx26) [3,4]. The extracellular loops, E1 and E2, mediate the docking of hemichannels (Fig. 2). Through these interactions, E1 and E2 make a tight seal in the extracellular space, separating the channel interior from the outside environment.

The permeation pathway of the Cx26 gap junction channel consists of an intracellular channel entrance, a pore funnel, a negatively charged path, and an extracellular cavity (Fig. 3). The intracellular channel entrance is composed of the cytoplasmic parts of TM2 and TM3. Positive charge residues are concentrated in this region and surround the entrance, creating a positively charged microenvironment around the channel pore. The pore funnel is formed by six NTHs and is the constriction site of the pore. The negatively charged path is located at the TM1/E1 boundary and the channel is narrowed again here. The extracellular

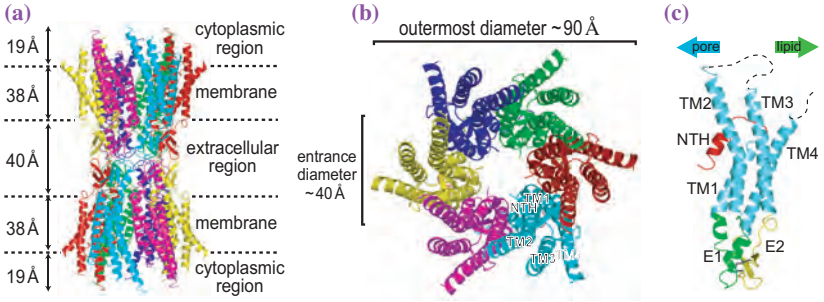

Fig. 1. Overall and monomer structures of human Cx26 gap junction channel in ribbon representation. **(a)** Side view of the Cx26 gap junction channel with the locations of plasma membranes and scale of each region. **(b)** Top view of the Cx26 gap junction channel representing the arrangement of the transmembrane helices and N-terminal helix. **(c)** Structure of the Cx26 monomer in ribbon representation.

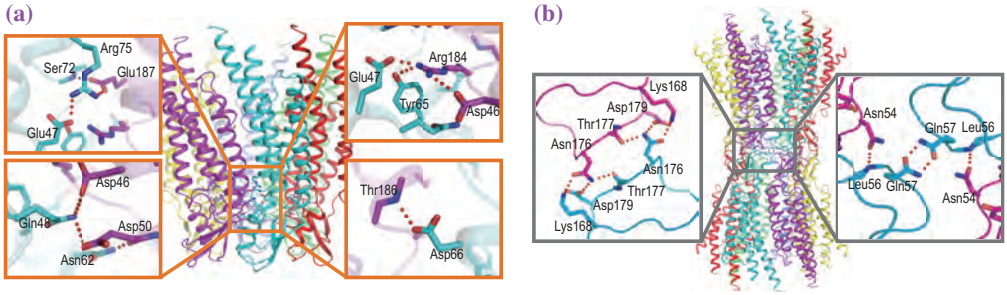

Fig. 2. Structural organization of Cx26 hexamer. **(a)** Intermonomer interactions in a connexon. Each interaction is shown in the magnified image. **(b)** Interactions between apposing connexons. Interactions in E1 and E2 are each shown in the magnified image.

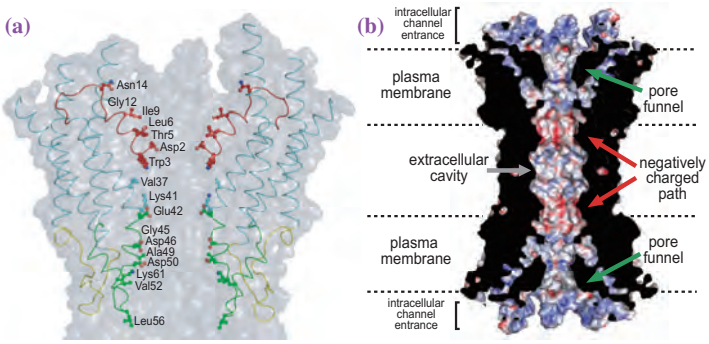

Fig. 3. Pore architecture of the Cx26 gap junction channel. **(a)** Side view of the Cx26 gap junction channel pore. Side chains of the pore-lining residues are drawn as sticks. **(b)** Surface potential distribution of the Cx26 gap junction channel interior.

cavity is formed by twelve portions of E1 from each subunit, creating a tight continuous inner wall of the channel in the extracellular region.

Six N-terminal helices form the "pore funnel" (Fig. 4). The circular hydrogen bond network at the bottom of the funnel stabilizes the pore funnel. The hydrophobic interactions draw the pore funnel onto the innermost wall of the channel, making it an open state (Fig. 4). Gap junction channels have the transjunctional voltage dependent gating mechanism [5]. A number of experiments using chimeras or substitutions suggest that NT, particularly the second amino acid residue, is the voltage sensor. Together with the recent EM-determined structure of the Met34Ala mutant, a novel mechanism of V_j-gating is suggested [4,6] (Fig. 4).

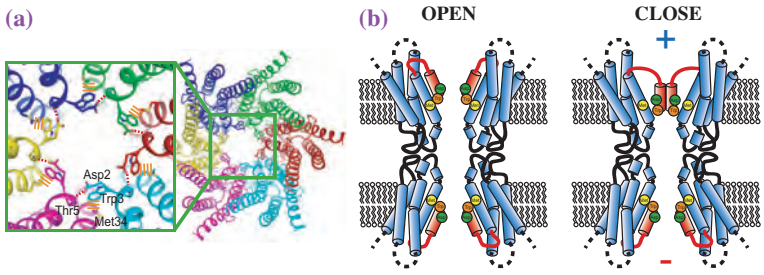

Fig. 4. Structure of the pore funnel and the plug gating model. **(a)** The six NTHs form a pore funnel, which is stabilized by a circular hydrogen bond network (red dashed lines) and attached to the inner wall of the channel by hydrophobic interactions (orange dashed lines). **(b)** Proposed plug gating model. The pore funnel senses the transjunctional voltage difference and forms a pore plug that blocks the channel.

Shoji Maeda [a] and Tomitake Tsukihara [a,b,*]

[a] Institute for Protein Research, Osaka University
[b] Department of Life Science, University of Hyogo

*E-mail: tsuki@protein.osaka-u.ac.jp

References

[1] A.L. Harris: Q. Rev. Biophys. **34** (2001) 325.
[2] A.M. Simon *et al.*: Trends Cell Biol. **8** (1998) 477.
[3] V.M. Unger *et al.*: Science **283** (1999) 1176.
[4] A. Oshima *et al.*: Proc. Natl. Acad. Sci. USA **104** (2007) 10034.
[5] F.F. Bukauskas *et al.*: Biochim. Biophys. Acta **1662** (2004) 42.
[6] *S. Maeda, S. Nakagawa, M. Suga, E. Yamashita, A. Oshima, Y. Fujiyoshi and T. Tsukihara: Nature* ***458*** *(2009) 597.*

Location and Function of Chloride Ions in Oxygen-Evolving Photosystem II Revealed by X-Ray Crystallography

Most of the oxygen on the earth is produced by photosystem II (PSII), a membrane protein complex found in thylakoid membranes from prokaryotic cyanobacteria to eukaryotic higher plants. PSII performs a series of light-induced electron transfer reactions, coupled with this is the water-splitting reaction leading to the evolution of molecular oxygen, which is indispensable for oxygenic life on the earth. PSII from cyanobacteria contains 17 membrane-spanning subunits and 3 peripheral, membrane-extrinsic proteins, and over 70 cofactors including chlorophylls, carotenoids, plastoquinones, heme-irons and a non-heme iron, Mn, Ca, Cl, with a total molecular mass of around 350 kDa for a monomer. The structure of cyanobacterial PSII has been reported at resolutions of 3.8-2.9 Å [1-4], which provided much information on the overall arrangement of protein subunits and most of the cofactors, although the current resolution is not high enough to elucidate the detailed structure of PSII required for the full understanding of the light-induced water oxidation reaction.

The water-oxidizing complex of PSII is composed of 4 Mn atoms and 1 Ca atom, most of which are coordinated by D1, one of the reaction subunits of PSII, with only one residue provided by CP43, a chlorophyll-binding protein. It has been long known that in order for the Mn_4Ca-cluster to operate properly, chloride ions (Cl^-) are required. In the absence of Cl^-, the water-splitting reaction cannot proceed beyond some steps, and oxygen cannot be formed. However, the exact number and binding site(s) of Cl^- in PSII have not been identified due to the limited resolution of the current structure available, as well as the difficulty to detect Cl^- by X-ray diffraction analysis.

In order to identify the binding sites for Cl^- within PSII, we substituted Cl^- with either bromide ions (Br^-) or iodide ions (I^-), and crystallized, solved the crystal

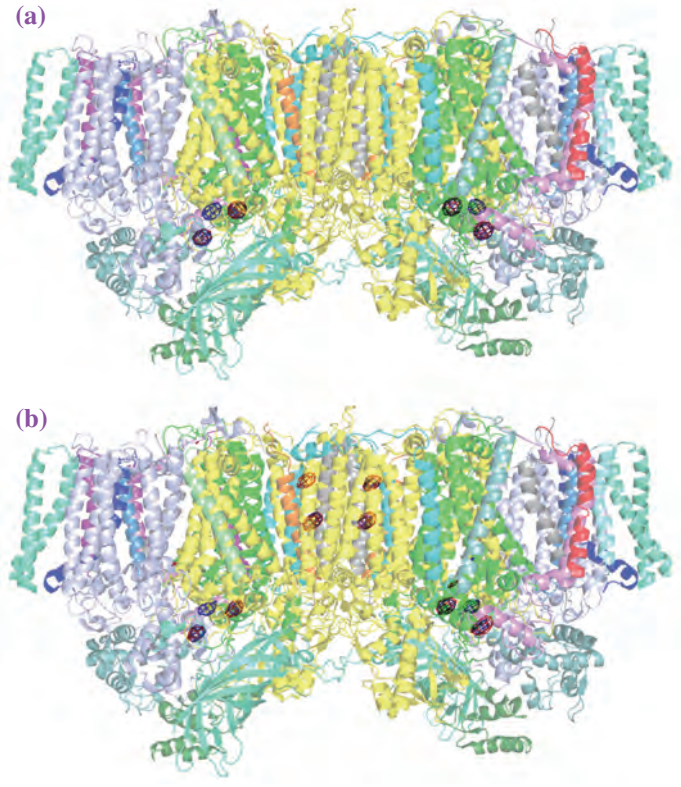

Fig. 1. Difference-Fourier maps and anomalous Fourier maps of Br^- or I^--substituted PSII, overlapped with the structure of PSII dimer. **(a)** Difference-Fourier map of Br^--substituted PSII *minus* Cl^--PSII, and anomalous Fourier map of Br^--substituted PSII collected at 0.9 Å wavelength, which were superimposed with the PSII dimer structure at a view perpendicular to the normal of the membrane plane. Red: Difference-Fourier map; Blue: Anomalous Fourier map. **(b)** Difference-Fourier map of I^--substituted PSII *minus* Cl^--PSII, and anomalous Fourier map of I^--substituted PSII collected at 1.0 Å wavelength superimposed with the PSII dimer structure. Red: Difference-Fourier map; Blue: Anomalous Fourier map.

structure of Br^--substituted and I^--substituted PSII respectively [5]. Since both Br^- and I^- have significant effects of anomalous dispersion around 1.0 Å, their detection was greatly facilitated by their anomalous scattering effects. Fig. 1 shows the difference Fourier maps between native-PSII (Cl^--PSII) and Br^- or I^- substituted PSII, as well as the anomalous Fourier maps of Br^- and I^- substituted PSII, respectively, which were overlapped with the overall structure of PSII dimer. It was found that two binding sites for Br^- are existed around the Mn_4Ca-cluster in both the difference Fourier map and anomalous Fourier map of Br^--substituted PSII, and there were no additional binding sites for Br^- in the other area of PSII. The same two sites were also found in the difference Fourier map and anomalous Fourier map of I^--substituted PSII, indicating that both Br^- and I^- bind to the same two sites around the Mn_4Ca-cluster. In the I^--substituted PSII, however, three additional sites were found which are located distantly from the Mn_4Ca-cluster, these three sites are thus concluded not involved in the oxygen-evolving reaction [5].

Since I^--substitution for Cl^- completely inhibited oxygen evolution, and this inhibition was completely reversed upon re-substitution of I^- with either Br^- or Cl^-, we concluded that both Br^- and I^- bind to the Cl^--binding sites in PSII; in other words, the above determined two sites surrounding the Mn_4Ca-cluster represent the Cl^--binding sites in native PSII [5]. The structure around these binding sites is depicted in Fig. 2. It was found that these two sites are coordinated to two residues that provided direct ligands to the Mn_4Ca-cluster, namely, Glu333 of D1 subunit and Glu354 of CP43 subunit [5], suggesting that Cl^- ions may be required for maintaining the correct structure of these residues, thereby maintaining the structure of the Mn_4Ca-cluster required for the water-splitting reaction to proceed. In addition, one of the two Cl^--binding sites was located in the exit of a proposed proton channel, suggesting that this site may be required to maintain the structure of the channel [5]. X-ray diffraction experiments were performed at beamline **BL41XU**.

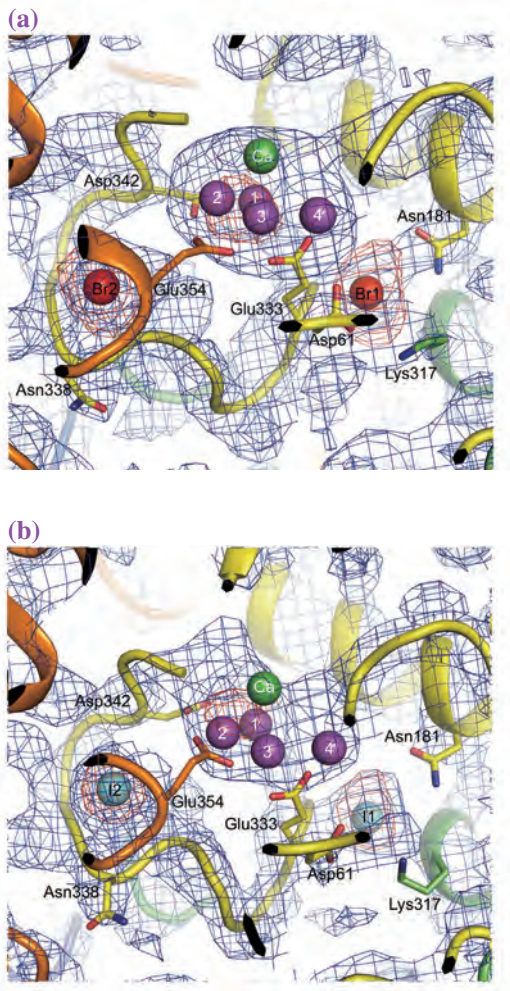

Fig. 2. Location of the two anion binding sites in PSII. **(a)** Composite omit Fo-Fc map (blue) and anomalous map (red) of Br^--substituted PSII (blue), respectively, superimposed with the structure of the Mn_4Ca-cluster and its surrounding regions. Color codes for the residues are as follows: Yellow, D1; Green, D2; Orange, CP43. **(b)** Composite omit Fo-Fc map (blue) and anomalous map (red) of I^--substituted PSII (red), respectively, superimposed with the structure of the Mn_4Ca-cluster and its surrounding regions. The color codes for the residues are the same with panel **(a)**.

Jian-Ren Shen

Graduate School of Natural Science and Technology, Okayama University

E-mail: shen@cc.okayama-u.ac.jp

References

[1] A. Zouni *et al.*: Nature **409** (2001) 739.
[2] N. Kamiya and J.-R. Shen: Proc. Natl. Acad. Sci. USA **100** (2003) 98.
[3] K.N. Ferreira *et al.*: Science **303** (2004) 1831.
[4] A. Guskov *et al.*: Nat. Struct. Mol. Biol. **16** (2009) 334.
[5] *K. Kawakami, Y. Umena, N. Kamiya and J.-R. Shen: Proc. Natl. Acad. Sci. USA **106** (2009) 8567.*

Mechanism of Hormone and Effector Recognition by the Gibberellin Receptor

Plant hormones are a group of structurally different small molecules essential for various developmental processes in higher plants. In the last decade, receptors for all classical plant hormones have been identified and several emerging hormones have been recognized [1]. Current structural biology would be able to contribute toward the better understanding of the molecular mechanisms of plant hormone actions at an atomic resolution.

In the 1920s, gibberellin (GA) was initially identified as a fungus toxin from *Gibberella fujikuroi*, which causes the bakanae disease of rice, characterized by super-elongation and male sterility that reduces the rice harvest. In the 1950s, it became known that GAs were synthesized by plants, and thus GAs were accepted as an endogenous hormone. A plausible model of GA actions, however, has emerged only recently, with the remarkable findings of GA receptor GID1s, its direct downstream DELLA proteins and an F-box protein, SLY1. Here, we report the structural studies on the basis of gibberellin-induced DELLA recognition by *Arabidopsis* GID1 [2].

Gibberellins stimulate plant growth and development including seed germination, stem growth and floral development. GAs regulate the turnover of DELLA proteins, the negative transcriptional regulators, through the ubiquitin-proteasome pathway. In the absence of GA, DELLA proteins repress the GA responses. GA binds to its receptor GID1, which leads to a direct interaction with DELLA proteins. This interaction triggers the DELLA protein recognition by the ubiquitin E3 ligase SCF (SKP1-CULLIN-F-box) complex. Ubiquitylation of DELLA proteins results in the degradation of DELLA proteins at 26S proteasomes, and then the transcriptional factors liberated from the negative control by DELLA proteins start GA responses [3]. In *Arabidopsis thaliana*, there are three homologues of GA receptors, GID1A, GID1B and GID1C and five DELLA proteins, GAI, RGA and RGL1,2,3. DELLA proteins bind to GID1 through its N-terminal region referred to as DELLA domain, whereas a GRAS domain located in the C-terminus is involved in transcriptional regulation. We have succeeded in determining the structure of the ternary complex of *Arabidopsis thaliana* GID1A, bioactive GAs, GA_3 or GA_4, and the DELLA domain of GAI at 1.8 Å resolution using the data collected at **BL41XU** beamline [2].

The GID1A comprises a core domain (GID1 core) that adopts an α/β hydrolase fold with the N-terminal extension (GID1 N-Ex), which consists of three

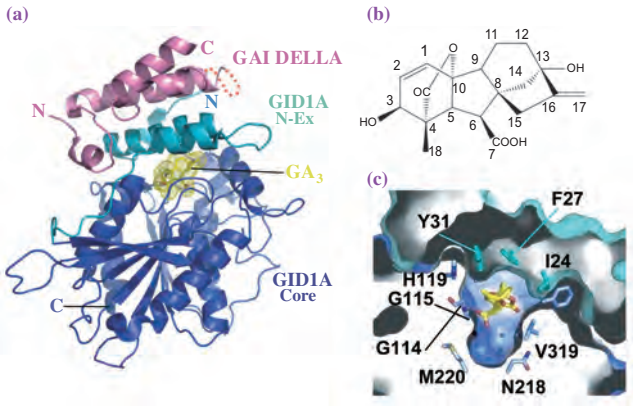

Fig. 1. Structure of the GA_3–GID1A–DELLA complex. **(a)** Ribbon representation of the GA_3–GID1A–DELLA complex, with the GAI DELLA domain (pink), GID1A N-terminal extension (N-Ex, cyan) and GID1A α/β core domain (light blue). The bound GA_3 molecule is represented in yellow. **(b)** Chemical structures and numbering of GA_3. **(c)** Binding pocket of GID1A.

α-helices loosely packed with each other (Fig. 1). The structure of the GID1 core resembles carboxylesterase as predicted, harboring a pocket for the substrate, although GID1A has no esterase activity owing to the alteration of the essential histidine residue forming a catalytic triad. Gibberellins are confined in the binding pocket between the GID1 core and GID1 N-Ex (Fig. 1(c)). This binding pocket is suitable for GA perception, by forming hydrophobic walls that tightly fit the shape of GA aliphatic rings and placing the polar residues and water molecules inside to form hydrogen bonds with all four polar groups of GA (Fig. 1(c), Fig. 2).

Hydroxylation on GA C-2, which should cause a steric clash with Tyr 31 and lead to a disadvantageous conformation for GID1A binding, is well characterized as a metabolic deactivation of GA in plants (Fig. 2(b)).

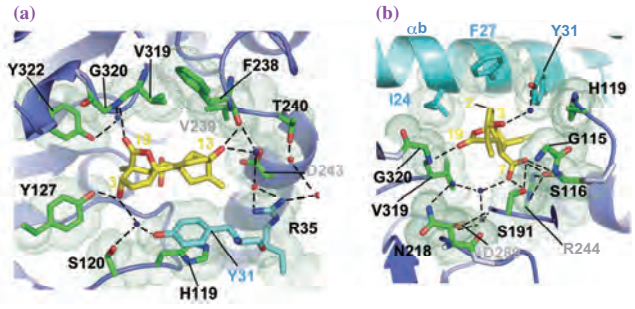

Fig. 2. Recognition of GA3 by GID1A. **(a)** Top view of the GID1A-bound GA_3. **(b)** Side view of the GID1A-bound GA3. GID1A residues that contact GA3 are highlighted in green (GID1 core) or cyan (GID1 N-Ex) and shown as stick models with van der Waals surfaces (dots) and hydrogen bonds (dotted lines).

Methylation of GA 7-carboxylate is also known to decrease the affinity by two to three orders of magnitude owing to the disruption of multiple hydrogen bonding and charge compensation by the oxyanion hole and GID1-specific arginine (Fig. 2(b)). Only a few GAs including GA_1, GA_3 and GA_4 serve as bioactive hormones although more than 100 natural gibberellins have been identified to date, which implies the rigorous GA recognition by the receptor. Our structures show the precise GA perception by the receptor and reveal the structure-activity relationship of bioactive and inactive GAs.

The DELLA domain of GAI forms four α-helices, αA to αD. The flat-shaped DELLA domain resembles a palm consisting of helices αB to αD, with helix αA being off-plane like a thumb (Fig. 3(a)). We define three conserved motifs of the DELLA domain, DELLA, LExLE and VHYNP motifs, which are essential for direct contact with the hormone receptor (Fig. 3(a)). The DELLA thumb helix αA is hooked onto the crevice of GID1A formed by the GID1A N-Ex and the GID1A core through nonpolar interactions and hydrogen bonds involving Asp 29 (Fig. 3(b)).

In view of the results from structural inspection and protease sensitivity assays, we propose that GID1 N-Ex serves as a conformational switch that senses GA. GID1 N-Ex adopts a relatively flexible conformation in the GA-unbound state, but once it perceives a GA molecule, it folds back to close the lid on the GA binding pocket and to generate the binding surface toward the DELLA domain. This conformational transition induces the structural conversion of the DELLA domain from a random coil to a helix bundle. This conversion may cause changes in the overall shape of DELLA proteins including the GRAS domain, which allows the F-box protein SLY1 to recognize DELLA proteins. GA functions as an allosteric effector of GID1A that closes the lid and triggers ubiquitylation of DELLA proteins by SCF complex without direct contact with DELLA proteins.

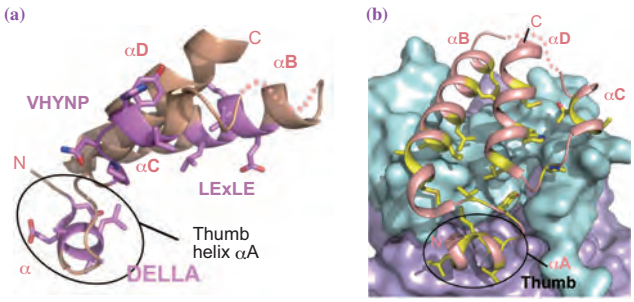

Fig. 3. Architecture of the DELLA domain of GAI and its recognition by GID1A. **(a)** A ribbon representation of DELLA domain of GAI. **(b)** Interaction between GAI and GID1. The hydrophobic palm (αB-αD) of GAI covers GID1 N-Ex by mainly hydrophobic interaction.

We refer to GID1 as a 'ubiquitylation chaperon' based on the function assisting a folding transition to stimulate a ubiquitylation by the SCF complex (Fig. 4).

Protein ubiquitylation is widely used as a degradation signal involved in diverse cellular activities as well as in several plant hormone signaling, including auxin, jasmonate and gibberellin. Notably, auxin and jasmonate receptors are F-box proteins. A recent structural study illustrates that auxin serves as the "molecular glue" that mediates contacts between the F-box protein and its substrate protein [4], whereas gibberellins, by contrast, act as the 'ubiquitylation chaperon'. Remarkably, both mechanisms are novel in that they generate an exposed degradation signal in the protein to be degraded, compared with other mechanisms that involve phosphorylation by protein kinases, unmasking by protein dissociation or creation of a destabilized N terminus by proteolysis. Thus, the structural investigation of plant hormone receptors has deepened our understanding of the degradation-signal-dependent regulation of cellular functions.

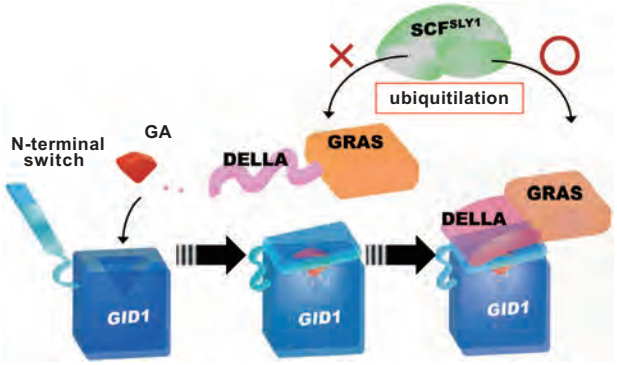

Fig. 4. A model of GA-regulated cell signaling by GID1–DELLA protein interactions.

Yoshinori Hirano, Kohji Murase and Toshio Hakoshima*

Structural Biology Laboratory, Nara Institute of Science and Technology

*E-mail: hakosima@bs.naist.jp

References

[1] A. Santner and M. Estelle: Nature **459** (2009) 1071.
[2] *K. Murase, Y. Hirano, T.P. Sun and T. Hakoshima: Nature* ***456*** *(2008) 459.*
[3] J. Griffiths *et al.*: Plant Cell **18** (2006) 3399.
[4] X. Tan *et al.*: Nature **446** (2007) 640.

Structural Basis for Gibberellin Recognition by Its Receptor GID1

Gibberellins are a large family of tetracyclic diterpenoid plant hormones that induce a wide range of plant growth responses including seed germination, stem elongation, leaf expansion, pollen maturation and induction of flowering. Gibberellins were first discovered by a Japanese plant pathologist, Eiichi Kurosawa, from the pathogenic fungus *Gibberella fujikuroi* in 1926 [1]. Kurosawa was working on rice plant diseases caused by this fungus, bakanae (foolish seedling), and found that some metabolite of this fungus might be responsible for the stimulated seedling growth. In 1935, an agricultural chemist, Teijiro Yabuta, isolated a crystalline active material that he named gibberellin [2]. In the 1950s, it was identified as natural components of noninfected plants and recognized as a plant hormone. Since then, some 136 different kinds of structurally similar gibberellins have been identified, although not all of them are biologically active as hormones in plants. Only a few gibberellins, such as GA_1, GA_3, and GA_4 (Fig. 1), are bioactive hormones in plant [3]. In 2005, a research group led by Makoto Matsuoka discovered a nuclear receptor of gibberellins, gibberellin-insensitive dwarf1 (GID1), from rice [4]. Unexpectedly, GID1 has sequence similarity to hormone-sensitive lipases (HSLs), which are enzymes involved in lipid metabolism. This fact raises the following two questions. (i) How different are their tertiary structures? (ii) How does GID1 manage to specifically interact with bioactive gibberellins while maintaining the conserved structure of the HSL family?

We investigated the structural basis of gibberellin recognition in the rice, *Oryza sativa* GID1 (OsGID1) and revealed, on the basis of the structure, how GID1 has acquired the gibberellin reception ability that is lacking in HSLs [5]. The crystal structures of OsGID1 complexed with GA_4 or GA_3 have been solved by the Hg-SAD method and refined at 1.9 Å resolution. X-ray diffraction data for phasing and refinement were collected at beamline **BL41XU**. The structures revealed an α/β-hydrolase fold resembling that of HSLs (Fig. 2(a)). The gibberellin-binding cavity extends above Ser198 that corresponds to the catalytic residue of HSLs (Fig. 2(b)). Aside from having this catalytic Ser, the residues corresponding to the catalytic triad of HSLs, namely, Ser, His, Asp, are similarly arranged except for the replacement of His with Val in GID1 (Fig. 2(b)). The most notable difference between GID1 and HSL structures appears in the function of an amino-terminal lid (Fig. 2(a)). In HSLs, the lid covers the substrate binding site and opens upon substrate binding. In contrast, in GID1, the lid is open in the absence of the substrate

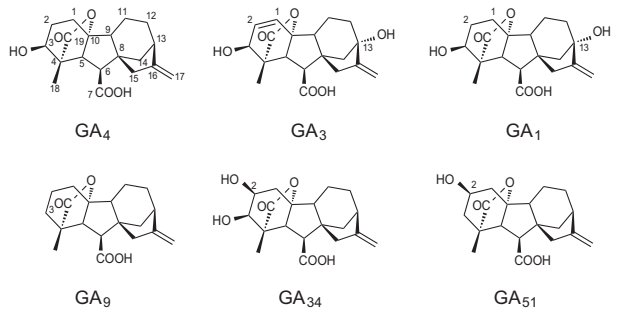

Fig. 1. Chemical structures of the typical gibberellins. GA_4, GA_3, and GA_1 are biologically active gibberellins in higher plants. The subscript numbers for GA are the chronological order of their identification.

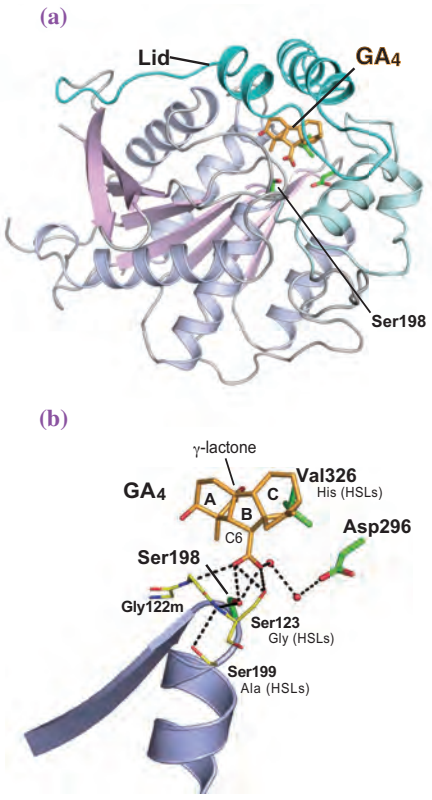

Fig. 2. Crystal structures of rice GID1 complexed with GA_4. **(a)** GA_4—GID1 complex structure shown as a ribbon diagram. **(b)** GID1 structure around the GA binding site including corresponding residues for the catalytic triad of HSLs, Ser198, Asp296, and Val326. The residues of GID1 are indicated and the corresponding residues of an HSL(AeCXE1) are in parentheses. Water molecules are shown as red spheres. Reprinted from Ref. [5] with some modifications.

and closes upon gibberellin-binding. The bound gibberellin is held in place by a network of hydrogen bonds as well as many nonpolar interactions that are considered to facilitate the closing of the lid over the binding pocket, in which the molecular shape of the gibberellin structure is firmly recognized.

To verify the structural assignment, we produced 17 OsGID1 mutants in which residues assigned to be involved in gibberellin-binding were replaced with Ala, and examined their gibberellin-binding activity *in vitro* (Fig. 3). The mutants showed little or no activity, confirming their critical role in gibberellin recognition. Most of the residues important for gibberellin-binding are conserved within plant GID1s but not in HSLs. Interestingly, GID1 proteins in the lycophyte, *Selaginella moellendorffii* (SmGID1s), contain nonconserved residues (Fig. 3) and as a result have lower affinity and specificity for certain gibberellins. We hypothesized that such amino acid replacements in SmGID1s may have led to their lower affinity and specificity for certain gibberellins. To examine this hypothesis, we exchanged the amino acid residues of OsGID1 with the corresponding residues of SmGID1s. We found that some mutated proteins had lower affinity for the biologically active gibberellin, GA_4, but were more accommodating of its 2-hydroxy derivative, such as GA_{34} (Fig. 1). These observations indicated that GID1 evolved from HSL through the loss of its catalytic function and alteration of the substrate binding pocket to increase the affinity and specificity for bioactive gibberellins.

The structure determination of GID1 allows us to design more effective and useful gibberellin agonists and antagonists for agriculture. These compounds may contribute to solving the global issues related to food and biofuel productions.

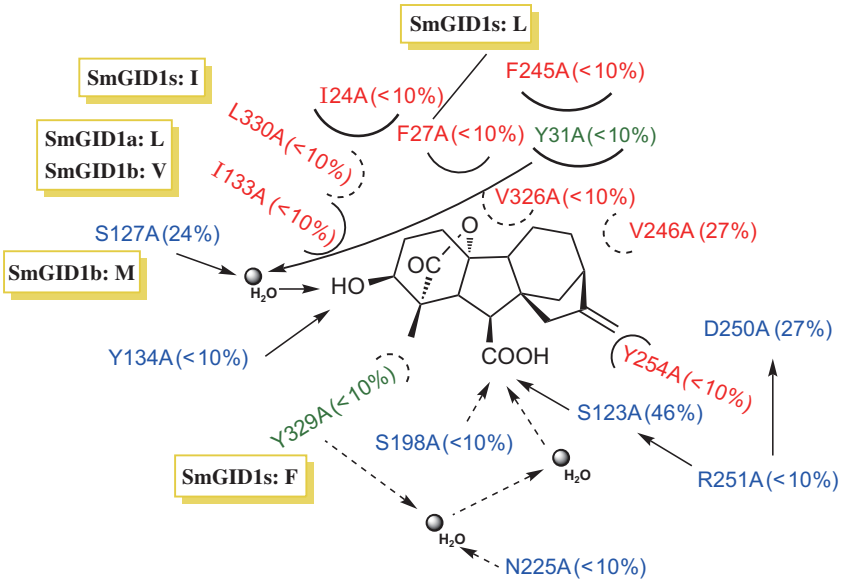

Fig. 3. GA binding activity of mutagenized rice GID1(OsGID1). Binding activities of mutants and their interaction sites with GA_4, relative to the native OsGID1. Polar and nonpolar interactions are indicated by arrows and circles, respectively. The interactions occurring behind GA are shown as broken lines. Mutants related with polar, nonpolar, and both interactions are shown in blue, red, and green, respectively. The amino acid residues corresponding to those in lycophyte GID1s (SmGID1s: both SmGID1a and SmGID1b) are in yellow boxes. Reprinted from Ref. [5] with some modifications.

Hiroaki Kato

Graduate School of Pharmaceutical Sciences,
Kyoto University

E-mail: katohiro@pharm.kyoto-u.ac.jp

References

[1] E. Kurosawa: Nat. Hist. Soc. Formosa **16** (1926) 213.
[2] T. Yabuta: Nogyo-oyobi-Engei **10** (1935) 17.
[3] P.J. Davis: Ed. "Plant Hormones: Biosynthesis, Signal Transduction, Action!" - Kluwer, Dordrecht, 2004.
[4] M. Ueguchi-Tanaka *et al.*: Nature **437** (2005) 693.
[5] *A. Shimada, M. Ueguchi-Tanaka, T. Nakatsu, M. Nakajima, Y. Naoe, H. Ohmiya, H. Kato and M. Matsuoka: Nature **456** (2008) 520.*

Structure of Rat Liver Vault at 3.5 Å Resolution

Vaults are barrel-shaped particles with overall dimensions of 35 × 35 × 65 nm^3 [1], and are highly conserved in a wide variety of eukaryotes. The rat liver vault is composed of three proteins: the 99-kDa major vault protein (MVP), the 193-kDa vault poly(ADP-ribose) polymerase (VPARP), and the 290-kDa telomerase-associated protein TEP1. Additionally, the complex contains a small untranslated RNA consisting of 141 bases (vRNA). Most vault particles are present in the cytoplasm, but a few localize to the nucleus. Although several functions have been proposed for vaults since their first discovery in 1986, including roles in multidrug resistance, cell signaling and innate immunity, their cellular function remains unclear. To elucidate the structure, structural organization and physiological function of this macromolecular complex, we determined the X-ray crystal structure of the rat liver vault at 3.5 Å resolution [2]. The structure analysis was carried out using beamline **BL44XU**.

The vault shell comprises a 78-mer of MVP molecules with 39-fold dihedral symmetry [3], and has a unique barrel-like shape measuring 670 Å in length and 400 Å in maximum diameter (Fig. 1). The barrel-like particle has two protruding caps, shoulders and a body with an invaginated waist. The barrel wall has a very thin, skin-like structure, and is only 15-25 Å thick. The internal cavity of the vault particle is sufficient large to enclose most objects found within the cell. The large internal cavity suggests that the vault functions as a carrier of various molecular cargoes.

The structure of the MVP monomer is depicted by a ribbon drawing in Fig. 2. The MVP monomer folds into nine structural repeat domains, a shoulder domain, a cap-helix domain, and a cap-ring domain. Each structural repeat is a small domain consisting of antiparallel strands. The shoulder domain folds into a single α/β globular domain with four-stranded antiparallel β-sheets on one side and four α-helices on the other side. The cap-helix forms a long α-helix with 42 turns and exhibits one-fourth turn of superhelical structure (Fig. 2). The cap-ring, the polypeptide segment from Gly803 to Ala845, is at the top of the cap and forms a U-shape structure; both ends of this domain are short helical structures.

There are a total of 74 side-by-side interactions between two MVPs, of which 44 interactions were included in the cap-helix domain (Fig. 3(a)), which consists of 170 residues. Although the side chain structures of the cap-ring domain have not yet been determined, the cap-ring domain is closely packed in a restricted space. Structural studies of the intersubunit interactions suggest that the side-by-side interactions within the cap of the vault particle are the primary factors in the structural organization of the vault shell. Each MVP interacts with a neighboring MVP that is related by a twofold symmetry axis. The N-terminal residues of each MVP, Met1-Glu4, form an intermolecular antiparallel β-sheet with the corresponding residues of the other protein. An ionic bond between Glu4 and Arg42 was also detected around the twofold axis. No other intermolecular interaction between two half-vaults was observed, except for the ionic bond and three hydrogen bonds in the β-sheet.

A three-dimensional structure search for similarity to the shoulder, using the DALI server, revealed that this domain is structurally similar to the core domain of stomatin from *Pyrococcus horikoshii* (PhSto^{CD})

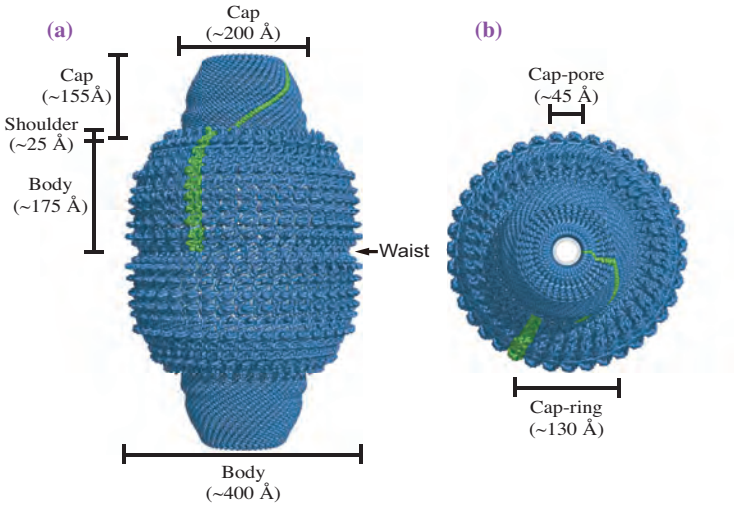

Fig. 1. Overall structure of the vault shell. One molecule of MVP is colored green, and the others are colored blue. **(a)** Side view of the ribbon representation. The whole vault shell comprises a 78-mer of MVP molecules. **(b)** Top view of the ribbon representation.

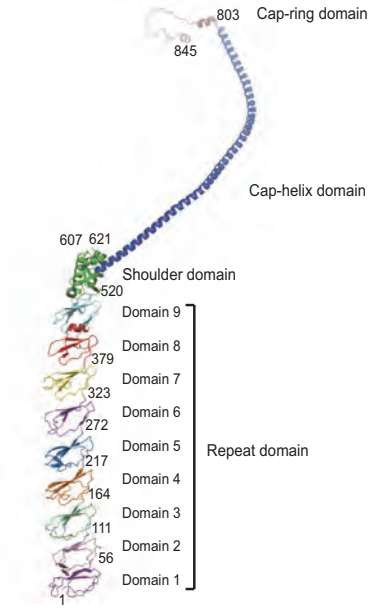

Fig. 2. Ribbon drawing of the overall fold of MVP monomer. The MVP monomer is folded into nine structural repeat domains, a shoulder domain, a cap-helix domain and a cap-ring domain. Each domain is depicted in a different color.

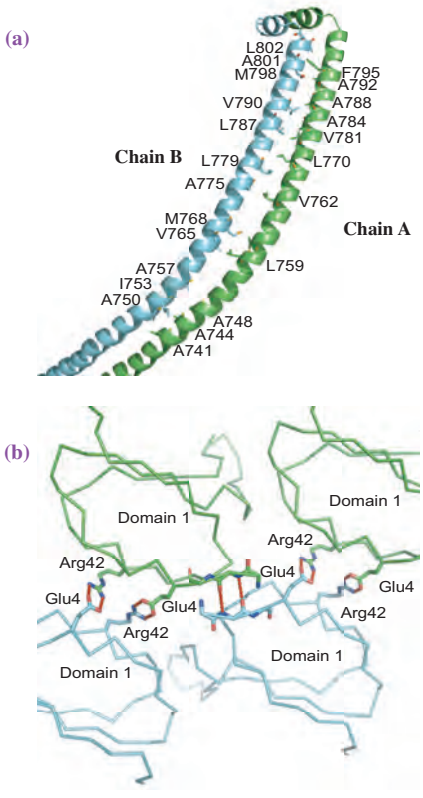

Fig. 3. **(a)** Hydrophobic interactions of the cap-helix domain. In the cap-helix domain, most of the hydrophobic residues appear at the interface between two helices, where they are able to engage in hydrophobic interactions. **(b)** Intermolecular interactions between two half-vaults. The N-terminal residues of domain 1, Met1-Glu4, form an intermolecular antiparallel β-sheet of the same residues of an MVP molecule related by a twofold rotational symmetry. Another specific interaction between two half-vaults is the ionic bond between Glu4-Arg42.

(Protein Data Bank entry 3BK6) and the flotillin-2 band-7 domain ($Flot^{BD7}$) (Protein Data Bank entry 1WIN). Three structures of the shoulder domain, $PhSto^{CD}$ and $Flot^{BD7}$, can be superposed well (Fig. 4). Human stomatin, which has 40.3% and 18.4% sequence identities with $PhSto^{CD}$ and $Flot^{BD7}$, respectively, is a major integral membrane protein of human erythrocytes. The core domain of stomatin is evolutionarily conserved, and falls within the stomatin/prohibitin/flotillin/HflK/C (SPFH) domain family [4]. Although the physiological function of stomatin is not yet clearly understood, the protein is known to be a lipid raft protein; the SPFH domain is involved in lipid raft association. The structural similarity among the shoulder domain and SPFH domain family supports the hypothesis that MVP is recruited to lipid rafts when human lung epithelial cells are infected with *Pseudomonas aeruginosa* [5].

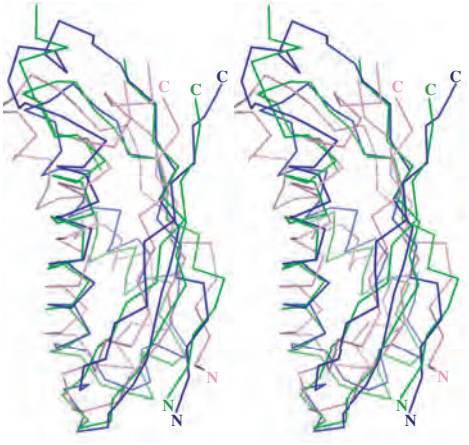

Fig. 4. Three-dimensional structure comparison of the MVP shoulder domain with $PhSto^{CD}$ and $Flot^{BD7}$. The shoulder domain (green), $PhSto^{CD}$ (blue) and $Flot^{BD7}$ (pink), are superposed well within 2.2 Å of root-mean-square deviation of equivalent Cα atoms by least-squares fitting.

Koji Kato[a], Hideaki Tanaka[b] and Tomitake Tsukihara[a,b,*]

[a] Department of Life Science, University of Hyogo
[b] Institute for Protein Research, Osaka University

*E-mail: tsuki@protein.osaka-u.ac.jp

References

[1] N.L. Kedersha *et al.*: J. Cell Biol. **110** (1990) 895.
[2] *H. Tanaka, K. Kato, E. Yamashita, T. Sumizawa, Y. Zhou, M. Yao, K. Iwasaki, M. Yoshimura and T. Tsukihara: Science **323** (2009) 384.*
[3] K. Kato *et al.*: Acta Crystallogr. D **64** (2008) 525.
[4] H. Yokoyama *et al.*: J. Mol. Biol. **376** (2008) 868.
[5] M.P. Kowalski *et al.*: Science **317** (2007) 130 (2007).

Conformational Transition of Sec Machinery Inferred from Bacterial SecYE Structures

Most proteins synthesized in the cytoplasm are secreted across or integrated into membranes. The protein-conducting channel, called Sec translocon, provides a channel-like pathway for protein translocation [1]. In bacteria, the core component of the translocon complex is composed of SecY, SecE and SecA ATPase that drives the protein movement across the membrane (Fig. 1(a)). In 2008, we determined the first crystal structure of the bacterial Sec translocon at 3.2 Å resolution and proposed the initiation mechanism of the SecA-driven protein translocation from structural-based functional analysis [2].

Although the three-dimensional structure of the Sec translocon had not been solved for a long time, the first structure of the SecY complex, archaeal SecYEβ, reported in 2004 provided a lot of findings about the Sec machinery [3]. As shown in Fig. 1(b), the transmembrane (TM) 1-5 and TM6-10 of SecY are arranged like a 'clam shell' and SecE backs up the architecture. There is an hourglass-shaped pathway in the center of SecY for protein transport, which is blocked by a 'plug helix'. During protein translocation, conformational changes have been suggested, such as removal of the plug and expansion of the inner space of SecY. Because the archaeal SecYEβ structure was in a closed state with the plug blocking the channel and archea lacks SecA, the structure determination of different states of the Sec translocon, as well as that of the bacterial Sec translocon, is crucial to fully understand the SecA-dependent pathway. We collected the X-ray diffraction data of SecYE from a SecA-containing organism, *Thermus thermophilus*, at 3.2 Å resolution at beamline **BL41XU** and determined its crystal structure after seven years of trial and error. The structure, solved as a complex with an anti-SecY Fab fragment, is similar to that of the archaeal SecYEβ, except that it has a novel crevasse on the cytoplasmic side (Fig. (2)). The Fab interacts with the protruded cytoplasmic parts to which SecA binds, which raises a possibility that Fab mimics SecA to interact with SecY. Structural comparison with the closed form (archaeal SecYEβ) revealed that expanding the TM2-TM8 distance creates the crevasse that is composed of highly conserved hydrophobic residues. Interestingly, this region just corresponds to a potential signal peptide-binding site. Here, we named the Fab-bound form of SecYE as 'pre-open' state. Molecular dynamics and disulphide mapping analysis suggested that SecA binding induces the conformational changes from the stably closed state to the pre-open state.

From site-specific cross-linking analysis based on the structures of *T. thermophilus* SecYE and SecA, a normally embedded conserved region of SecA, Motif IV, interacts with the protruded region of SecY (Fig. 3(a) dashed line). The observation that the interaction physically separates NBF1 (ATPase domain) and IRAa (regulatory domain of ATPase activity) of SecA excellently explains the Sec translocon-mediated stimulation of the ATPase activity. Taken all together, we proposed the model of SecY and SecA interactions in the first stage of protein translocation (Fig. 3(a)); first, SecY and SecA specifically interact with each other; next, the binding simultaneously induces their cooperative conformational changes, transformation of SecY from the closed to pre-open form and exposure of Motif IV of SecA; finally, after the transfer of the pre-protein with its signal sequence to the hydrophobic crevasse of SecY, the protein translocation starts. We are currently performing experiments to verify whether the model is reasonable.

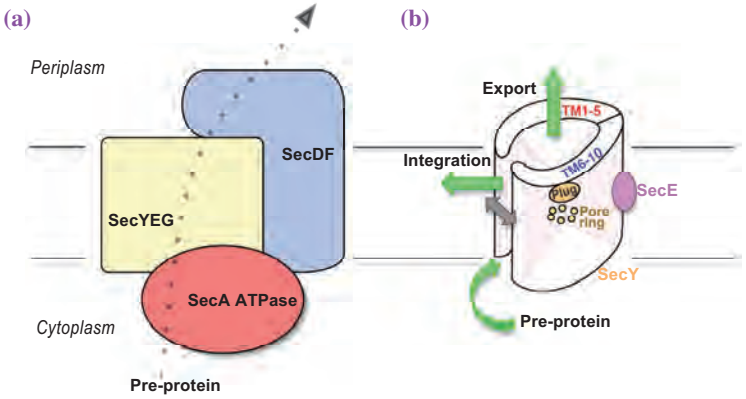

Fig. 1. Protein translocation *via* Sec machinery. **(a)** Sec translocon membrane protein complex, **(b)** Architecture of hourglass-shaped SecY complex.

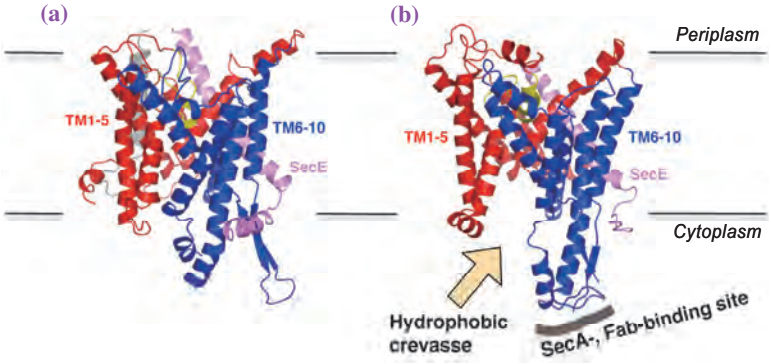

Fig. 2. Crystal structures of Sec translocon. **(a)** Closed form (Archae SecYEβ), **(b)** Pre-open form (*T. thermophilus* SecYE).

In the same issue as our original paper [2], the structure of the SecYEG-SecA complex (4.5 Å) was reported [4]. In that article, conformational changes of SecY and SecA were also observed. The pre-protein binding domain of SecA formed the 'clamp' that was located just above the channel pore of SecY. On the other hand, the clam shell architecture of SecY was slightly opened more than the pre-open form. This structural analysis suggested that the IRA1 of SecA repeatedly pushes the pre-protein into the pore of SecY, which drives protein transport [Fig. 3(b) red arrow]. Our proposed model in Fig. 3(a) may represent the conformational changes of Sec translocon prior to the stage shown in Fig. 3(b).

In Fig. 3(a), we represented the model that dimeric SecY complexed with monomeric SecA functions. Here, we did not discuss the oligomeric state of Sec proteins owing to space limitations, whereas it still remains unclear. To fully understand the SecA-dependent protein translocaiton, we are attempting to obtain much more information about the Sec translocon machinery. It is endlessly interesting [5].

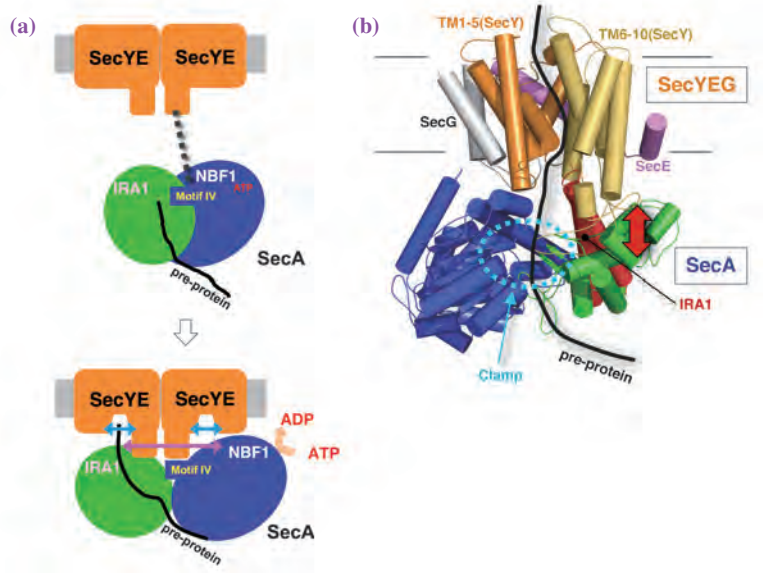

Fig. 3. SecA-SecY interactions. **(a)** Our proposed model of the protein translosation. Both SecA and SecY components undergo conformational changes of their interactions. **(b)** SecA-driven protein translocation model inferred from the crystal structure of SecA-SecYEG complex. SecA is shown in red, green and blue. SecY, SecE and SecG are shown in orange, pink and gray, respectively.

Tomoya Tsukazaki* and Osamu Nureki

The Institute of Medical Science,
The University of Tokyo

*E-mail: ttsukaza@ims.u-tokyo.ac.jp

References

[1] T.A. Rapoport: Nature **450** (2007) 663.
[2] *T. Tsukazaki, H. Mori, S. Fukai, R. Ishitani, T. Mori, N. Dohmae, A. Perederina, Y. Sugita, D.G. Vassylyev, K. Ito and O. Nureki: Nature **455** (2008) 988.*
[3] B. van den Berg *et al.*: Nature **427** (2004) 36.
[4] J. Zimmer *et al.*: Nature **455** (2008) 936.
[5] *H. Mori and T. Tsukazaki: Tanpakushitu Kakusan Koso **54** (2009) 685 (in Japanese).*

Crystallographic Study of the Conserved N-Terminal Domain of the Peroxisomal Matrix-Protein-Import Receptor, Pex14p

Peroxisome is a ubiquitous, single-membrane-bound organelle in eukaryotic cells [1]. It functions in various metabolisms such as detoxification using hydrogen peroxide (H_2O_2), and β-oxidation of very long fatty acids. Its deficiency is involved in inherited diseases such as Zellweger syndrome. Peroxisomal matrix proteins synthesized in the cytosol are imported into the peroxisome by a dynamic system consisting of many peroxins (Pex1p~Pex26p). Peroxisomal matrix proteins harbor the peroxisomal targeting signals. The signals are specifically recognized by Pex5p or Pex7p, depending on their types. The Pex5p and Pex7p-Pex5p complex are docked with the peroxisomal matrix-protein-import receptor Pex14p, which is a central component in the peroxisomal protein import system. The conserved N-terminal domain of Pex14p is involved in interactions with Pex5p, Pex13p and Pex19p [2]. The interaction between Pex14p and Pex5p is mediated via the WXXXF/Y motifs located in the N-terminal half of Pex5p. Pex14p is in different oligomeric states according to the interacting partners. However, no structural information on Pex14p is available.

The full-length Pex14p was less likely suitable for structure determination by X-ray crystallography because the protein is a membrane protein with a multi-domain structure. However, it is known that the amino acid sequences of a domain in the N-terminus of Pex14p are highly conserved between eukaryotic species. Limited proteolysis assays and circular dichroism spectroscopy were employed for constructing variants suitable for crystallographic studies. Consequently, we successfully prepared high-quality crystals using a truncation variant (Pex14p(25-70)) of the domain from *Rattus norvegicus* (rat). Native PAGE analysis indicated that Pex14p(25-70) retained binding ability with the WXXXF/Y motif peptides. The crystals belong to the space group I23 with cell parameters of $a=(b=c=)$ 90.6 Å. The structure was determined at 1.8 Å resolution using diffraction data collected at **BL41XU** beamline [3]. The conserved N-terminal domain of Pex14p has three α helices (α1– α3) with a right-handed twist as shown in Fig. 1. In addition, a short 3_{10} helix is located between the α1 and α2 helices. Similar structures are frequently observed in DNA/RNA-binding proteins. The domain is stabilized by the rigid hydrophobic core. Two pockets are formed at a side of the molecule (Fig. 2). The residues of the side are conserved in a high degree. Two phenylalanine residues (Phe35 and Phe52) are exposed to the solvent, while these are highly

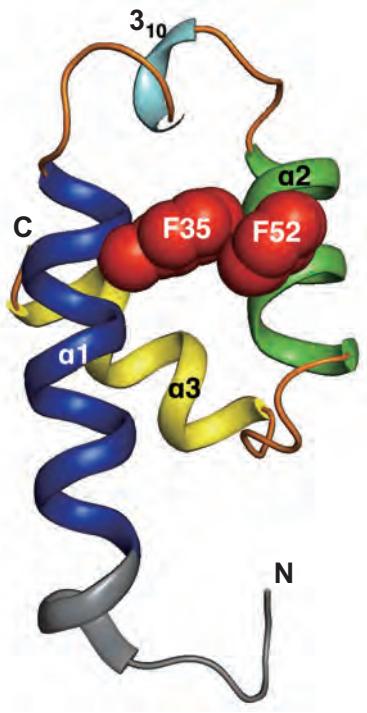

Fig. 1. Overall structure of the conserved N-terminal domain of Pex14p. The completely conserved phenylalanine residues (Phe35 and Phe52) are represented as CPK models in red.

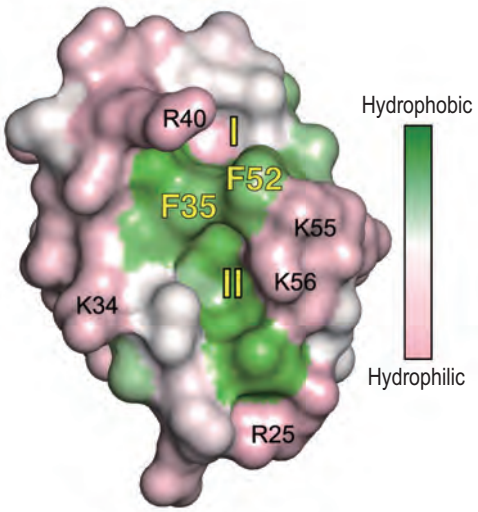

Fig. 2. Hydrophobicity for the hydrophobic side of the conserved N-terminal domain of Pex14p. The molecular surface of the domain is colored in a gradation from pink (hydrophilic) to green (hydrophobic) according to the degree of hydrophobicity. It should be noted that the surface around the two putative binding pockets (I and II) is divided by the hydrophobic phenylalanine residues (Phe35 and Phe52) exposed to the solvent.

hydrophobic. The pockets are surrounded by several basic residues such as Arg25, Lys34, Arg40, Lys55 and Lys56. Consequently, the two pockets are suitable for recognizing the helical WXXXF/Y motif of Pex5p, in which the two conserved aromatic residues of the motif are at the same side of the helix. The aromatic residues of the WXXXF/Y motif can be stabilized by π–π and cation–π interactions in the binding pockets (Fig. 3). Further *in vitro* and *in vivo* assays confirmed that the Phe35 and Phe52 of Pex14p are essential for the interaction between Pex14p and Pex5p [3].

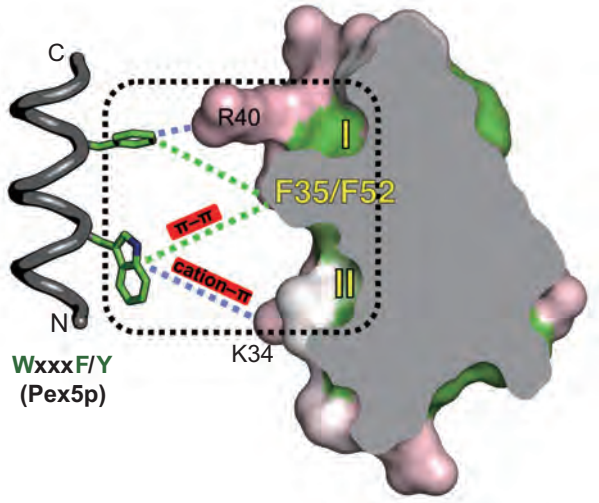

Fig. 3. Molecular model for the interaction between Pex14p and Pex5p. The section view of Pex14p is rotated by 90 degrees from Fig. 2 around the vertical axis. The helical WXXXF/Y motif utilizes its conserved aromatic residues to plug the pockets of Pex14p *via* π–π interactions between aromatic residues. The cation–π interactions may enhance the binding affinity.

Jian-Rong Su [a], Kazuki Takeda [a] and Kunio Miki [a,b,*]

[a] Dept. of Chemistry, Graduate School of Science, Kyoto University
[b] SPring-8 / RIKEN

*E-mail: miki@kuchem.kyoto-u.ac.jp

References

[1] S. Subramani *et al.*: Annu. Rev. Biochem. **69** (2000) 399.
[2] R. Itoh and Y. Fujiki: J. Biol. Chem. **281** (2006) 10196.
[3] *J.-R. Su, K. Takeda, S. Tamura, Y. Fujiki and K. Miki: Proc. Natl. Acad. Sci. USA* ***106*** *(2009) 417.*

Insights into the Stator Assembly of the Na^+-Driven *Vibrio* Flagellar Motor from the Crystal Structure of MotY

Motile bacteria swim by rotating a helical filamentous organelle called flagellum. Each flagellum is driven by a reversible rotary motor embedded in the cell envelope. The flagellar motor is about 45 nm in diameter and divided into a rotating part (rotor) and a stationary part (stator) (Fig. 1). The energy source of the motor is a membrane gradient of a specific ion (H^+ or Na^+), and its flux through the stator channel is coupled with rotor-stator interactions to generate torque [1]. Marine bacterium *Vibrio alginolyticus* swims using a single polar flagellum in liquid environment. Its Na^+-driven motor rotates surprisingly fast, up to 1700 rps at 300 mM NaCl, and requires unique proteins, MotX and MotY, in addition to the PomA/PomB stator proteins for torque generation (Fig. 1, right). MotX and MotY form a complex in the periplasm, and MotX affects the membrane localization of PomB, suggesting that MotX interacts with PomB. Recently, MotX and MotY have been found to form a ring-like structure (T-ring) beneath the P-ring of the flagellar basal body in *V. alginolyticus*. Furthermore, in the absence of MotX or MotY, the PomA/PomB stator does not localize to the flagellated cell pole, suggesting that these two proteins are involved in the incorporation and/or stabilization of the PomA/PomB complex within the motor [2]. To understand the role of MotY in the assembly and function of the Na^+-driven motor, we determined the structure of MotY from *V. alginolyticus* at 2.9 Å resolution using diffraction data collected at beamline **BL41XU** [3].

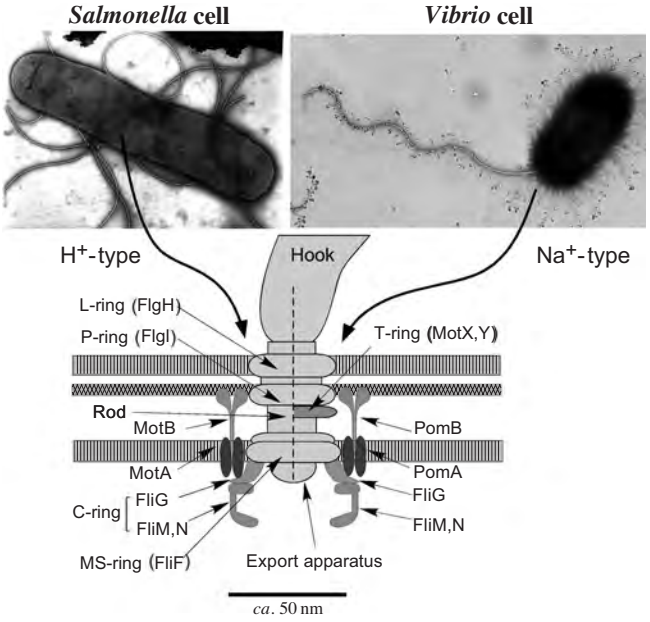

Fig. 1. Cell body and flagellar basal body structure of the H^+- and Na^+-driven types. The stator consists of MotA and MotB for the H^+-driven motor, and of PomA and PomB for the Na^+-driven type. For *Vibrio*'s Na^+-driven polar flagellar motor, MotX and MotY, which form the T-ring in the basal body, are also essential for rotation.

The structure shows two distinct domains: an N-terminal domain (MotY-N) and a C-terminal domain (MotY-C) (Fig. 2(a)). MotY-N has a unique structure, composed of two β-sheets and two α-helices. The C-terminal end of helix α2, which is followed by MotY-C, is anchored to sheet-B through a disulfide bridge between Cys-25 in β3 and Cys-147 in α2 (Fig. 2(b)). The two Cys residues are conserved in MotY from various bacteria with polar flagella. Therefore, MotY proteins containing the C25S, C147S, and C25S/C147S substitutions were susceptible to proteolysis and resulted in cells with reduced or lost motility, indicating that the disulfide stabilizes MotY-N [4]. MotY-C that contains a putative peptidoglycan-binding motif forms an α/β sandwich structure showing remarkable similarity to other OmpA/MotB-like proteins, such as the core domain of Pal and the OmpA-like domain of RmpM. The structural similarity suggests that MotY interacts with the peptidoglycan layer like those proteins. In the crystal structure, however, the putative peptidoglycan-binding site of MotY-C was more widely open than those of Pal and RmpM, and most of the loops forming the peptidoglycan-binding pocket were disordered (Fig. 2(c,d)). A disordered peptidoglycan-binding pocket may be an important property for free MotY since, after secretion into the periplasm, MotX and MotY presumably must diffuse around until they collide with the basal-body and form the T-ring structure. Therefore, MotY should not bind tightly to the peptidoglycan layer before it encounters the basal-body. Interaction with the basal-body may induce folding of the disordered chains into a functional peptidoglycan-binding pocket.

On the basis of the structure and lines of evidence obtained from biochemical experiments using MotY fragments, we propose a model for stator assembly (Fig. 3). MotY may form a complex with MotX and diffuse around the periplasm with little or no affinity for the peptidoglycan layer (Fig. 3(a)). When the complex associates with the basal-body via MotY-N, conformational changes are induced that greatly increase the affinity of MotY-C for peptidoglycan. The

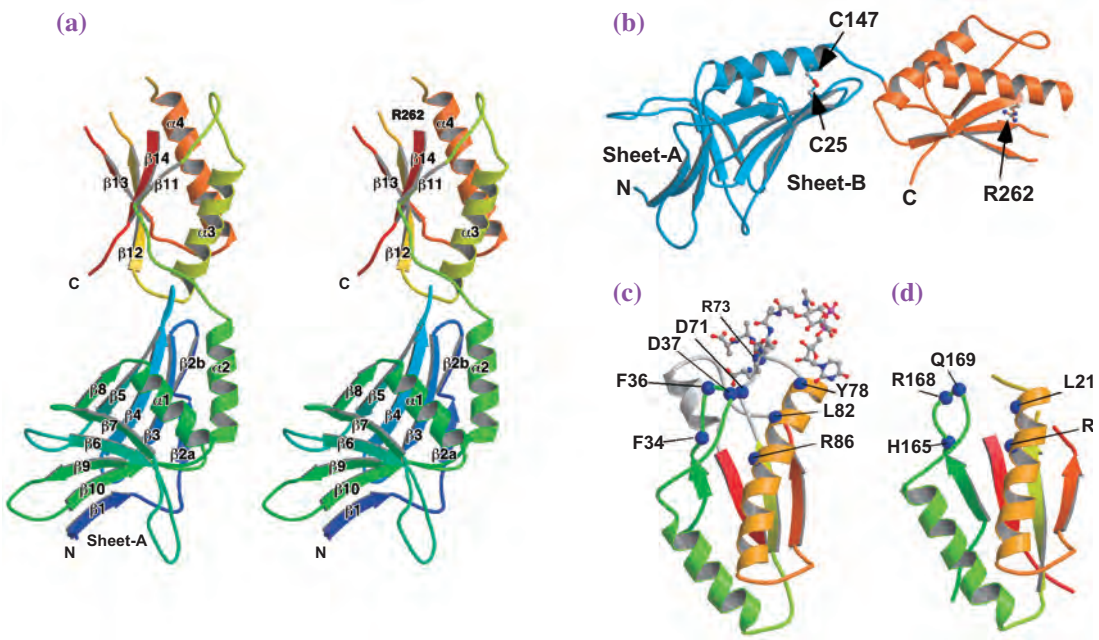

Fig. 2. Structure of MotY. **(a)** Stereo view of the Cα ribbon drawing of MotY. **(b)** The N-terminal and C-terminal domains are shown in blue and orange, respectively. The disulfide bond between Cys-25 and Cys-147 and the Arg-262 residue are displayed in a ball-and-stick format. **(c)** **(d)** Structure of Pal in complex with the peptidoglycan precursor **(c)** [5] and putative peptidoglycan-binding regions of MotY **(d)**. The residues contributing to the binding of the peptidoglycan precursor and the corresponding residues in MotY are indicated by blue balls. The peptidoglycan precursor is shown in a ball-and-stick representation.

PomA/PomB complex also forms before associating with the motor and diffuses around in the cytoplasmic membrane (Fig. 3(b)). When the PomA/PomB complex encounters the basal-body, the association of the periplasmic C-terminal domain of PomB with MotX positions PomB to bind to the peptidoglycan layer in the proper orientation to interact productively with the rotor (Fig. 3(c)).

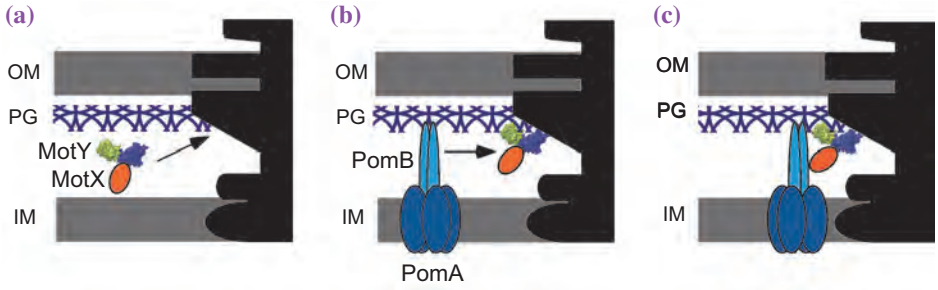

Fig. 3. Model of stator assembly in the Na^+-driven polar flagellar motor of *Vibrio*. MotY is shown as a space-filling model colored blue for MotY-N and yellow for MotY-C. MotX, PomA, and PomB are shown in orange, dark blue, and cyan, respectively. Details of the model are described in the text.

Seiji Kojima[a], Michio Homma[a] and Katsumi Imada[b,*]

[a] Division of Biological Science, Nagoya University
[b] Department of Frontier Biosciences, Osaka University

*E-mail: kimada@fbs.osaka-u.ac.jp

References

[1] H. Terashima *et al.*: Int. Rev. Cell Mol. Biol. **270** (2008) 39.
[2] H. Terashima *et al.*: Mol. Microbiol. **62** (2006) 1170.
[3] *S. Kojima, A. Shinohara, H, Terashima, T, Yakushi, M. Sakuma, M. Homma, K. Namba and K. Imada: Proc. Natl. Acad. Sci. USA* ***105*** *(2008) 7696.*
[4] J. Yagasaki *et al.*: J. Bacteriol. **188** (2006) 5308.
[5] L.M. Parsons *et al.*: Biochemistry **45** (2006) 2122.

Stator Assembly and Activation Mechanism of the Flagellar Motor Revealed by the Crystal Structure of the Periplasmic Region of MotB

The bacterial flagellar motor is a supramolecular nanomachine powered by the electrochemical potential difference of ions across the cell membrane and spins flagellar filaments to drive cell motility [1]. In the *Salmonella* motor, torque is generated by rotor-stator interactions coupled with proton translocation through the channel within the $MotA_4MotB_2$ stator complex. To produce a fully functional motor, multiple stator units have to be incorporated into appropriate positions around the rotor and anchored to the peptidoglycan (PG) layer by the peptidoglycan-binding (PGB) domain of MotB. The motor complex is not a rigid structure; the stators dynamically assemble to and disassemble from the functional motor. Moreover, overproduction of the MotA/MotB complex does not affect cell growth, suggesting that the proton-conducting activity of the MotA/MotB complex is tightly coupled to its incorporation around the rotor. To elucidate the molecular mechanisms of the stator assembly and activation, we determined the 1.75 Å resolution structure of a C-terminal fragment of *Salmonella* MotB ($MotB_C$) that contains the PGB domain and covers the entire periplasmic region essential for motility using X-ray diffraction data collected at beamline **BL41XU** [2].

$MotB_C$ (residues 99-276) appears as a single domain structure with a long N-terminal α-helix (α1) protruding from the domain (Fig. 1). The core of the domain has a typical OmpA-like structure and shows considerable structural similarities to other PGB domains such as the C-terminal regions of PAL, RmpM, and MotY. Although the N-terminal region of $MotB_C$ shows a relatively low sequence similarity among MotB proteins from various bacterial species, secondary structure prediction using the PSIPRED server suggests that α1, α2 and β1 are common structural elements. $MotB_{C2}$ forms a dimer through the interaction between the PGB domains. Mutation analyses of the residues on the dimer interface indicated that dimerization through the PGB domain is crucial to the motor function.

Superposition of the structure of PAL bound to the PG precursor [3] on the $MotB_{C2}$ structure allowed us to predict the PGB site of $MotB_C$ (Fig. 2(a)). The identified PGB sites are present on the top surface of the $MotB_{C2}$ dimer and located opposite to α1. Since $MotB_{\Delta L}$, which is a mutant MotB whose internal fifty residues (Ser51 to Lys100) were deleted, can form a functional stator with MotA, the $MotA/B_{\Delta L}$ complex must be anchored to the PG layer around the rotor. However, the size of the $MotB_C$ dimer is too small to reach the PG layer. Therefore, a large conformational change is required for anchoring the stator. Because the PGB core forms a conserved compact domain, the N-terminal region of $MotB_C$ is the most plausible candidate for the conformational change (Fig. 2(b)). Mutation in α1 (L119P or L119E) of $MotB_{\Delta L}$ affected the cell growth when overproduced, and mutant cells showed significantly better motility than wild-type $MotB_{\Delta L}$ under non-inducing conditions, supporting the idea that the mutations alter the structure of the $MotA/B_{\Delta L}$ complex to an active conformation for proton translocation across the cell membrane as well as for the functional motor assembly.

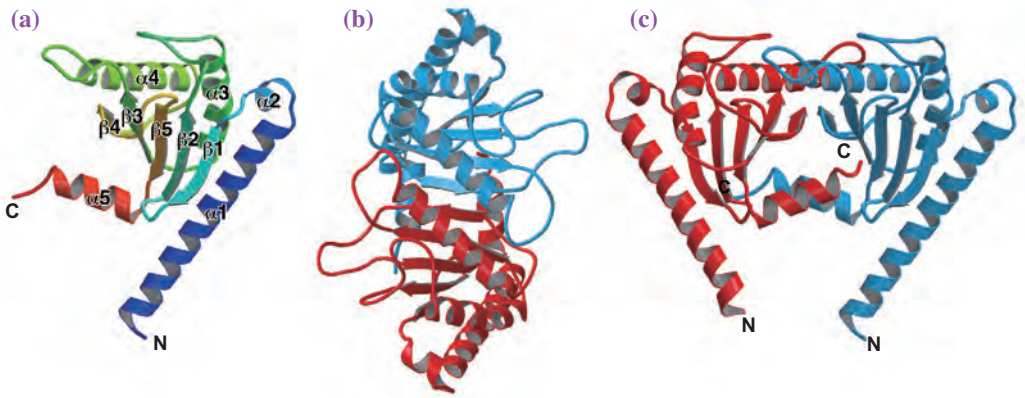

Fig. 1. Structure of the C-terminal fragment of MotB and its dimer. **(a)** Cα ribbon drawing of $MotB_C$, color coded from blue to red from the N- to the C-terminus. $MotB_C$ is composed of a typical common PGB core domain (α3, α4, β2, β3, β4 and β5) and N- and C-terminal sub-structures (α1, α2, α5 and β1). **(b)** and **(c)** Cα ribbon representation of the $MotB_C$ dimer along and perpendicular to the 2-fold axis. Two subunits are colored cyan and red.

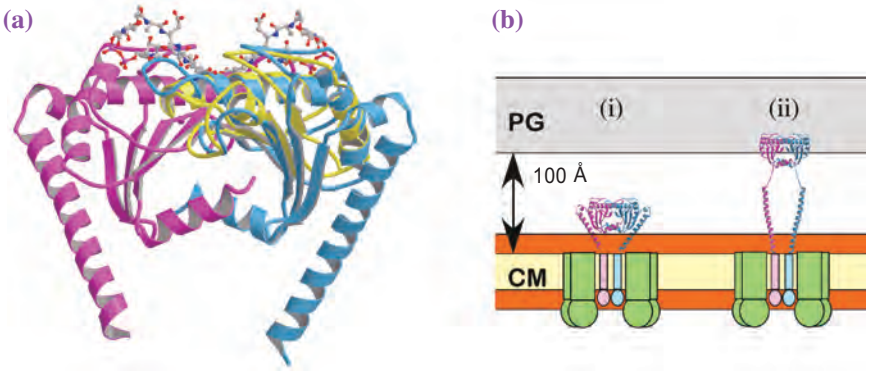

Fig. 2. Conformational changes of PEM required for anchoring the stator. **(a)** Possible PG binding site of $MotB_C$. The structure of *Haemophilus influenzae* Pal (yellow) in complex with a PG precursor (ball-and-stick) is superimposed on subunit A (cyan) and subunit B (magenta) of the $MotB_C$ dimer. Note that only the PG precursor is shown for the Pal complex superimposed on subunit B. **(b)** Plausible models of $MotB_{\Delta L}$ in a freely diffusing, inactive form (i) and in a PG layer-anchored, active stator form assembled into the motor with the proton channel opened (ii). The cytoplasmic segments and transmembrane helices of $MotB_{\Delta L}$ are displayed as rods and ellipsoids colored in pink and cyan. The green boxes and balls represent MotA subunits. The hydrophilic surface and hydrophobic core layers of the cell membrane (CM) are shown in orange and yellow, respectively. The relative sizes of $MotB_{\Delta L}$, PG, and CM are shown in the correct scale.

On the basis of these results, we propose the assembly and activation mechanism of the stator (Fig. 3). Before associating with the rotor, the MotA/B complex would dynamically diffuse in the cytoplasmic membrane. When the MotA/B complex is incorporated into an appropriate position around the rotor, the association signal triggers the conformational changes of the N-terminal region of $MotB_C$ to allow the PGB domain to anchor to the PG layer as well as to open the proton channel to activate the motor. Our study thus unveiled a novel activation mechanism of the stator coupled with its own assembly.

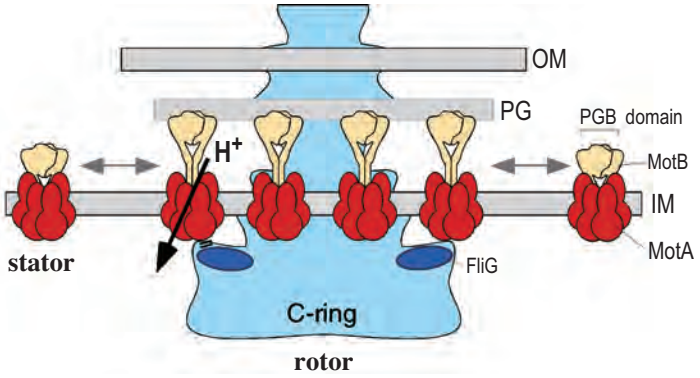

Fig. 3. Proposed model for activation of the proton channel by association with the motor. The MotA/MotB stator complex diffuses through the cytoplasmic membrane with inactive form for proton conduction. When incorporated, the conformational change in the N-terminal region of $MotB_C$ is induced to open the proton channel and allow the PGB domain to anchor the PG layer at the appropriate position near the rotor.

Seiji Kojima[a], Katsumi Imada[b,*] and Keiichi Namba[b]

[a] Division of Biological Science, Nagoya University
[b] Department of Frontier Biosciences, Osaka University

*E-mail: kimada@fbs.osaka-u.ac.jp

References

[1] H. Terashima *et al.*: Int. Rev. Cell Mol. Biol. **270** (2008) 39.
[2] *S. Kojima, K. Imada, M. Sakuma, Y. Sudo, C. Kojima, T. Minamino, M. Homma and K. Namba: Mol. Microbiol. 73 (2009) 710.*
[3] L.M. Parsons *et al.*: Biochemistry **45** (2006) 2122.

Life Science:

X-ray imaging is a relatively new application of synchrotron radiation. It is still not widely recognized as a major tool in biology. However, since the emergence of third-generation synchrotron radiation facilities, imaging techniques have been developed extensively. Even though there are other competitive methods for structural studies, high resolution synchrotron imaging is now established as a useful tool in biology, as well as in many other fields of sciences. In particular, microtomography, which enables one to investigate the three-dimensional structure of an object at high resolution, is a unique method. As a result of intensive development, several variations of the imaging techniques are now available.

Professor Takahashi used high resolution tomography to investigate a fossil flower. The study revealed the structure of a flower smaller than 3 mm in size, and from its details, it is now established as a new fossil species. Dr. Mizutani also used microtomography to visualize neurons in the brain. The samples were stained with high-Z elements to enhance contrast. A neuronal network was beautifully visualized at sub-micron resolution.

Professor Takeda' s group used phase-contrast tomography to investigate the microstructures of glomeruli and tubular structures of the kidney. This technique makes use of a Bonse-Hart type interferometer. Its advantage over conventional absorption-based tomography is its much higher density resolution. Thus, biological samples with only small density variations can be visualized. The kidney of a human disease model hamster was studied, and the details of the lesions were detected.

Medical Biology

Dr. Maeshima and Dr. Nishino used X-ray coherent diffraction. This technique is different from other imaging techniques in that it does not record an image but reconstructs it from the X-rays scattered by an object. This reconstruction is performed entirely by a computer and facilitated by oversampling the scattering intensity distribution. Just as with the other imaging techniques, a 3D structure can be obtained by rotating the sample and recording many scattering data. They used this technique to visualize a human chromosome. The 2D resolution was 38 nm and the 3D resolution was 120 nm. This technique is just an early stage of application because it is expected to become a more powerful tool when combined with XFEL, which will be available in a few years.

There are two other reports using diffraction. Dr. Inui used small-angle scattering to investigate the function of PGDS, a protein that may be useful as a drug delivery vehicle. It is interesting to note that small-angle scattering is based on the same principle as the diffraction imaging used by Maeshima and Nishino. The difference is that within the X-ray beam, there is only one object with a fixed orientation in the case of diffraction imaging, whereas there are nusmerous identical objects with random orientations in small-angle scattering. Dr. Oda used a fiber diffraction technique to study the structure of an actin filament, which is a ubiquitous component of cell motility. Information obtained by electron microscopy was combined with the fiber diffraction data to reveal the structural change in actin monomers when they assemble into a filament.

These articles make a good showcase of a variety of techniques for studying non-crystalline biological samples using synchrotron radiation. They help us to recognize how these structure-oriented X-ray techniques, from projection imaging (radiograph) to fiber diffraction and eventually to crystalline diffraction, are related to each other.

Naoto Yagi

"Lupinasu" - *Lupin*

Inner Structure of Cretaceous Fossil Flower Revealed by X-Ray Microtomography (XRMT)

Flowering plants (angiosperms) consisting of more than 350,000 living species dominate the vegetation of most terrestrial ecosystems. The origin and early evolution of angiosperms had remained as an abominable mystery in evolutionary biology in the last twenty-five years. Recent paleobotanical studies of the early fossil history of angiosperms have, however, been revolutionized with the discovery of small and well-preserved three-dimensional fossil flowers (mesofossils) from Cretaceous between 125 and 65 million years before present. The mesofossils that are usually preserved as charcoal from ancient forest fires provide unrivalled insights into the structure, biology and evolutionary relationships of ancient angiosperms. The paleobotanical studies have greatly increased the quantity and quality of information available about the structure and relationships of Cretaceous flowers [1].

There are usually one or a few specimens available for the paleobotanical studies of mesofossils in Cretaceous, and synchrotron radiation X-ray microtomography (SRXTM) is a useful new tool for obtaining details of the internal structure without the need for destructive analysis. The SRXTM at beamline **BL20B2** is a powerful tool for obtaining a new level of detail from fossil angiosperm flowers from Cretaceous.

The Kamikitaba plant mesofossil assemblage, the first and unique record of mesofossil preservation from eastern Asia, was isolated from carbonaceous, black, poor-sorted sandy siltstone (Late Cretaceous; early Coniacian, *ca*. 89 million years before present) in Fukushima Prefecture, Japan [2]. After drying in the laboratory, the sedimentary rock samples were disaggregated in water and sieved through a 150 μm mesh. The carbonaceous debris recovered was then cleaned of adhering mineral material by treatment with hydrofluoric and hydrochloric acids, thoroughly rinsed in water, and dried in air. Individual specimens were separated by picking under a dissecting microscope. The assemblage includes well-preserved angiosperm flowers, fruits, seeds, leaf fragments and wood [2].

During the study of the Kamikitaba assemblage, a new specific and well-preserved fossil flower, less than 3 mm in diameter, was recovered from the assemblage [3]. The fossil flower was observed in detail with FE-SEM (field emission scanning electron microscopy) and then exposed to an 8-keV X-ray at beamline BL20B2 for microtomography analysis to characterize the internal structures. The three-dimensional microtomography (micro-CT) images of the fossil flower were reconstructed with Tri3DVOL software by Ratoc System Engineering Co. (Tokyo). These reconstructions also allowed the electronic removal of the androecium (male organ) to better reveal the structure of the gynoecium (female organ).

The structure of the fossil flower revealed by SRXTM at beamline BL20B2 is as follows. The fossil flower is small, pedicellate, bisexual, and actinomorphic (Fig. 1). The floral receptacle is flattened and disk-shaped, with a perianth consisting of a small number of tepals, born in at least two cycles, around the rim. The androecium (male organ) comprises ~90-100 stamens that are curved toward the center of the flower. Stamens are stout, with no clear differentiation into anther (pollen organ) and filament. The thecae (pollen sacs) are lateral to abaxial in position, extended for most of the length of the stamen, and have latrorse-extrorse dehiscence. The connective is expanded above the thecae into a prominent, flattened, sterile apical appendage. The gynoecium (female organ) is composed of ~100-120 free carpels born on a small, conical projection in the center of the receptacle (Fig. 2). SRXTM now provides new information on important organizational features of the fossil flower and therefore allows a more thorough discussion of the phylogenetic position of the fossil flower. On the basis of comparison with extant plants, the fossil flower is established a new fossil species of Annonaceae (Custard-Apple family)

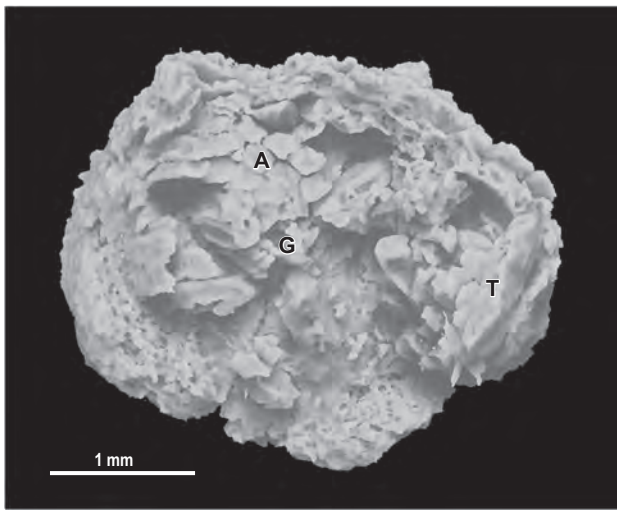

Fig. 1. XRMT image of fossil flower of *Futabanthus asamigawaensis* Takahashi *et al*. (Annonaceae) from the Futaba Group (89 Ma, Late Cretaceous) of northeastern Japan. Scale bar = 1 mm. T: tepal (perianth), A: androecium (male organ), G: gynoecium (female organ).

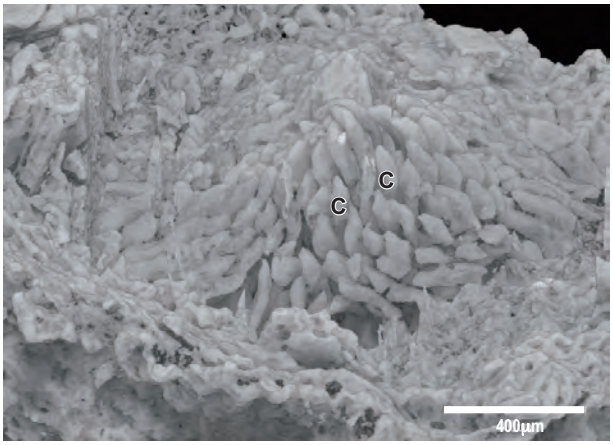

Fig. 2. Lateral view of closely packed carpels revealed after stamens are removed from the XRMT image. Scale bar = 400 μm. C: carpel.

under a scientific name, *Futabanthus asamigawaensis* Takahashi *et al.* (Fig. 3) [3].

The extant Annonaceae is a large family of chiefly tropical trees and shrubs, comprising ~128 genera and ~2500 species. The family is the most diverse group of basal angiosperms, some of which are used for their fruits. A most striking feature of the *Futabanthus* flower, compared with flowers of extant Annonaceae, is its very small size and the corresponding small size of the stamens and carpels. The small size of the fossil flower fits the consistent pattern observed when many other Late Cretaceous flowers are compared with flowers of their extant relatives. The fossil provides the earliest record of the family and documents the presence of Annonaceae in eastern Eurasia during the middle part of the Late Cretaceous. Evidence that Annonaceae were already differentiated in the Late Cretaceous of Asia is also interesting with respect to the biogeography of the family. Recognition of probable crown-group Annonaceae in the middle of the Late Cretaceous (Coniacian, 89 Ma) in Japan extends significantly the age of the family and indicates an earlier presence in eastern Eurasia than might have been expected. The results have been spectacular and promise to open up new levels of insight into the evolution of flowers and flowering plants from the age of Cretaceous.

Fig. 3. Reconstructed illustration of Cretaceous fossil flower, showing two trimerous perianth cycles, numerous stamens, and numerous carpels.

Masamichi Takahashi

Graduate School of Science and Technology,
Niigata University

E-mail: masa@env.sc.niigata-u.ac.jp

References

[1] E.M. Friis *et al.*: Palaeo **232** (2006) 251.
[2] M. Takahashi *et al.*: J. Plant Res. **112** (1999) 187.
[3] *Masamichi Takahashi, Else Marie Friis, Kentaro Uesugi, Yoshio Suzuki and Peter R. Crane: Int. J. Plant Sci.* ***169*** *(2008) 908.*

Revealing Human Brain Circuits by Microtomography

The three-dimensional cellular and subcelluar structures of biological tissues and organs are essential for their functions. This particularly holds true with the brain. Neurons build up neuronal circuits as three-dimensional networks in the brain tissue. Human brain functions, including verbal ability and scientific thinking that you are now exerting to read this report, solely depend on neuronal circuits. Therefore, visualizing the three-dimensional neuronal networks of the brain tissue is the first step to understanding the functional mechanisms of the human brain.

Computed tomography (CT) is a noninvasive technique for visualizing visceral structures. The application of X-ray microscopy approaches to CT analysis has led to the visualization of three-dimensional microstructures, although biological samples composed of light elements give little contrast in hard X-ray images. Although the application of phase contrast techniques to unstained biological tissues delineated the distribution of native electron densities, the electron density itself has no inherent relationship with biological functions or cellular organization.

In clinical diagnosis, luminal structures of a living body are visualized using X-ray contrast media. These contrast media contain high-atomic-number (high-Z) elements that absorb hard X-rays efficiently. Therefore, the X-ray visualization of microstructures of soft tissues can be performed by contrasting each biological constituent with high-Z probes, which corresponds to fluorescent labels in light microscopy. Labelling with high-Z probes allows radiographic analysis of the three-dimensional structure of neural tissues [1]. The distributions of multiple high-Z probes can be individually visualized using the X-ray absorption edge of each probe element [2].

Staining neurons with a high-Z probe facilitates the three-dimensional structural study of neuronal networks. We have recently reported the three-dimensional microstructural analysis of human brain tissue using microtomographs [3]. Human neuronal networks were clearly revealed in the microtomographic image of the brain tissue stained with the high-Z probe. Therefore, microtomographic analysis leads to the revealing of the neuronal circuits responsible for human brain functions (Fig. 1).

Human samples were obtained with informed consent, using protocols approved by the clinical research review board. Normal brain tissue from the middle part of the inferior frontal gyrus was dissected at autopsy. The tissue was stained and embedded as described previously [2-4]. Microtomographic analyses were performed at **BL20XU**, **BL20B2** and **BL47XU** beamlines. Radiographs taken by rotational scan were subjected to CT reconstruction using the program RecView (available from http://www.el.u-tokai.ac.jp/ryuta/) accelerated with CUDA parallel-computing processors. The spatial resolutions of the microtomographs were estimated using three-dimensional test patterns [e.g. Ref. 5].

The obtained structure indicated that the neuronal networks and capillary vessel architectures were visualized as the three-dimensional distribution of X-ray absorption coefficients. Skeletonized wire models of the structural constituents were built by placing and connecting nodes in the three-dimensional density maps. The model-building procedures were similar to those reported for crystallographic analyses of macromolecular structures, while neuronal processes were automatically traced using a three-dimensional Sobel filter [4]. The cell types of the models were determined from the morphology of somata and dendrites. Electron density maps and a skeletonized wire model of pyramidal neuron 3013 in Layer III of the gray matter are shown in Fig. 1(b).

The three-dimensional structure of the obtained models clarified the network structures embedded in the brain tissue (Fig. 1(c)). The neuronal circuits were then resolved from the neuronal models. The analytical approach based on the three-dimensional structure of the neuronal networks allows discussions of the operating mechanism of the neuronal circuits in the human frontal cortex [4].

At present, the primary method for visualizing three-dimensional structures of soft tissues including neural tissue is confocal light microscopy. However, the absorptive and refractile nature of ultraviolet, visible and infrared lights with respect to biological tissues makes it difficult to visualize three-dimensional structures of block samples. Results obtained in our studies indicated that the three-dimensional microstructure of human brain tissue can be visualized by using the microtomographs. Therefore, the synchrotron radiation microtomography along with high-Z probe contrasting is a potential method of revealing the neuronal circuits of brain, like X-ray crystallography in molecular biology.

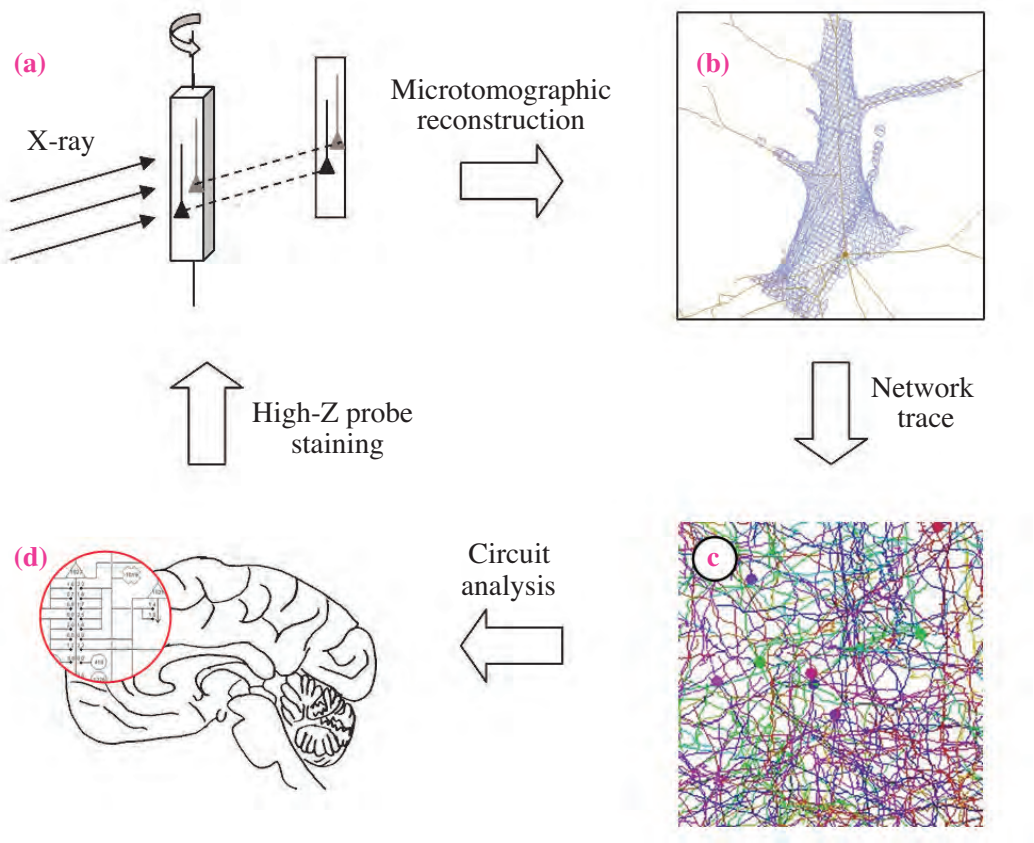

Fig. 1. Schematic diagram of microtomographic analysis of neuronal circuits in human brain. Human brain tissue dissected at autopsy was subjected to high-Z probe staining. The three-dimensional microstructure of the brain tissue was determined by microtomographic analysis **(a)**. The obtained three-dimensional maps were used for density tracing **(b)**, giving the neuronal networks **(c)**. Neuronal circuits responsible for human brain functions were analytically resolved from the traced networks **(d)**.

Ryuta Mizutani

Department of Applied Biochemistry,
Tokai University

E-mail: ryuta@tokai-u.jp

References

[1] R. Mizutani *et al*.: J. Synchrotron Rad. **14** (2007) 282.
[2] R. Mizutani *et al*.: Tissue Eng. **C14** (2008) 359.
[3] R. Mizutani *et al*.: Brain Res. **1199** (2008) 53.
[4] *R. Mizutani, A. Takeuchi, K. Uesugi, S. Takekoshi, R.Y. Osamura and Y. Suzuki: Cerebral Cortex (2010) - in press. DOI: 10.1093/cercor/bhp237.*
[5] R. Mizutani *et al*.: Micron **41** (2009) 90.

X-Ray Phase-contrast Microtomography for Visualizing of Renal Microstructures in Albino-Panda-Albino Hamsters

Small laboratory animal model of human diseases such as the albino-panda-albino (APA) hamster, which is known to develop spontaneous renal focal segmental glomerulosclerosis (FSGS) with age, has been used in basic and premedical research of the kidney. Since the pathological diagnosis of FSGS with a scattered small pathological lesion is often missed when only a few sliced sections are examined, a sufficiently large sample, the sample site, and serial sliced sections are often required for exact diagnosis.

X-ray crystal interferometer-based (Bonse-Hart type [1]) X-ray phase-contrast microtomography (phase-contrast microtomography) [2] enables us to reveal the microstructures of soft tissue, such as cancerous mass, necrosis, fibrous capsule, fat tissue and surrounding normal tissue without the use of a contrast agent [3]. An experimental imaging by phase-contrast microtomography was performed with fixed renal specimens of hamster to confirm the feasibility of this technique as a nondestructive method. This system consists of a triple Laue-case X-ray interferometer with a 40-μm-thick analyzer [4], a sample cell and an X-ray CCD camera with the pixel size of 4.34 μm (Fig. 1). Experiments were carried out at the undulator beamline **BL20XU**.

In our study [5], albino-panda-albino (APA) hamsters and age-matched Syrian hamsters were used. After whole-body perfusion with physiological saline solution, the kidneys were quickly extracted and fixed with formalin. The images of glomeruli and tubular structures were similar to those observed using 40-100 folds magnification on an optical microscope. In four specimens from two female APA hamsters, 7 scattered lesions were detected. Wedge-shaped pathological lesions including mild atrophic tubular walls, markedly dilated tubular lumen, high-density glomeruli and widening of Bowman's space were observed quantitatively. Wall thickness and lumen diameter of tubules were calculated in normal and abnormal areas of the cortex. The thinnest tubular wall was about 12 μm. The glomerular volume was calculated and compared between the normal (n = 25) and abnormal glomeruli (n = 17) (Fig. 2(a)). The ratio of Bowman's space against glomerular volume in abnormal glomerulus was higher than those in normal glomerulus (Fig. 2(b)). In addition, the mean density of glomerulus in pathological regions was higher than that in normal regions (Fig. 2(c)). On measuring the density of normal glomerulus, the percentile of abnormal glomerulus [normal mean density + 2SD (standard deviation)] was approximately 57.7% in pathological regions in APA hamster.

The renal microvasculature was extracted from 3D phase-contrast microtomography images using the density threshold-based rendering technique. The distributions of the glomeruli, renal arteries and veins were successfully visualized. Glomerular capillary tufts formed by capillary loop and surrounding tubules and vessels were clearly observed (Fig. 3).

In this experiment, blood was washed out from renal vessels to eliminate artifacts. After the injection of physiological saline, the hepatic vessel of the rat could be visualized clearly by X-ray phase-contrast radiography, whereas the X-ray absorption-contrast image could not reveal the vessel at the same X-ray dose and energy [6]. This procedure was much easier and is considered to preserve more the physiological condition than using conventional contrast agents with high viscosity. The fine density difference among physiological saline within tubules, vessels, and surrounding soft tissue of kidney was discriminated sufficiently on the images. In addition, by volume

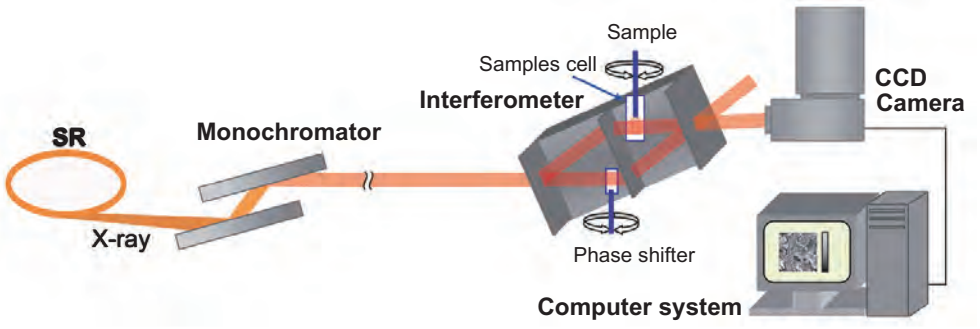

Fig. 1. System of X-ray crystal interferometer-based X-ray phase-contrast microtomography. [5]

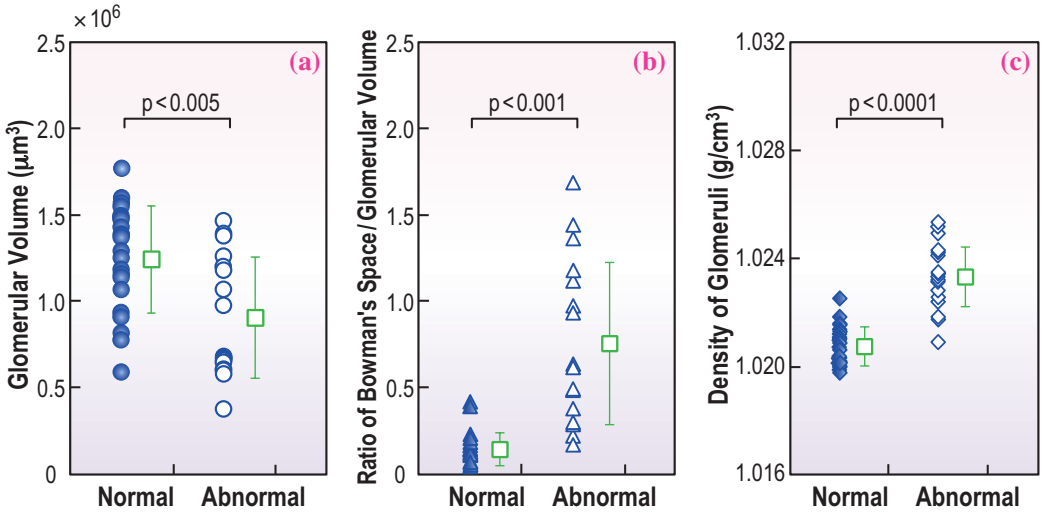

Fig. 2. Quantitative analysis of glomerulus images obtained by X-ray phase-contrast microtomography. **(a)** The mean volumes are $(1.24 \pm 0.31) \times 10^6$ μm^3 and $(0.91 \pm 0.35) \times 10^6$ μm^3 in normal and abnormal glomeruli, respectively ($p < 0.005$). **(b)** The ratio of Bowman's space against glomerular volume in abnormal glomeruli was higher than those in normal glomeruli (0.74 ± 0.47 *vs.* 0.13 ± 0.10, $p < 0.001$). **(c)** The density of abnormal glomerulus is about 2.6 mg/cm^3 higher than that of normal glomerulus (1023.3 ± 1.1 mg/cm^3 *vs.* 1020.7 ± 0.7 mg/cm^3, $p < 0.0001$). [5]

rendering technique, the renal microstructures and microvasculature could be depicted from the same specimen at one scan without any contrast agents.

We considered that phase-contrast microtomography might be used as a powerful auxiliary tool for pre-histological evaluation to detect and analyze the position of a small scattering lesion and its spread in the renal disease models.

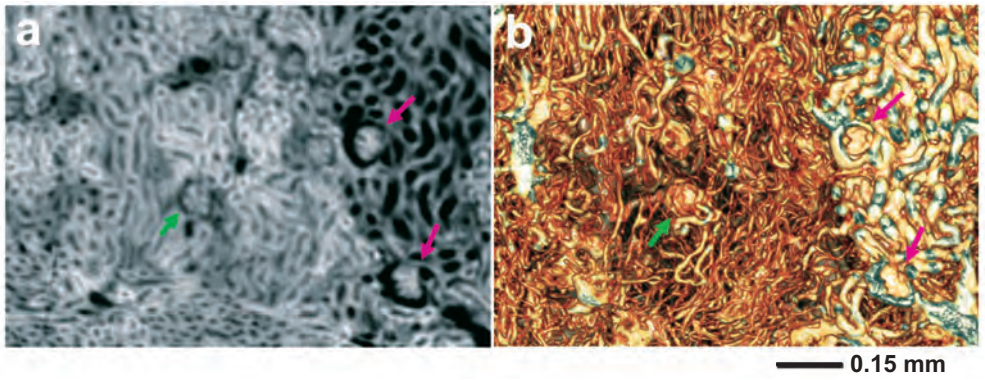

Fig. 3. X-ray phase-contrast microtomogram of renal cortex **(a)** and three-dimensional extracted renal microvasculature and tubule **(b)**. The distributions of renal arteries and veins were successfully visualized. The capillary tufts are clearly observed in normal glomerulus (green arrow), whereas the widening of Bowman's space and the indistinct pattern of the capillary loop are observed in abnormal glomerulus (pink arrow). In the three-dimensional image, non-dilated tubules and non-atrophic glomeruli are shown in normal cortical areas, whereas dilated tubules and atrophic glomeruli are clearly revealed in FSGS lesions. [5]

Jin Wu[a], Tohoru Takeda[b,*] and Atsushi Momose[c]

[a] Division of Clinical Neuroscience, Chiba University Center for Forensic Mental Health
[b] Allied Health Sciences, Kitasato University
[c] Graduate School of Frontier Sciences, The University of Tokyo

*E-mail: t.takeda@kitasato-u.ac.jp

References

[1] U. Bonse and M. Hart: App. Phys. Lett. **6** (1965) 155.
[2] A. Momose *et al.*: Nature Medicine **2** (1996) 473.
[3] T. Takeda *et al.*: Radiology **214** (2000) 298.
[4] A. Momose *et al.*: J. Phys. **104** (2003) 599.
[5] *J. Wu, T. Takeda, T.T. Lwin, A. Momose, N. Sunaguchi, T. Fukami, T. Yuasa and T. Akatsuka: Kidney International 75 (2009) 945.*
[6] T. Takeda *et al.*: Circulation **105** (2002) 1708.

Three-Dimensional Visualization of a Human Chromosome Using Coherent X-Ray Diffraction

When we want to know the structure of a protein or its complex, we have to make its crystals in advance. If we are lucky, we will obtain the crystals and then X-ray crystallography will yield the structure of the protein or its complex with about 1 Å resolution. However, when we want to know the detailed structure of much bigger objects such as cellular organelles, for example, chromosomes or nuclei, what should we do? Such objects with varying sizes and shapes do not form crystals for X-ray crystallography. Moreover, they are too thick for electron microscopy. Coherent X-ray diffraction microscopy (XDM) is the method to achieve it [1].

When a noncrystalline object is illuminated by coherent, monochromatic X-rays having a well-defined phase, a continuous diffraction pattern called speckles occurs (Fig. 1(b)). In the case of light microscopy, this kind of diffraction from an object is converted into a real-space image by lenses. Unfortunately, we do not have good optical lenses for X-rays. Recently, it became possible to convert the diffraction into a real-space image by computational calculation, instead of lenses [2]. If the diffraction speckle pattern is recorded finely enough to satisfy the "oversampling condition," which is related to the Shannon sampling theorem [3], the structure can be reconstructed by an "iterative phase retrieval method," a process by which computers find a structure to fit the diffraction pattern [2]. That is, XDM is an emerging technique for "lensless" high-resolution X-ray microscopy.

We observed a human chromosome using XDM [1]. Chromosomes are essential organelles for the transmission of replicated genomic DNA into two daughter cells during cell division [4]. Although more than 100 years have passed since chromosomes were first observed, how a long string of genomic DNA is packaged into compact chromosomes remains unclear.

A schematic of XDM measurement of a human chromosome at beamline **BL29XUL** is shown in Fig. 1(a). X-rays at an energy of 5 keV passed through a 20-μm-diameter pinhole to illuminate the target chromosome only, which was stuck to a thin silicon nitride membrane. The coherent diffraction (speckles) from the chromosome was recorded with an X-ray direct-detection charge-coupled device (CCD) 1.32 m downstream from the sample. A beamstop before the CCD blocked the unscattered direct X-ray beam.

From the coherent diffraction pattern (Fig. 1(b)), a human chromosome image was reconstructed. A two-dimensional (2D) reconstruction of the human chromosome is shown in grayscale (Fig. 2(a)) and in color (Fig. 2(b)). Note that the intensities are proportional to the projection of the electron density. The spatial resolution of the 2D reconstruction is 38 nm. The most striking feature in the reconstruction is the high-intensity region near the chromosome axes with a width of ~200 nm (Fig. 2(b)). The axial structure has so far been detected only using immunoelectron microscopy or fluorescence microscopy on labeling condensin and topoisomerase IIα, which are essential proteins for the chromosome assembly process [4].

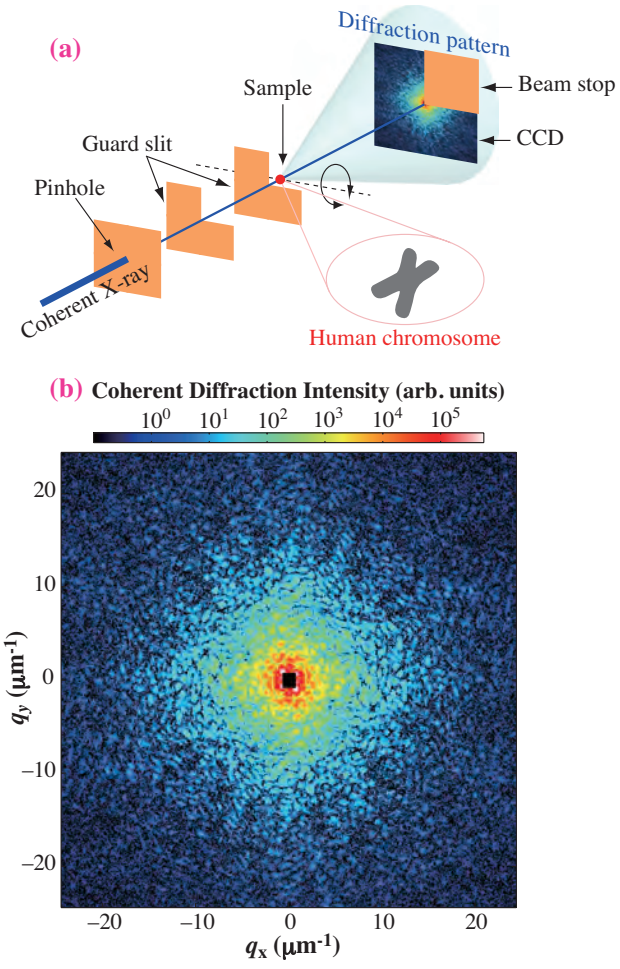

Fig. 1. **(a)** Schematic of XDM measurement of an unstained human chromosome at BL29XUL. **(b)** Coherent diffraction (speckles) from the chromosome.

For three-dimensional (3D) reconstruction, we obtained data at different incident angles ranging from –70° to +70°(38 diffraction data sets). A reconstructed 3D electron density map of the chromosome is shown in Fig. 2(c). The reconstructed chromosome image also has the highest electron density around the centromere. This can be explained by the fact that the centromere region is more condensed than other chromosomal regions. We estimate the spatial resolution of the 3D reconstruction to be 120 nm. This is the first 3D electron density mapping of an unstained cellular organelle using XDM.

Since the spatial resolution of microscopy is determined by the wavelength, hard X-rays can achieve atomic resolution in principle. With third-generation synchrotron radiation X-rays, the spatial resolution is often limited by the radiation damage or the X-ray intensity. Both limitations may be removed or lowered dramatically with the X-ray free electron lasers (XFELs) to produce high peak-brilliance coherent hard X-rays, which is currently being developed [6]. X-ray diffraction resolved the structure of DNA almost 50 years ago [5] and it resolved that of the nucleosome, where DNA is wrapped around histone proteins, 10 years ago [4]. XFELs will enable a dramatic improvement in the spatial resolution of XDM and would accelerate research for the atomic structure analysis of chromosomes and other cellular organelles, including macromolecular complexes [6].

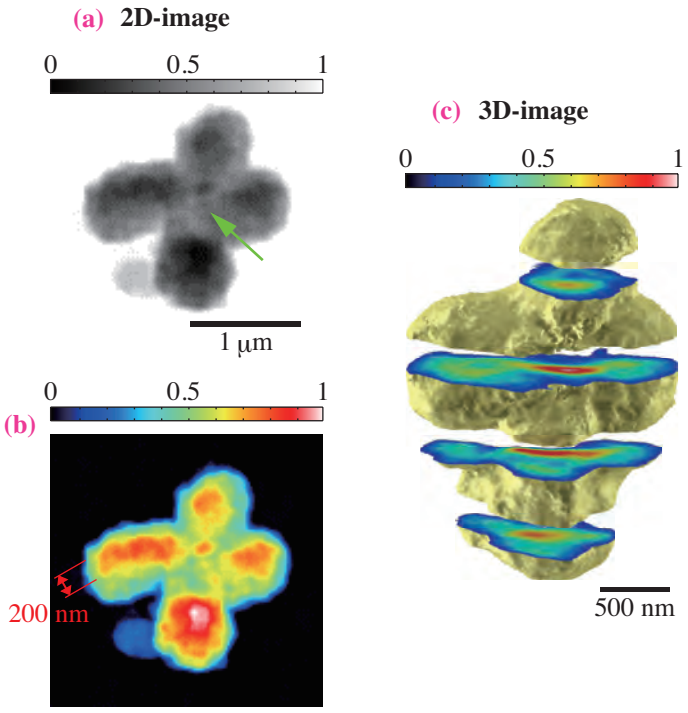

Fig. 2. A two-dimensional reconstruction of the human chromosome is shown in grayscale **(a)** and in color **(b)**. Note that the intensities are proportional to the projection of the electron density. The centromere region is indicated by an arrow in **(b)**. **(c)** Reconstructed 3D electron density map of the chromosome. Cross-sectional images of the chromosome at 409 nm intervals are shown.

Kazuhiro Maeshima[a,*] and Yoshinori Nishino[b,†]

[a] Structural Biology Center, National Institute of Genetics
[b] SPring-8 / RIKEN

*E-mail: kmaeshim@lab.nig.ac.jp

[†] Present address: Research Institute for Electronic Science, Hokkaido University

References

[1] *Y. Nishino, Y. Takahashi, N. Imamoto, T. Ishikawa and K. Maeshima: Phys. Rev. Lett.* ***102*** *(2009) 18101.*
[2] J. Miao *et al.*: Nature **400** (1999) 342.
[3] D. Sayre: Acta Cryst. **5** (1952) 843.
[4] K. Maeshima and M. Eltsov: J. Biochem. **143** (2008) 145.
[5] J.D. Watson and F.H.C. Crick: Nature **171** (1953) 737.
[6] T. Shintake *et al.*: Nat. Photonics **2** (2008) 555.

Compact Packing of Lipocalin-Type Prostaglandin D Synthase Induced by Binding of Lipophilic Ligands

Lipocalin-type prostaglandin D synthase (L-PGDS; prostaglandin-H_2 D-isomerase, EC 5.3.99.2) is responsible for the biosynthesis of prostaglandin D_2 (PGD_2) from prostaglandin H_2, which is a common precursor of all prostanoids [1]. L-PGDS is also known as a member of the lipocalin superfamily, which comprises lipid-transporter proteins such as β-lactoglobulin (βLG), retinol-binding protein (RBP), major urinary protein, aphorodisin, and tear lipocalin. It is well known that the lipocalins are small proteins of approximately 200 amino acid residues and 20 kDa in molecular weight. Their tertiary structures are very similar despite their wide range of functions and high levels of sequence divergence. That is, the lipocalin proteins have a highly symmetrical all-β structure dominated by a single 8-stranded antiparallel β-sheet closed back on itself to form a continuous hydrogen bonded β-barrel. This β-barrel commonly encloses a ligand binding site composed of both an internal cavity and an external loop scaffold [2]. So far, we have clarified that L-PGDS can act not only as an enzyme but also as a lipid transporter. The results of such studies also revealed that L-PGDS can bind a large variety of lipophilic ligands such as retinoids, biliverdin, bilirubin, thyroid hormones, gangliosides, and amyloid beta peptides *in vitro* with high binding affinity. We defined such a feature as 'broad ligand selectivity' [3]. However, in contrast to the extensive data obtained on L-PGDS from many biochemical studies, detailed information about the conformational changes that it undergoes when it forms a complex with a ligand still remains to be forthcoming. Thus, in the present study, we measured the structure of L-PGDS and its complexes with three kinds of lipophilic ligand in solution by the small-angle X-ray scattering (SAXS) method.

Before the SAXS measurements, we first measured the ability of lipophilic ligands to bind L-PGDS by conducting an intrinsic tryptophan fluorescence quenching assay. The fluorescence intensity decreased to less than 13, 10, and 14% of that of L-PGDS itself in the presence of 10 μM RA, BV, and BR, respectively, and the K_d values of L-PGDS were calculated from the quenching curves to be 138 ± 8 nM for RA, 103 ± 5 nM for BR, and 70 ± 7 nM for BV. These results demonstrate that L-PGDS exhibits high binding affinities for RA, BV, and BR. We then determined the SAXS of L-PGDS in the presence or absence of those lipophilic ligands to investigate the structural changes caused by the ligand binding. All SAXS data were collected at beamline **BL40B2** using an R-AXIS IV^{++} system (RIGAKU, Tokyo Japan) as a detector. The X-ray wavelength was tuned to 1.000 Å, and the camera distance was set at 1050 mm. The temperature of the samples was kept at 25°C. For each polypeptide, SAXS profiles were collected at the concentrations of 2.5, 5.0, 8.0, and 12.5 mg ml^{-1}. The molecular structures of the polypeptides were predicted by applying the *ab initio* structure determination program GASBOR [4]. The 10 predicted molecular structures having almost the same overall structures were averaged, and then aligned. The scattering intensity curves of L-PGDS in both the presence and absence of ligands showed a large central peak at a reciprocal vector (S) < 0.032 Å^{-1}, a second peak at S = 0.044 Å^{-1}, and a small maximum at S = 0.075 Å^{-1} (Fig. 1). These curves revealed that L-PGDS has a globular shape in both the presence and absence of ligands. The binding of ligands to L-PGDS caused clear changes in the scattering curve only in the small-angle region (S < 0.02 Å^{-1}, Fig. 1 *inset*). From the Guinier analysis of each scattering curve, the radius of gyration $R_g(0)$ was calculated to be 19.4 ± 0.03 Å for L-PGDS, 18.8 ± 0.10 Å for L-PGDS/RA, 17.3 ± 0.12 Å for L-PGDS/BR, and 17.8 ± 0.04 Å for L-PGDS/BV, indicating that L-PGDS became compact after binding these ligands.

The molecular weights of L-PGDS and its complexes with the ligands were calculated to be 2.0×10^4 – 2.1×10^4 Da from the linear relation

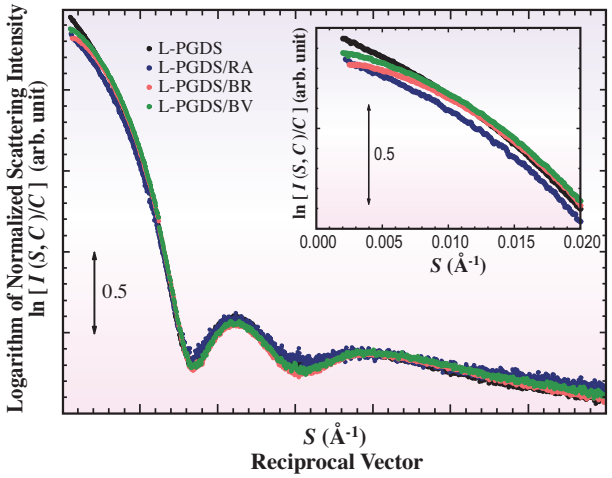

Fig. 1. SAXS profiles of L-PGDS and each L-PGDS complex. SAXS profiles of L-PGDS (black), L-PGDS/RA (blue), L-PGDS/BR (orange) and L-PGDS/BV (green) are shown. The logarithm of scattering intensity is shown as a function of reciprocal vector (S). The inset shows the logarithm of scattering intensity in the small S region.

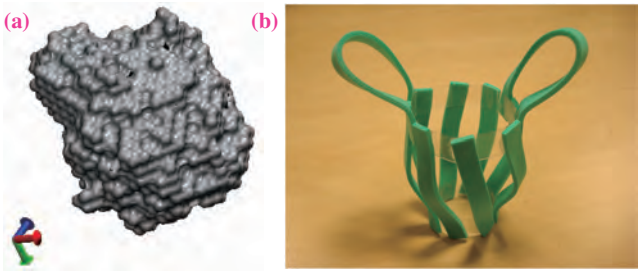

Fig. 2. **(a)** *Ab initio* model of L-PGDS, and **(b)** conceptual 3D molecular model. The *ab initio* model was calculated from $P(r)$ functions using GASBOR. The χ^2 of each model was less than 2.0.

between the forward scattering intensity and the molecular weight of the protein. These values are in good agreement with the molecular weight of L-PGDS calculated from its amino acid sequence (1.9×10^4 Da). To visualize the structure of L-PGDS and its complexes, we calculated their molecular models by the *ab initio* method. The *ab initio* model of L-PGDS showed that the overall structure of the molecule was globular in shape (Fig. 2(a)). Furthermore, to compare the shapes of L-PGDS and its complexes, we superimposed the model of each complex onto that of L-PGDS. The other three models of complexes also had globular shapes, and they became more compact than L-PGDS upon ligand binding (Figs. 3(b), 3(c) and 3(d)). Our data also revealed that the magnitude of compactness may depend on the size of the ligand that binds to L-PGDS. We consider that these results directly indicate the structural flexibility of the L-PGDS molecule. Such structural flexibility may be due to the particular molecular structure of L-PGDS itself and the origin of the compact packing observed only in L-PGDS.

We propose the following model for the binding of the ligands to L-PGDS: a lipophilic ligand enters the large cavity of the β-barrel, which triggers a conformational change such that the molecule of L-PGDS becomes compact, and thus, the ligand is held tightly inside the L-PGDS molecule. This study was published in the Journal of Biochemistry [5].

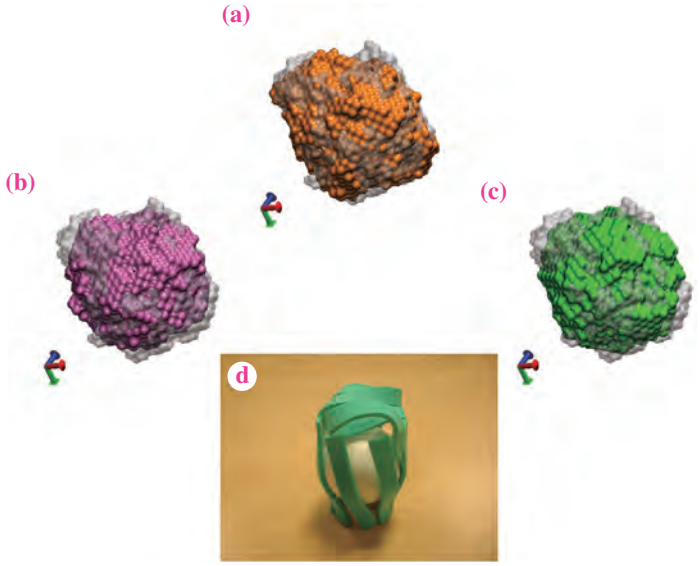

Fig. 3. **(a)** The *ab initio* model of L-PGDS/RA (yellow-colored model) is superimposed on that of L-PGDS (gray-colored transparent model). **(b)** The *ab initio* model of L-PGDS/BR (pink-colored model) is superimposed on that of L-PGDS (gray-colored transparent model). **(c)** The *ab initio* model of L-PGDS/BV (green-colored model) is superimposed on that of L-PGDS (gray-colored transparent model). **(d)** Conceptual 3D molecular model of the L-PGDS complex. Each *ab initio* model was calculated from $P(r)$ functions using GASBOR. The χ^2 of each model was less than 2.0.

Takashi Inui[a,*] and Katsuaki Inoue[b,†]

[a] Laboratory of Protein Sciences, Osaka Prefecture University
[b] SPring-8 /JASRI

*E-mail: inuit@bioinfo.osakafu-u.ac.jp

† Present address: Diamond Light Source, U.K.

References

[1] Y. Urade *et al.*: Prostaglandins Other Lipid Mediat **68-69** (2002) 375.
[2] D.R. Flower *et al.*: Biochim. Biophys. Acta **1482** (2000) 9.
[3] T. Inui *et al.*: J. Biol. Chem. **278** (2003) 2845.
[4] D.I. Svergun *et al.*: Biophys. J. **80** (2001) 2946.
[5] *K. Inoue, N. Yagi, Y. Urade and T Inui: J. Biochem.* ***145*** *(2009) 169.*

Actin Molecule Becomes a Flat Conformation by Polymerization

"Movement" or "Motility" is a fundamental activity in life at multiple scales from body to molecules. In eukaryote cells, there are two kinds of motility system. One is a system composed of motor proteins and rails. The motor proteins move along the rail that is formed by polymerizable proteins, while hydrolyzing ATP, a source of chemical energy. A characteristic of the systems is a high efficiency to convert chemical energy to motility or mechanical work; it exceeds 80% in muscle. The other is the system driven by a polymerization and depolymerization cycle of polymerizable proteins. Actin and tubulin are classified in this category called "cytomotive protein." Similar motility systems are also observed in prokaryote cells, whereas no motor proteins have been found. Therefore, this is an evolutionally primitive system for motility.

Actin monomer (G-actin) bound with ATP is incorporated into actin filament (F-actin), and thereby the actin molecule hydrolyzes the ATP into ADP and phosphate, followed by the release of the cleaved phosphate, and finally, the actin molecule bound with ADP dissociates from the F-actin. The dissociated G-actin exchanges the bound nucleotide from ADP to ATP. Two ends of the F-actin are called the barbed-end and the pointed-end. Owing to the actin ATPase, the critical actin concentration for polymerization is low at the barbed-end while it is high at the pointed-end. Thus, under the physiologically steady condition, the elongation of F-actin mainly occurs at the barbed-end while shrinking is dominant at the pointed-end. The unidirectional polymerization process is a driving force for motility.

To understand the mechanisms of their functions, the structures of G-actin and F-actin are essential. The crystal structure of G-actin was solved in 1990 [1], and an atomic model for the F-actin structure was also proposed, by piling up the G-actin crystal structure according to its helical symmetry [2]. The model accounted for the results of many biochemical experiments. However, the model without any conformational changes does not account for actin functions accompanied by polymerization, such as the activation of the actin ATPase. The conformational changes remained enigmatic.

X-ray fiber diffraction method is suitable for structural analysis of rod-like macromolecule complexes with a helical symmetry. An X-ray fiber diffraction pattern is essentially a section through the cylindrically averaged diffraction pattern from a single fibrous molecule. The cylindrical averaging leads to a significant loss of information. High resolution is essential to obtain a clear answer. To achieve high resolution, we combined several technical advances: we controlled the filament length by adding gelsolin, prepared well-oriented sols of F-actin using an 18 tesla superconducting magnet, and recorded X-ray fiber diffraction patterns to 3 Å at beamlines **BL40B2**, **BL41XU** and **BL45XU**. We created a model of F-actin by using the X-ray fiber diffraction intensities, obtained from well-oriented sols of rabbit skeletal muscle F-actin to 3.3 Å in the radial direction and 5.6 Å along the equator, by altering the crystal structure of G-actin, using the normal modes of actin and a molecular dynamics simulation, while monitoring the R-factor-non-fit, which is equivalent to the free R-factor.

Actin has a nucleotide-binding cleft enclosed by two major domains (Fig. 1(a)). In almost all actin crystal structures, the cleft is closed and the two major domains are in a propeller-like twist with each other.

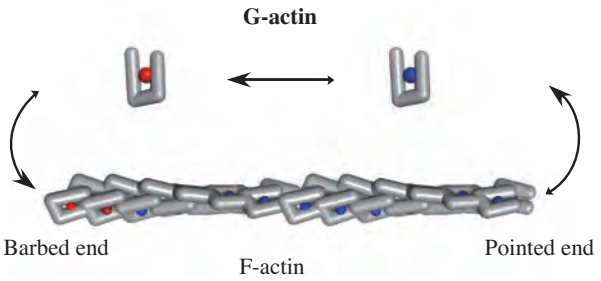

Fig. 1. A polymerization and depolymerization cycle of actin. The cycle is coupled with the actin ATPase. The red sphere represents ATP and the blue sphere represents ADP. Actin has two states: a monomeric G-actin and a polymeric F-actin [4].

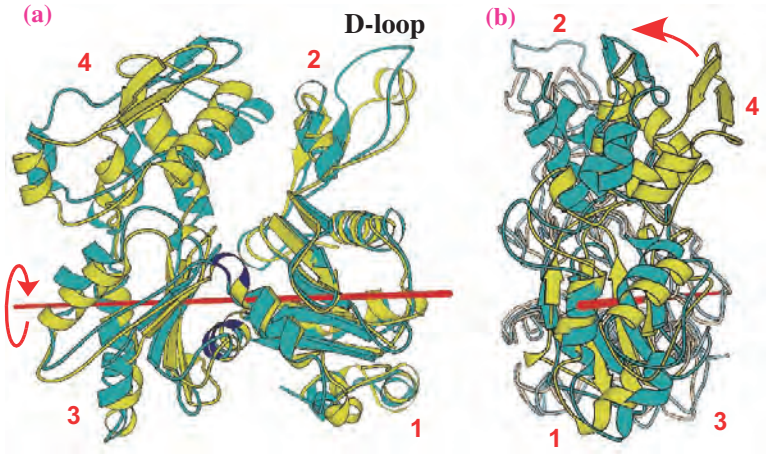

Fig. 2. Comparisons between G-actin (pdb code: 1J6Z: yellow) and F-actin subunit (cyan). **(a)** front view. **(b)** side view. The red line is a rotation axis. The red numbers represent subdomain numbers [5].

This is characteristic of the G-actin conformation (yellow in Figs. 1(a), 1(b)). In our F-actin model, we found a previously unknown flat conformation, in which the cleft remains closed and the two domains are untwisted (cyan in Figs. 1(a), 1(b)). The two conformations are related by a 20° rotation of the two major domains around the axis passing along the front of subdomain 1 and the side of subdomain 3. As a result, the F-actin subunit shows a flat conformation. The overall structure of our F-actin model is shown in Fig. 3(a). The contacts between the actin subunits are shown in Figs. 2(b) and 2(c). A comparison of our F-actin model with the non-helical arrangement of normal G-actin observed in the crystal [3] suggests that the flattening generates extensive intrastrand and interstrand connections.

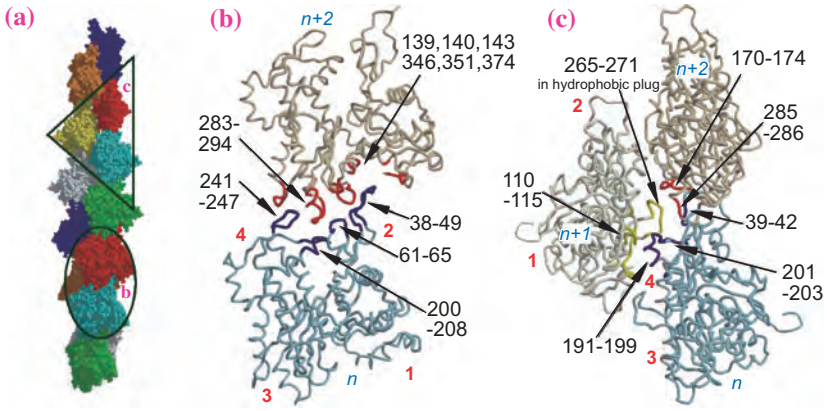

Fig. 3. Overall structure of F-actin. **(a)** Descriptions of F-actin using 13 subunits. In the experiment, the average filament length was controlled to be *ca.* 1 μm (*ca.* 400 subunits). **(b, c)** Contact sites between subunits within F-actin [5].

Toshiro Oda

SPring-8 / RIKEN

E-mail: toda@spring8.or.jp

References

[1] W. Kabsch *et al.*: Nature **347** (1990) 37.
[2] K.C. Holmes *et al.*: Nature **347** (1990) 44.
[3] T. Otomo *et al.*: Nature **433** (2005) 488.
[4] T. Oda: Tanpakushitsu Kakusan Koso **54** (2009) 1864 (in Japanese).
[5] *T. Oda, M. Iwasa, T. Aihara, Y. Maéda and A. Narita: Nature* ***457*** *(2009) 441.*

Materials Science:

As a powerful probe for structural study, beamlines at SPring-8 has been widely recognized so far in Materials Science. A number of internationally top-class research groups have achieved successful results at the cutting-edge of Materials Science. This year, eight outstanding papers have been selected as Research Frontiers in the research field of Materials Science I, Structure. Magnetism is one of the most attractive and challenging research fields in Synchrotron Radiation Science. In the past few years, Dr. H. Ohsumi (RIKEN) has developed magnetic scattering diffractometry by using the high quality diamond X-ray phase retarder at SPring-8. The collaboration with Dr. H. Takagi' s group has lead to success in the research on the magnetism of the 5*d* metal, Ir, in Sr_2IrO_4. This is a milestone success research on magnetism in synchrotron radiation science. Other topical research has also been carried out on the novel superconductor, LaFeAsO, and fulleride superconductor Cs_3C_{60}, to uncover the mechanism of superconducting behavior. Dr. K. Tashiro of Professor T. Aida' s group revealed the molecular arrangement in a newly developed columnar liquid crystalline assembly by amphiphilic molecular design enabling us to understand its prominent electron transport property.

In recent years, the utilization of SPring-8 facilities by international users has been increasing. As a result, "Fulleride Superconductors are Three-Dimensional Members of the High-T_c Family" by Professor Kosmas Prassides and Professor Matt Rosseinsky (UK), "Nature of Structural Transformations in the B_2O_3 Glass under High Pressure" by Professor Vadim V. Brazhkin (Russia) and "Angular Anomaly in the Dynamic Structure Factor of Graphite close to Bragg Reflections" by Professor Lucia Reining (France) have been selected as outstanding research frontiers this year.

Nano applications of structural measurement are also another trend these days. "Analyses on Crystalline Structures of Carbon Nanowalls by Grazing-incidence X-ray Diffraction using Synchrotron Light Source" by Professor M. Hori (Nagoya University) and "X-ray Diffractometry for the Structure Determination of a Submicrometer-scale Single Powder Grain" by Dr. S. Kimura (JASRI) may open the door to a new research field of photon science in SPring-8.

Masaki Takata

STRUCTURE

"Seiyoukinshibai" - *Aaron's Beard or St. Johnswort*

Electronic and Magnetic Structures of Spin-Orbit Coupling Induced Mott Insulator Sr_2IrO_4

Perovskite-type transition metal oxides (TMOs) show many fascinating phenomena, such as high-T_c superconductivity in cuprates and colossal magnetoresistance in manganites. 3*d* TMOs have been extensively studied since their rather narrow *d* band can induce a Mott instability. Valence *d* orbitals of a transition metal ion in an octahedral crystal field are split into the t_{2g} and e_g levels, where the d_{xy}, d_{yz} and d_{zx} orbitals are lower in energy than the $d_{3z^2-r^2}$ and $d_{x^2-y^2}$. When the *d* orbitals are partially and selectively occupied (e.g., by Jahn-Teller effect), the orbital angular momentum of the transition metal ion is totally quenched because the orbitals that are stabilized by the Jahn-Teller distortion are expressed using real wave functions. With increasing period number of an element, the spatial extent of *d* orbitals tends to increase, and therefore, their bandwidth is expected to be broad. Indeed, Sr_2RhO_4 ($4d^5$) is a fairly good metal compared with Sr_2CoO_4 ($3d^5$). Sr_2IrO_4 ($5d^5$) is a magnetic insulator [1], whereas it would have a t_{2g}^5 low-spin state and become a metal with a partially filled wide t_{2g} band. Recently, it has been predicted that the strong spin-orbit coupling recovers the orbital motion of 5*d* electrons; the resultant spin-orbit integrated states form two narrow bands, so that even a small on-site Coulomb repulsion opens a Mott gap [2].

To confirm the realization of a spin-orbit coupling induced Mott insulator, we have conducted resonant X-ray magnetic scattering (RXMS) experiments at beamlines **BL19LXU** and **BL29XU**. We used highly brilliant SR with a photon energy corresponding to Ir *L*-edge (2*p*-5*d*) to explore unconventional electronic states. A selection rule of RXMS identifies a 5*d* state as a complex spin-orbit integrated state and not as a crystal field state [3]. Figure 1 shows RXMS spectra of the magnetic reflection (1 0 22) at the Ir *L* edge. The reflection intensity at the L_2 edge is less than 1% of that at the L_3 edge, which is a direct consequence of a selection rule for RXMS. Figure 2 illustrates 5*d* level splitting by a crystal field and a spin-orbit coupling. RXMS at the L_2 edge becomes forbidden for the spin-orbit integrated state, whereas equal resonant intensities are expected at the L_2 and L_3 edges for the crystal field state. The spin-orbit integrated state well explains the experimentally obtained RXMS spectra.

The magnetic structure of Sr_2IrO_4 remained undetermined, because Ir is a strong neutron absorber. Using the enhancement at the L_3 edge, we have tried to determine the magnetic structure of Sr_2IrO_4. The crystal structure is of the K_2NiF_4 type and shown in Fig. 3(a). Our RXMS results revealed that the magnetic structure is canted antiferromagnetic (see Fig. 3(b)). In zero field, magnetic reflections are observed at (1 0 4*n*+2), (0 1 4*n*) and (0 0 *odd*) as shown in Figs. 3(c)-3(e). By representational analysis with the extinction rule for magnetic reflections, a symmetrically allowed possible magnetic structure is considerably restricted to two candidates. One is compatible with metamagnetism of Sr_2IrO_4 and the other is not, so that the magnetic structure is uniquely specified. The application of a magnetic field induces metamagnetic transition and rearrangement of magnetic moments. The determined magnetic structure also well explains the appearance of a net magnetic moment in the metamagnetic state and an accompanying change in the extinction rule for magnetic reflections [3].

The experimental establishment of the spin-orbit integrated states of valence electrons is a first step for developing a new research field of relativistic materials. For materials characterized by a spin-orbit coupling, RXMS is an ideal method to probe the phase of the outer electron wave function. Our study opens up a new exclusive feature of X-ray magnetic scattering.

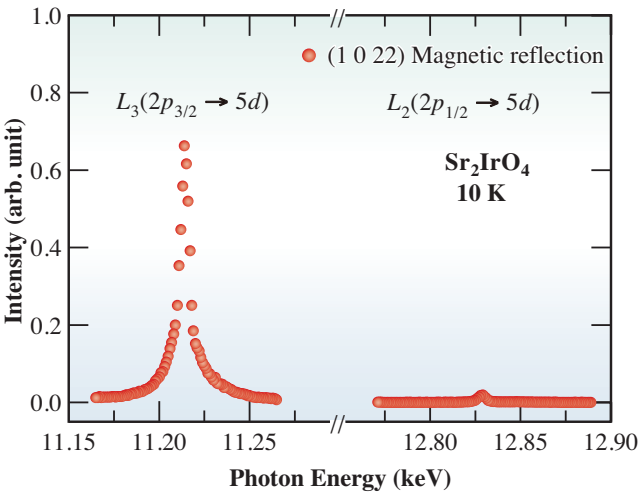

Fig. 1. RXMS spectra of the magnetic reflection (1 0 22) at the *L* edge.

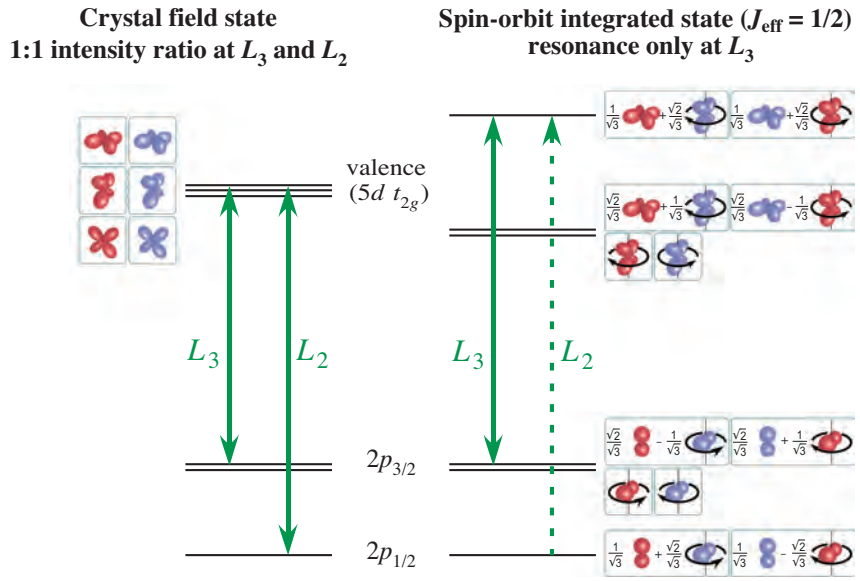

Fig. 2. 5*d* level splitting diagram of (left) a tetragonal crystal field and (right) the spin-orbit coupling. Equal resonant intensities are expected at the L_2 and L_3 edges for the crystal field state. For the spin-orbit integrated state (J_{eff}=1/2), RXMS at the L_2 edge becomes forbidden. Wave functions of 5*d* electrons are depicted with their orbital form and spin. Red and blue correspond to up and down spins, respectively.

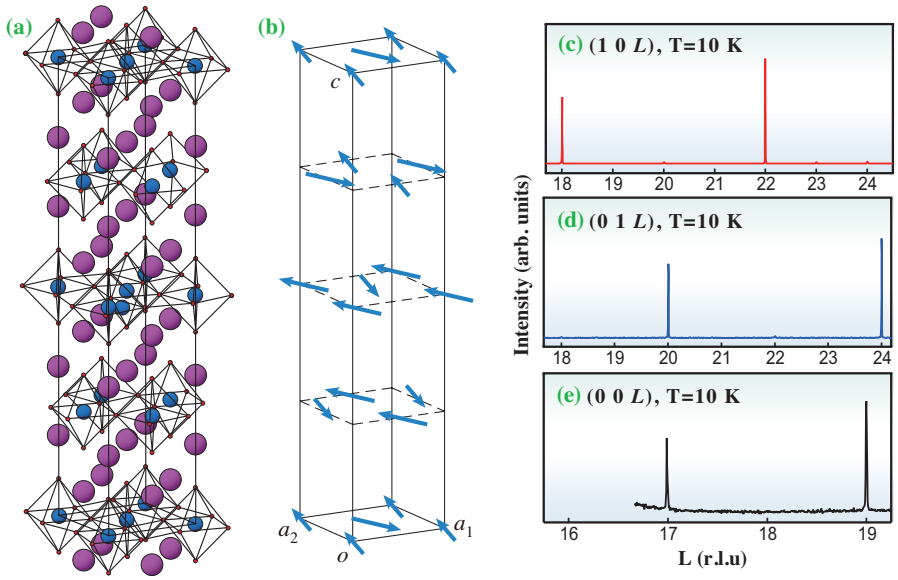

Fig. 3. Crystal and magnetic structures of Sr_2IrO_4. **(a)** Crystal structure of Sr_2IrO_4 (space group $I4_1/acd$). The blue, red and purple spheres represent Ir, O and Sr, respectively. **(b)** Magnetic structure of Sr_2IrO_4 in zero magnetic moment. Arrows represent J_{eff}=1/2 moments. **(c)** Scan profile along the (1 0 *L*) direction at 10 K in zero magnetic field. **(d)** Scan profile along the (0 1 *L*) direction at 10 K in zero magnetic field. **(e)** Scan profile along the (0 0 *L*) direction at 10 K in zero magnetic field.

Hiroyuki Ohsumi[a,*], Taka-hisa Arima[a,b] and Hidenori Takagi[c,d]

[a] SPring-8 / RIKEN
[b] Institute of Multidisciplinary Research for Advanced Materials, Tohoku University
[c] Department of Advanced Materials Science, The University of Tokyo
[d] RIKEN Advanced Science Institute (Wako)

*E-mail: ohsumi@spring8.or.jp

References

[1] G. Cao *et al.*: Phys. Rev. B **57** (1998) R11039.
[2] B. J. Kim *et al.*: Phys. Rev. Lett. **101** (2008) 076402.
[3] *B. J. Kim, H. Ohsumi, T. Komesu, S. Sakai, T. Morita, H. Takagi and T. Arima: Science* ***323*** *(2009) 1329.*

Tetragonal-Orthorhombic Phase Transition in LaFeAsO – Relevant to High-Temperature Superconductivity

The discovery of the high-temperature superconductor, F-substituted LaFeAsO (superconducting temperature: T_c = 26 K) [1] has caused a recurrence of a new superconductivity fever similar to that caused by the finding of the copper oxide superconductors. By replacing La with other rare-earth elements (ex. Sm, Gd), it has been possible to achieve T_c beyond 55 K, which convinced us that the Fe-based superconductors is the "second" high-T_c superconductors beyond the T_c limit of phonon-mediated superconductors (30~40 K).

LaFeAsO is formed by an alternating stack of positively charged LaO layer and negatively charged FeAs layer (Fig. 1) and belongs to the tetragonal *P4/nmm* space group at room temperature (Fig. 1(a)). It is noteworthy that the stoichiometric (parent) LaFeAsO does not exhibit any superconductivity, however, their resistivity and magnetic susceptibility show a sudden decrease at approximately 160 K (T_{anom}) as seen in Fig. 4(a) [1]. They disappear by the F-substitution for O, and coincidentally, the superconducting states appear. On the other hand, no such anomalies have been observed in isostructural low-T_c superconductors including LaFePO (T_c ~4 K), LaNiPO (T_c ~3 K) and LaNiAsO (T_c ~2.4 K), which implies that the phenomena are closely associated with the high-T_c superconductivity. Therefore, to search the origins of the anomalies was one of important missions in the studies of high-T_c superconductivity. In this study, the low-temperature crystal structures of parent and 14 at% F-substituted LaFeAsO (T_c ~20 K) were examined by synchrotron powder X-ray diffraction (XRD) analysis.

The high-resolution synchrotron XRD measurements at various temperatures were conducted at beamline **BL02B2**. All the diffraction peaks of the parent sample at temperatures above 170 K were consistently assigned to the conventional tetragonal phase (*P4/nmm*). However, several peaks including the 110, 111, 112, 211 and 322 reflections of the tetragonal phase start to broaden at around 170 K, and they clearly split into two peaks below 160 K (Fig. 2). On the other hand, such splitting was not observed in the diffraction peaks for the 14% F-substituted sample, which indicates that the superconductivity occurs in the tetragonal phase.

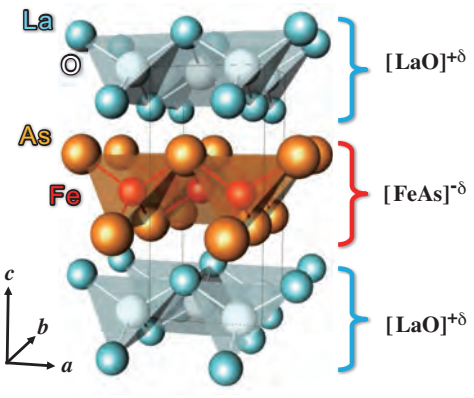

Fig. 1. Layered crystal structure of LaFeAsO. In each layer, the O/Fe atoms are tetrahedrally coordinated by the La/As atoms, respectively.

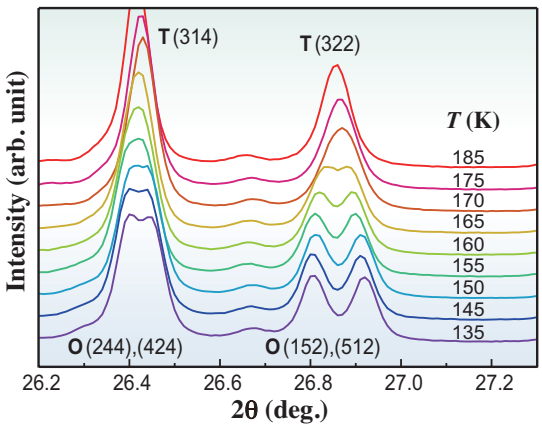

Fig. 2. Diffraction profiles of tetragonal (**T**) 314 and 322 reflections of parent LaFeAsO over the temperature range from 135 K to 185 K. The split peaks below 165 K are indexed as 244, 424 and 152, 512 in the orthorhombic (**O**) symmetry, respectively.

The Rietveld fitting results of each sample at 300 K and 120 K are shown in Fig. 3. The XRD patterns of the F-substituted sample were well fitted with the *P4/nmm* space group over the measured temperature range. For the parent LaFeAsO, the patterns measured above 170 K were also fitted with the tetragonal symmetry; however, the symmetry should be lowered to fit the doublet peaks of the patterns measured below 165 K. The orthorhombic *Cmma* space group provided the smallest R_I and R_{wp} values of 2.1% and 4.6% for the data at 120 K (Fig. 3(b)). Figure 4(b) clearly shows that the *a*-axis lengths split and grow at around 160 K, which corresponds to the temperature where anomalies occur (Fig. 4(a)). The results led us to the conclusion that the anomaly is associated with the crystallographic phase transition from the tetragonal to orthorhombic phase.

As a result of the transition, the *a*- and *b*-axes were rotated by 45° along the *c*-direction relative to those of the tetragonal phase and the lattice constants expand by a multiple of $\sqrt{2}$, although the axis lengths are no longer unequal (Fig. 4(c)). The symmetry of the *Cmma* space group is obtained by removing the confinement

of "*a* = *b*" from the symmetry of *P*4/*nmm*, while keeping the other symmetry elements. Cruz *et al.* have reported the structure phase transition of parent LaFeAsO from the result of the neutron diffraction measurement, but they assigned the monoclinic *P*112/*n* space group for the low-temperature phase [2]. We checked our fitting results with the orthorhombic *Cmma* space group, but no peaks violating the extinction rule have been found in the diffraction patterns down to 25 K. The structural studies of other LnFeAsO structures, such as CeFeAsO [3] and so on, have also shown that the crystal symmetry of the low-*T* phase can be successfully assigned to the *Cmma* space group, citing our report [4]. These results support our determination of the space group.

The neutron diffraction measurement also revealed that a stripe-type antiferromagnetic phase transition occurs at 140 K, a slightly lower temperature than the T_{anom}, and some *ab initio* calculations [4,5] also supported the stability of the antiferromagnetic Fe-spin ordering in the orthorhombic phase. Such tetragonal-orthorhombic and antiferromagnetic phase transitions are common in the parent phases of other high-T_c Fe-based superconductors, and considering the similarity to antiferromagnetic order in the parent phase of copper oxide superconductors, the phase transitions would be closely associated with the appearance of high T_c. Further experimental and theoretical studies are expected to reveal the mysteries of the high-T_c superconductivity.

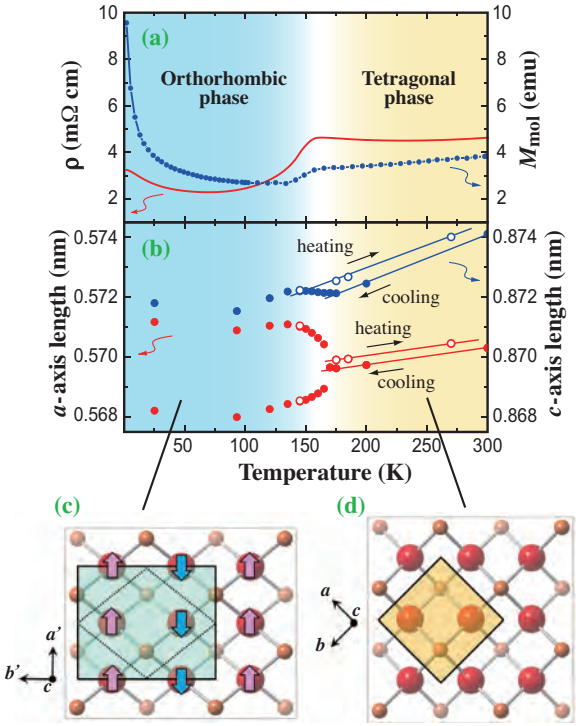

Fig. 4. **(a)** Temperature-dependent resistivity (ρ) and molar magnetization (M_{mol}) of parent LaFeAsO. **(b)** Temperature-dependent *a*-, *b*- and *c*-axis lengths of parent LaFeAsO. The *a*-axis lengths of tetragonal phases are multiplied by $\sqrt{2}$ for comparison with the orthorhombic phases. Closed and open symbols represent heating and cooling processes, respectively. **(c)**,**(d)** A view from *c*-direction of the FeAs layer for orthorhombic **(c)** and tetragonal **(d)** phases. The arrows in **(c)** represent the stable strip-type spin configuration on Fe atoms determined by DFT calculation [4,5].

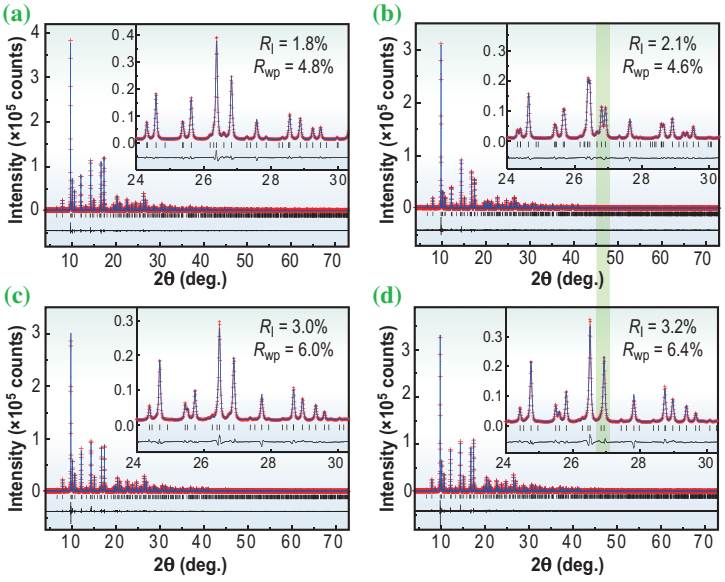

Fig. 3. Rietveld fitting results of the diffraction patterns of the parent LaFeAsO at **(a)** 300 K and **(b)** 120 K, and those of the 14% F-substituted LaFeAsO at **(c)** 300 K and **(d)** 120 K. The XRD patterns of the parent LaFeAsO below 160 K were fitted with the orthorhombic *Cmma* space group. Insets show magnified view ranging from 24° to 30°. The structure phase transition (i.e., peak split) of the parent sample is suppressed in the F-substituted sample (the green shade).

Takatoshi Nomura* and Hideo Hosono

Materials and Structures Laboratory,
Tokyo Institute of Technology

*E-mail: t-nomura@lucid.msl.titech.ac.jp

References

[1] Y. Kamihara *et al.*: J. Am. Chem. Soc. **130** (2008) 3296.
[2] C. de la Cruz *et al.*: Nature **453** (2008) 889.
[3] J. Zhao *et al.*: Nature Mater. **7** (2008) 953.
[4] *T. Nomura, S.-W. Kim, Y. Kamihara, M. Hirano, P.V. Sushko, K. Kato, M. Takata, A.L. Shluger and H. Hosono: Supercond. Sci. Technol.* ***21*** *(2008) 125028.*
[5] T. Yildirim: Phys. Rev. Lett. **101** (2008) 057010.

Fulleride Superconductors are Three-Dimensional Members of the High-T_c Family

A_3C_{60} (A = alkali metal) superconductors adopt face-centred cubic (*fcc*) structures and their superconducting T_c increases monotonically with increasing interfullerene spacing, reaching a 33 K maximum for $RbCs_2C_{60}$ – this physical picture has remained unaltered since 1992. Trace superconductivity (s/c fraction<0.1%) at 40 K under pressure was reported in 1995 in multiphase samples with nominal composition Cs_3C_{60}. Despite numerous attempts by many groups worldwide, this remained unconfirmed and the structure and composition of the material responsible for superconductivity unidentified. Thus the possibility of enhancing fulleride superconductivity and understanding the structures and properties of these archetypal strongly correlated molecular solids close to the Mott-Hubbard metal-insulator (M-I) transition had remained elusive.

It was evident to us that new synthetic ideas coupled with detailed property measurements were needed to remove this bottleneck. We developed qualitatively new synthetic protocols employing new solvents to access high-symmetry hyperexpanded alkali fullerides in the vicinity of the M-I boundary and at previously inaccessible intermolecular separations; we then used the accumulated synthetic expertise to specifically target high-symmetry (i.e. retaining t_{1u} orbital degeneracy in the solid) fullerides with varying C_{60} orientations and packings (i.e. tuning geometrical frustration) in order to enhance molecular superconductivity. This approach culminated in the discovery of pressure-induced bulk superconductivity at 38 K in body-centred-cubic (*bcc*) structured A15 Cs_3C_{60} (Fig. 1) – the highest T_c known for any molecular material [1]. This is also the first example of a superconducting C_{60}^{3-} fulleride with non-*fcc* sphere packing – this single non-*fcc* material has a higher T_c than all the *fcc* A_3C_{60} fullerides studied over the past 18 years. Moreover, we found that the electronic ground state in competition with superconductivity, and found at ambient pressure, not only contains magnetic moments localised on the C_{60}^{3-} anions but is antiferromagnetically ordered with T_N = 46 K – this is the hallmark of strong electron correlations [2]. High-resolution synchrotron X-ray powder diffraction at 14.6 K (beamline **BL10XU**) showed that the application of hydrostatic pressure to the cubic-localised electron C_{60}^{3-} antiferromagnetic insulator (AFI) with the *bcc*-derived A15 structure (space group $Pm\bar{3}n$) produces no structural change over the range 1 bar to 25 kbar [2]. The effect of increased pressure is thus solely to decrease the interfullerene contact distances isotropically, thereby increasing the overlap between t_{1u} orbitals on neighbouring C_{60}^{3-} anions and thus the bandwidth W, favouring electron delocalisation. Therefore the antiferromagnetic insulator-superconductor transition maintains the threefold degeneracy of the active orbitals in both competing electronic states, and is thus a purely electronic transition to a superconducting state. The dependence of the transition temperature on pressure-induced changes of anion packing density is not explicable by BCS theory – once the superconducting state is established, T_c initially increases with decreasing V in complete contrast to the behaviour of the conventional *fcc* fullerides under pressure. Then above ~7 kbar, the sign of $\partial T_c/\partial V$ changes to positive. The resulting maximum in T_c as a function of the interC_{60} separation – unprecedented in fullerene systems but reminiscent of the T_c vs hole density behavior of atom-based cuprate superconductors – is attributed to the key role of strong electronic correlations near the onset of the M-I transition (Fig. 2).

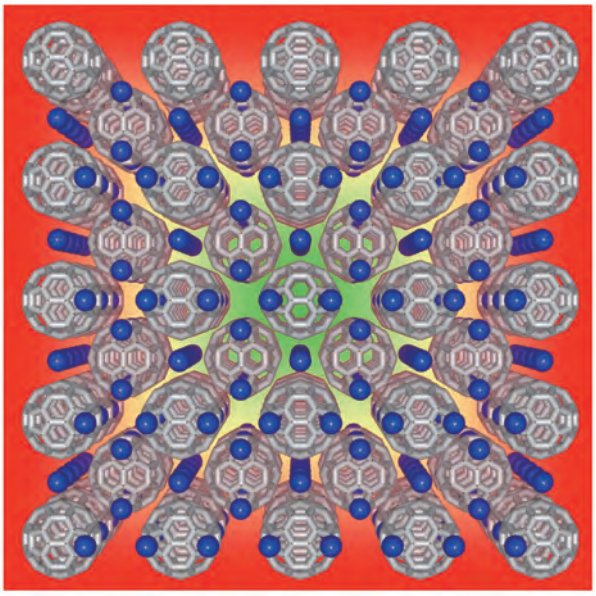

Fig. 1. Crystal structure of A15 Cs_3C_{60} (space group $Pm\bar{3}n$) based on *bcc* anion packing with orientationally ordered C_{60}^{3-} anions. Cs^+ cations are shown in blue. The lower density of the body-centred packing offers more spacious sites (with four fulleride neighbours) for the large Cs^+ cation when compared to *fcc* A_3C_{60} fullerides.

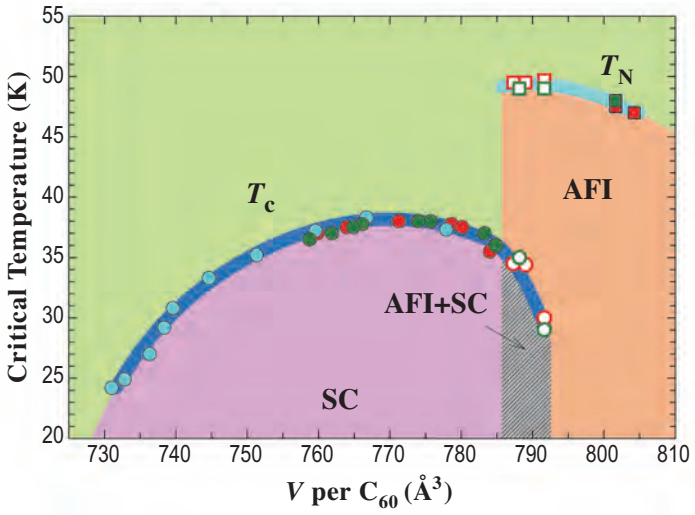

Fig. 2. Electronic phase diagram of A15 Cs_3C_{60} showing the evolution of the Néel temperature, T_N (squares) and the superconducting transition temperature, T_c (circles) and thus the isosymmetric transition from the ambient pressure antiferromagnetic insulating (AFI) state to the high pressure superconducting (SC) state as a function of volume occupied per fulleride anion, V at 14.6 K. Different symbol colours represent data obtained for different sample batches. Open symbols represent data in the AFI-SC coexistence regime.

The high symmetry of the C_{60} building unit imposes a robust cubic three-dimensional structure on A15 Cs_3C_{60} free of positional, chemical, or orientational disorder with a fixed charge state in which magnetism is transformed into superconductivity solely by changing an electronic parameter, the extent of overlap between the outer wave functions of the constituent anions. The pressure-induced transition in A15 Cs_3C_{60} from a localized electron AFI to a superconductor with two distinct dependences of T_c on packing density is purely electronic in nature, driven by increased overlap between the C_{60}^{3-} anions and the associated enhanced tendency to delocalise the t_{1u} electrons. The unconventional nature of the superconducting state that emerges from the AFI can be associated with its proximity to the M-I transition where conventional Fermi liquid theories are not expected to be valid, and quasi-localized effects produced by electronic correlation enhancing the role of intramolecular Jahn-Teller (electron-phonon) and Hund's rule (electron-electron) coupling are directly controlled by the persistent orbital degeneracy in both the insulating and superconducting states, clearly traceable to the molecular origin of the electron states. The observed superconductivity dome is consistent with theoretical treatments [3], which explicitly take account of the orbital degeneracy and the repulsion between the electrons as well as the classical electron-phonon coupling. These effects are not seen in the conventional *fcc* A_3C_{60} systems, which are too far from the M-I transition for differences from the conventional BCS predictions of the dependence of T_c on $N(E_f)$ to become apparent. Therefore, A15 Cs_3C_{60} emerges as an ideal material for understanding the interactions producing superconductivity in structurally and chemically complex correlated electron systems such as the cuprates and oxypnictides as it allows the isolation of the influence of only electronic factors (including orbital degeneracy) without any other complications.

Kosmas Prassides[a,*] and Matthew J. Rosseinsky[b]

[a] Department of Chemistry, Durham University, UK
[b] Department of Chemistry, University of Liverpool, UK

*E-mail: K.Prassides@durham.ac.uk

References

[1] A.Y. Ganin *et al.*: Nature Mater. **7** (2008) 367.
[2] *Y. Takabayashi, A.Y. Ganin, P. Jeglič, D. Arčon, T. Takano, Y. Iwasa, Y. Ohishi, M. Takata, N. Takeshita, K. Prassides and M. J. Rosseinsky: Science **323** (2009) 1585.*
[3] M. Capone *et al.*: Rev. Mod. Phys. **81** (2009) 943.

Entry of Novel π-Conjugated Molecules into Liquid Crystalline Materials

Liquid crystallization of π-conjugated molecules is an attracting methodology to make ordered molecular assemblies applicable for organic electronic and/or memory devices. Entry of new families of π-conjugated molecules with unique properties for the research community of liquid crystal is important, as it allows to realize not only better performance but also unprecedented functions of such liquid crystalline materials. We have successfully designed the first examples of liquid crystalline fused metalloporphyrin dimer **(1)** [1] and corannulene **(3)** [2] (Fig. 1). The π-conjugated cores did not show any liquid crystallinity, when they were structurally modified, based on the conventional molecular design strategy, with long alkyl side chains (**2** and **4** in Fig. 1). For liquid crystallization of fused metalloporphyrin dimers, we developed an original molecular design strategy, where two incompatible hydrophobic and hydrophilic side chains are site-specifically introduced to the core. By taking advantage of nanoscale phase separation of these side chains, fused metalloporphyrin core can stack one another to form a rectangular columnar lattice with lattice parameters *a* and *b* of 65.3 and 37.2 Å, respectively (Fig. 2), which was unambiguously determined by variable-temperature, one- and two-dimensional X-ray diffraction analyses of sheared and unsheared samples at beamlines **BL02B2** and **BL45XU**. On the other hand, for corannulene, we used hydrogen-bonding interaction to induce its columnar assembly, by adding amide functionalities in the side chains. In fact, corannulene **3** forms a hexagonal columnar liquid crystalline phase with a lattice parameter of 35.0 Å, as clearly demonstrated by one-dimensional X-ray diffraction analysis at beamline **BL02B2**. It is also noteworthy that both **1** and **3** exhibited liquid crystallinity in wide temperature ranges including room temperature (**1**: from –17 to 99 °C; **3**: from –10 to 154 °C on heating), advantageous for device processing and operation.

Because of its extra-large π-conjugated system, fused copper porphyrin dimer **1** has HOMO-LUMO band gap of 1.15 V, which is obviously smaller than those of several representative semiconducting π-conjugated molecules such as perylene diimides (1.4 – 2.2 V), phthalocyanines (1.4 – 1.8 V), and C_{60} (1.7 V). Such a narrow band gap suggests the large potential of fused metalloporphyrin dimers as an organic semiconductor. In fact, **1** was found to serve as an *n*-type semiconductor. Its intrinsic one-dimensional electron mobility μ_{1D}, as evaluated by non-contacting flash-photolysis time-resolved microwave conductivity (TRMC) measurements of the film samples at the liquid crystalline state, reached up to the order of 10^{-1} $cm^2/V{\cdot}s$. μ_{1D} of such value is one-order of magnitude larger than the previous champion data reported for room-temperature columnar liquid crystalline materials, studied by TRMC. Since high-performance *n*-type organic semiconductors are still rare, this novel liquid crystalline material will give a great impact on the research community of organic electronics.

The columnar assemblies of **1** and **3**, in their as prepared liquid crystalline films, orient randomly on the macroscopic level. We have found, however, that the latter can be aligned electrically. When a liquid crystalline sample of **3** in an applied electric field was continuously monitored by polarized optical microscopy, the birefringent image, initially observed in the entire view of the sample, gradually changed

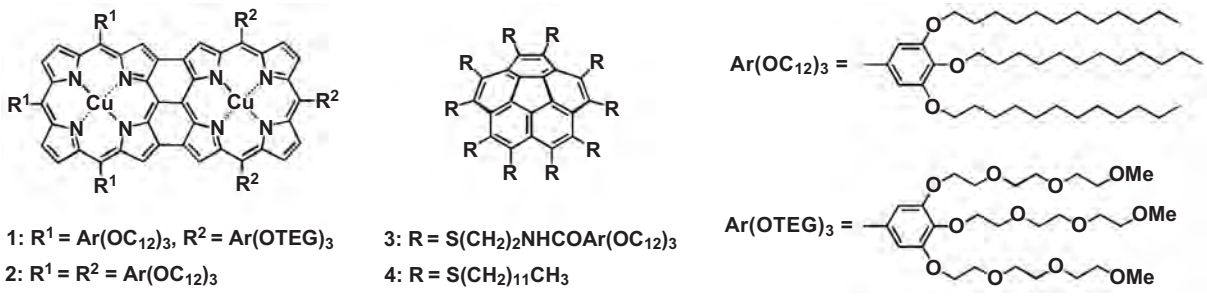

Fig. 1. Molecular structures of fused metalloporphyrin dimers **1**, **2** and corannulenes **3**, **4**.

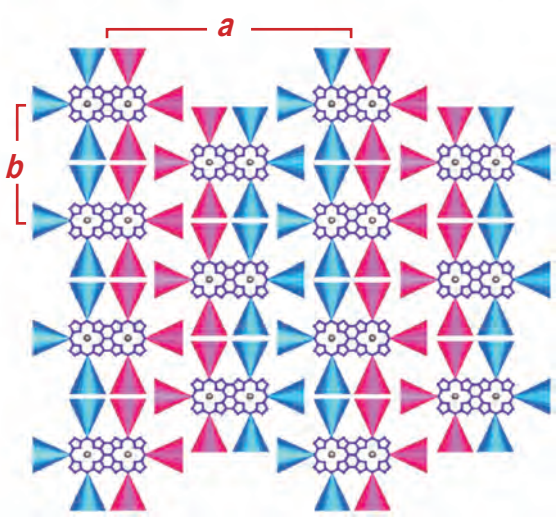

Fig. 2. Schematic representation of rectangular 2D molecular packing diagram of liquid crystalline **1**. The blue and red moieties in the cartoon correspond to the hydrophobic and hydrophilic side chains in **1**, respectively.

and eventually displayed a certain pattern with a dark field only in a section sandwiched by the electrodes (Fig. 3), demonstrating that columns of assembled **3** adopt a homeotropic orientation with respect to the electrodes. Thus corannulene **3** is a rare example of electrically alignable discotic liquid crystals. Due to the bowl-shaped π-conjugated skeleton, corannulene has concave and convex faces with different electron densities, and hence a dipole moment whose direction is switchable upon inversion of the skeleton. Therefore, liquid crystalline **3** responsive to electric field, possesses unique potentials for e.g., anisotropic charge transporting and ferroelectric applications.

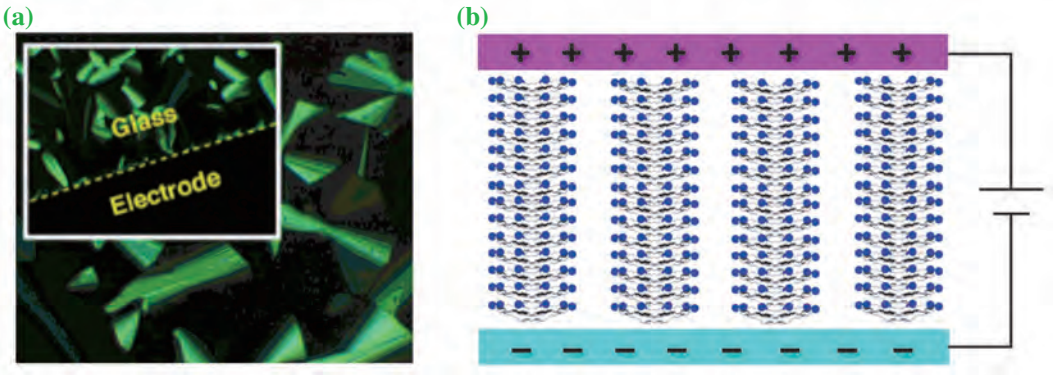

Fig. 3. **(a)** Polarized optical micrograph (POM) of **3** at 115 °C. Inset shows POM at 125 °C of **3**, sandwiched by glass plates with patterned ITO electrodes (5-μm separation) under an applied electric field of 15 V· μm^{-1}. **(b)** Schematic representation of the orientation of columnar assemblies of **3** under applied electric fields.

Kentaro Tashiro

International Center for Materials Nanoarchitectonics, National Institute for Materials Science

E-mail: TASHIRO.Kentaro@nims.go.jp

References

[1] *T. Sakurai, K. Shi, H. Sato, K. Tashiro, A. Osuka, A. Saeki, S. Seki, S. Tagawa, S. Sasaki, H. Masunaga, K. Osaka, M. Takata and T. Aida: J. Am. Chem. Soc.* ***130*** *(2008) 13812.*

[2] *D. Miyajima, K. Tashiro, F. Araoka, H. Takezoe, J. Kim, K. Kato, M. Takata and T. Aida: J. Am. Chem. Soc.* ***131*** *(2009) 44.*

Analyses on Crystalline Structures of Carbon Nanowalls by Grazing-Incidence X-Ray Diffraction Using Synchrotron Light Source

Recently, carbon nanomaterials, such as fullerenes, carbon nanotubes (CNTs), graphene sheets, carbon nanowalls (CNWs), and so forth have attracted much attention because of their unique structures, chemical and physical strengths, and excellent electronic properties [1]. In particular, the CNWs, which are two-dimensional stacked graphene sheets vertically standing on substrates, are promising for applications in various devices, owing to their high aspect ratio, large specific surface area, high carrier mobility, and large current-carrying capability (Fig. 1). Figures 2(a) and 2(b) show top-view and cross-sectional SEM images of typical CNWs grown on a Si substrate using a C_2F_6/H_2 mixture gas plasma with O_2. We have succeeded to control the shapes and crystalline structures of CNWs using a radical injection plasma-enhanced chemical vapor deposition system (RI-PECVD) [1]. We have also reported that the crystallinity of CNWs can be improved by adding O_2 gas into the growth ambient [2]. On the other hand, the electrical properties of CNW strongly depend on their structures and crystallinity. The interfacial layer, which is grown at an initial stage of CNWs growth between the CNWs and substrates, is also essential to the crystalline structures and electrical properties of CNWs. Therefore, it is important to investigate the crystalline structures of CNWs and interfacial layers. However, it is difficult in general to evaluate the crystalline structures of nanomaterials such as CNWs using laboratory equipment, since most of them have quite low coverage and filling fraction on the substrate surfaces. Therefore, a high-resolution X-ray diffraction using a high-intensity synchrotron (SR) light source is required to evaluate the crystalline structures of carbon nanomaterials. On the other hand, grazing-incidence X-ray diffraction (GIXD) is also used to realize the substrate-insensitive measurement in this study.

In this study, the crystalline structures of CNWs were analyzed by high-resolution SR X-ray diffraction measurements with in-plane scattering geometry at beamline **BL13XU**. A multi-axis diffractometer was used in this experiment. The glancing angles of incident X-ray beams were 0.05° and 0.3°. The CNWs were fabricated using the RI-PECVD with and without the addition of O_2 gas to C_2F_6/H_2 plasma.

Figures 3(a) and 3(b) show the diffraction patterns of CNWs. In Fig 3(a), the 002 diffraction peaks of graphite are clearly observed at 16.98°. The weak 100/101, 004, and 110 peaks are also found at 27.49°, 34.16°, and 48.28°, respectively. Using Bragg's law and wavelength (λ = 0.1003 nm) of incident beam, the interlayer spacing (d_{002}) was estimated to be 0.342 nm for all the samples. This value is slightly larger than that of bulk graphite (0.335 nm) [3]. A degree of verticalness was evaluated using an intensity ratio of 002 peak to 100/101 one ($I_{002}/I_{100/101}$). It is found that the $I_{002}/I_{100/101}$ for CNWs grown without O_2 addition is twice larger than that with O_2 addition. This indicates that much more graphene sheets tilting to the substrates are included in the CNWs grown without O_2 addition, compared with those in CNWs grown with O_2 addition. Therefore, in the CNWs grown using RI-PECVD with a C_2F_6/H_2 mixture, the degree of verticalness can be

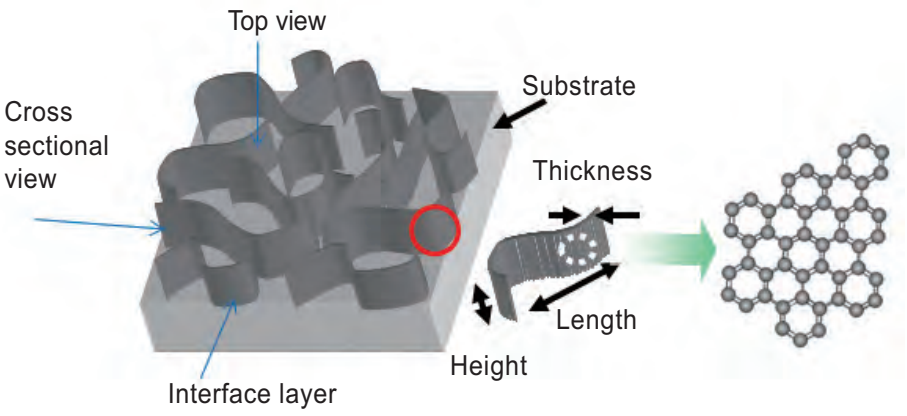

Fig. 1. Schematics of CNWs.

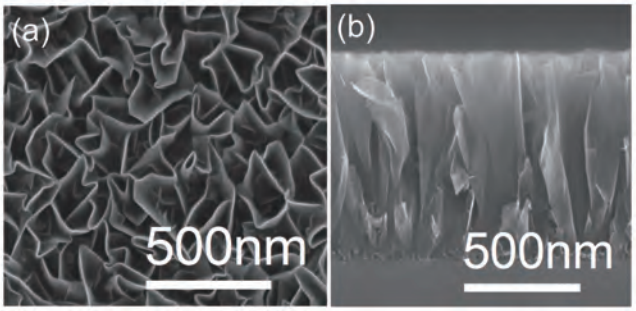

Fig. 2. **(a)** Top-view and **(b)** cross-sectional SEM images of CNWs grown on a Si substrate using a C_2F_6/H_2 mixture gas plasma with an additional O_2 gas.

improved by adding O_2 into the plasma.

In the inset of Fig 3(a), a slight and broad peak at 22.88°, which is assigned to β-SiC (111), is only observed in the absence of O_2. In Fig. 3(b), the similar peak is also found only for the glancing angle of 0.3°. Since this peak does not appear for the measurement at the glancing angle of 0.05°, it is guessed that a near-amorphous β-SiC layer exists between the CNWs and substrates. These experimental results suggest that, by employing the GIXD with the SR light source, not only the crystalline structures and orientation of carbon nanomaterials but also those of their interfacial layers can be evaluated.

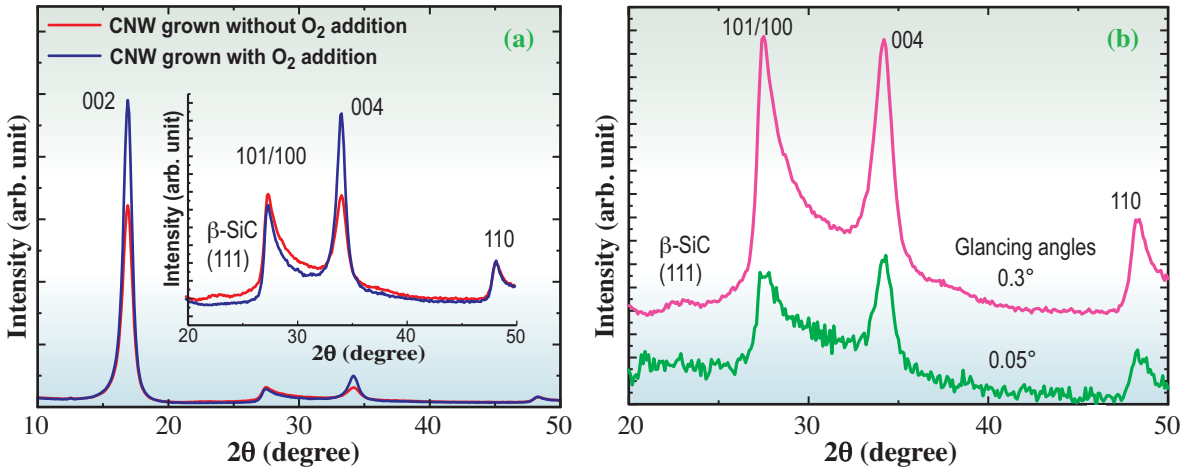

Fig. 3. X-ray diffraction (XRD) profiles of **(a)** CNWs grown with and without O_2 addition measured at a glancing angle of 0.3°, and those of **(b)** CNWs grown without O_2 addition measured at glancing angles of 0.05° and 0.3°.

Wakana Takeuchi, Hiroki Kondo and Masaru Hori*

Dept. of Electrical Engineering and Computer Science, Nagoya University

*E-mail: hori@nuee.nagoya-u.ac.jp

References

[1] M. Hiramatsu and M. Hori: Jpn. J. Appl. Phys. **45** (2006) 5522.
[2] *W. Takeuchi, K. Takeda, M. Hiramatsu, Y. Tokuda, H. Kano, S. Kimura, O. Sakata, H. Tajiri and M. Hori: Phys. Status Solidi A* ***207*** *(2009) 139.*
[3] Y. Sato *et al.*: Carbon **44** (2006) 664.

Nature of Structural Transformations in the B_2O_3 Glass under High Pressure

Atomic rearrangements and phase transformations in glasses under high pressure (polyamorphism) are one of the most intriguing and puzzling topics of physics.

B_2O_3 represents an archetypical oxide glass alongside such glasses as SiO_2 and GeO_2, with the important difference that at the ambient conditions, the structural units are planar BO_3 triangles as opposed to tetrahedra. The *in situ* investigations of B_2O_3 glass under pressure have been performed previously by using Raman and Brillouin spectroscopies [1], and through inelastic X-ray scattering spectroscopy [2]. Besides, there have been attempts to examine the B_2O_3 glass under pressure by molecular dynamics computer simulation, using empirical inter-atomic potentials [3,4]. According to the data of [1] B_2O_3 glass under compression experiences a transformation in the pressure range P~ 6-15 GPa, with the reverse transformation at decompression occurring sharply at P~ 3 GPa. According to the Ref. [2] B_2O_3 glass, under compression, features a considerable change in the bonding type in the 6-20 GPa pressure range. It should be underlined that the quantitative estimates of the degree of transformation based on the indirect experiments [2] and those based on the computer simulation data with empirical potentials [3,4] are drastically different.

In [5] we report the results of the *in situ* diffraction experiments, *in situ* volumetric measurements, and complement them with the data from *ab initio* calculations. The *in situ* structural study of the B_2O_3 glass has been done at the beamline **BL14B1**. The *in situ* volumetric measurements of the B_2O_3 glass were conducted by the strain gauge technique. We have used the SIESTA method for high-pressure *ab initio* simulations.

The *in situ* diffraction structural data for the B_2O_3 glass at different pressures are presented in Fig. 1. At P < 5 - 6 GPa, the 1st peak of the total correlation function does not change. The basic changes take place in the distant coordination spheres. At higher pressures the structural changes begin affecting the 1st coordination sphere: the fraction of the 4-coordination boron atoms can be assessed as being about 40-45% at P~ 9.5 GPa, T~ 650 K.

Glass structures under compression from *ab initio* simulations are shown in Fig. 2. At high pressures glass structure consists mostly of BO_4 tetrahedra (Fig. 2 (b,c)). At the initial stage of the coordination transformation (P ~ 5-7 GPa) there is a slight shift of the B-O average distance whereas the fraction of the 4-coordinated boron is close to zero. One can suppose that it is associated with the distortion of BO_3 triangles. The *ab initio* simulations indeed show that before transforming into the 4-fold coordination, BO_3 triangles loose their planarity, as the B atom is pushed out of the plane of three O atoms starting from 4 - 5 GPa.

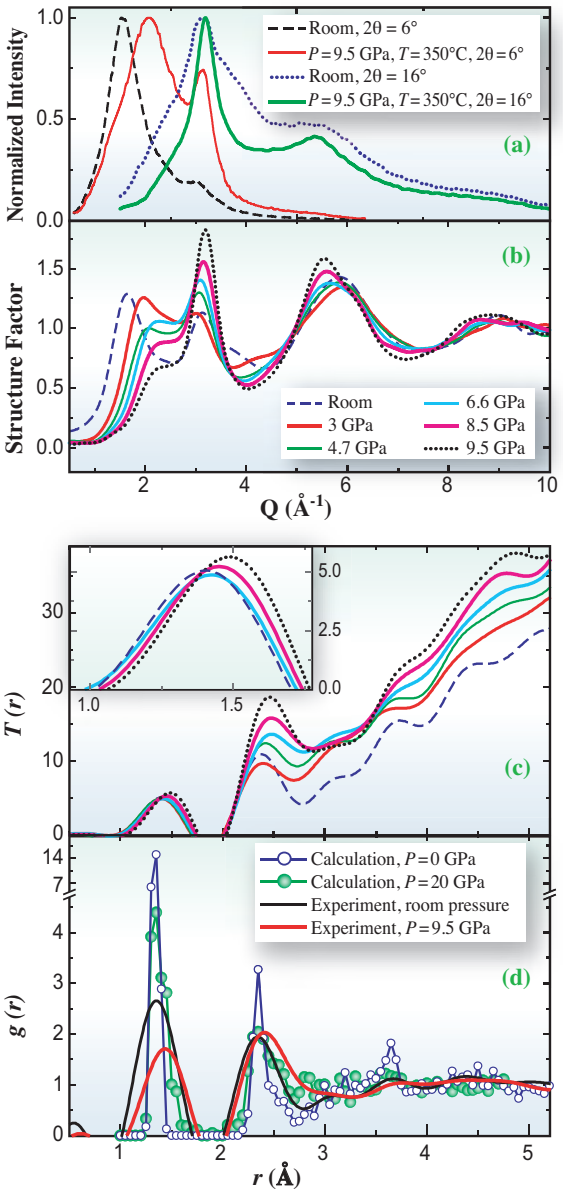

Fig. 1. Examples of the energy dispersive X-ray diffraction (EDXD) data for the glassy B_2O_3 **(a)**, measured at different pressures at the two angles of the detector; calculated from the experimental EDXD data structure factor **(b)**; total correlation function **(c)**, and comparison of the experimental and computer simulated structural correlation functions for different pressures **(d)**. All experimental curves for $P = 9.5$ GPa correspond to the sample obtained after heating to 650 K.

The "relaxed" bulk modulus of the B_2O_3 glass obtained from the volumetric measurements does not increase monotonically: the transformation in the B_2O_3 glass consists of two broad overlapping transitions occurring at P > 1 GPa and P > 5 GPa. The 1st transformation corresponds to the structural changes in the distant coordination spheres, while the 2nd one at P > 5 GPa conforms to the coordination transformation in glass. The coordination transition is fully reversible. The decrease of the coordination of the boron atoms from 4 to 3 begins at P~4.5 GPa and ends at P~1 GPa. This transformation is smooth in hydrostatic conditions. Therefore, the conclusion made in Ref. [1] about the first-order character of this transition is untrue and is likely to be an artifact associated with strongly non-hydrostatic conditions near the sample.

Figure 3 presents the comparison of the experimental and calculated coordination changes with pressure. A reasonable agreement between experiment and first-principles calculations can be seen. As follows from this figure, previous simulations with empirical potentials significantly underestimated the fraction of increased coordination, especially the results from [4], whereas previous inelastic X-ray scattering data [2] overestimated the coordination changes under compression.

The first-principles simulations enable us to analyze the behavior of glass at much larger pressures than those available in the experiments that use large volume presses. We observe that unlike its crystalline counterpart BO_4 tetrahedra in glass at high pressure can be connected in edges (see Fig. 1(b)). The fraction of edge-shared tetrahedra increases with density, and under further compression face-shared tetrahedra with 5- and 6-coordinated B atoms appear in the glass (Fig. 1(c)).

The present study demonstrates the necessity of direct structural measurements and direct volumetric measurements and importance of *ab initio* computer simulation study. The interpretation of indirect study of structural transformation, e.g. using inelastic X-ray scattering data, should be considered with caution.

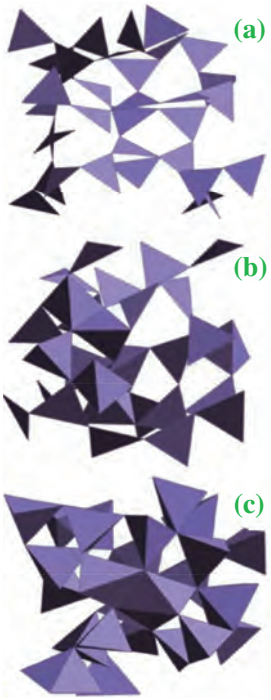

Fig. 2. Polyhedron representation of the simulated B_2O_3 glass structure at zero pressure **(a)**, P = 20 GPa **(b)**, and P = 200 GPa **(c)**, where triangles correspond to the BO_3 structure units (3-fold coordinated boron), tetrahedrons - to BO_4, and there are the single BO_5 and BO_6 units on **(c)**.

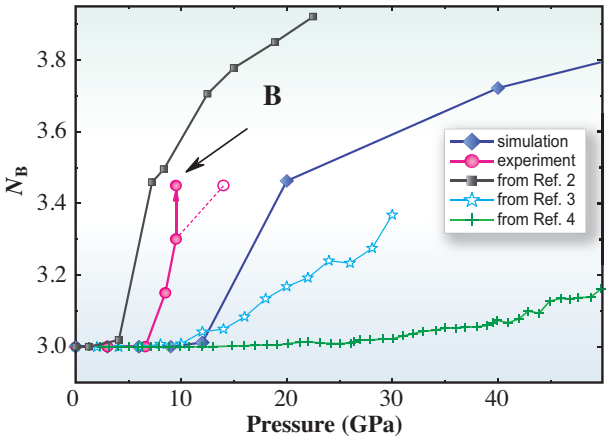

Fig. 3. Pressure dependences of the 1st coordination number for B from the current experiment (X-ray diffraction) and simulation and according to the data from Refs. [2-4]. Point B in the experimental dependence corresponds to the heated sample, whereas the open point is the estimation of the point B position which should be observed under room-temperature compression.

V. V. Brazhkin[a,*], Y. Katayama[b] and K. Trachenko[c]

[a] Institute for High Pressure Physics RAS, Russia
[b] SPring-8 / JAEA
[c] Dept. of Earth Sciences, University of Cambridge, UK

*E-mail: brazhkin@hppi.troitsk.ru

References

[1] J. Nicholas *et al.*: Phys. Rev. Lett. **92** (2004) 215701.
[2] S.K. Lee *et al.*: Nature Mat. **4** (2005) 851.
[3] A. Takada: Phys. Chem. Glasses **45** (2004) 156.
[4] L. Huang *et al.*: J. Phys.: Condens. Matter **20** (2008) 075107.
[5] *V.V. Brazhkin, Y. Katayama, K. Trachenko, O.B. Tsiok, A.G. Lyapin, Emilio Artacho, M. Dove, G. Ferlat, Y. Inamura and H. Saitoh: Phys. Rev. Lett.* ***101*** *(2008) 035702.*

X-Ray Diffractometry for the Structure Determination of a Submicrometer-Scale Single Powder Grain

So far, the structure identification and characterization of various new materials have been carried out by powder diffraction experiments since newly synthesized materials are obtained in powder and/or in polycrystalline forms in most cases. This research technical trend is accelerated by the high-photon flux monochromatic X-rays of synchrotron radiation (SR) in addition to the progress of computers and software for structure determination. Consequently, the development of an *ab initio* structure analysis technique, which denotes unknown structure determination, is now one of the most topical research subjects in powder crystallography. On the other hand, an X-ray SR beam with high brilliance and small divergence allows us to suggest an alternative method by which we can determine the crystal structure of a micrometer- or submicrometer-scale single crystal corresponding to a single grain of powder sample. In fact, some structure determinations of a few micrometer-sized single crystals have recently been reported using an SR focusing technique [1].

However, the structure determination of a submicrometer-scale single crystal has not been carried out yet. This is mainly caused by three technical difficulties that need to be overcome: the accurate intensity data collection of very weak diffraction spots, the precise centering of the invisible sample and the infallible manipulation of a submicron-scale single crystal. The combination of the SR focusing technique and the precise-axis control of the diffractometer is one of the solutions for the first and second difficulties. The latest focusing technique for an SR diffraction experiment can firmly produce the micrometer-scale high-flux SR beam. The precise-axis control enables to move and keep the submicrometer-scale sample within the micrometer-scale focused SR beam. We have therefore developed and optimized a high-precision diffractometer, which combined an SR focusing technique and a low eccentric sample rotation at the undulator beamline **BL40XU**, to enable the structure analysis of a submicrometer-scale single powder grain [2]. As for the third difficulty, since the development of systematic manipulation techniques to select and capture one single grain of powder sample is still in progress, several submicrometer-scale single powder grains have been presently attached to a fine glass fiber by the conventional sample manipulation technique.

We designed the phase zone plate for the structure analysis of a submicrometer-scale single powder grain. The diameter and focal length of the phase zone plate are 100 μm and 300 mm for the 15 keV SR beam, respectively.

The schematic diagram of the developed system and the experimental setup around the phase zone plate focusing system are shown in Fig. 1. The beam size and photon flux density at the focal position (= sample position) were 1.4×2.9 μm^2 (vertical × horizontal) and 3.1×10^9 photons/sec/μm^2,

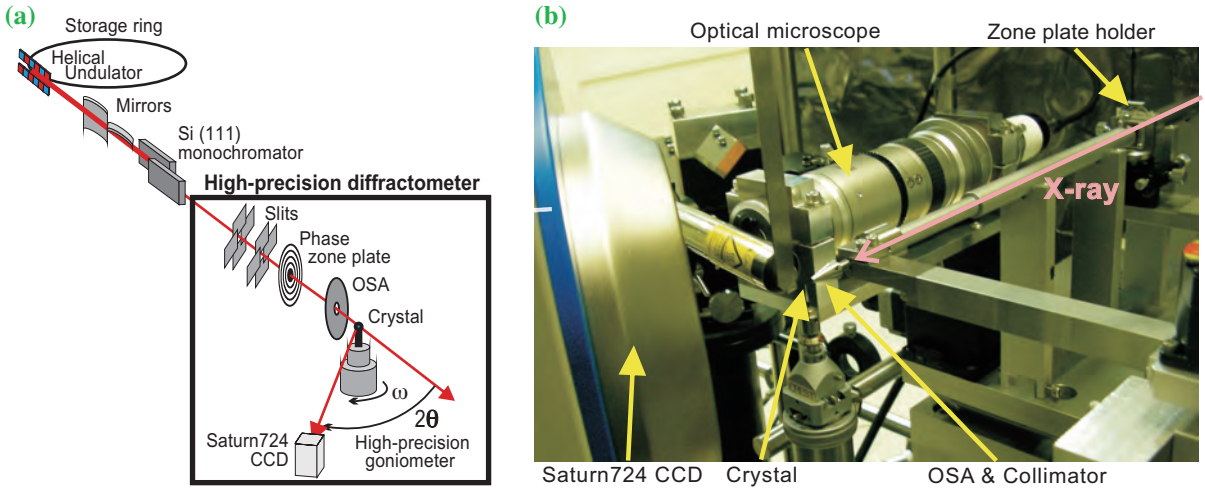

Fig. 1. **(a)** Schematic of the experimental setup. **(b)** Experimental setup around the phase zone plate focusing system.

respectively. The corresponding gain factor, therefore, is nearly 400.

Structure analysis was performed for the submicron-scale $BaTiO_3$ single powder grain. The grains of $BaTiO_3$ were attached to the tip of a fine glass fiber with epoxy adhesive using an optical microscope and a micromanipulator. Figures 2(a) and 2(b) show the optical microscope and SEM images of the tip of a fine glass fiber, respectively. Several $BaTiO_3$ grains were attached to the glass fiber. The maximum grain size was about 600 × 600 × 300 nm^3.

The diffraction data were collected using the ω-oscillation mode at room temperature. The exposure time and the ω-axis scan step, Δω, were 15 s and 1°, respectively. With this setup, the 360 diffraction images were collected in 180 min. The overlapped diffraction pattern of the 360 images is shown in Fig. 2(c). The accidentally diffracted spots of the other $BaTiO_3$ grains sometimes interfered with the diffraction pattern during ω-oscillation. These extra spots can be discriminated systematically, because the diffraction pattern no longer shows the Debye-Scherrer pattern but the superposition of several single-crystal diffraction patterns. At present, however, it is very difficult to directly identify the sample grain corresponding to the diffraction spots among several sample grains (Fig. 2(b)). The solved crystal structure is shown in Fig. 2(c). Only the thermal vibration of the Barium atoms was refined anisotropically. The reliability factor of the refinement finally became R_1 = 5.24%.

The crystal structure of a submicron-scale $BaTiO_3$ single powder grain was successfully determined with several single powder grains. This success proves that the diffraction measurement of a single powder grain has a sufficient advantage in the determination of an unknown crystal structure for any powder-formed crystalline sample.

We have also developed a laser-pump and SR-probe diffraction technique using the same diffractometer system. Now, we are ready to apply the structure analysis of a single powder grain for the research of the photo-induced phase transition combined with the pump and probe technique [3-5].

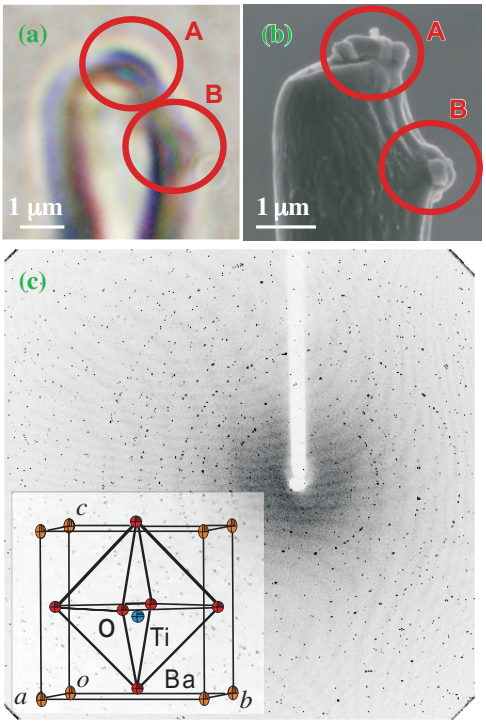

Fig. 2. Photographs of $BaTiO_3$ powder grains attached to the tip of a fine glass fiber: **(a)** optical microscope image. **(b)** SEM image of the same sample. The size of the large grain is about 600 × 600 × 300 nm^3. A and B in each figure indicate the positions of existing $BaTiO_3$ grains. **(c)** Measured diffraction image of $BaTiO_3$ grains. All the measured images are overlapped on one image to show the Bragg diffraction spots clearly.

Shigeru Kimura

SPring-8 / JASRI

E-mail: kimuras@spring8.or.jps

References

[1] C. Riekel *et al.*: Curr. Opin. Struct. Biol. **15** (2005) 556.
[2] *N. Yasuda, H. Murayama, Y. Fukuyama, J. Kim, S. Kimura, K. Toriumi, Y. Tanaka, Y. Moritomo, Y. Kuroiwa, K. Kato, H. Tanaka and M. Takata: J. Synchrotron Rad.* ***16*** *(2009) 352.*
[3] Y. Fukuyama *et al.*: Appl. Phys. Express **1** (2008) 045001.
[4] Y. Tanaka *et al.*: Jpn. J. Appl. Phys. **48** (2009) 03A001.
[5] Y. Fukuyama *et al.*: Appl. Phys. Express **3** (2010) 016601.

Angular Anomaly in the Dynamic Structure Factor of Graphite Close to Bragg Reflections

Collective excitations of valence electrons allow one to describe the physics of condensed matter systems in a compact way. The recent advance of inelastic X-ray scattering experiments using synchrotron light sources enables the investigation of collective excitations at large momentum transfers with high momentum and energy resolution and offers access to striking phenomena. At the same time, *ab initio* calculations allow us to analyze and predict experimental results and to unravel the underlying physics.

The present work is an example for a successful collaboration between theory and experiment: we have predicted, measured and explained an angular anomaly in the momentum-resolved dynamic structure factor $S(\mathbf{q},\omega)$ of graphite. Contrary to what one would expect naively, our calculations predicted drastic changes in the spectra upon very small variations in **q**, whenever the momentum transfer is close to specific reciprocal-lattice vectors **G** [1]. This effect has been clearly confirmed by our IXS measurements (Fig. 1). Unlike previous experiments [2], we did not consider momentum transfers exactly along the *c*-axis of graphite, but added a small in-plane component q_1=0.37 Å^{-1} that was kept constant, while the momentum along the *c*-axis q_3 was varied from 0.94 Å^{-1} to 2.84 Å^{-1}. Approaching the Bragg reflection at **G**=(002), the peak in the spectra is strongly shifted in energy and, most importantly, it abruptly disappears next to **G** ($q_3 = 2 \cdot 2\pi/c = 1.88$ Å^{-1}).

This striking behavior can be understood in terms of an interplay of anisotropy and crystal local field effects (LFE). The latter originate from the periodic modulation of the electron density in the crystal. Let us therefore first compare the excitation spectrum of electrons in a homogeneous electron gas (HEG) and in a solid. Figure 2 (left panel) shows the well known electron-hole excitations (shaded region) and plasmon excitations (red line) in the HEG. The energy of the plasmon increases quadratically with momentum **q** until it reaches the electron-hole continuum at q_c.

Assuming a weak periodic crystal potential, the excitation spectrum of a *solid* is given by folding back the free electron excitations into the first Brillouin zone (Fig. 2, right panel). Interband transitions to bands from higher Brillouin zones become possible and contribute to the damping of the plasmon at low momentum $q<q_c$ (1). Additionally, crystal local field effects become more and more important with increasing strength of the crystal potential. They couple excitations with momentum **q** and **q+G** from different Brillouin zones via internal Bragg scattering (**G** denotes a reciprocal lattice vector of the crystal). When this coupling is strong, the plasmon dispersion can develop several plasmon bands. In analogy to the electron bandstructure, an energy splitting at the Brillouin zone boundary at **q**=**G**/2 can occur (2) [3] or, most interestingly for the present work on

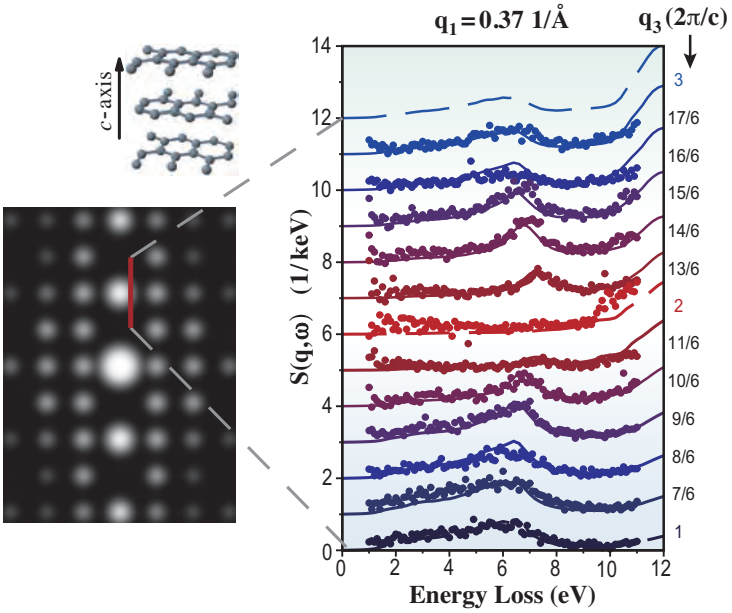

Fig. 1. The dynamic structure factor $S(q,\omega)$ of graphite was calculated (lines) and measured (dots) for different off-axis momentum transfers $q=(q_1,0,q_3)$ (given in reciprocal lattice units, compare with sketch of the diffraction pattern on the left). From [1].

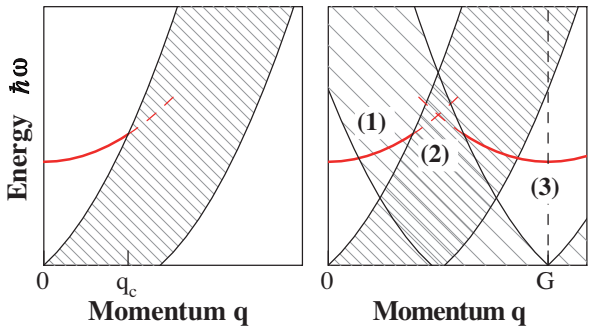

Fig. 2. Excitation spectrum of free electrons (left) and electrons in a weak periodic crystal potential (right). Hatched regions indicate electron-hole excitations, thick, red lines the plasmon dispersion (adapted from [3]).

graphite, the plasmon with small momentum $q<q_c$ may reappear in higher Brillouin zones (3) [4,5].

To illustrate this point, we artificially suppress the coupling via LFE in our *ab initio* calculations (Fig. 3, left panel). For small momentum-transfers q_3 along the *c*-axis (bottom), the spectra *without* LFE show a strong in-plane π-plasmon peak, which is shifted to lower energies with increasing q_3 due to the anisotropy of the system, and finally damped at large q_3 (top). If LFE are included (left panel), the plasmon excitation from the first Brillouin zone reappears at large momentum transfers (compare bold, red lines). Thus, in agreement with the plasmon band picture, we find a strong periodic dispersion at large q_3. Further analysis [1] of the coupling strength between excitations with momentum **q** and **q+G** shows that in graphite the coupling is particularly strong for **G**=(002), while it is forbidden for **G**=(001) by crystal symmetry. This explains the observed periodicity of the peak shift. But most importantly, the coupling depends on the angle between **q** and **q+G**. In particular, it vanishes completely if the two vectors are perpendicular, which is the reason for the completely flat spectrum at q_3=2 (bold, dashed line).

The presented effect might be observed in any solid that shows strong crystal local field effects, such as heterostructures or quasi-1D systems. Its identification has been possible due to a joint experimental and theoretical effort, which illustrates the power of such a combined approach.

The measurements were carried out at the Taiwan inelastic scattering beamline **BL12XU** in SPring-8.

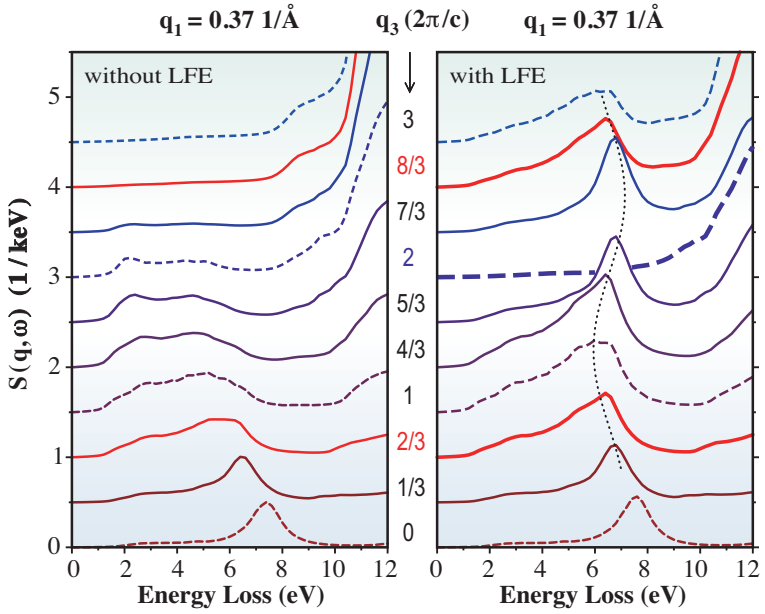

Fig. 3. *Ab initio* calculations of S(q,ω), without (left) or with (right) crystal local field effects (compare with Fig. 1).

R. Hambach[a,b], C. Giorgetti[a,b], N. Hiraoka[c] and Lucia Reining[a,b,*]

[a] Laboratoire des Solides Irradiés, Palaiseau, France
[b] European Theoretical Spectroscopy Facility (ETSF)
[c] National Synchrotron Radiation Research Center, Taiwan

*E-mail: lucia.reining@polytechnique.fr

References

[1] *R. Hambach, C. Giorgetti, N. Hiraoka, Y. Q. Cai, F. Sottile, A. G. Marinopoulos, F. Bechstedt and L. Reining: Phys. Rev. Lett.* ***101*** *(2008) 266406.*
[2] N. Hiraoka *et al.*: Phys. Rev. B **72** (20058) 075103.
[3] L.E. Oliveira and K. Sturm: Phys. Rev. B **22** (1980) 6283.
[4] Y.Q. Cai *et al.*: Phys. Rev. Lett. **97** (2006) 176402.
[5] K. Sturm *et al.*: Phys. Rev. Lett. **68** (1992) 228.

Materials Science:


"Kuchinashi" - *Gardenia*

One of the most progressing research methods in spectroscopy is a photoemission spectroscopy in the hard-X-ray regime, which provides bulk sensitive and valuable information on materials. This is the so-called hard X-ray photo-electron spectroscopy (HAXPES) and SPring-8 is surely a leader in this field. In this volume, two topics based on HAXPES are introduced. The first one reported by C. S. Fadley and co-workers at BL15XU, is based on the combination of standing waves with HAXPES. This enables us to obtain a detailed profile of multilayer interfaces. Furthermore, they demonstrated the angle-resolved HAXPES for the first time, which opened a new frontier in the investigation of bulk-sensitive band structures in detail. The second HAXPES activity concerns the study of the mixed valence nature of Yb compounds. Matsunami and co-workers confirmed the fully occupied nature of 4*f* states in bulk YbS and Yb metal.

Activities in angle-resolved photoelectron spectroscopy in the soft-X-ray regime at SPring-8 are also leading the field, and provide bulk-sensitive information on band structures. The detailed band and Fermi surface structures of $CeRu_2(Si_{1-x}Ge_x)_2$ has been obtained by Okane *et al*. at BL23SU.

The area of application of photoelectron emission microscope (PEEM) is becoming wider. The dependence of the electronic properties of epitaxial few-layer grapheme on the number of layers was clearly observed by Hibino *et al*. at BL17SU.

ELECTRONIC & MAGNETIC PROPERTIES

Studies in very high-energy-resolution inelastic X-ray scattering (IXS) at SPring-8 are also leading the world. In order to detect the transverse acoustic phonon mode of liquid Ga, IXS was successfully measured by Hosokawa *et al*. at BL35XU.

Investigations of magnetic materials are performed in very wide energy range (from IR to hard-X-ray) at SPring-8. For the hard-X-ray region, not only magnetic circular dichroism (MCD) in absorption spectra but also magnetic scattering measurements are performed. Here, an example of high resolution Compton scattering for transition metal oxides, which was obtained by Barbiellini *et al*. at BL08W, is shown. At BL11XU, Seto *et al*. developed energy domain Mössbauer spectroscopy. This method offers the potential for unique measurement capabilities for various scientific requirements including microscopic measurements. Finally, at BL39XU, very high field MCD measurements have become possible. Matsuda *et al*. developed a miniature magnet with which a 40 T magnetic pulse is available. The valence transition of Eu compounds depending on the field has been clearly observed.

As shown in this volume, some new changes have produced a variety of activities that show us the frontier of materials science.

Toyohiko Kinoshita

Looking Deeper into Buried Nanolayers and Complex Materials: Standing-Wave and Angle-Resolved Hard X-Ray Photoemission

Photoelectron spectroscopy (photoemission) is a well established and widely used technique for studying the atomic, electronic, and magnetic structure of materials, with in fact a history of over 100 years from Einstein's first explanation of it. However, it is only within the past decade that experiments have begun with energies in the hard X-ray regime above 2 keV and going up to 10 keV or more [1,2]. Such hard X-ray photoemission (HXPS or HAXPES) measurements are of high interest because they permit obtaining information from deeper below the surface of a solid sample, due to electron inelastic mean free paths (IMFPs) that increase roughly as (kinetic energy)$^{0.75}$. HAXPES is thus rapidly developing worldwide, and SPring-8 is a leader in this field, with many papers already published in leading journals.

The work described here involves exploring two new dimensions of HAXPES in order to enhance its power for the characterization of complex and nanoscale materials.

If the sample to be studied is grown as, or on, a synthetic multilayer mirror, then tuning the X-ray incidence angle to the mirror Bragg angle creates a strong standing wave (SW) in the mirror and above its surface. This nm-scale standing wave can then be moved vertically through the sample, by scanning the incidence angle through the Bragg angle (a rocking curve); by scanning the photon energy through the Bragg condition; or if one layer of the sample has been grown in a suitable wedge profile, also by moving the X-ray spot along the sample. In previous soft X-ray experiments, these techniques have been shown to provide a powerful new approach for studying buried layers and interfaces with sub-nm resolution [3]. However, soft X-ray measurements are limited in depth sensitivity due to the short IMFPs of ~10-20 Å involved. Recent experiments at beamline **BL15XU** have extended this technique into the hard X-ray regime with ~50-100 Å IMFPs, thus providing data that can reach into deeper layers and interfaces of technologically relevant multilayer nanostructures [4,5,6].

Some results of the rocking-curve type for a $SrTiO_3/La_{0.67}Sr_{0.33}MnO_3$ multilayer are shown in Fig. 1(a), based on SPring-8 hard X-ray data at 5.9 keV and analogous Berkeley ALS soft X-ray data at 833 eV [5]. These curves show effects both from the multilayer Bragg reflection (the large peaks at 1.9° and 14°) and from reflection at the top and the bottom of the multilayer (Kiessig fringes). From detailed X-ray optical simulations of this data, it has been determined that the bilayer distance has changed by about 6% in going from the top to the bottom of the multilayer. Further analysis of this data finally leads to the detailed surface and interface profiles shown in Fig. 1(b). Other studies at SPring-8 using the SW method in HAXPES have involved the Fe/MgO interface of relevance to spintronics, and the TiN/Si interface of relevance to semiconductor integrated circuits [4], thus demonstrating the broad applicability of this new approach.

Angle-resolved photoemission (ARPES) is a technique of choice in the soft X-ray regime for studying the valence-level electronic structure of solids and surfaces. Most measurements to data are done with photon energies below about 150 eV, and so are very surface sensitive. A limited number of studies have pushed this into the 0.5-1.0 keV range [7], thus achieving greater bulk sensitivity. In recent

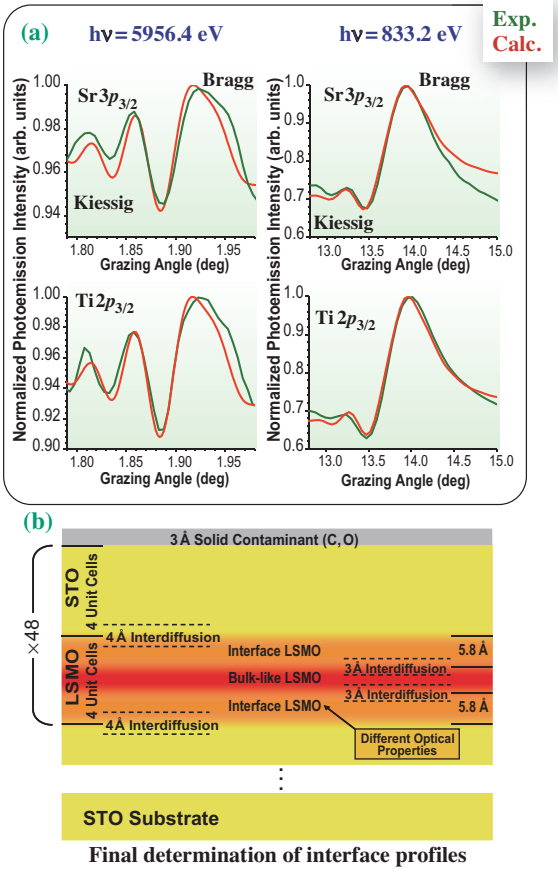

Fig. 1. **(a)** Standing-wave (SW) rocking-curves from Sr $3p_{3/2}$ and Ti $2p_{3/2}$ core levels excited by 5956 eV photons (data from SPring-8) and 833 eV photons (data from the ALS) from a $SrTiO_3/La_{0.67}Sr_{0.33}MnO_3$ multilayer, with both experiment and best-fit X-ray optical theory shown. **(b)** The detailed interface profiles of concentration derived from the best fit.

work at beamline BL15XU, it has been demonstrated that such measurements can be carried out at up to 6 keV [8], provided that the sample is cryogenically cooled to suppress phonon effects that tend to smear the data out over all occupied stated in the Brillouin zone [6,8]. Figure 2 shows such hard X-ray ARPES (HARPES) data obtained with 5.9 keV excitation for W(110): in (a) the data corrected for phonon effects and photoelectron diffraction, and in (b) the results of one-step theoretical calculations. Figure 3 shows similar data for 3.2 keV excitation of GaAs(100), here with its Brillouin zone (BZ) in (a), and the corrected data in (b). The more localized and core-like As 4*s* band at about 13 eV binding energy exhibits intensity modulation due to photoelectron diffraction instead of dispersing band structure, whereas the delocalized bands extending over 5-8 eV binding energy show clear dispersion that agrees well with band structure and one-step photoemission theory [8]. Hard X-ray photoelectron diffraction (HXPD) in fact promises to provide an additional new element-specific structural tool for complex materials, e.g. of dopant site determination [9]. Other theoretical calculations indicate that many materials should be amenable to such measurements in the 2-3 keV, if not higher, energy range [6].

These are thus first-of-a-kind HAXPES measurements of two different types that should permit future studies of the bulk, buried-layer, and interface compositions and electronic structures of various complex materials and nanostructures.

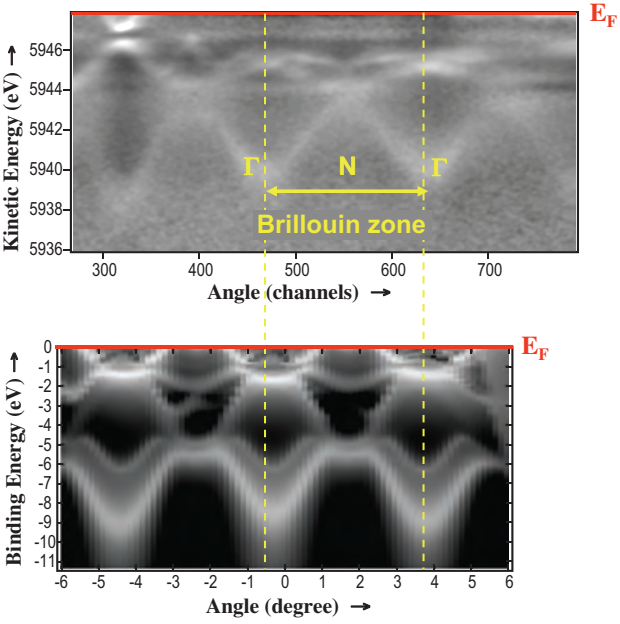

Fig. 2. HARPES data from W(110) at 30 K with excitation at a photon energy of 5956 eV. **(a)** The data at 30 K, corrected for DOS and HXPD effects, clearly exhibiting dispersive bands. **(b)** One-step photoemission theory, which exhibits good agreement with experiment.

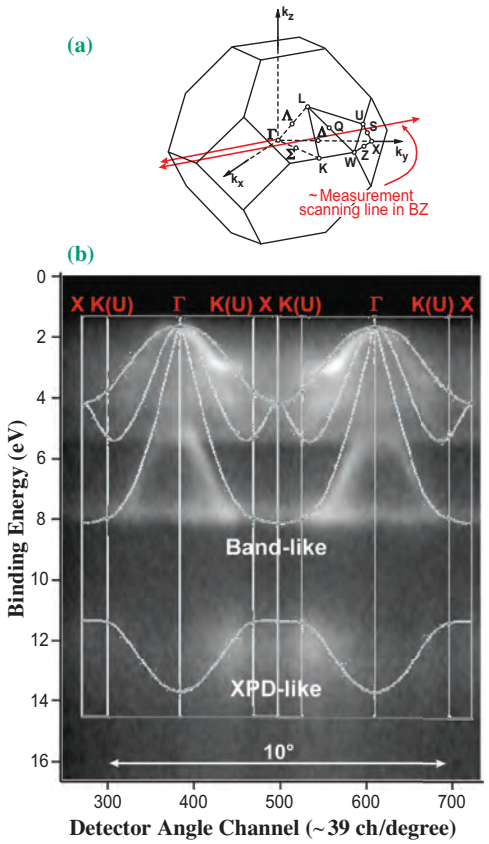

Fig. 3. HARPES data from GaAs(001) at 30 K with excitation at a photon energy of 3242 eV. **(a)** The Brillouin zone, with the expected sampling line shown in red. **(b)** The corrected data are overlaid with the band structure region that is predicted by a simple free-electron final-state calculation to be involved in direct transitions. The band at *ca*. 13 eV is mostly non-bonding As 4*s* and so is core-like, exhibiting HXPD effects. The bands above it are more delocalized, and show dispersion.

C. S. Fadley[a,b,*], S. Ueda[c] and K. Kobayashi[c]

[a] Dept. of Physics, University of California Davis, USA
[b] Materials Sciences Division, Lawrence Berkeley National Laboratory, USA
[c] NIMS Beamline Station at SPring-8, National Institute for Materials Science

*E-mail: fadley@physics.ucdavis.edu

References

[1]K. Kobayashi *et al*.: Appl. Phys. Lett. **84** (2004) 1005.
[2]K. Kobayashi: Nucl. Instrum. Meth. in Phys. Res. A **601** (2009) 32.
[3] S.-H. Yang *et al*.: J. Appl. Phys. **103** (2008) 07C519.
[4] *C. Papp, B. Balke, S. Ueda, K. Kobayashi, Y. Yamashita, H. Yoshikawa, G. Conti, C.M. Schneider and C.S. Fadley: publications on SPring-8 standing-wave data for Fe/MgO and TiN/Si - in preparation.*
[5] A. Gray *et al*.: STO/LSMO multilayer - in preparation.
[6] C.S. Fadley: J. Electr. Spectrosc. and Rel. Phen. **178-179** (2010) 2.
[7] L. Plucinski *et al*.: Phys. Rev. B **78** (2008) 035108 and references therein.
[8] S. Ueda *et al*.: HARPES for W and GaAs - in preparation.
[9] A. Winkelmann *et al*.: New J. Phys. **10** (2008) 113002.

Definitive Evidence for Fully Occupied 4*f* Electrons in YbS and Yb Metal

A wide variety of physical properties in solids arise from the delicate balance between the localized and itinerant states of electrons. It is absolutely necessary to know the degree of electron localization to understand novel phenomena. Therefore, the mean valence of ions, which provides a direct measure of the degree of electron localization, must be determined with a high level of accuracy. High-energy spectroscopies, such as photoemission spectroscopy (PES) and X-ray absorption spectroscopy (XAS), have been used as fundamental probes for the directly observation of the electronic structure, including mean valence determination. Nonetheless, the reported valence values have often been inconsistent with respect to basic physical properties. For example, YbS and Yb metal have been considered as prototypical divalent Yb systems, in which the 4*f* shell is completely filled (f^{14} configuration), at ambient pressure. However, a low trivalent (f^{13} configuration) signal intensity has been observed in Yb L_{III}-edge XAS and Yb $L_{\alpha 1}$ resonant inelastic X-ray scattering (RIXS) [1]. Hence, it is important to clarify whether YbS and Yb metal have intrinsically mixed-valence ground states. In particular, YbS has been identified as the ionic insulator $Yb^{2+}S^{2-}$. Only at high pressures above 10 GPa, a mixed-valence state is realized, coupled with the insulator-to-metal transition [2]. Thus, it seems contradictory that XAS and RIXS indicate mixed-valence states in YbS coexisting with the insulating ground state. Compared with XAS and RIXS, rare-earth 3*d* core-level PES is a preferable probe for determining the mean valence because, with the PES, signature features of divalent and trivalent states are well separated. However, Yb 3*d* core levels, located at binding energies of 1500~1600 eV, could not be excited by a conventional soft X-ray source. Recent advances in hard X-ray photoelectron spectroscopy (HAXPES) make it possible to observe not only the valence band but also the Yb 3*d* core levels under bulk-sensitive conditions, based on the increased probing depth [3].

In this paper, we report the HAXPES of Yb 3*d* core levels and valence band for YbS and Yb metal [4]. The measured HAXPES spectra are compared with the energy loss functions in the bulk and surface, measured by optical spectroscopy. This comparison enables us to distinguish between the energy loss satellite of the Yb^{2+} peak and the Yb^{3+} multiplet. The obtained results clearly indicate the purely divalent Yb state of bulk YbS and Yb metal.

HAXPES experiments were carried out at a photon energy of 7.94 keV in the undulator beamline **BL29XUL**. The total energy resolution was set to 200 meV. The clean surfaces of YbS and $YbCu_2Si_2$ (as a reference of typical mixed valence compound) were obtained by cleaving *in situ*. Yb metal was prepared as films by *in situ* evaporation under ultrahigh-vacuum conditions.

Figure 1 shows the Yb 3d core-level spectra of YbS, Yb metal, and $YbCu_2Si_2$ recorded at two emission angles. Since θ is defined as shown in the inset in Fig. 1, θ = 0° and 80° are bulk- and surface-sensitive configurations, respectively. These spectra are separated into $3d_{5/2}$ and $3d_{3/2}$ components by spin-orbit splitting. In addition, for $YbCu_2Si_2$, both spin-orbit components show the final state configuration $3d^94f^{14}$ (Yb^{2+}) line and $3d^94f^{13}$ (Yb^{3+}) multiplets, which result from valence fluctuations. From the ratio of their integrated intensities, the Yb valence of $YbCu_2Si_2$ can be estimated as +2.8, which agrees well with its bulk value. As is clear from the

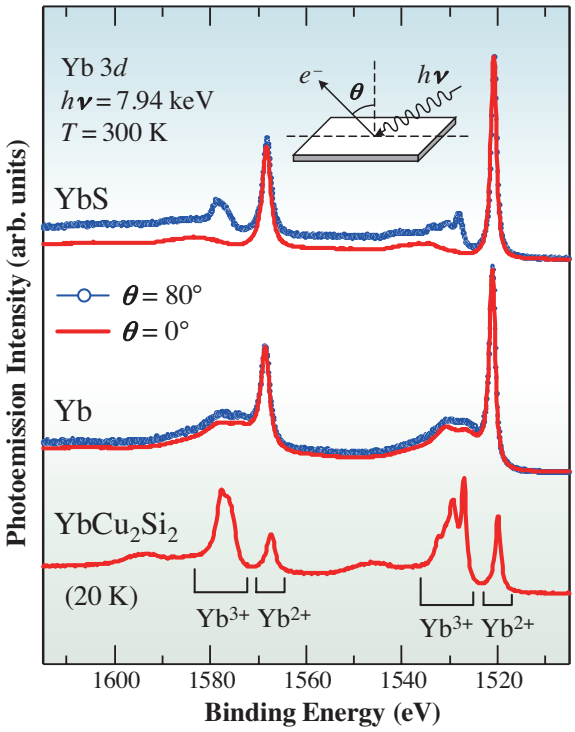

Fig. 1. Yb 3*d* core-level spectra for YbS and Yb metal recorded at emission angles θ = 0° and 80°, in comparison with that of $YbCu_2Si_2$ (θ = 0°). The definition of θ is also shown in the inset.

spectral shape, the Yb^{3+} multiplet feature also appears in the 80° spectrum for YbS. This is due to the growth of Yb_2O_3 [i.e., $(Yb^{3+})_2(O^{-2})_3$] by surface oxidation, which can be regarded as the origin of the previously reported trivalent signal. In contrast, the spectra at 0° for YbS and at both angles for Yb metal show the Yb^{2+} peak and its broad satellite feature as discussed in the following.

Figure 2 shows a comparison of the satellite features in Yb $3d_{5/2}$ core-level spectra of YbS and Yb metal with their bulk and surface loss functions, where the loss functions are plotted relative to the Yb^{2+} $3d_{5/2}$ peak energy. For YbS, the satellite feature in the 0° spectrum shows good correspondence with the peaks in the bulk loss function. Hence, the satellite is attributed to the energy loss caused by electronic interband transitions. On the other hand, the main feature in the 80° spectrum shows no such correspondence with the energy loss functions, indicating that such a feature is mainly due to the Yb^{3+} multiplet. For Yb metal, both loss functions are mainly composed of two features, which are due to the plasmon excitations at 8-10 eV and the interband transitions at 5-7 eV. The satellite features at both angles can be well reproduced by combining bulk and surface loss functions. In addition, the spectral shapes of the satellites at both 0° and 80° are very different from that of the Yb^{3+} multiplet. As a result, this method unambiguously elucidates the purely divalent Yb state of bulk YbS and Yb metal.

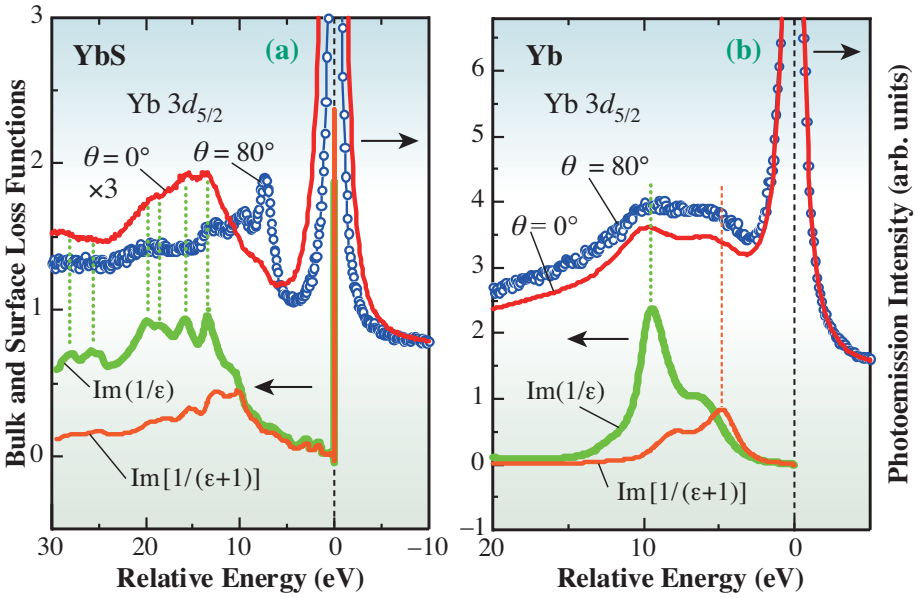

Fig. 2. Satellite structures in Yb $3d_{5/2}$ core-level spectra for YbS **(a)** and Yb metal **(b)**, in comparison with energy loss functions in bulk Im(1/ε) and surface Im[1/(ε+1)], where ε is complex dielectric function obtained by Kramers-Kronig analysis of optical reflectivity. Dotted lines indicate main peak positions in the loss functions.

Masaharu Matsunami[a,b,†]

[a] Institute for Solid State Physics, The University of Tokyo
[b] SPring-8 / RIKEN

E-mail: matunami@ims.ac.jp

[†] Present address: Institute for Molecular Science, UVSOR Facility

References

[1] E. Annese *et al.*: Phys. Rev. B **70** (2004) 075117.
[2] M. Matsunami *et al.*: Phys. Rev. Lett. **103** (2009) 237202.
[3] H. Sato *et al.*: Phys. Rev. Lett. **93** (2004) 246404.
[4] *M. Matsunami, A. Chainani, M. Taguchi, R. Eguchi, Y. Ishida, Y. Takata, H. Okamura, T. Nanba, M. Yabashi, K. Tamasaku, Y. Nishino, T. Ishikawa, Y. Senba, H. Ohashi, N. Tsujii, A. Ochiai and S. Shin: Phys. Rev. B* ***78*** *(2008) 195118.*

Fermi Surface Variation Near Quantum Critical Point of $CeRu_2(Si_{1-x}Ge_x)_2$ Studied by Resonant ARPES

$CeRu_2Si_2$ is a representative heavy-fermion (HF) compound with a paramagnetic ground state. The large specific heat coefficient γ~350 mJ/mol K^2 indicates the itinerancy of the Ce 4*f* electrons in the ground state, and the Kondo crossover temperature T_0 is estimated to be ~20-25 K. A magnetic ground state appears upon substitution of Ge atoms for Si atoms, i.e., $CeRu_2(Si_{1-x}Ge_x)_2$, corresponding to the application of a negative chemical pressure: The system is antiferromagnetic for x = 0.07-0.57 and ferromagnetic for x = 0.57-1.0 [1]. The boundary of the emergence of the antiferromagnetic ground state, namely, the critical composition x_c = 0.07, at a very low temperature is considered to be the quantum critical point (QCP), where the Ce 4*f* electrons may be transformed from itinerant electrons to localized electrons, possibly accompanied by variations in the shape and volume of Fermi surfaces (FSs). The de Haas van Alphen (dHvA) experiment indicated that the 4*f*-itinerant FSs are observed in paramagnetic $CeRu_2Si_2$, while the FSs of ferromagnetic $CeRu_2Ge_2$ are almost the same as those of $LaRu_2Ge_2$, indicating that the 4*f* electrons are localized in $CeRu_2Ge_2$ [2,3]. The important issue is in the point where the variation from the 4*f*-itinerant FSs to the 4*f*-localized FSs occurs upon the substitution of Ge atoms for Si atoms, and one of the most possible candidates is the point near QCP, i.e., around x_c. Therefore, in order to verify the existence of the FS variation across x_c, we have investigated the Fermi surfaces $CeRu_2Si_2$ and $CeRu_2(Si_{0.82}Ge_{0.18})_2$ in paramagnetic state at around T_0 by soft X-ray angle-resolved photoelectron spectroscopy (ARPES) [4]. In order to enhance the photoemission signals of the Ce 4*f* electrons, we have performed an ARPES experiment in the Ce $3d \rightarrow 4f$ resonance energy region. ARPES was also performed for $LaRu_2Si_2$ as a reference material where the 4*f* electrons do not participate in the FS formation. The experiments were performed at beamline **BL23SU**.

Figures 1(b) and 1(c), 1(d) and 1(e), and 1(f) and 1(g) show ARPES spectra of the valence bands of $LaRu_2Si_2$, $CeRu_2Si_2$, and $CeRu_2(Si_{0.82}Ge_{0.18})_2$, respectively, along the *X*-*Z* and Γ-*X* directions of the Brillouin zone (BZ) illustrated in Fig. 1(a). The angle-scanning measurements were performed at photon energies $h\nu$ corresponding to the Γ-*X*-*Z* plane, i.e., $h\nu$ = 765, 860, and 855 eV (*off-resonance* hereafter) for $LaRu_2Si_2$, $CeRu_2Si_2$, and $CeRu_2(Si_{0.82}Ge_{0.18})_2$, respectively. As indicated by the red broken lines, the observed dispersions of energy bands are similar between $CeRu_2Si_2$ and $CeRu_2(Si_{0.82}Ge_{0.18})_2$, while the energy dispersions of $LaRu_2Si_2$ are remarkably different from those of $CeRu_2Si_2$.

Figures 2(a)-2(c) show off-resonance FS images of $LaRu_2Si_2$, $CeRu_2Si_2$, and $CeRu_2(Si_{0.82}Ge_{0.18})_2$, respectively, represented by the intensities of the ARPES spectra integrated near Fermi energy (E_F)

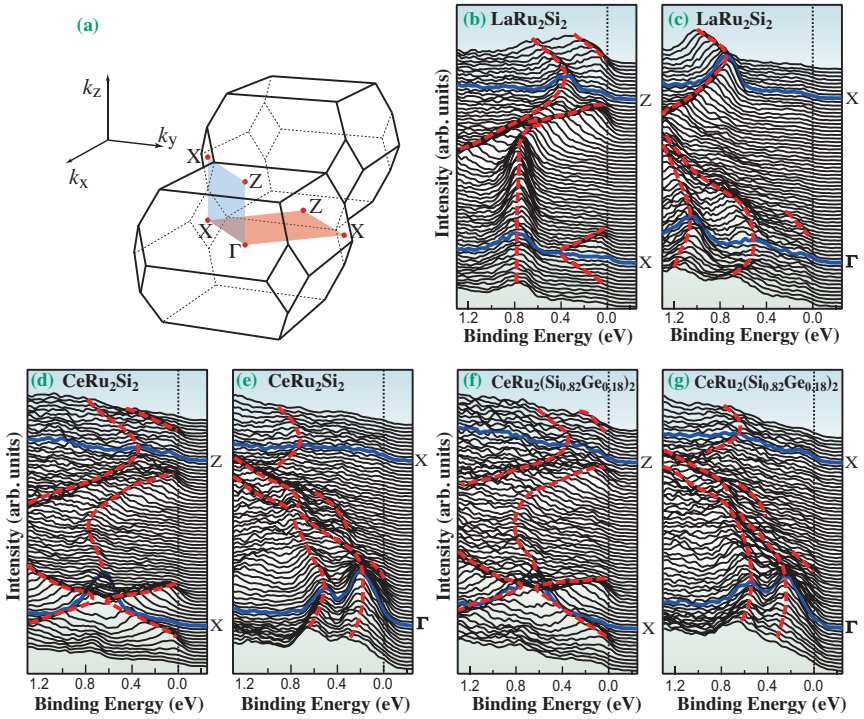

Fig. 1. **(a)** Brillouin zone for $CeRu_2(Si_{1-x}Ge_x)_2$. Off-resonance ARPES spectra of $LaRu_2Si_2$ along **(b)** *X*-*Z* and **(c)** Γ-*X* directions, those of $CeRu_2Si_2$ along **(d)** *X*-*Z* and **(e)** Γ-*X* directions, and those of $CeRu_2(Si_{0.82}Ge_{0.18})_2$ along **(f)** *X*-*Z* and **(g)** Γ-*X* directions.

as a function of momenta (k_x, k_y). For comparison, the calculated FSs of $LaRu_2Si_2$ and $CeRu_2Si_2$ in the k_x–k_y plane [5] are shown in Figs. 2(d) and 2(e), respectively. The numbers 1-4 and 5 designate the hole FSs and the electron FS, respectively. Figures 2(f) and 2(g) show the calculated three-dimensional (3D) images of the large hole FS of band 4 of $CeRu_2Si_2$ and $LaRu_2Si_2$, respectively, indicating a significant volume variation due to the participation of the Ce 4*f* electrons in the FS formation [5]. A large FS surrounding the *Z* point was experimentally detected in every compound. While the experimental large FS of $LaRu_2Si_2$ has a square shape and agrees well with the calculated hole FS of band 4, the experimental large FS of $CeRu_2Si_2$ has a circular shape and agrees well with the calculated electron FS of band 5. The large FS of $CeRu_2(Si_{0.82}Ge_{0.18})_2$ is almost identical to that of $CeRu_2Si_2$. A residual drawback in this assignment is that the hole FS of band 4 in Fig. 2(e), which is considered to be the heaviest FS branch including the largest contribution of the Ce 4*f* electrons [5], is not observed in both $CeRu_2Si_2$ and $CeRu_2(Si_{0.82}Ge_{0.18})_2$.

Therefore, angle-scanning measurements were performed at the Ce 3*d*→4*f* resonant energy of $h\nu$ = 881 eV (*on-resonance*) for $CeRu_2Si_2$ and $CeRu_2(Si_{0.82}Ge_{0.18})_2$ to enhance the signals of the 4*f*

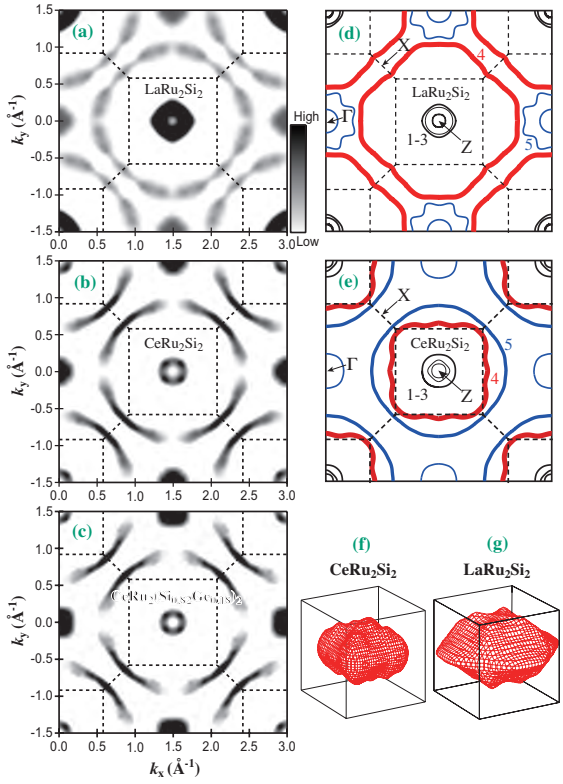

Fig. 2. Off-resonance FS images of $LaRu_2Si_2$ **(a)**, $CeRu_2Si_2$ **(b)**, and $CeRu_2(Si_{0.82}Ge_{0.18})_2$ **(c)** in the k_x-k_y plane, compared with calculated FS images of $LaRu_2Si_2$ **(d)** and $CeRu_2Si_2$ **(e)** [5]. BZ is illustrated by broken lines. Calculated 3D images of hole FS of band 4 of $CeRu_2Si_2$ **(f)** and $LaRu_2Si_2$ **(g)** around Z point (body center) [5].

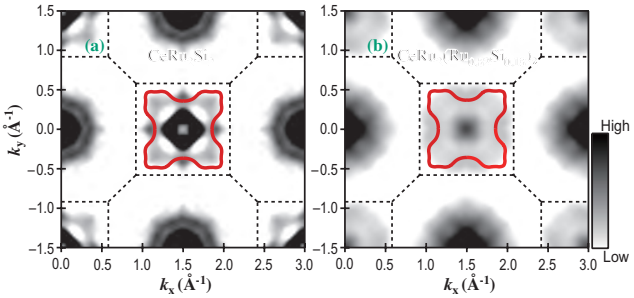

Fig. 3. On-resonance FS images in k_x-k_y planes of **(a)** $CeRu_2Si_2$ and **(b)** $CeRu_2(Si_{0.82}Ge_{0.18})_2$, compared with calculated hole FS of band 4 at $k_z = 0.3\ \pi/c$ away from *Γ*-*Z*-*X* plane, represented by red lines [5].

electrons. The resonance energy corresponds to k_z = 0.29 π/c and 0.37 π/c for $CeRu_2Si_2$ and $CeRu_2(Si_{0.82}Ge_{0.18})_2$, respectively. Figures 3(a) and 3(b) show on-resonance FS images of $CeRu_2Si_2$ and $CeRu_2(Si_{0.82}Ge_{0.18})_2$, respectively. Surprisingly, the large circular FS surrounding the *Z* point in the off-resonance images becomes invisible in the on-resonance images. On the other hand, another FS appears only inside the square BZ boundary surrounding the Z point in both $CeRu_2Si_2$ and $CeRu_2(Si_{0.82}Ge_{0.18})_2$. The size and shape of this FS are comparable to those of the calculated hole FS of band 4 at k_z = 0.3 π/c away from the *Γ*-*Z*-*X* plane, shown by red lines in Figs. 3(a) and 3(b), and thus the observed FS is assigned to be the FS of band 4, which includes the largest contribution of the Ce 4*f* electrons. Thus, the assignment of the FSs in Figs. 2 and 3 is totally consistent.

The observation of the FS including a strong 4*f* contribution in both $CeRu_2Si_2$ and $CeRu_2(Si_{0.82}Ge_{0.18})_2$ indicates that the 4*f*-delocalized regime is extended beyond the critical composition x_c. The absence of the FS change near x_c is strongly implied in the paramagnetic state below T_0, and it can be considered that the spin-density-wave model is suitable for the quantum criticality of $CeRu_2(Si_{1-x}Ge_x)_2$.

Tetsuo Okane

SPring-8 / JAEA

E-mail: okanet@spring8.or.jp

References

[1] M. Sugi *et al.*: Phys. Rev. Lett. **101** (2008) 056401.
[2] H. Aoki *et al.*: Phys. Rev. Lett. **71** (1993) 2110.
[3] C.A. King *et al.*: Physica B. **171** (1991) 161.
[4] *T. Okane, T. Ohkochi, Y. Takeda, S.-i. Fujimori, A. Yasui, Y. Saitoh, H. Yamagami, Y. Matsumoto, M. Sugi, N. Kimura, T. Komatsubara and H. Aoki: Phys. Rev. Lett.* ***102*** *(2009) 216401.*
[5] H. Yamagami *et al.*: J. Phys. Soc. Jpn. **61** (1992) 2388; J. Phys. Soc. Jpn. **62** (1993) 592.

Dependence of Electronic Properties of Epitaxial Few-Layer Graphene on Number of Layers Investigated by Photoemission Electron Microscopy

Few-layer graphene (FLG) is attracting considerable attention as a future electronics material owing to its superior electronic transport properties and compatibility with standard lithographic techniques. FLG whose transport properties have been studied has been mainly produced by exfoliating graphene flakes from bulk graphite and depositing them on SiO_2/Si substrates [1]. In general, however, its size is very small and its productivity is very low for practical applications. For a large-scale production of FLG, therefore, the epitaxial growth of FLG on SiC by thermal decomposition is being investigated actively.

During annealing SiC substrates, Si atoms preferentially desorb from the surface and C atoms left behind to form graphene layers, as schematically shown in Fig. 1. We hope that single-crystal FLG wafers produced by simple annealing methods will become a basis of the large-scale integration of graphene devices.

However, because the epitaxial FLG we have obtained so far still exhibits a thickness distribution, we should establish a reproducible method of growing wide, uniform FLG with the desired thickness. Toward this target, we have already demonstrated that the number of graphene layers N_G can be digitally counted from the quantized oscillation in the energy dependence of electron reflectivity using low-energy electron microscopy (LEEM) [2]. Another important aspect that should be clarified before device applications of epitaxial FLG is how the SiC substrate affects the electronic properties of FLG. The N_G dependence of the electronic properties provides important clues for understanding the effects of the substrate. Because it is still difficult to grow uniform epitaxial FLG, it is desirable to investigate the electronic properties using techniques that can resolve N_G microscopically. In this work, we use a spectroscopic photoemission and low-energy electron microscopy (SPELEEM) instrument at beamline **BL17SU** to observe the same area using LEEM and photoelectron emission microscopy (PEEM), which enables us to investigate the electronic properties of epitaxial FLG for each N_G microscopically [3].

Figures 2(a)-2(c) show secondary-electron (SE) PEEM images of epitaxial FLG grown on 6H-SiC(0001) obtained at various electron energies. Numbers in Fig. 2(c) correspond to N_G values determined by LEEM. Areas with different N_G values can be discriminated in the SE PEEM images, but their relative intensities depend on the SE energy. Figure 2(d) shows the SE emission spectra obtained from the sequential PEEM images. The SE emission spectra depend on N_G in two aspects, namely, the threshold start voltage of the SE emission and the spectrum shape. The threshold voltage corresponds to the vacuum level. Therefore, Fig. 2(d) shows that the work function increases with N_G, and the measured work functions are plotted in Fig. 2(e).

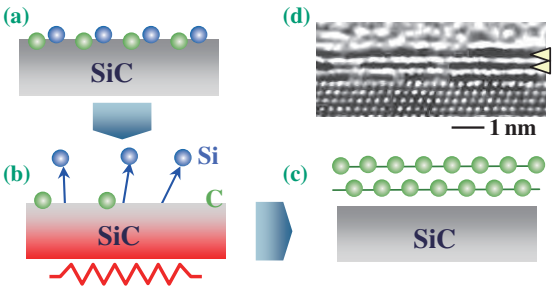

Fig. 1. **(a)**-**(c)** Schematic illustrations of SiC surface structures **(a)** before, **(b)** during, and **(c)** after annealing. **(d)** Cross-sectional transmission electron microscopy image of epitaxial FLG grown on 6H-SiC(0001).

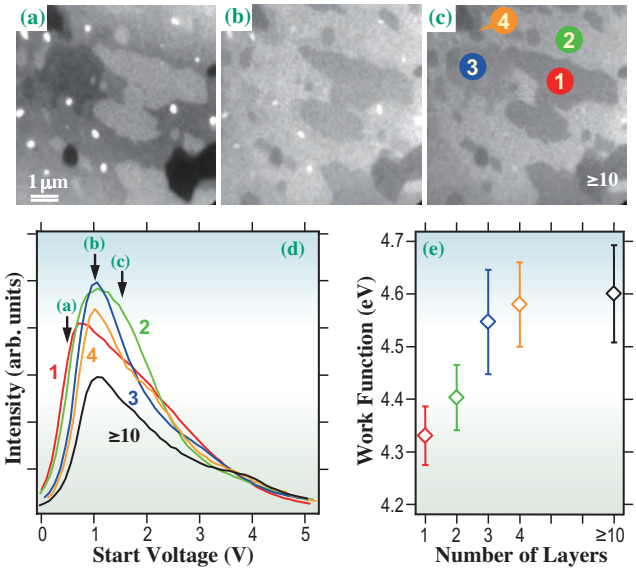

Fig. 2. **(a)**-**(b)** SE PEEM images of epitaxial FLG grown on 6H-SiC(0001) obtained under irradiation by monochromatized synchrotron radiation at energy of 400 eV. Here, we use the start voltage as a measure of the electron energy, and the start voltage multiplied by the electron unit charge is nearly equal to the electron energy. The start voltages used to obtain **(a)**-**(c)** were 0.5, 1.0, and 1.5 V, respectively. **(d)** SE emission spectra obtained from sequential SE PEEM images. Numbers in **(c)** and **(d)** indicate the N_G values. **(e)** N_G dependence of work function. We assumed that the work function of the thick graphene is equal to the reported value for bulk graphite (4.6 eV).

From the monolayer graphene to the thick graphene, the vacuum level gradually increases by about 0.3 eV. The SE emission spectra also include information about the unoccupied electronic structures [4]. The electronic structure of FLG changes with N_G, which leads to the spectrum shape change.

Figure 3(a) shows a PEEM image of epitaxial FLG obtained using C1*s* photoelectrons. Areas with different numbers of graphene layers can be discriminated in the C1*s* PEEM image. The C1*s* core-level photoelectron spectra in Fig. 3(b) show that the peak energy of the C1*s* photoelectron intensity depends on N_G, indicating that the C1*s* binding energy of the monolayer graphene is about 0.4 eV larger than that of the thick graphene (Fig. 3(c)).

It is known that the Dirac point falls below the Fermi level owing to the charge transfer from the substrate to FLG and that the shift from the Fermi level decreases with the number of graphene layers [5]. The Dirac point, C1*s* core level, and vacuum level of FLG move with N_G rather similarly. In the first approximation, all the electronic structures of FLG rigidly shift due to the charge transfer. More strictly, however, the shift in the work function seems smaller than those in the Dirac point and C1*s* binding energies. To determine the reason for this, we need further experimental and theoretical studies.

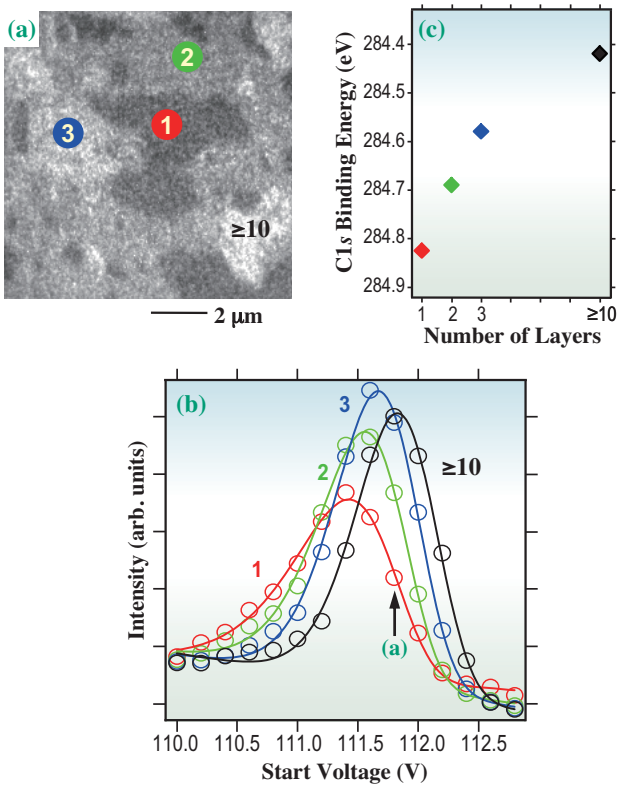

Fig. 3. **(a)** C1*s* PEEM images at start voltage of 111.8 V. The photon energy was 400 eV and the exposure time was 600 s. The areas whose N_G values are indicated are the same as those in Fig. 2(c). **(b)** C1*s* core-level photoelectron spectra obtained from sequential C1*s* PEEM images. Open circles denote the experimental data, and solid lines the results of fitting the data to an asymmetric Gaussian function with a linear background. **(c)** N_G dependence of C1*s* binding energy. The peak start voltage was converted to the binding energy by assuming that the binding energy of the thick graphene is the same as that of bulk graphite (284.42 eV).

Hiroki Hibino[a,*] and Yoshio Watanabe[b]

[a] NTT Basic Research Laboratories
[b] SPring-8 / JASRI

*E-mail: hibino@will.brl.ntt.co.jp

References

[1] A.K. Geim and K.S. Novoselov: Nature Mater. **6** (2007) 183.
[2] H. Hibino *et al.*: Phys. Rev. B **77** (2008) 075413.
[3] *H. Hibino, H. Kageshima, M. Kotsugi, F. Maeda, F.-Z. Guo and Y. Watanabe: Phys. Rev. B* ***79*** *(2009) 125437.*
[4] H. Hibino *et al.*: Appl. Surf. Sci. **254** (2008) 7596.
[5] T. Ohta *et al.*: Phys. Rev. Lett. **98** (2007) 206802.

Transverse Acoustic Excitations in Simple Liquid

Lattice modes are modes of vibration of a macroscopic part of a system. In the long-wavelength limit, they may be described by the classical theory of elasticity in which the system is treated as a continuum. As the wavelength of the vibrations becomes comparable to the distance between the atoms, the microscopic structure of the system and the forces between individual pairs of atoms become the dominant features in determining the nature of the modes of vibration.

In simple liquids, longitudinal acoustic (LA) phonon modes are easily observed by ultrasonic, optical, or inelastic scattering experiments because density fluctuations occur owing to a strong repulsive force between atoms when they approach each other. However, transverse acoustic (TA) phonon modes cannot usually be detected in liquids by ultrasonic or optical measurements since the shear force over long distances is very weak. Over short distances, however, there may be a cage effect that acts as a restoring force for TA modes. The TA modes can be observed even in liquid metals in the dynamic structure factor $S(Q,\omega)$ measured by inelastic X-ray or neutron scattering (IXS or INS). Although the TA modes in simple liquids have been discussed theoretically for more than thirty years [1], experimental evidence has not yet been obtained. To detect the TA modes, we carefully measured IXS from liquid Ga at 40°C at beamline **BL35XU** [2]. A Ga sample, 50 μm in thickness, was contained in a thin-walled (0.25 mm) single-crystal sapphire cell [3].

Figure 1 shows the $S(Q,\omega)/S(Q)$ result measured at Q = 10.6 nm^{-1}. LA excitations are clearly seen as large peaks at about 17 meV. In addition, small extra excitations can be detected at about 8 meV between the central quasielastic peak and the LA peaks. The solid curves in the figure indicate the best fits and residuals for the single and double damped harmonic oscillator (1DHO and 2DHO, respectively) models; the 1DHO model includes only the LA excitation, and the 2DHO model, both the LA and TA modes. We focus on the second, weak mode as a signature of a TA excitation. As clearly observed in the figure, the 2DHO model reproduces the experimental $S(Q,\omega)$ spectrum well.

Figure 2 shows the dispersion relation of the weak (open circles) and strong (full triangles and full circles) excitations obtained from the 2DHO fits. The solid curve represents the TA phonon excitations obtained by orbital-free *ab initio* molecular dynamics (MD) simulation. This curve almost coincides with the present experimental data. However, the TA phonon

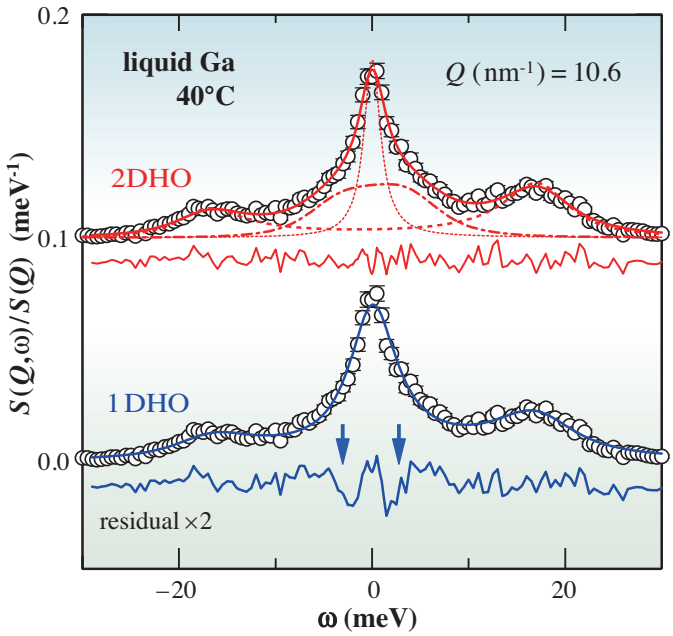

Fig. 1. $S(Q,\omega)/S(Q)$ spectrum at Q = 10.6 nm^{-1}. Solid curves represent the best fits and residuals obtained using the 1DHO (lower panel) and 2DHO (upper panel) models, and dotted, dashed, and chain curves denote the quasielastic, LA, and TA contributions, respectively. See the text for details.

modes cannot be detected in crystals in the first Brillouin zone by IXS experiment, since the direction of TA oscillations is perpendicular to the *Q* direction. On the other hand, the MD simulation reveals that a mixing of the TA and LA excitations occurs in liquid Ga, and the peaks of the quasi-TA branch in the LA excitations detectable by IXS are given by the dashed curve in Fig. 2. This curve almost coincides with the present experimental data, which is clear evidence of the existence of the TA mode in liquid Ga. The velocity of the TA sound is slightly larger than 1050 m/s, indicating a shear modulus of about 6.5 GPa, about 20% of the solid Ga value.

In accordance with the Heisenberg uncertainty principle, the lifetime τ of the phonons can be estimated to be $\tau = \pi/\Gamma_Q$, where Γ_Q is the width of the DHO close to half width at half maximum. Figure 3(a) shows the τ values of the TA (open circles) and LA (other marks) phonons. The τ value of the TA phonons is about 0.5 ps, which is almost the same as that of the LA phonons. Figure 3(b) shows the propagation length *L* of the TA and LA phonons (lifetime times velocity of sound). The *L* value of the TA phonons is 0.4-0.5 nm, which is much smaller than the Ioffe-Regel limit (dashed curve), indicating that the TA phonons are localized. This value may correspond to the size of the cages formed instantaneously (0.5 ps) in liquid Ga.

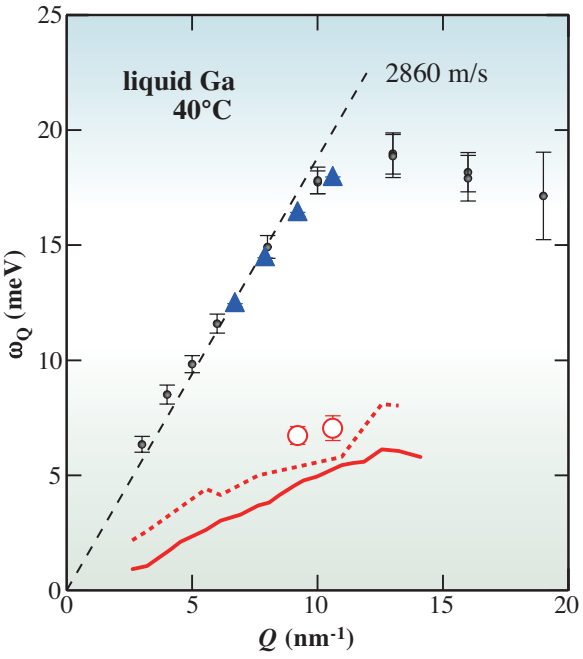

Fig. 2. Dispersion relation of TA (open circles) and LA (full triangles and full circles) phonon excitation modes obtained from the DHO fits. See the text for details.

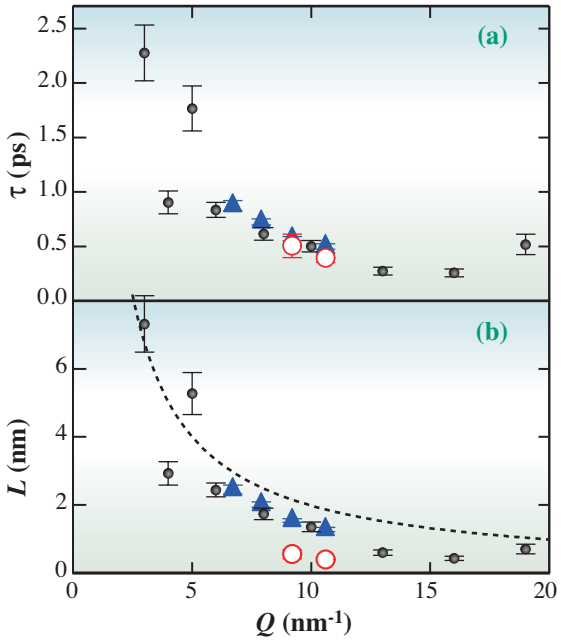

Fig. 3. **(a)** Lifetime τ and **(b)** propagation length *L* of TA (open circles) and LA (other marks) phonons. See the text for details.

Shinya Hosokawa[a,*], Masanori Inui[b] and Alfred Q. R. Baron[c]

[a] Center for Materials Research Using Third-Generation Synchrotron Radiation Facilities, Hiroshima Institute of Technology
[b] Graduate School of Integrated Arts and Sciences, Hiroshima University
[c] SPring-8 / RIKEN·JASRI

*E-mail: hosokawa@cc.it-hiroshima.ac.jp

References

[1] J.-P. Hansen and I. R. McDonald: Theory of Simple Liquids, 3rd ed. (Elsevier, Amsterdam, 2006).
[2] *S. Hosokawa, M. Inui, Y. Kajihara, K. Matsuda, T. Ichitsubo, W.-C. Pilgrim, H. Sinn, L. E. González, D. J. González, S. Tsutsui, and A. Q. R. Baron: Phys. Rev. Lett.* ***102*** *(2009) 105502.*
[3] K. Tamura *et al.*: Rev. Sci. Instrum. **70** (1999) 144.

Metal-Insulator Transitions in Complex Oxides Probed by High Resolution X-Ray Compton Scattering

The Coulomb repulsion in transition metal oxides (TMO) tends to localize individual d electrons on metal atoms while the hybridization with the oxygen *p* electron states de-localizes these same electrons. These competing effects explain the metal insulating transition (MIT) in a TMO. Several theories have been put forward to explain the MIT, some generalize the concept of the Fermi liquid, while others attempt to describe highly correlated behavior by using Hubbard models. In this context, the comparison of the measured electron momentum density with the predictions of theories gives an indication of their correctness. Detecting the energy of photons scattered at a fixed angle in back-scattering geometry from a mono-energetic beam incident on the sample gives access to the Compton profile (CP), which is a projection onto one dimension of the electron momentum density.

Recently, the combination of X-ray Compton scattering experiments and reliable density functional theory (DFT) calculations has revealed unique information about the MIT in the bi-layer manganite $La_{2-2x}Sr_{1+2x}Mn_2O_7$ [1]. This TMO undergoes a characteristic MIT when a magnetic field is applied, which is known as the colossal magneto-resistance (CMR) effect. Presently, intensive research is being carried out in developing spintronics technology based on this property. Until now, the CMR effect has been understood with models in which only the *d* electronic states of Mn are involved. The X-ray Compton scattering results have helped to gain a deeper understanding of the phase transition under consideration and have demonstrated the need to consider the *p* electronic states of oxygen as well. CP differences between the metallic and insulating state have shown that Compton scattering is an incisive probe of the electronic behaviour across the MIT.

Figure 1 shows results of the Compton scattering experiment compared to the DFT. The $La_{2-2x}Sr_{1+2x}Mn_2O_7$ single crystal with x = 0.35 has been studied as a function of temperature and magnetic field. Quantitative agreement has been found between DFT calculations and experiment with respect to the CP anisotropy in the two metallic phases (i.e. the low temperature ferromagnetic and the CMR phase under a magnetic field of 7 T). Robust signatures of the metal-insulator transition (MIT) have been identified in the momentum density for the paramagnetic phase above the Curie temperature. In particular, a strong deviation for low electron momentum has been noticed by comparing the CP anisotropies of the paramagnetic (insulating) and ferromagnetic/CMR (metallic) phases as shown in Fig. 1.

In Fig. 2, the power spectra of the CP anisotropies reveal that the experimental data for the metallic phases and the theory are in agreement and that

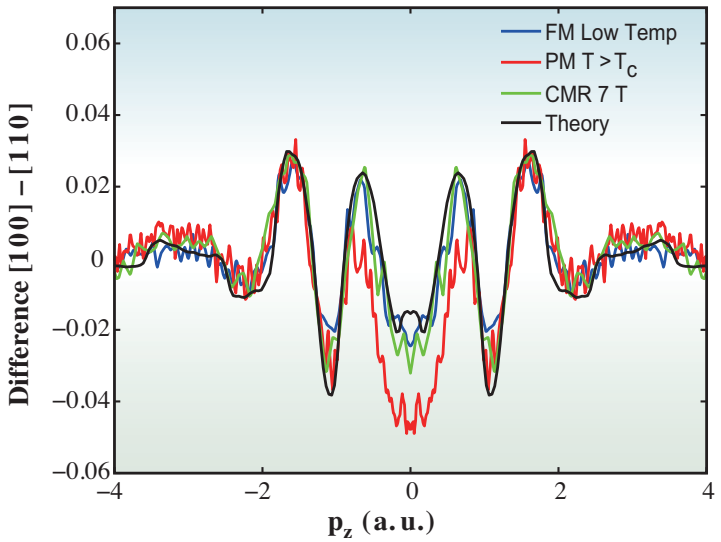

Fig. 1. Anisotropy of the CP [100]-[110]. In the legend, Low Temp FM is for the ferromagnetic phase at 20 K, PM $T>T_c$ is for the paramagnetic phase at 131 K, CMR 7 T is for the colossal magnetoresistance phase in an external field of 7 T at 131 K and Theory is for the DFT calculations. The data are in units of the CP amplitude at the origin.

the wave functions are of a delocalized nature. However, the experiment for the insulator shows a clear tendency to shift spectral weight towards short distances. Thus, the localization trend for the insulator wave functions becomes clear.

The anisotropy of the 2-dimensional momentum density in Fig. 3 shows important contributions of oxygen *p* electrons to the Fermi surface (FS). In the insulator, some of these *p* electron contributions at low momentum must redistribute since the FS vanishes. Thus, an important outcome of this work is the determination of the number n_e of displaced electrons across the metal-to-insulator transition. The value of n_e (about 0.7 electron per Mn atom) can in fact be extracted from the area enclosed by the anisotropy difference of Fig. 1. Therefore, by measuring the number of displaced electrons across the MIT, X-ray Compton scattering opens new opportunities for studying quantitatively the phase diagrams of other complex materials such as magnetite [2].

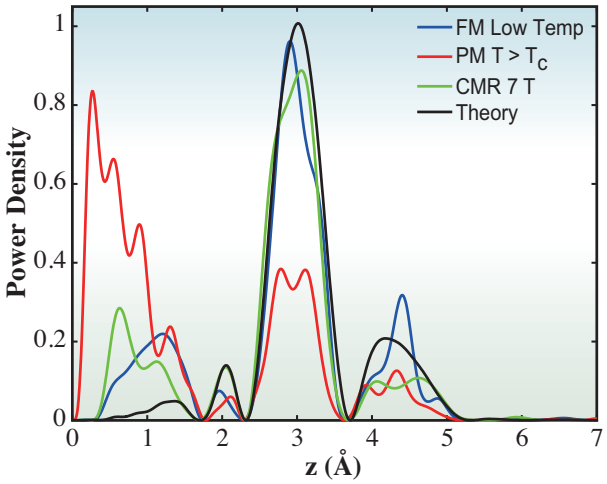

Fig. 2. Comparison in real space of the power spectra of the CP anisotropies. All the curves are normalized to a unit area. The notations in the legend are as in Fig. 1.

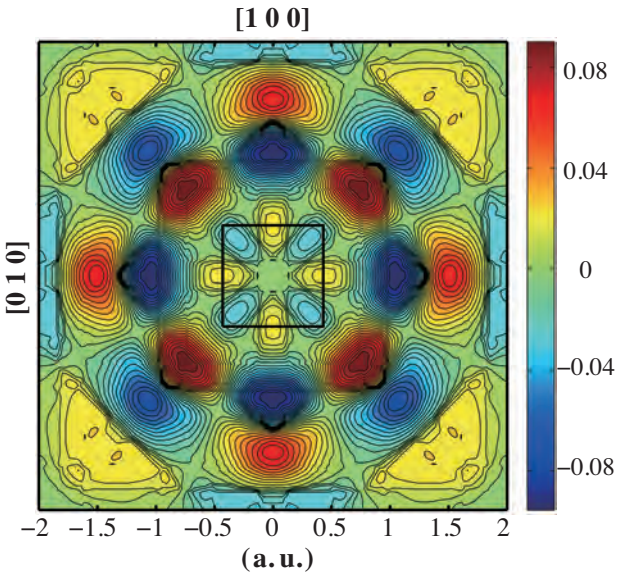

Fig. 3. Anisotropy of 2D projection of the theoretical electron momentum density onto the (001) plane. The first Brillouin zone is shown by a square. The anisotropy integration along the [0 1 0] axis yields the theory curve of Fig. 1. The data are in units of the momentum density amplitude at the origin.

B. Barbiellini[a,*], A. Koizumi[b] and M. Itou[c]

[a] Physics Department, Northeastern University, USA
[b] Graduate School of Material Science, University of Hyogo
[c] SPring-8 / JASRI

*E-mail: bba@neu.edu

References

[1] *B. Barbiellini, A. Koizumi, P. E. Mijnarends, W. Al-Sawai, Hsin Lin, T. Nagao, K. Hirota, M. Itou, Y. Sakurai, and A. Bansil: Phys. Rev. Lett.* ***102*** *(2009) 206402.*
[2] H. Kobayashi *et al.*: Phys. Rev. B **80** (2009) 104423.

Energy Domain Mössbauer Spectroscopy Using Synchrotron Radiation

Mössbauer spectroscopy is a powerful and well-established method for a wide range of research fields, including physics, chemistry, biology, and earth science [1]. Information about magnetism, valence, electronic state anisotropy, and electron densitiy can be obtained through hyperfine interactions between the nucleus and surrounding electrons. Since the hyperfine interactions induce the split and/or shift in nuclear energy level, a precise measurement of nuclear energy level gives information regarding electronic states. The Mössbauer effect occurs when the nucleus absorbs γ-rays resonantly without recoil, thereby allowing the precise measurement of nuclear energy level without the effect of recoil. In Mössbauer spectroscopy, energy level is measured by an energy scan using a narrow single line of a radioisotope source; the energy scan is performed by the Doppler effect. The information regarding the electronic states obtained by Mössbauer spectroscopy is concentrated on the electrons surrounding the nucleus that cause the Mössbauer effect. The element-specific information, which is obtained by Mössbauer spectroscopy, is important and is required for modern precise materials science and complex systems, such as biological substances. As an alternative Mössbauer source, third-generation synchrotron radiation has many superior features, such as high brilliance, high directionality, and energy selectivity. It affords unique opportunities to measure hyperfine interactions in very small samples, samples at high pressures, and ultrathin films, all of which are difficult to measure using conventional radioactive sources. However, since the bandwidth of synchrotron radiation is much wider than those of Mössbauer radioactive sources, other measuring methods must be adopted. The most frequently used method involves the detection of the time-differential nuclear resonant forward scattering of synchrotron radiation, which is a time analogue of Mössbauer spectroscopy [2]. This method is effective and efficient for nuclides with long-lifetime and relatively low-energy excited states; however, nuclides with short-lifetime and high-energy excited states may be difficult to measure. Moreover, in the case of contaminated or complex samples, it is sometimes difficult to carry out spectrum analysis by the time differential method.

We have developed a method that yields Mössbauer absorption-type spectra using synchrotron radiation and is applicable to many Mössbauer nuclides, including those with short-lifetime and high-energy excited levels [3]. This method enables us to carry out a unique Mössbauer spectroscopy, retaining the excellent features of synchrotron radiation. Figure 1 shows the schematic of the measuring concept. In this method, in addition to a measurement sample, a reference sample is used; these samples are used as a transmitter and a scatterer, respectively. The Mössbauer spectrum is measured by determining the intensity of delayed scattering from the excited Mössbauer nuclei in the scatter as a function of Doppler velocity. Since part of the incident radiation with an energy the same as the excitation energy of the nuclides in the transmitter is absorbed and therefore decreases after passing through the transmitter, the intensity of nuclear resonant scattering in the scatterer decreases, provided that the nuclear excitation energy of the scatterer is the same as that of the transmitter. Usually, nuclear resonant excitation energies in different electronic states differ from each other. Therefore, by scanning the relative nuclear resonant energy using the Doppler effect, the relative energy shift of the sample being measured from the reference sample is found as the local minimum of scattering intensity. It should be noted that we can use the

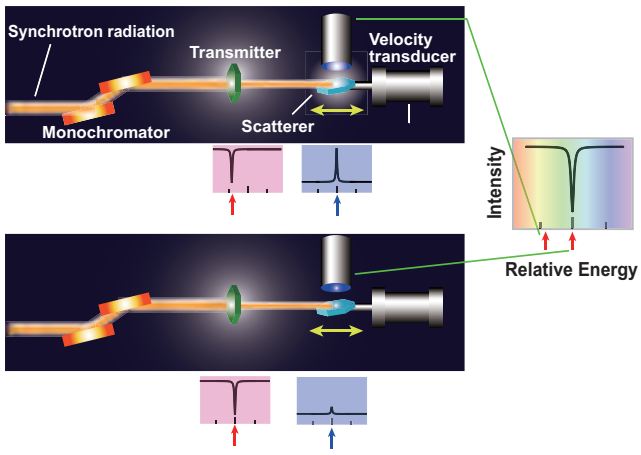

Fig. 1. Schematic of concept of energy domain in Mössbauer spectroscopy. A component of synchrotron radiation with the same energy as the resonant excited states of the Mössbauer nucleus in a transmitter is absorbed by the transmitter. Therefore, the transmitted radiation induces nuclear resonant scattering in a scatterer if the relative resonant excited state energy of the scatterer is different from that of the transmitter (upper part of the figure) but not if they are the same (lower part). Consequently, by counting the scattering intensity with the Si-APD detector as a function of their relative energy, the Mössbauer absorption-type spectrum is obtained. The relative energy shift is obtained using the velocity transducer.

measurement sample as either the transmitter or the scatterer, depending on the sample conditions and/or experimental purposes. This flexibility broadens the experimental possibilities. We can set the sample as a transmitter for measurement under extreme conditions, such as high pressures, strong magnetic fields, and high temperatures. For the study of very thick samples and samples kept in a special holder through which X-rays cannot penetrate and for the study of surface states, such as nanostructured materials, the sample can be set as the scatterer.

To confirm the validity of this method, we have measured a well-known ^{57}Fe Mössbauer spectrum using an α-Fe_2O_3 (unenriched) powder sample as the transmitter and a Pd metal foil containing ^{57}Fe (2%) as a single-line reference scatterer. The measurement was performed at the JAEA beamline **BL11XU** at 298 K. The scattered γ-rays at de-excitation from a resonantly excited nucleus were measured using a multi-element (4 × 2) Si-APD detector. The measured Mössbauer spectrum is shown in Fig. 2. The hyperfine split sextet can be clearly seen, and the peak positions of the spectrum are in agreement with previous observations using an RI source [4]. This result provides evidence that the developed system functions well. We have also measured the ^{73}Ge Mössbauer spectrum at a high resonance energy of 68.752 keV and a short lifetime of 2.51 ns in the third excited state, which is difficult to measure with a radioactive source. The measurement was carried out at beamline **BL09XU** using a Li_2GeO_3 (unenriched) powder sample as the transmitter and an enriched GeO_2 powder sample (96.4% ^{73}Ge enriched, a rutile structure with a tetragonal unit cell) as the scatterer.

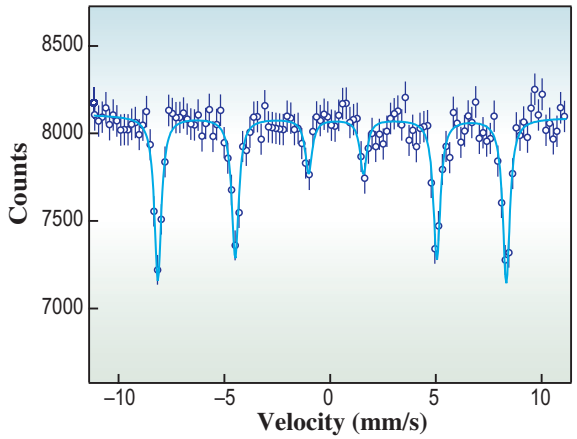

Fig. 2. Mössbauer spectrum of ^{57}Fe observed by nuclear resonant scattering of synchrotron radiation [3]. A powder sample of α-Fe_2O_3 (unenriched) was used as the transmitter, and a Pd metal foil containing ^{57}Fe (2%) was used as the scatterer. The solid line shows the fitted spectrum with Lorentz line shapes.

The scatterer and the transmitter were cooled to 77 K and 20 K, respectively. The Mössbauer spectrum of ^{73}Ge is shown in Fig. 3. The exact line shape of the measured spectrum can be obtained theoretically [5]. The isomer shift of Li_2GeO_3 relative to tetragonal GeO_2 was obtained as –0.21(12) mm/s; isomer shifts depend directly on the *s*-electron densities and indirectly on *p*-, *d*-, and *f*-electrons through shielding effects and give the difference between the electronic state of the transmitter and that of the scatterer.

Since Mössbauer nuclides are widely available for use with synchrotron radiation, this method offers the potential for unique measurement capabilities for various scientific requirements including microscopic measurements, measurements under extreme conditions for ultrasmall samples, and measurements of complex nanostructured materials.

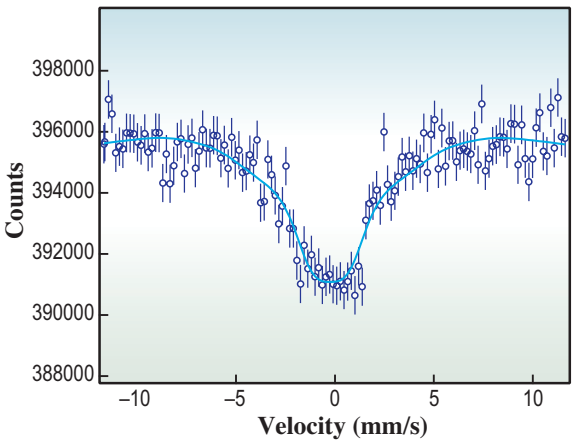

Fig. 3. Mössbauer spectrum of ^{73}Ge measured by nuclear resonant scattering of synchrotron radiation [3]. A powder sample of Li_2GeO_3 (unenriched, 20 K) was used as the transmitter, and a powder sample of GeO_2 (95% enriched, 77 K) was used as the scatterer. The solid line shows the fitted spectrum obtained using the developed theory [5].

Makoto Seto

Research Reactor Institute, Kyoto University

E-mail:seto@rri.kyoto-u.ac.jp

References

[1] R.L. Mössbauer: Naturwissenschaften **60** (1973) 493.
[2] J.B. Hastings *et al.*: Phys. Rev. Lett. **66** (1991) 770.
[3] *M. Seto, R. Masuda, S. Higashitaniguchi, S. Kitao, Y. Kobayashi, C. Inaba, T. Mitsui and Y. Yoda: Phys. Rev. Lett.* ***102*** *(2009) 217602.*
[4] C. Kistner and A.W. Sunyar: Phys. Rev. Lett. **4** (1960) 412.
[5] G.V. Smirnov and V.G. Kohn: Phys. Rev. B **52** (1995) 3356.

High-Magnetic-Field XMCD Using Pulsed Magnet

X-ray magnetic circular dichroism (XMCD) is a powerful and unique means to study magnetism because of element and shell selectivity. Although there have been many excellent works on the XMCD of magnetic materials, most of them focus on ferromagnetic materials. This is partly because a sufficiently high magnetic field for magnetizing antiferromagnetic or paramagnetic materials was not available at synchrotron X-ray facilities. Fields of 1-2 T are generally used for conventional XMCD experiments, and even the highest field using a large superconducting magnet is about 10 T.

Over several years, we have been developing experimental techniques for high magnetic field X-ray experiments in the 40 T range. We utilize a very small pulsed magnet with an inner diameter of 3-5 mm and a portable capacitor bank to perform several experiments, such as those involving X-ray diffraction [1] and X-ray absorption spectroscopy (XAS) [2]. In this work, we applied this technique to XMCD spectroscopy and investigate the valence fluctuating state of Eu atoms in $EuNi_2(Si_{0.82}Ge_{0.18})_2$. The ground state of this material at low temperatures is nonmagnetic owing to the strong *c-f* (conduction electron – *f* electron) hybridization. Therefore, so far, no one has considered it as a candidate material for the XMCD study. The high magnetic fields of up to 40 T can induce the magnetic moment and enable us to study the XMCD. We can expect the characteristic features in the XMCD spectra due to the Eu valence fluctuation, i.e., the quantum mechanical mixing of Eu^{2+} and Eu^{3+} states.

The XMCD experiment with the Eu $L_{2,3}$-edge ($2p_{1/2,3/2} \rightarrow 5d$) was carried out at beamline **BL39XU**. Figure 1 shows the photograph of the miniature magnet used. The crystal is powdered and diluted in order to achieve an effective sample thickness of about 10 μm for the transmission measurement. A diamond X-ray phase plate was introduced to generate circularly polarized X-rays. The XMCD signal ($\Delta\mu t = \mu^+t - \mu^-t$) is determined as the difference in absorption intensity between the right (μ^+t) and left (μ^-t) circular polarizations. μ^+t and μ^-t were measured by successively applying two shots of a pulsed field at a fixed X-ray energy while reversing the photon helicity every shot.

The measured XMCD spectra of $EuNi_2(Si_{0.82}Ge_{0.18})_2$ are shown in Fig. 2 together with the XAS spectra obtained at several magnetic fields [3]. Here, we only show the L_2 edge spectra. The valence fluctuation manifests itself as a double-peak structure in the XAS spectra. The higher energy XAS peak is attributed to the Eu^{3+} state, while the lower energy peak is attributed to the Eu^{2+} state. The XAS spectrum strongly depends on the magnetic field and exhibits a valence change induced by the magnetic field. We found that the double-peak structure corresponding to the two valence states is observed in the XMCD spectra as well as in the XAS spectra. The double peaks indicate that the electrons in the Eu 5*d* orbital, to where electron is finally excited from 2*p* levels, are magnetically polarized not only in the Eu^{2+} state (f^7; J=7/2 in the ground state) but also in the Eu^{3+}state (f^6; J=0 in the ground state). We also observed a similar double peak structure in the L_3-edge XMCD spectra [3]. It is worth noting that it is nontrivial to obtain a finite XMCD signal for the nonmagnetic Eu^{3+} state.

To clarify the origin of the valence-selective XMCD, we plot the field dependence of the integrated intensity of the XMCD peak (I_{mcd}), as well as the magnetic polarization of the 5*d* electrons (P_{5d}), in Fig. 3. The degree of magnetic polarization of the Eu 5*d* electrons in each valence state is defined here as $P_{5d} = \int\Delta\mu t\, dE / \int\mu t\, dE$, where $\Delta\mu t$ and $\mu t = (\mu^+t + \mu^-t)/2$ are the XMCD and absorption intensities, respectively. $\int\Delta\mu t\, dE$ ($=I_{mcd}$) is deduced by the integration of the XMCD peak shown in Fig. 2 for each valence state. $\int\Delta\mu t\, dE$ is obtained from the integrated intensity of the absorption peak. Curve fitting analysis is performed in order to evaluate the absorption intensities $\int\Delta\mu t\, dE = I_2$ and I_3 for the Eu^{2+}

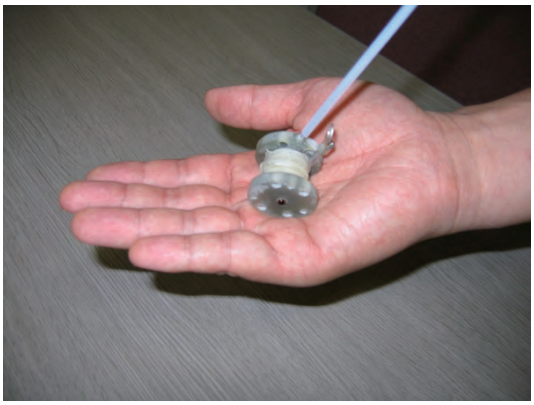

Fig. 1. Photograph of solenoid miniature magnet for XMCD measurement. The inner diameter is 3 mm. Maximum fields of up to 50 T can be generated. For a repetition of more than 300 shots, the maximum field is limited to 40 T for the XMCD experiment.

and Eu^{3+} states, respectively, at different magnetic fields. The magnetization (M) of the sample at 4.2 K [4] is shown in Fig. 3 in order to compare it with the dependence of I_{mcd} and P_{5d} on the field. An increase in magnetization caused by the valence change is observed at around 35 T. In addition, the I_{mcd} of Eu^{2+} and that of Eu^{3+} scale together with the magnetization, as expected for XMCD experiments. However, P_{5d} qualitatively differs between the Eu^{2+} and Eu^{3+} states, suggesting the different origins of the XMCD in such valence states.

We have now two possible origins of the valence-selective Eu^{3+}–XMCD: (i) the effect of the excited state of Eu^{3+} (J=1) and (ii) the magnetic polarization of the conduction electrons through *c-f* hybridization. Since the first excited state of Eu^{3+} is magnetic (J=1), the first possible origin (i) should have some effects. The energy separation between the first excited and ground states is about 480 K. If we take the Van Vleck term of Eu^{3+} into account, the contribution of the magnetization is found to be too small to explain the experimental result. However, in compounds exhibiting valence fluctuations, the mixing between the Eu^{3+}: J=0 and Eu^{3+}: J=1 states can be enhanced by the strong *c-f* hybridization. Therefore, the effect of the Eu^{3+}: J=1 state is one of the plausible origins of the Eu^{3+}-XMCD observed in the present work. The second possible origin is that the conduction electrons are polarized by the strong hybridization with the 4*f* electrons in the magnetic Eu^{2+} states, and these polarized conduction electrons induce the magnetic polarization of the 5*d* electrons in the nonmagnetic Eu^{3+} state. Owing to the strong *c-f* hybridization, this mechanism is also regarded as a plausible one.

Although further studies are required to quantitatively understand the valence-selective XMCD, it is likely that the *c-f* hybridization strength plays an important role. It is very unique to use the high-field XMCD to clarify the strong correlation between the conduction and localized electrons in other valence fluctuating or heavy fermion compounds.

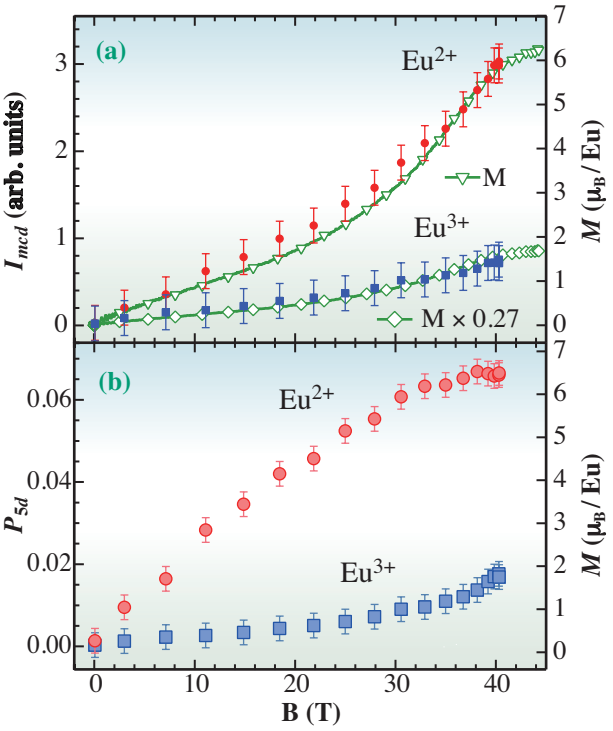

Fig. 3. Magnetic field dependences of **(a)** XMCD intensity and **(b)** normalized XMCD intensity P_{5d}.

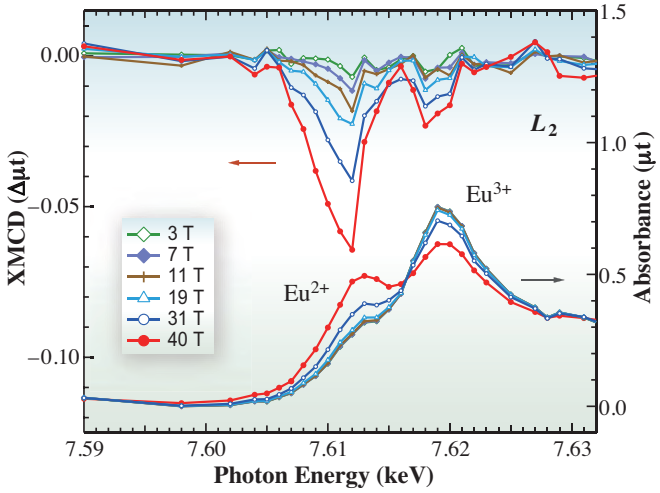

Fig. 2. XMCD and XAS spectra of L_2 edge in $EuNi_2(Si_{0.82}Ge_{0.18})_2$ at several magnetic fields at 5 K.

Yasuhiro H. Matsuda

Institute for Solid State Physics,
The University of Tokyo

E-mail: ymatsuda@issp.u-tokyo.ac.jp

References

[1] Y.H. Matsuda *et al.*: J. Phys. Soc. Jpn. **75** (2006) 024710.
[2] Y.H. Matsuda *et al.*: J. Phys. Soc. Jpn. **76** (2007) 034702.
[3] *Y.H. Matsuda, Z.W. Ouyang, H. Nojiri, T. Inami, K. Ohwada, M. Suzuki, N. Kawamura, A. Mitsuda, H. Wada: Phys. Rev. Lett.* ***103*** *(2009) 046402.*
[4] H. Wada *et al.*: J. Phys. Condens. Matter **9** (1997) 7913.

Chemical

"Yamamomo" - *Waxberry or Red Bayberry*

Synchrotron-radiation-related science, including accelerator, light source, beamline, monochromator, and X-ray imaging optics technology have undergone intense development over the past three decades. Cutting-edge X-ray science and technology is concentrated at synchrotron radiation facilities such as SPring-8, enabling synchrotron radiation experiments at the highest level. The hospitality to users is also excellent, providing an ideal environment even for non-specialists. Excellent research was conducted at all of the beamlines in 2009, and we introduce here some special topics in the field of chemical science.

The research team of Professor Ueda at Tohoku University have investigated C1*s* photoemission from CO_2 molecules, carrying out electron-ion coincidence momentum-imaging measurements at BL27SU. The first evidence for excitation by internal inelastic scattering was found. In this process, a photoelectron and a valence electron collide, resulting in one of them being promoted and the other ejected. The research team of Professor Shin, The University of Tokyo/RIKEN, has studied liquid water by applying X-ray emission spectroscopy (XES) using a liquid flow cell at BL17SU, revealing two different structures. Small angle X-ray scattering (SAXS) showed that the density of the hydrogen-bond distorted structure decreased and approached that of the tetrahedral-like structure with increasing water

SCIENCE

temperature. A comparison of the results revealed fluctuations between the two structures. The XES method has also been used to study acetic acid in an aqueous solution under ambient conditions at BL17SU. Here, Professor Shin' s group concluded that the anionic and neutral forms of acetic acid do not interact with each other, and only the population of the two components depends on pH. This method promises to be a powerful tool for the study of biological and chemical systems. Professor Sakurai *et al*. of The University of Kitakyushu have developed a new drug-delivery system (DDS) technique at BL40B2, integrating nanotechnology with biology, chemistry, and polymer science. They used SAXS to study DNA/cationic lipid, DNA/polysaccharide, and hydrophobic-drug/polymer micelles, and to correlate their pharmacological efficiencies and particle-inner structures. The research team of Professor Kitagawa at Kyoto University has demonstrated the synthesis of hybridized porous coordination polymer (PCP) crystals. The structural relationship between the shell crystal and the core crystal was determined using X-ray diffraction at BL13XU. The results showed that the shell crystal grows as a single crystal on the core crystal. Crystals with different adsorption and separation properties can thus be integrated into a single crystal, resulting in "multi- functional PCPs." Prof. Makiura *et al*. of Kyushu University have synthesized poly-*N*-vinyl-2-pyrrolidone (PVP)-coated AgI nanoparticles, and studied them using temperature-dependent X-ray powder diffraction at BL02B2. PVP can be used as a stabilizer to isolate new families of nanoscale (super) ionic conductors with controlled sizes and morphologies, promising new applications in nanobatteries and other electrochemical devices. Professor Hosono *et al*. of Tokyo Institute of Technology have succeeded in the synthesis of new Fe-1111 type compounds in which the $(LnO)^{\delta+}$ layers in *Ln*FeAsO are replaced by $(AeF)^{\delta+}$ layers. X-ray powder diffraction studies at BL02B2 confirmed that the tetragonal to orthorhombic crystallographic transition occurs in the *Ae*FeAsF system, and revealed the relationship between T_c and the crystal structure. CaFeAsF was shown to be a promising high-T_c superconductor. Professor Masuno *et al*. of The University of Tokyo have investigated the structures of glassy $BaTi_2O_5$, fabricated by a containerless method by combining X-ray diffraction results from BL04B2 with neutron diffraction, X-ray absorption near-edge structure (XANES) analyses, and computer simulations. The results showed that the glass-forming ability was enhanced by the containerless processing. Professor Haines *et al*. of Université Montpellier II have determined the structure of amorphous silica obtained from the pressure-induced amorphization of pure SiO_2 zeolite, silicalite-1-F. High energy total X-ray scattering data were obtained at BL04B2. The structural topologies of the new material were compared to those of amorphous silica obtained by temperature-induced vitrification.

Yuden Teraoka

Molecular-Frame Photoelectron Angular Distributions of Gas-Phase Molecules

Gas-phase free molecules are randomly oriented in space. Photoelectron angular distributions (PADs) in the laboratory frame defined by the electric vector of radiation are described by an anisotropy parameter β using the expression $I(\theta_e) \propto 1 + \beta P_2(\cos\theta_e)$, where $P_2(\cos\theta_e)$ is the Legendre second order polynomial and θ_e is the angle between the electric vector and the direction of the electron emission. However, to discuss molecular photoionization the use of a molecular frame is more natural. Furthermore, molecular-frame PADs (MFPADs) have a much more richer structure than the laboratory frame PAD and thus may be used for extracting further information about the target molecule. Due to these evident reasons, significant experimental efforts have been devoted to MFPAD measurements in the last decade or so.

To measure MPFADs, one has to fix the target molecule in space. This has been realized by two alternative ways. To temporary align the molecule in space prior to photoionization, one can use dynamical alignment caused by the pulsed IR laser. Recent pump-probe MFPAD measurements using this approach with ultrafast pulse lasers have been successfully applied to probe the evolution of the electronic structure in time for a photoexcited CS_2 molecule [1]. The alternative way of fixing the molecule in space and measuring MFPADs is to record momenta of electrons and fragment ions in coincidence. When the molecular dissociation is faster than the molecular rotation, one can determine the molecular orientation from the momenta of the fragment ions and thus, by measuring the momentum correlation between the ions and the photoelectron, one can realize MFPAD measurements. Since the pioneering work by Shigemasa *et al.* [2], this approach has been widely used in investigating detailed photoionization dynamics including shape resonance phenomena.

In the present work, we have investigated C 1*s* photoemission from a linear CO_2 molecule. As in other molecules, the C 1*s* photoionization of CO_2 is also governed by the shape resonance that appears at ~14 eV above the C 1*s* ionization threshold. Thus, we have carried out electron-ion coincidence momentum-imaging measurements for CO_2 at several photon energies across the shape resonance [3,4] at beamline **BL27SU**. The employed momentum imaging is based on electron and ion time-of-flight (TOF) measurements with two multi-hit two-dimensional (2D) position-sensitive detectors. A supersonic jet of CO_2 in the vertical direction crosses the photon beam in the horizontal direction. The TOF axis is in the horizontal direction and perpendicular to both the gas and photon beams. Photoelectrons and fragment ions ejected in all directions are driven to each of the electron and ion detectors using uniform electrostatic and magnetic fields. Each detector is equipped with a 2D multi-hit readout delay-line anode that permits measurements of both the time of detection and the 2D position coordinates and thus allows us to extract 3D momenta. The orientation of the molecular axis at the time of photoemission is extracted from the momentum vectors of the CO^+ and O^+ fragments resulting from the Coulomb dissociation of CO_2^{2+} subsequent to a rapid Auger decay.

To compare the measured and calculated MFPADs, we select the reaction in which the electron is emitted in the plane defined by the molecular axis and the E vector, as shown in Fig. 1. Here, the angle θ_n between the E vector and the molecular axis is shown along the horizontal axis and the electron emission polar angle θ relative to the molecular axis is shown along the vertical axis. The electron emission intensity is plotted on a false color scale at five photon energies. At first glance, the agreement between experimental and theoretical results is reasonable. Theoretically, the shape resonance located at ~312 eV is assigned to electron promotion from the $2\sigma_g$ (C 1*s*) core orbital to the $4\sigma_u$ unoccupied molecular orbital and thus the final

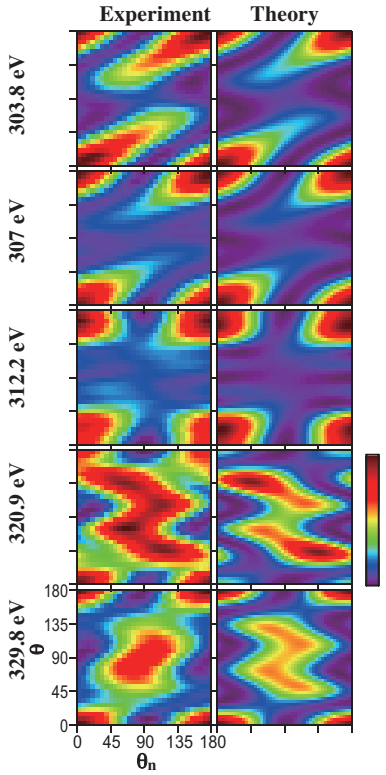

Fig 1. Experimental and theoretical 2D plots of C 1*s* MFPADs of CO_2 at five photon energies across shape resonance at ~312 eV. $\theta = 0°$ and 180° are the directions of O^+ and CO^+, respectively [3].

state may be described as $2\sigma_g^{-1}$ ($^2\Sigma^+_g$) $4\sigma_u$ $^1\Sigma_u$. This $\Sigma_g \rightarrow \Sigma_u$ photoexcitation is a parallel transition and the ejected electron has predominantly σ_u symmetry. In Fig. 1, θ_n = 0° and 90° correspond to parallel ($\Sigma \rightarrow \Sigma$) and perpendicular ($\Sigma \rightarrow \Pi$) transitions, respectively. The observed electron emission at ~312 eV is mostly at θ_n=0° along the molecular axis with a nodal plane at θ=90°. These observations are consistent with the expectation that the shape resonance is the parallel $\Sigma_g \rightarrow \Sigma_u$ transition emitting photoelectrons of σ_u symmetry.

Looking at Fig. 1 carefully, we note that the measured MFPADs at ~312 and ~321 eV do not show a complete symmetry relative to the center, though the calculated MFPADs always exhibit a complete point symmetry because of the assumed $D_{\infty h}$ molecular symmetry. To confirm this asymmetry, in Fig. 2, we made polar plots of the electron emission at θ_n = 0° for these two energies. The observed asymmetry is evidence of the breakdown of the theoretical model in Ref. [3], which is commonly employed for the description of the MFPADs. A recent theoretical study by Miyabe *et al.* [5] successfully elucidated the origin of the asymmetry. According to Miyabe *et al.*, the memory of the instantaneous position of the nuclei at the time of photoionization is imprinted on the final dication state, provided that the Auger decay occurs before the vibrational motion on the transient core-hole surface can erase that memory. They therefore incorporated the asymmetric-stretch motion of the neutral target into the observed MFPAD by confining the average to half of the allowed range of nuclear geometries, where one CO distance is elongated relative to the other. In Fig. 2, their calculations are shown by a solid black line. We can see that the observed asymmetry is well accounted by their model.

The upper panel of Fig. 3 shows the electron spectrum recorded at ~312 eV. In addition to the main line, we can see the satellite at a binding energy of ~12 eV relative to the main line. MFPADs for the main line and the satellite, measured within the reaction plane in Fig. 1, are compared in the lower panel of Fig. 3. The satellite emission is mostly at θ_n = 0°, revealing the predominance of the $\Sigma_g \rightarrow \Sigma_u$ transition, as shown in the case of the main line. In contrast to the main line, however, the satellite clearly shows a maximum intensity at θ = 90°. These observations suggest that the plausible assignment for the major contribution to the satellite is $2\sigma_g^{-1}1\pi_g^{-1}2\pi^*_u(^2\Sigma_u)\varepsilon\sigma_g{}^1\Sigma_u$, which is the parallel $\Sigma_g \rightarrow \Sigma_u$ transition emitting photoelectrons of σ_g symmetry. This assignment implies that this satellite is of the conjugate type, where the symmetry of the ionic final state ($^2\Sigma_u$) is different from that of the main line ($^2\Sigma^+_g$). A well-known shake-up mechanism, however, cannot excite this conjugate satellite state. We can conclude that this satellite is excited by internal inelastic scattering, where a photoelectron ($2\sigma_g \rightarrow \varepsilon\sigma_u$) and a valence electron ($1\pi_g$) collide and one of them is promoted to $2\pi^*_u$ and the other is ejected to $\varepsilon\sigma_g$. The present observation is the first experimental evidence of a conjugate satellite excited by internal inelastic scattering.

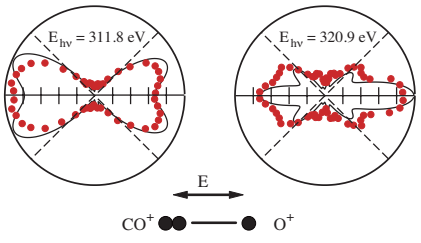

Fig. 2. Polar plots of C 1*s* MFPADs of CO_2 with molecular orientation parallel to E vector at photon energies of 311.8 eV and 320.8 eV. Experimental points (red dots), from Ref. [3]; theoretical curves (black solid curves) [5].

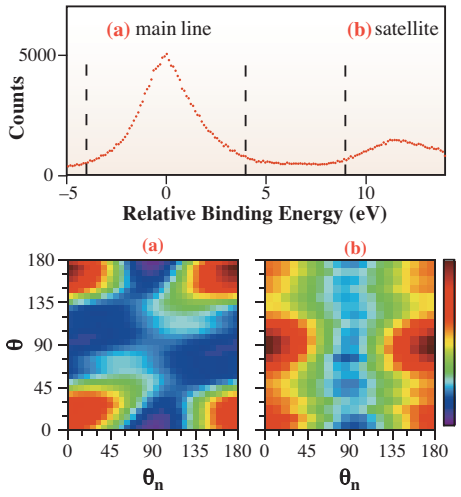

Fig. 3. Upper panel: photoelectron spectrum of CO_2 recorded at 311.8 eV. Lower panel: 2D plots of MPFADs for **(a)** C 1*s* main line and **(b)** lowest satellite of CO_2 recorded at photon energy of 311.8 eV [4].

K. Ueda[a,*], X. Liu[a], H. Fukuzawa[a] and N. Saito[b]

[a] Institute of Multidisciplinary Research for Advanced Materials, Tohoku University
[b] National Institute of Advanced Industrial Science and Technology (AIST)

*E-mail: ueda@tagen.tohoku.ac.jp

References

[1] C.H. Bisgaard *et al.*: Science **323** (2009) 1464.
[2] E. Shigemasa *et al.*: Phys. Rev. Lett. **74** (1995) 359.
[3] *X.-J. Liu, H. Fukuzawa, T. Teranishi, A. De Fanis, M. Takahashi, H. Yoshida, A. Cassimi, A. Czasch, L. Schmidt, R. Dörner, K. Wang, B. Zimmermann, V. Mckoy, I. Koyano, N. Saito and K. Ueda: Phys. Rev. Lett.* ***101*** *(2008) 109901.*
[4] *X.-J. Liu, H. Fukuzawa, T. Teranishi, A. De Fanis, M. Takahashi, H. Yoshida, A. Cassimi, A. Czasch, L. Schmidt, R. Dörner, I. Koyano, N. Saito and K. Ueda: Phys. Rev. Lett.* ***101*** *(2008) 023001.*
[5] S. Miyabe *et al.*: Phys. Rev. A **79** (2009) 053401.

Inhomogeneity of Liquid Water - Two Structural Motifs

Liquid water shows many anomalies in its thermodynamic properties, such as compressibility, density variation and heat capacity. In the low-temperature regime, below the freezing point, these properties deviate strongly from normal. Hence, theories related to a liquid-liquid phase transition between high- and low-density water have been proposed to account for these anomalies.

Recently, we have obtained interesting results in X-ray emission spectroscopy (XES) for liquid water using an X-ray emission spectrometer and the liquid flow cell developed at beamline **BL17SU** [1]. In principle, X-ray emission spectra reflect valence electronic states; thus, the three molecular orbitals $1b_2$, $3a_1$ and $1b_1$ are expected to appear in the spectra. The spectra of gas phase water and crystalline ice show a simple three-peak structure that comes from these three valence molecular orbitals. However, X-ray emission spectra of liquid water show two sharp splitting peaks ($1b_1$' and $1b_1$") in the $1b_1$ region, and these two sharp peaks show clear dependences on phase (gas, liquid, and solid) and temperature. The XES spectra of water in three phases and the temperature dependence of liquid water lead us to interpret the two peaks as representing tetrahedral ice-like and hydrogen-bond distorted structural motifs in liquid water. The existence of two distinct lone-pair peaks provides evidence against an unstructured continuum model of the liquid but is easily explained within a two-component mixture model.

To demonstrate the presence of density fluctuations due to two structural motifs in ambient water, small-angle X-ray scattering (SAXS) was conducted at SSRL [2]. Scattering techniques such as SAXS and small-angle neutron scattering (SANS), provide us the most direct information about density variations or fluctuations in a liquid. Figure 1 shows the normalized structure factor $S(Q)$ derived from the SAXS intensity in ambient water (H_2O) as a function of Q for various temperatures. Different from a normal liquid, like CCl_4, all scattering curves of water show an enhancement approaching Q = 0 after experiencing a minimum at around 0.4-0.5 Å^{-1}. Although a similar enhancement is reported for water in a supercooled region [3] as a proof of density inhomogeneity, the SAXS results indicate the existence of inhomogeneity at around room temperature.

For a further study of thermal properties of two structures, the temperature dependence of XES spectra for liquid heavy water was measured at SPring-8. Figure 2 shows XES spectra of liquid heavy water at various temperatures. The $1b_1$ peak of the tetrahedral ice-like component ($1b_1$') is relatively insensitive to temperature, whereas that of the hydrogen-bond distorted component ($1b_1$") continuously changes its energy as it becomes thermally excited and expands. The SAXS profile at higher temperatures, which shows small enhancement approaching Q=0, indicates that the density contrast between the high- and low-density components is smaller at higher temperatures. According to thermal properties of the tetrahedral ice-like and hydrogen-bond distorted structures deduced from the XES results, we can conclude that the density of the high-density (hydrogen-bond distorted) component decreases and approaches that of the low-density (tetrahedral) component when the water temperature increases.

Combined with the experimental results of SAXS

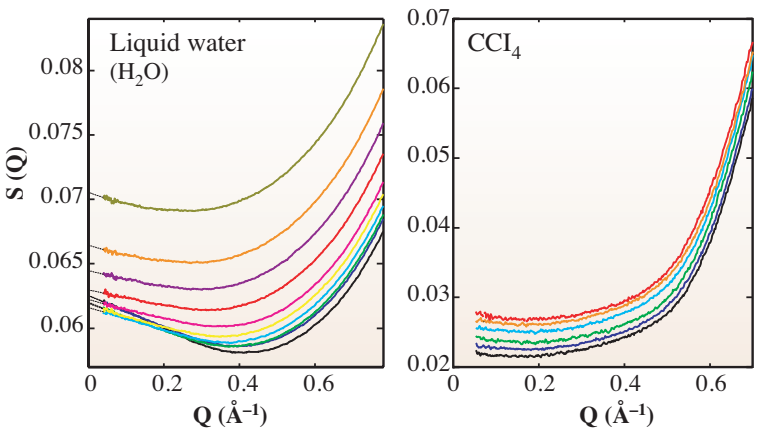

Fig. 1. Experimental structure factor $S(Q)$ derived from scattering intensity for ambient water and CCl_4 liquid as a function of scattering momentum transfer Q. For liquid water, the curves, from bottom to top, correspond to the temperatures 7, 11, 16, 20, 25, 29, 38, 47, 56, and 74°C. For liquid CCl_4, the curves, from bottom to top, correspond to the temperatures 6, 11, 16, 21, 25, and 30°C.

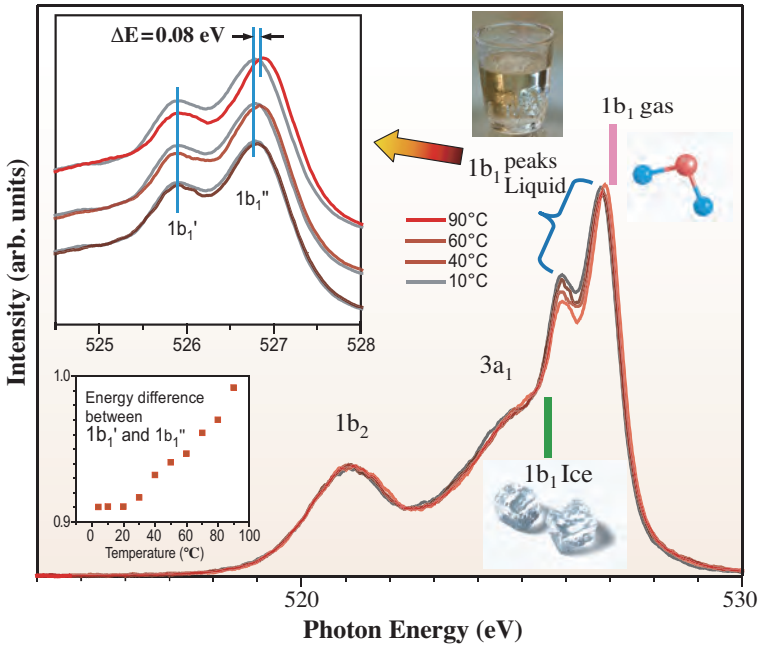

Fig. 2. O 1*s* X-ray emission spectra of liquid heavy water (D_2O) at different temperatures. The excitation energy is 550 eV, which is well above the ionization threshold. Peak components are labeled on the basis of the molecular orbitals of water molecule. The $1b_1$ peaks of the gas phase and the crystalline ice are indicated by red and green vertical lines, respectively.

and XES, we propose that the contrast of density difference in SAXS is due to fluctuations between tetrahedral ice-like and hydrogen-bond distorted structures related to, low- and high-density water, respectively. Figure 3 shows an illustration based on the results of our present studies, which indicates the presence of density fluctuations in ambient water on a physical length scale of around 1 nm.

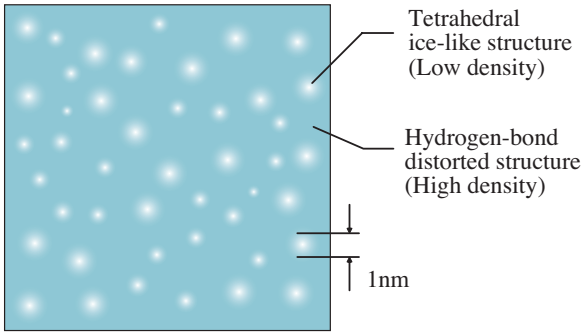

Fig. 3. Illustration of inhomogeneity of water based on results obtained using X-ray emission spectra, X-ray Raman scattering, and small-angle X-ray scattering. The different microstructures in water are shown in color. The structure is actually three-dimensional, but it is two-dimensionally drawn for simplicity.

Takashi Tokushima[a,*], Yoshihisa Harada[a,b], Shik Shin[a,c] and Anders Nilsson[d]

[a] SPring-8 / RIKEN
[b] Dept. of Applied Chemistry, The University of Tokyo
[c] Inst. for Solid State Physics, The University of Tokyo
[d] Stanford Synchrotron Radiation Lightsource (SSRL), Stanford Linear Accelerator Center, USA

*E-mail: toku@spring8.or.jp

References

[1] T. Tokushima *et al.*: Chem. Phys. Lett. **460** (2008) 387.
[2] *C. Huang, K.T. Wikfeldt, T. Tokushima, D. Nordlund, Y. Harada, U. Bergmann, M. Niebuhr, T.M. Weiss, Y. Horikawa, M. Leetmaa, M.P. Ljungberg, O. Takahashi, A. Lenz, L. Ojamä e, A.P. Lyubartsev, S. Shin, L.G.M. Pettersson and A. Nilsson: Proc. Natl. Acad. Sci. USA **106** (2009) 15214.*
[3] L. Bosio *et al.*: Phys. Rev. Lett. **46** (1981) 597.

Identification of Valence Electronic States of Aqueous Acetic Acid in Acid-Base Equilibrium Using Site-Selective X-Ray Emission Spectroscopy

The electronic structure of a material is important for many fields of science, because valence electrons play important roles in properties of many systems including molecules in liquids and solutions. Due to its importance in chemistry and biology, recent studies have applied direct methods to observe electronic states of aqueous solutions. One characteristic phenomenon in the solution is deprotonation. Deprotonation plays an important role in many biological and chemical reactions. The pH dependence of chemical reactivity and property is known to be directly associated with geometric/steric and electronic changes accompanying deprotonation. Well-known examples include those of sulphuric acid, phenol, the helix structure of poly-L-glutamine, pH dependence of micellization, and pH-sensitive fluorescence of proteins. It is expected that the valence electrons contributing to the chemical bonding of hydrogen will undergo changes upon deprotonation. Hence, it is extremely important to study the occupied valence electronic structure of solutions in acid-base equilibrium.

The method we applied for the study of aqueous acetic acid solutions is X-ray emission spectroscopy (XES). In recent studies, XES was successfully used as a powerful element-selective tool to elucidate the electronic states of liquid water [1]. We have recently reported the site-selective observation of two oxygens in different chemical environments, namely, C=O and OH, using resonant XES at the oxygen 1*s* edge for liquid acetic acid (CH_3COOH) under ambient conditions [2]. Using the site selectivity of resonant X-ray emission spectroscopy, we report here chemical-state-selective observations of the valence electronic states for acetic acid molecules in an aqueous solution. Furthermore, we report the systematic pH dependence of the occupied valence electronic structure of aqueous acetic acid solutions under ambient conditions. Acetic acid is a simple and common acid containing a single carboxyl group (-COOH) and has been well studied in terms of acid-base equilibrium. It represents a model case used to discuss deprotonation inducing the neutral to anionic transition.

X-ray absorption spectroscopy (XAS) and XES spectra were recorded using circularly polarized soft X-rays at beamline **BL17SU** [3]. Details of the emission spectrometer were reported elsewhere [4]. To perform a selective excitation XES of acetic acid molecules in solvent water, we have tuned the incident energy to the $O_{C=O}$ 1*s* → π* resonance excitation, which is absent in water (Fig. 1(a)). Figure 1(b) shows the XES spectra obtained for the samples at pH 0.29 and pH 11.44 [5]. The origin of the difference in spectral feature at pH 11.44 and pH 0.29 are readily explained by chemical equilibrium considerations. According to the well-known Henderson-Hasselbalch equation, more than 99.9% of acetic acid at pH 11.44

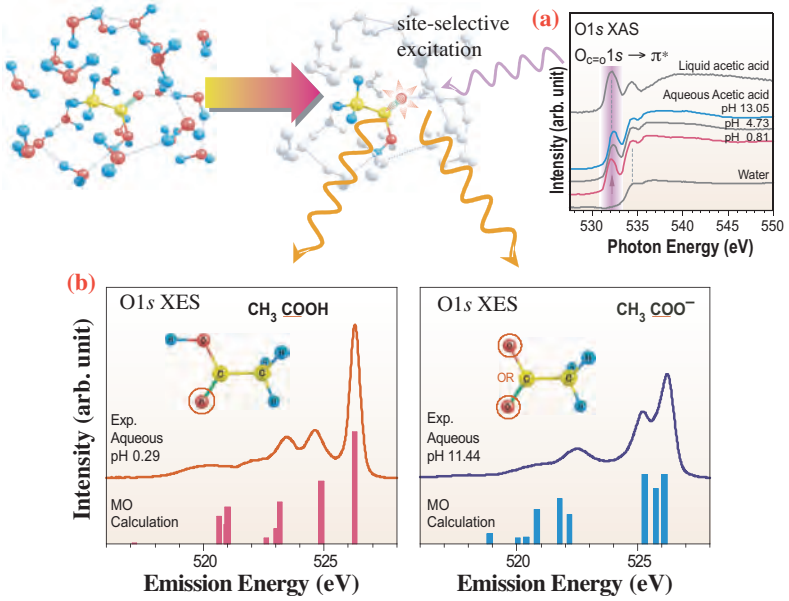

Fig. 1. Illustration showing site-selective excitation. Under non-resonant conditions, one cannot distinguish the oxygen atom of an acetic acid from that of water. Using resonant site-selective excitation, we can selectively excite the oxygen in the C=O structure of acetic acid molecule. **(a)** XAS spectra of liquid acetic acid, aqueous acetic acid and water. Excitation energy was tuned to the resonance peak structure indicated by an arrow. **(b)** Measured and calculated XES spectra of neutral (left) and ionic (right) acetic acid in aqueous solutions. Red circles indicate selectively excited oxygen atoms.

exists in the anionic form, while the neutral form predominates (more than 99.9%) at pH 0.29. The calculated energy levels for the XES spectra of neutral and anionic acetic acid, by performing density functional (DFT) calculations of XES spectra for both forms of the molecule using the ground state wave functions by the StoBe-deMon code, are also shown in Fig. 1(b). All peak structures in the experiment are well reproduced in the calculation with a small difference in energy position. From the XES spectra obtained at $O_{C=O}$ 1s site-selective resonant excitation and comparison with the DFT calculation of XES spectra, it is confirmed that we could successfully extract the occupied valence electronic structure of the acetic acid molecules in aqueous solutions.

So far, valence electronic structures of anionic and neutral acetic acid under extreme pH conditions (strongly acidic and strongly basic) have been determined. It is interesting to examine the electronic structures under intermediate pH conditions, especially at a pH value of the acid dissociation constant, where the molar fraction of anionic and neutral acetic acid varies drastically and is therefore suspected to cause a spectral change through the interaction between the two species. In Fig. 2, we plot the area-normalized O 1*s* XES spectra of 2M acetic acid solutions obtained using an excitation energy of 532.1 eV. The spectra show systematic changes as a function of pH. Importantly, five isoemissive points are clearly observed (arrows in Fig. 2), indicating that the spectra consist of the overlapping signals of neutral and anionic forms. In fact, the obtained XES spectra of intermediate pH values can be accurately reproduced by summing the spectra of the two forms. The reconstructed spectra show a residual error for an area under the curve of less than 6% for all the intermediate pH values. If the interaction between solute molecules is strong, the molecular electronic states can be perturbed by the interaction, and isoemissive points cannot be observed owing to the interaction between the two species. Thus, we conclude that the anionic and neutral forms of acetic acid in aqueous solutions do not interact with each other to form new states, and only the population of the two components changes depending on solution pH. As shown on the left side of Fig. 2, ratio analysis leads to a successful matching of molar fractions derived from XES spectra and the Henderson-Hasselbalch equation. This result shows the validity of quantitative analysis using XES and the non-interactive nature in terms of the electronic structure between the anionic and neutral forms of acetic acid molecules in an aqueous solution at a low concentration.

Since it is the first observation of the valence occupied electronic state of solute molecules in a solution using XES, we need to study other liquid and solution systems to establish this method as a tool for observing valence electronic states. However, we believe that this method will be a powerful tool for biological and chemical systems.

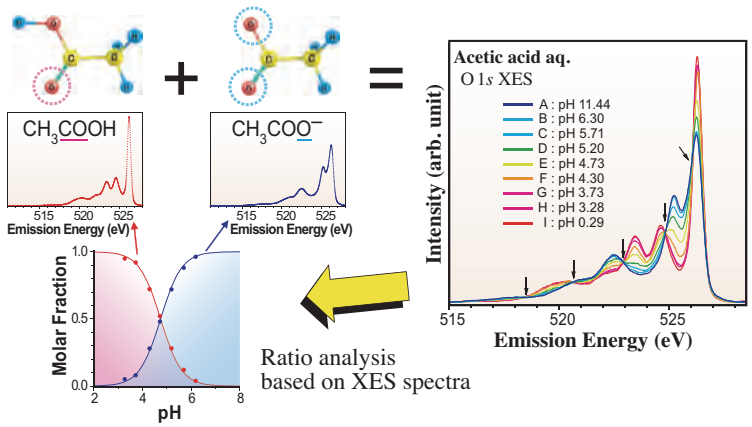

Fig. 2. pH dependence of XES spectra and molar fraction analysis. Each spectrum consists of two states and their molar fraction matches well with the values derived from the Henderson-Hasselbalch equation.

Yuka Horikawa[a,b,*], Takashi Tokushima[a] and Shik Shin[a,c]

[a] SPring-8 / RIKEN
[b] Dept. of Physical Science, Hiroshima University
[c] Institute for Solid State Physics, The University of Tokyo

*E-mail: horikawa@spring8.or.jp

References

[1] T. Tokushima *et al.*: Chem. Phys. Lett. **460** (2008) 387.
[2] T. Tokushima *et al.*: Phys. Chem. Chem. Phys. **11** (2009) 1679.
[3] H. Ohashi *et al.*: AIP Conf. Proc. **879** (2007) 523.
[4] T. Tokushima *et al.*: Rev. Sci. Instrum. **77** (2006) 063107.
[5] *Y. Horikawa, T. Tokushima, Y. Harada, O. Takahashi, A. Chainani, Y. Senba, H. Ohashi, A. Hiraya and S. Shin: Phys. Chem. Chem. Phys.* ***11*** *(2009) 8676.*

Small-Angle X-Ray Scattering from Drug Delivering Nanoparticles in Solutions: Pharmacological Efficiency and Particle-Inner Structures

Drug delivery using nanoparticles containing a pharmaceutical compound can dramatically improve therapeutic effects. This is because many biologically active materials, such as peptide and protein, antibody, vaccine and gene, in general may not be stable in bodies since they might be susceptible to enzymatic degradation or might be cleared by liver and other organs. Some of them cannot be absorbed into the systemic circulation efficiently owing to molecular size or electrostatic repulsion. For this reason, these drugs have to be delivered by exculpatiion with biologically stable nanoparticles. This technology is called a drug delivering system (DDS) and considered that nanotechnology and integrated science, including biology, chemistry, and polymer science, should play an important role. The current trend of drug delivery aims to develop a targeted delivery system, in which the drug is only active or delivered to the target and sustained-released in a controlled manner. We have been studying small-angle X-ray scattering (SAXS) from DNA/cationic lipid [1,2], DNA/polysaccharide [3], and hydrophobic-drug/polymer micelles [4] to correlate their pharmacological efficiency and particle-inner structures.

Complexes made from DNA and cationic lipids, become known as “lipoplexes,” have attracted enormous scientific and technical interest, because lipoplexes could be efficient vehicles for DNA or RNA delivery into a wide variety of eukaryotic cells. The mechanism of transfection is still not well understood, and further investigation is necessary to improve the transfection efficiency for the adaption of lipoplexes to clinical and practical use. SAXS studies of lipoplexes demonstrated that they take highly ordered structures, which are strongly related to the transfection efficiency. One of the proposed structures is a multilamellar phase where DNA is intercalated between lipid bilayers, as presented in Fig. 1(a) (perpendicular interaction). However, thermodynamic studies on the lipoplex formation have been interpreted by the so-called “lateral interaction of the alkyl tails and DNA”: cationic headgroups are localized at DNA phosphates, while hydrophobic tails would lay down on the DNA surface and coat DNA to make the complex hydrophobic (see the bottom of Fig. 1(b)). The resultant complex is presumably captured by the hydrophobic domain of the residual non-binding lipids, as presented in Fig. 1(b). Recent molecular dynamics studies suggest that the two models (lateral and perpendicular interactions) can exist depending on the alkyl chain length and/or the degree of hydrophobic interaction that results in the aggregate ion of alkyl chains.

We reported that aromatic amine and amidine derivatives can be used as transfection reagents with a higher efficiency and a lower toxicity than commercial products. Figure 2 shows the transfection efficiency of our benzyl amine (BA) as a function of composition. The efficiency strongly depends on the composition: the highest one is achieved at BA: DOPE: DLPC=1: 2: 1 (point B) and the lowest ones near the A point (BA: DOPE: DLPC = 1: 0: 1), where DOPE and DLPC are L-a-phosphatidyl ethanolamine dioleoyl and 1,2-dilauroyl-sn-glycero-3-phosphocholine, respectively. The coexisting DOPE and DLPC are considered to make BA to be compatible with water and to be less toxic for cells. However, there has been no information on how these two colipids affect the micellar structure. Figure 3(a) presents how the SAXS profile changes with the addition of DNA at the

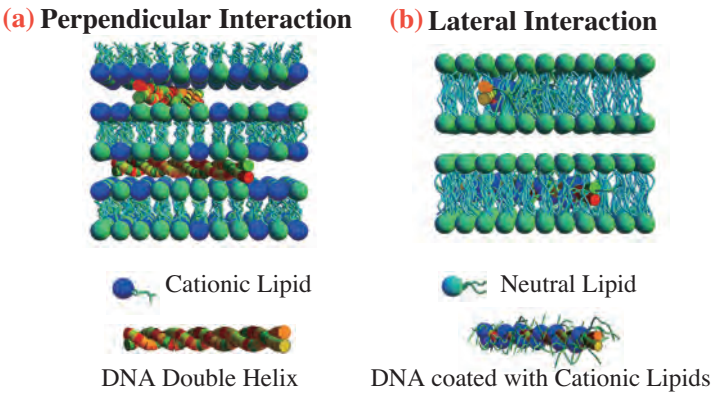

Fig. 1. Schematics of two models for DNA/cationic lipid complexes: **(a)** perpendicular and **(b)** lateral interactions. In the perpendicular interaction, the cationic lipids (blue) maintain the preformed hydrophobic alkyl domain and attach the DNA phosphate, while in the lateral interaction, after binding between the DNA phosphates and the lipid heads, the DNA surface is coated with the alkyl tails to make it hydrophobic and the bond DNA is transferred into the alkyl domains formed by the neutral co-lipids (green).

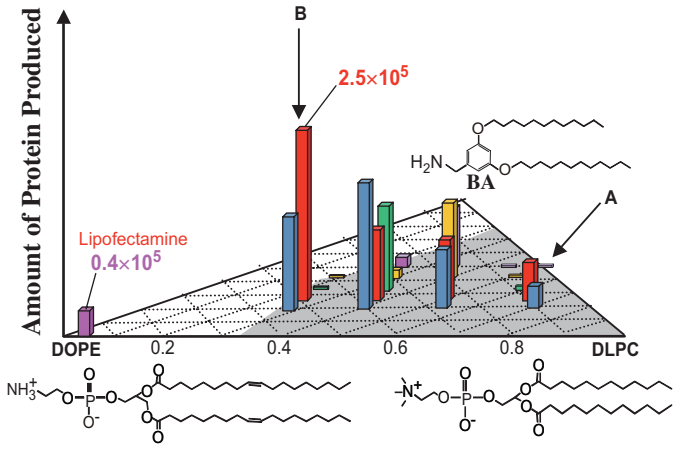

Fig. 2. Composition dependence of luciferase activity for BA/DOPE/DLPC system. N/P ratios were fixed at 3.3 for all samples, where N/P is defined by the molar ratio of the nitrogen of BA to the phosphate of DNA.

composition A (the lowest transfection efficiency). The SAXS profile before adding DNA could be characterized as a multilayered spherical micelle. When DNA was added to the micelle, diffraction peaks appeared and the peak positions satisfied the relation for hexagonally packed cylinders. Further addition of DNA led to the formation of a lamellar structure. Fitting analysis suggested the lateral interaction, as shown in Fig. 1(b). Figure 3(b) shows the changes of the SAXS profile at the composition B (the highest transfection efficiency). Before adding DNA, the profile exhibited peaks that correspond to a hexagonally packed cylinder. With increasing DNA, the first diffraction peak became sharper and more intense and other higher-order peaks became distinct. These features are obtained by the addition of DNA did not induce structural transitions, such as the composition A, but enhanced the hexagonal ordering as well as reduced the amount of the isolated scattering object. This may be interpreted by the intercalation of DNA between the preformed hexagonally packed micellar cylinders. Our results indicate that the location of DNA is related to the transfection efficiency.

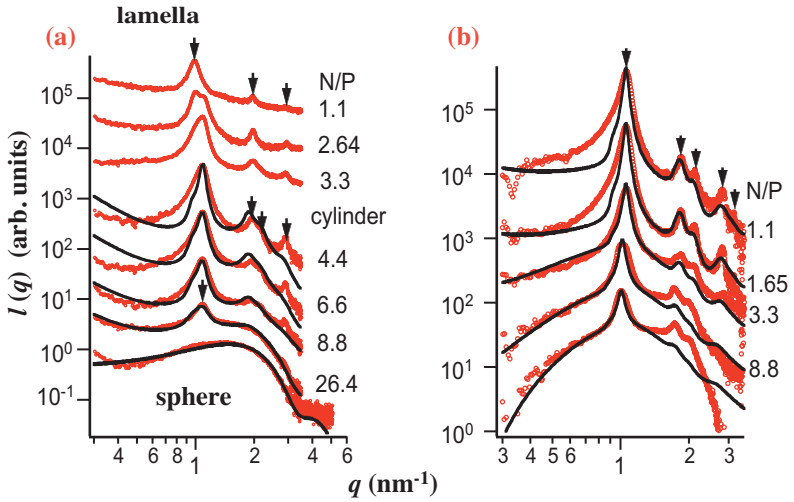

Fig. 3. N/P dependence of SAXS profile at compositions **(a)** and **(b)**.

Kazuo Sakurai

Dept. of Chemistry and Biochemistry,
University of Kitakyushu

E-mail: sakurai@env.kitakyu-u.ac.jp

References

[1] *M. Sakuragi, S. Kusuki, E. Hamada, H. Masunaga, H. Ogawa, I. Akiba and K. Sakurai: J. Phys.: Conference Series* ***184*** *(2009) 012008.*
[2] K. Koiwai *et al.*: Bioconjugate Chem. **16** (2005) 1349.
[3] N. Shimada *et al.*: Bioconjugate Chem. **18** (2007) 1280.
[4] I. Akiba *et al.*: submitted to Langmuir.

Evaluation of Structural Relationship in Hybridized Porous Coordination Polymer Crystals

Porous coordination polymers (PCPs) or metal-organic frameworks (MOFs) have attracted considerable attention owing to their wide variety of scientific and industrial applications, such as adsorption, separation, and catalysis [1]. Over the past decade, the chemical functionalization of the PCP framework scaffold has been intensively studied to improve their properties. The promising strategy for developing the PCP properties is to integrate several framework structures, thus several functions, into one crystal – the so-called hybridized PCP crystal. The key synthetic protocol is the epitaxial growth of the second crystal that surrounds the core crystal because a lattice match promises pore connections at the interface between two crystals. This class of hybridized PCP crystals allows for systematically tuning the framework composition of both metal ions and organic ligands. The careful choice of components enables us to design the spatial configuration of crystals and their structural relationship, leading to the novel porous property that a single PCP framework never achieves. Here, we demonstrate the syntheses of hybridized PCP crystals by epitaxial growth and the structural relationship between the shell crystal and the core crystal determined using X-ray diffraction analyses at beamline **BL13XU**.

A series of tetragonal frameworks (Fig. 1(a)), $[M_2(\text{dicarboxylate})_2(\text{N-ligand})]_n$, wherein dicarboxylate *layer* ligands link to dimetal clusters to form two-dimensional square lattices, which are connected by dinitrogen *pillar* ligands at lattice points, are good candidates for the hybridization of two distinct PCPs. We have established the systematic hybridization synthesis by a solvothermal method and present here two types of hybridized PCP crystals: heterometallic core/shell crystals (Fig. 1(b)) [2] and hetero-pillar-ligand sandwich-type crystals (Fig. 1(c)) [3].

The heterometallic core/shell crystal that consists of two different metal ions has been chosen for hybridization: $[Zn_2(ndc)_2(dabco)]_n$ **(1)** as the core crystal and $[Cu_2(ndc)_2(dabco)]_n$ **(2)** as the shell crystal (a = 10.921(1) and c = 9.611(1) for **1**, and a = 10.8190(3) and c = 9.6348(6) for **2**), (ndc = 1,4-naphthalene dicarboxylate, dabco = 1,4-diazabicyclo[2.2.2]octane). Synchrotron X-ray diffraction measurements were performed to investigate the structural relationship between the core crystal and the shell crystal at BL13XU. The core/shell crystal of **1/2** was fixed on a substrate with the a-axis oriented upward and diffractions were recorded at a desired Bragg position. The θ–2θ scan of **1/2** at the initial position (χ = 90°) provided two sharp peaks assigned to $h00$ Bragg peaks and the ϕ scan at the 110 Bragg position gave two sharp peaks every 180°, which where assigned to the 110 and $1\bar{1}0$ Bragg peaks (Fig. 2(a)). These results indicate that the shell crystal was grown on the core crystal as a single crystal.

In the same manner, the core/shell crystal (**1/2**) was mounted with the c-axis oriented upward. While the θ-2θ scan gave only 00ℓ Bragg peaks, the characteristic triplet peaks were periodically observed every 90° in the ϕ scan at the 101 Bragg position (Fig. 2(b)). The central peak of each triplet peak was assigned to the 101 or 011 Bragg peak from the core crystal **(1)**, whereas the two side peaks ($\Delta\phi_{av} = |\phi_{cen} - \phi_{side}| = 11.7$) were assigned to the diffraction from the shell crystal **(2)**. The emergence of the two side peaks implies that two in-plane domains of the shell crystal **(2)** were grown on the {001} surface of the core crystal **(1)** (Fig. 2(c)). The significant difference in lattice constant (*ca.* 0.1 Å) between **1** and **2** is compensated by in-plane

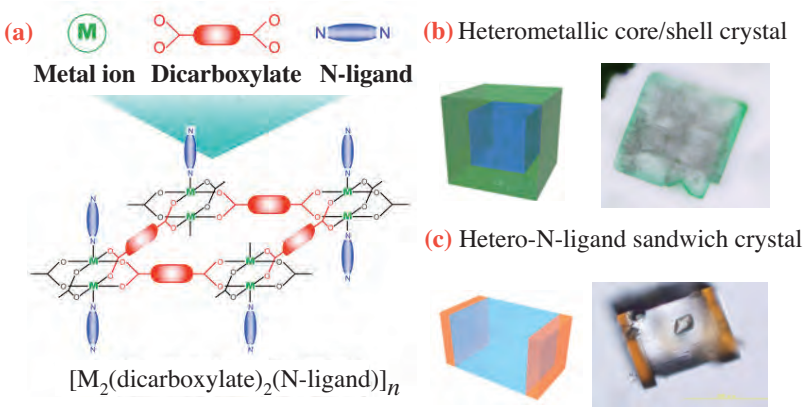

Fig. 1. **(a)** Schematic illustration of series of frameworks, $[M_2(\text{dicarboxylate})_2(\text{N-ligand})]_n$. Optical microscopy images and schematic illustrations of hybridized crystals of **(b)** 1/2 and **(c)** 1/3.

rotational epitaxial growth. Such a rotational structural relationship at the crystal interface can eventually work as a filter for the separation of guest molecules.

On the other hand, the choice of two different pillar ligands for hybridization leads to the fabrication of sandwich-type crystals; $[Zn_2(ndc)_2(dabco)]_n$ **(1)** as the core crystal and $[Zn_2(ndc)_2(dpndi)]_n$ **(3)** as the second crystal (a = 10.921(1) and c = 9.611(1) for **1**, and a = 10.906(2) and c = 22.456(4) for **3**, dpndi = *N,N'*-di(4-pyridyl)- naphthalenetetracarboxydiimide). This is because the secondary crystal growth at the {100} surface of the core crystal consisting of ndc and dabco was inhibited by mismatch of molecular lengths between dabco and dpndi. The second crystal **3** could only be grown at the {001} surface that consists of only the common component ndc.

The synchrotron X-ray diffraction measurement of the sandwich-type crystal (**1/3**) fixed on a substrate with the *c*-axis oriented upward was performed to successfully obtain two shape 00ℓ peaks from both **1** and **3** crystals in the θ–2θ scan. The ϕ scan at the 101 Bragg position gave four sharp peaks, which were assigned to the 101, 011, $\bar{1}01$ and $0\bar{1}1$ Bragg peaks (Fig. 3). The correspondence of the ϕ angles between **1** and **3** indicates that the second crystal **(3)** was grown epitaxially on the core crystal **(1)** with a perfect lattice match at the {001} surface. Unlike the heterometallic system (**1/2**), the negligible difference in lattice constant (*ca.* 0.015 Å) ensures pore connection at the crystal interface.

On the basis of the presented results that opened the way to unveil the structural relationship of hybridized PCPs, the crystals with various properties, such as adsorption and separation, are considered suitable for integration into a single crystal, resulting in the fabrication of "multifunctional PCPs."

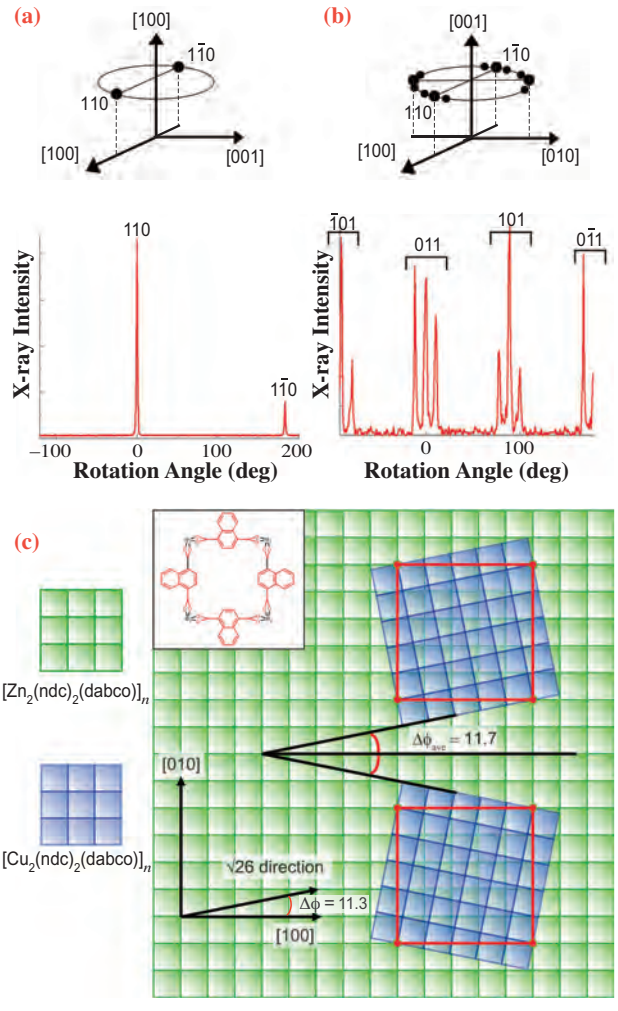

Fig. 2. Scan of rotation angles around **(a)** [100] ϕ scan and **(b)** [001] directions. **(c)** Schematic model of structural relationship between core lattice and shell lattice on (001) surface.

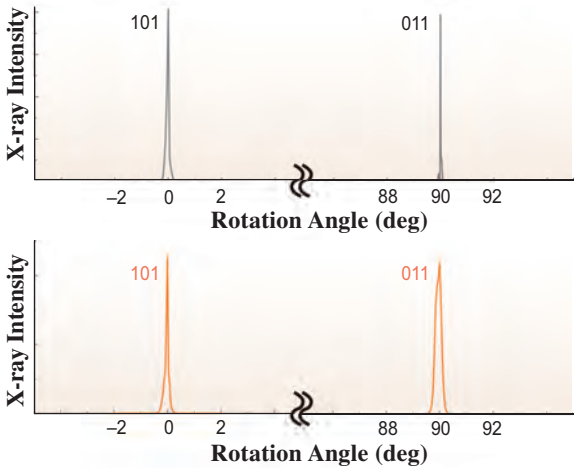

Fig. 3. Scan of rotational angles around [001] directions (ϕ scan) of **(a)** core crystal **1** and **(b)** second crystal **3**.

Kenji Hirai[a], Shuhei Furukawa[b,c,*], Osami Sakata[d] and Susumu Kitagawa[a,b,c]

[a] Graduate School of Engineering, Kyoto University
[b] ERATO Kitagawa Integrated Pores Project, JST
[c] Institute for Integrated Cell-Material Sciences, Kyoto University
[d] SPring-8 / JASRI

*E-mail: shuhei.furukawa@kip.jst.go.jp

References

[1] S. Kitagawa *et al.*: Angew. Chem. Int. Ed. **43** (2004) 2334.
[2] *S. Furukawa, K. Hirai, K. Nakagawa, Y. Takashima, R. Matsuda, T. Tsuruoka, M. Kondo, R. Haruki, D. Tanaka, H. Sakamoto, S. Shimomura, O. Sakata and S. Kitagawa: Angew. Chem. Int. Ed.* ***48*** *(2009) 1766.*
[3] S. Furukawa *et al.*: Chem. Commun. (34) (2009) 5097.

AgI Nanoparticles: Size-Controlled Stabilization of Superionic Phase to Room Temperature

Solid-state ionic conductors are actively studied for their large application potential in batteries and sensors. From the viewpoint of future nanodevices, nanoscaled ionic conductors are attracting much interest. Silver iodide (AgI) is a well-known ionic conductor whose high-temperature α-phase shows a superionic conductivity greater than 1 $\Omega^{-1}\cdot cm^{-1}$. Below 147°C, α-AgI undergoes a phase transition into the poorly conducting β- and γ-polymorphs, thereby limiting its applications.

We have recently reported the facile synthesis of variable-size AgI nanoparticles coated with poly-*N*-vinyl-2-pyrrolidone (PVP) and the controllable tuning of the α- to β-/γ-phase transition temperature ($T_{c\downarrow}$) [1]. When the size approaches 10-11 nm, the α-phase survives down to 30°C - the lowest temperature for any AgI family material. Moreover, the conductivity of 11 nm β-/γ-AgI nanoparticles at 24°C is ~1.5×10^{-2} $\Omega^{-1}\cdot cm^{-1}$ - the highest ionic conductivity for a binary solid at room temperature.

Ionic conductors are crucial for operating electrochemical devices, such as batteries and sensors. Although liquid phases principally give high ionic conductivity, solid-state materials are much more suitable from the perspectives of device fabrication (facile shaping, patterning and integration), stability (non-volatility) and safety (non-explosiveness). Silver-based ionic solids are excellent candidates of electrolytes for solid state batteries both because of their high conductivity and the high polarizability of Ag^+ ions that brings high exchange rate at the electrode reaction [2]. Actually, prototypes of all-solid batteries employing silver ionic conductors have been reported [3]. However, the performance of such devices is still in need of improvement for satisfying commercial applications. Efforts to obtain a high conductivity at lower temperatures have focused on the synthesis of ternary phases derived from AgI, of metal halide solid solutions, and of inorganic composite materials. An alternative way to attempt to stabilize the superionic phase at lower temperatures can be through the fabrication of nanoscaled AgI materials with controlled size and shape. For instance, when the size of materials is down to nanoscale, the temperatures of fusion and order-disorder phase transitions can be lowered as the proportion of surface atoms increases, resulting in the increase of surface energy.

Our aim in this work was to investigate in a systematic way the size effect on T_c in AgI nanoparticles without any pre-shaped inorganic mold, but with the application of a soft organic polymer as a stabilizer. We successfully synthesized PVP-coated AgI nanoparticles in a variety of particle sizes by a solution-based technique.

Figure 1 shows the extracted size dependence of the phase transition temperatures from the differential scanning calorimetry (DSC) measurements of as-prepared AgI nanoparticles measured on cooling. The size dependence of the α- → β-/γ-phase transition temperature $T_{c\downarrow}$ is very pronounced and $T_{c\downarrow}$ shifts considerably to lower temperatures with decreasing nanoparticle size, leading to a progressively enlarged thermal hysteresis. Specifically for the 10 and 11 nm nanoparticles, $T_{c\downarrow}$ is drastically suppressed down to 40 ± 1°C.

Detailed insight into the phase transition behavior of AgI nanoparticles was obtained from the temperature-dependent synchrotron X-ray powder diffraction at beamline **BL02B2**. Figure 2(a) shows the temperature evolution of the α-AgI fraction for 11 nm nanoparticles during the first thermal cycle, as derived from Rietveld refinements of the diffraction data. The results clearly show the same huge hysteresis observed by DSC, as shown in Fig. 2(b). The dominant structure of the as-prepared AgI nanoparticles at 21°C is the γ-polymorph (64.1(1)%). The β-polymorph (35.9(1)%) is also present. This phase assemblage remains stable on heating up to 138°C. Further heating leads to a gradual transformation to the α-phase that is complete at 165°C. Between 165 and 190°C, only α-AgI was observed. However, the β-/γ- → α-phase transition is strongly thermally hysteretic. On cooling, small fractions of β- and γ-phases appear initially at 128°C and grow only slightly down to 42°C, where the

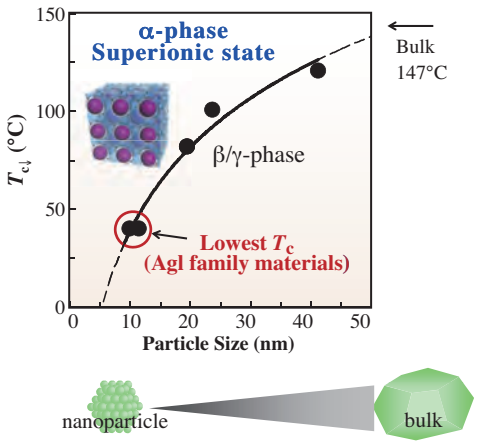

Fig. 1. Size dependence of phase transition characteristics in AgI nanoparticles on cooling. The mean diameters of the nanoparticles were extracted from the TEM images to be 9.9±2.4, 11.3±3.8, 19.4±3.7, 23.6±7.3 and 41.2±7.8 nm.

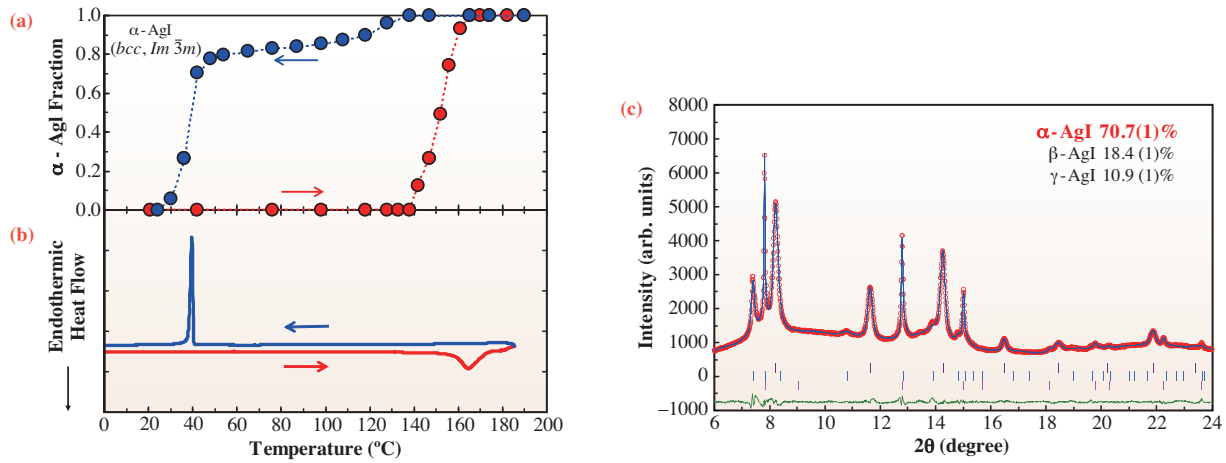

Fig. 2. Structural characterization of 11 nm AgI nanoparticles. **(a)** Temperature dependence of α-AgI fractions for the first thermal cycle, as extracted from Rietveld refinements of synchrotron X-ray diffraction data. **(b)** DSC thermograms for first thermal cycle. **(c)** Final observed (red circles) and calculated (blue solid line) synchrotron X-ray (λ = 0.5122 Å) powder diffraction profiles at 42°C following heating to 190°C and subsequent cooling (agreement factors: R_{wp} = 2.30% and R_{exp} = 4.44%). The lower solid lines show the different profiles and the tick marks show the reflection positions of α-AgI (top), β-AgI (middle) and γ-AgI (bottom) phases.

α-phase is still the dominant structure (α-phase 70.7(1)%, β-phase 18.4(1)%, and γ-phase 10.9(1)%) (Fig. 2(c)). Below this temperature, which coincides with the sharp endothermic peak observed in DSC, α-AgI rapidly begins to transform into β-AgI but survives down to 30°C (Fig. 2(a)). The structural transition is complete at 24°C.

Figure 3 shows the results of conductivity measurements for 11 nm AgI nanoparticles and AgI polycrystals. The huge thermal hysteretic behavior observed in DSC and diffraction measurements is also evident in the temperature dependence of the conductivity σ. We also note that the room-temperature conductivity for as-prepared 11 nm nanoparticles is significantly increased to ~1.5×10^{-2} Ω^{-1}•cm^{-1}. To the best of our knowledge, this is the highest ionic conductivity reported for a binary solid at room temperature and is five orders of magnitude higher than that of AgI polycrystals (~1.6×10^{-7} Ω^{-1}•cm^{-1}). On heating of the as-prepared nanoparticles, σ gradually increases and a notable change is observed at around 160°C, where both DSC and diffraction show a thermal event. On cooling, σ remains very high, which is consistent with the presence of superionic supercooled α-AgI whose activation energy is 0.06 eV, comparable to that of bulk α-AgI (~0.05 eV). Finally, σ approaches the same value as that in the heating process at 36°C.

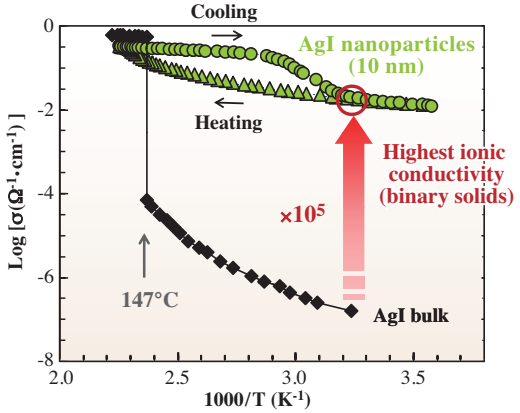

Fig. 3. Transport behavior of 11 nm AgI nanoparticles. Temperature dependence of conductivity σ for first thermal cycle. The activation energies derived using an Arrhenius expression are indicated. The conductivity data for AgI polycrystals are also included for comparison.

The solution-based chemistry using PVP as a stabilizer that has been employed here is sufficiently suitable for isolating new families of nanoscaled (super)ionic conductors with controlled size and morphology. This will facilitate a wide range of fundamental studies about ionic mobility at the nanoscale at a previously inaccessible temperature window and promises applications in nanobatteries or other electrochemical devices.

Rie Makiura[a,b,*,†], Hiroshi Kitagawa[a,b,c,d] and Kenichi Kato[e]

[a] Department of Chemistry, Kyushu University
[b] JST-CREST
[c] Department of Chemistry, Kyoto University
[d] INAMORI Frontier Research Center, Kyushu University
[e] SPring-8 / RIKEN•JASRI

*E-mail: r-makiura@21c.osakafu-u.ac.jp

[†] Present address: Nanoscience and Nanotechnology Research Center, Osaka Prefecture Univ.

References

[1] *R. Makiura, T. Yonemura, T. Yamada, M. Yamauchi, R. Ikeda, H. Kitagawa, K. Kato and M. Takata: Nature Mater. **8** (2009) 476.*
[2] S. Hull: Rep. Prog. Phys. **67** (2004) 1233.
[3] B.B. Owens: J. Power Sources **90** (2000) 2.

Synchrotron X-Ray Diffraction Study of Fe-1111 Type Superconductor *Ae*FeAsF (*Ae* = Ca and Sr): Possibility of Higher T_c

Since the discovery of superconductivity in F-doped LaFeAsO with T_c = 26 K, Fe-based layered compound systems have been intensively studied as candidates for high-T_c superconductors. With these efforts, T_c is increased to ~55 K in *Ln*FeAsO (Fe-1111 type: *Ln* = La, Ce, Pr, Nd, Sm,..). The Fe-1111-type superconductors consist of an $(FeAs)^{\delta-}$ layer forming a tetragonal iron lattice sandwiched by a $(LnO)^{\delta+}$ layer and suffer from the crystallographic transition from tetragonal to orthogonal, accompanied by an antiferromagnetic spin order at 120-160 K. The electron or hole doping to the $(FeAs)^{\delta-}$ layer through the doping of fluorine to $(LnO)^{\delta+}$ suppresses the crystallographic and magnetic phase transitions, and induces superconductivity. Therefore, the relationship among the structural and magnetic instabilities, and superconductivity have been studied, and much effort has been made for the synthesis of related compounds composed of similar iron lattices with the aim of increasing the T_c.

Recently, we have succeeded in the synthesis of a new member of the Fe-1111 type compounds *Ae*FeAsF (*Ae* = Ca, Sr), in which the $(LnO)^{\delta+}$ layers in *Ln*FeAsO are replaced by $(AeF)^{\delta+}$ layers (Fig. 1) [1,2]. These compounds exhibit the superconductivity induced by the partial substitution of Fe with Co, which is regarded as a direct electron doping to the $(FeAs)^{\delta+}$ layer. It is noteworthy that T_c = 22 K, which is realized for a Co content of 10% ($CaFe_{0.9}Co_{0.1}AsF$), is higher than the optimal T_c in Co-substituted *Ln*FeAsO (LaFeAsO: 13 K; SmFeAsO: 15 K), while the optimal T_c in Co-substituted SrFeAsF is below 4 K.

In this study, we have performed synchrotron X-ray powder diffraction measurements of $CaFe_{1-x}CoxAsF$ and $SrFe_{1-x}Co_xAsF$ (x = 0, 0.06, 0.12) at beamline **BL02B2** to confirm that the tetragonal to orthorhombic crystallographic transition also occurs in the *Ae*FeAsF system, as observed in the *Ln*FeAsO system and to analyze the relationship between T_c and crystal structure [3].

Tetragonal-to-orthorhombic phase transitions were observed at ~120 K for unsubstituted CaFeAssF and at ~180 K for unsubstituted SrFeAsF; such transition temperatures agree with kinks observed in temperature-dependent resistivity curves (Fig. 2). Although the transition temperature decreases, the structural phase transitions were observed below 100 K in both samples of x = 0.06, and finally, they were suppressed at the doping level of x = 0.12. The crystal structures refined by Rietveld analysis reveal that distortions of the $FeAs_4$ tetrahedron from the regular tetrahedron are likely to originate from mismatches in atomic radii among the constituent elements (Fig. 3). In this system, the enlarged $FeAs_4$ tetrahedron, resulting from the fact that the radius of Sr is larger than that of Ca, is flattened along the

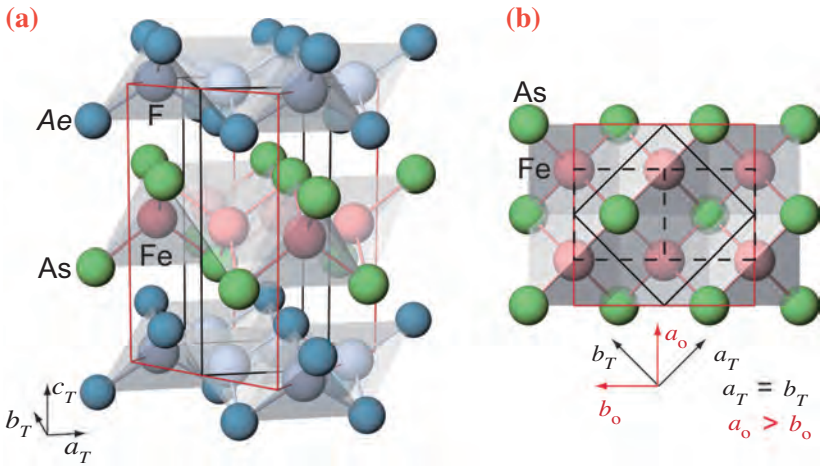

Fig. 1. Crystal structure of *Ae*FeAsF composed of alternate stacking of $(AeF)^{\delta+}$ and $(FeAs)^{\delta-}$ layers. Owing to the tetragonal-to-orthorombic transition, the unit cell setting is changed from a lattice (indicated by black solid lines) that is deformed to an orthogonal lattice (indicated by red lines.).

ab plane, and the smaller radius of Ca makes the tetrahedron closer to a regular one; their characteristic shapes are further enhanced by Co substitution. The positive relationship between the optimal T_c and regularity of the $FeAs_4$ tetrahedron is observed in various FeAs-based superconductors [4]. Furthermore, it is also observed that the optimal T_c in the Fe-1111 system realized by Co substitution is lower than that induced by F-doping. Our results suggest that the CaFeAsF compound is a promising candidate for a higher-T_c superconductor, if a substitutional doping to a $(CaF)^{\delta+}$ layer yielding an indirect electron doping to a $(FeAs)^{\delta-}$ layer is realized.

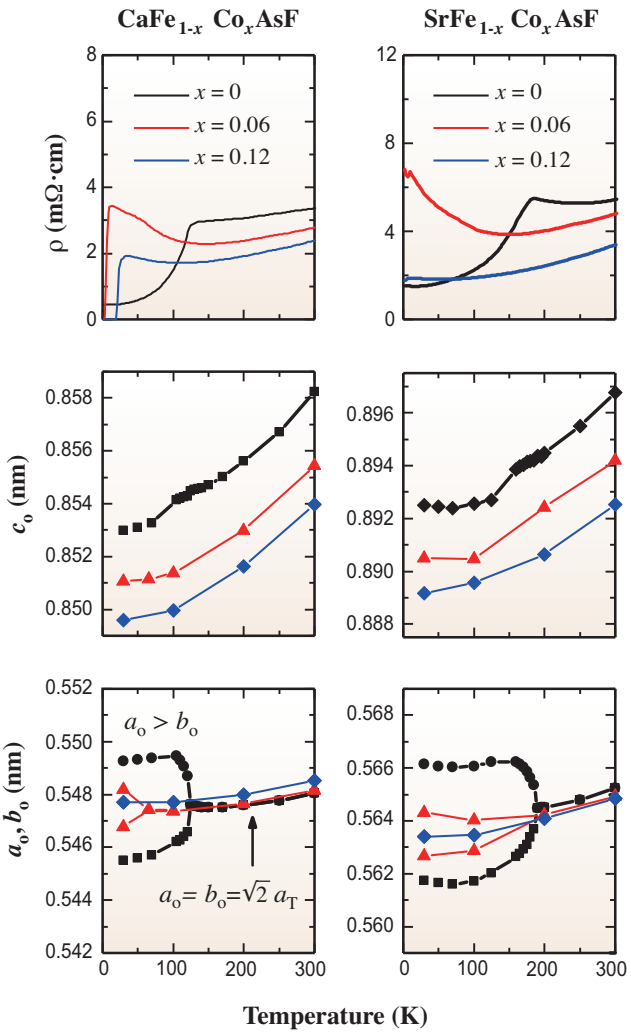

Fig. 2. Temperature dependences of electrical resistivity (ρ) and lattice constants (a_o, b_o, c_o) of $AeFe_{1-x}Co_xAsF$ (*Ae* = Ca, Sr; $x = 0, 0.06, 0.12$).

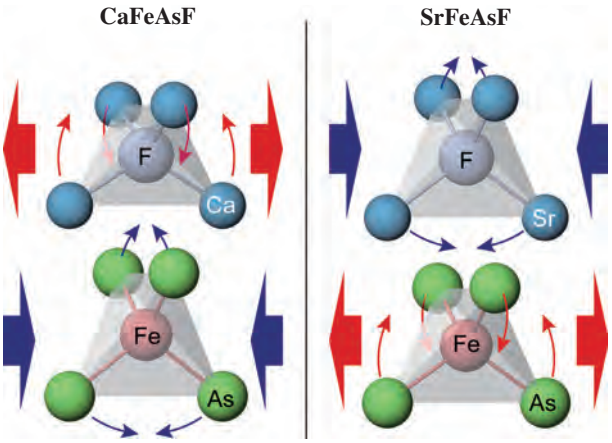

Fig. 3. Distortion of Ae_4F and $FeAs_4$ tetrahedra. For lattice-space matching between the $(AeF)^{\delta+}$ and $(FeAs)^{\delta-}$ layers, the As-Fe-As and *Ae*-F-*Ae* bond angles are changed from those of the regular tetrahedron to compensate for the difference in bond length ($r_{Sr\text{-}F} > r_{Fe\text{-}As} > r_{Ca\text{-}F}$).

Satoru Matsuishi[a,*] and Hideo Hosono[a,b]

[a] Frontier Research Center, Tokyo Institute of Technology
[b] Materials and Structures Laboratory, Tokyo Institute of Technology

*E-mail: satoru@lucid.msl.titech.ac.jp

References

[1] S. Matsuishi *et al.*: J. Am. Chem. Soc. **130** (2008) 14428.
[2] S. Matsuishi *et al.*: J. Phys. Soc. Jpn. **77** (2008) 113709.
[3] *T. Nomura, Y. Inoue, S. Matsuishi, M. Hirano, J. E. Kim, K. Kato, M. Takata, H. Hosono. Supercond: Sci. Technol.* ***22*** *(2009) 055016.*
[4] C-H. Lee *et al.*: J. Phys. Soc. Jpn. **77** (2008) 083704.

Comprehensive Structural Study of Glassy $BaTi_2O_5$

The structures of glassy $BaTi_2O_5$ fabricated by the containerless method were comprehensively investigated by combined X-ray and neutron diffraction analyses, X-ray absorption near-edge structure (XANES) analyses and computer simulations. The three-dimensional atomic structure of glassy $BaTi_2O_5$ (*g*-$BaTi_2O_5$), simulated by reverse Monte Carlo (RMC) modelling using diffraction data, shows that extremely distorted TiO_5 polyhedra interconnected with both corner- and edge-shared oxygen formed a structure with a higher packing density than that of conventional silicate glass linked only by the corner-sharing of SiO_4 polyhedra. Our results show that the glass-forming ability enhanced by containerless processing, not by a 'strong glass former', resulted in the fabrication of new bulk oxide glasses with novel structures and properties.

$BaTi_2O_5$ glass spheres were fabricated using containerless processing in an aerodynamic levitation furnace (ALF) [1]. The X-ray diffraction experiments were performed at beamline **BL04B2** of SPring-8 [2]. The neutron diffraction measurement for glassy sphere was carried out in the HIT-II spectrometer installed at the pulsed neutron source in the High Energy Accelerator Research Organization. The XANES spectra of the Ti *K*-edge were collected in the transmission mode at the undulator beamline NW14A of the PF-AR. The tructure modelling of *g*-$BaTi_2O_5$ was performed by reverse Monte Carlo (RMC) simulation on an ensemble of 4000, starting with a random configuration.

Figure 1 shows the X-ray and neutron structure factors $S(Q)$ as a function of the wave vector of *g*-$BaTi_2O_5$ together with the results of RMC simulation. It is noted that the agreement between the experimental data and the data obtained using the RMC model is excellent.

The derived total correlation functions $T(r)$ are shown in Fig. 2. The first peak in $T(r)$ was assigned to the Ti-O bond length, which is 1.92 Å in *g*-$BaTi_2O_5$, as determined from a positive peak of X-ray diffraction and a negative peak of neutron diffraction. The negative peak is due to the negative neutron scattering length of Ti. Intriguingly, the peak is skewed toward the high-*r* side, indicating the distribution of Ti-O distances from 1.60 Å to 2.50 Å due to highly distorted polyhedra. A fitting of the Ti-O peak using two Gaussian functions yielded two Ti-O correlation lengths at 1.91 Å and 2.13 Å, and the average coordination numbers $N_{Ti\text{-}O}$ obtained are 4.87±0.15 for X-ray data and 5.05±0.15 for neutron data. In the case of alkali titanium silicate glass, TiO_5 polyhedra generally exhibit a square pyramid having one shorter Ti-O bond and four longer Ti-O bonds [3]. In contrast to this, the partial pair distribution function $g_{ij}(r)$ of Ti-O derived using the RMC model shows a prominent peak at 1.90 Å that corresponds to the four shorter Ti-O bonds and a small peak at 2.10–2.5 Å corresponding to one longer Ti-O bond. A strong peak at 2.80 Å in the neutron data indicates the correlation length of O-O.

Figure 3(a) represents the distributions of Ti-O and Ba-O polyhedra obtained from the RMC configuration. Inhomogeneous distributions of Ti and Ba appear to exist within a space of 20 Å × 20 Å × 10 Å modeled by RMC simulation. The same tendency of forming Ti-rich and Ba-rich regions was observed by the RMC simulation of a titanium-silicate glass [4]. In the Ti-rich region, distorted trigonal bipyramidal TiO_5 was connected by both edge- and corner-sharing to form network rings (Fig. 3(b)). The Ti-O network was

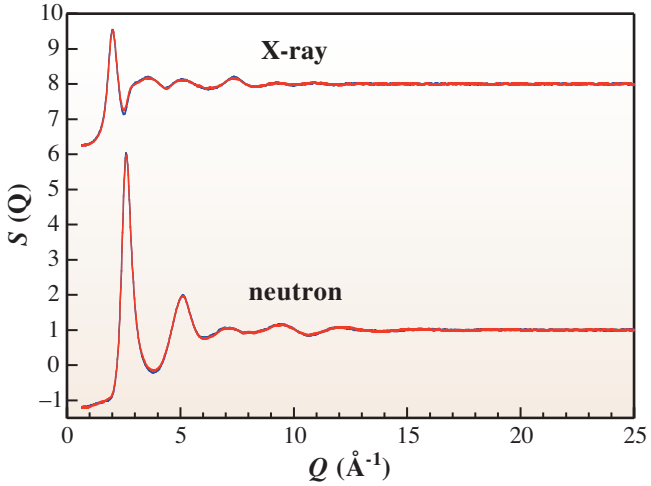

Fig. 1. Total structure factors $S(Q)$ of *g*-$BaTi_2O_5$ (blue, experimental data; red, RMC simulation data). The different features of the X-ray and neutron structure factors are due to the different scattering amplitudes of Ba, Ti, and O atoms, and the different weighting factors between the two techniques.

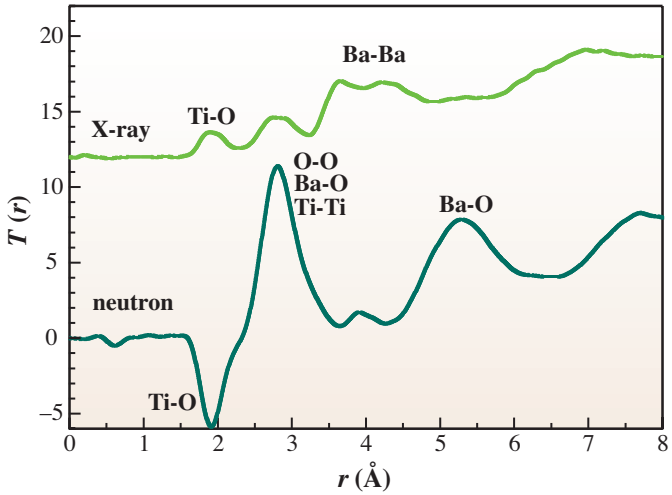

Fig. 2. Total correlation functions $T(r)$ of g-$BaTi_2O_5$.

dominated by small rings with the following distribution: threefold rings (35%), fourfold rings (25%) and fivefold rings (20%). This distribution is similar to that of chalcogenide glass exhibiting both corner- and edge-sharing [5], and is different from that of typical silicate glass linked only by the corner-sharing of SiO_4 tetrahedra [6].

Figure 3(c) depicts the Ba polyhedra connected by edge-, face- and vertex-sharing to form a random dense packing. Similarly to Ti polyhedral linkage, Ba polyhedral linkages included threefold rings (35%), fourfold rings (22%) and fivefold rings (15%). In addition, the average coordination number $N_{Ba\text{-}O}$ in g-$BaTi_2O_5$ calculated using the RMC model was about 7.5, which is significantly higher than the values of 6 to 6.5 in barium silicate glass and is near 8 in crystalline β-$BaTi_2O_5$. This feature implies that the high-density packing of polyhedra is realized in g-$BaTi_2O_5$.

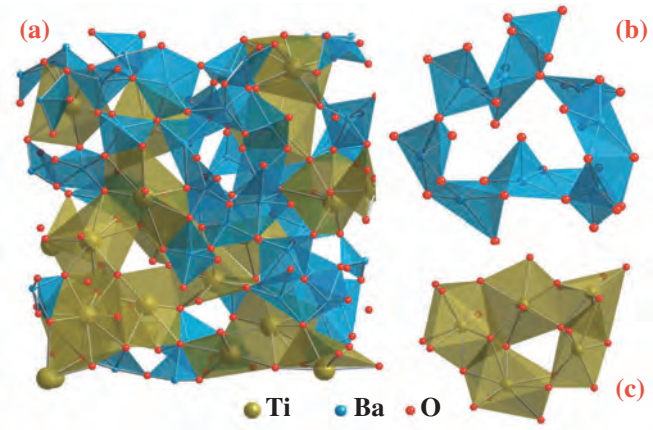

Fig. 3. **(a)** Representation of glass structure in slice (20 Å × 20 Å × 10 Å) modeled by RMC simulation. **(b)** Network configuration of TiO_5 polyhedra linked by both edge- and corner-sharing. **(c)** Network configuration of BaO_x ($x > 7$) polyhedra connected by edge-, face- and vertex-sharing to form random dense packing.

Jianding Yu[a,*], Shinji Kohara[b] and Atsunobu Masuno[c]

[a] ISS Science Project Office, Japan Aerospace Exploration Agency
[b] SPring-8 / JASRI
[c] Institute of Industrial Science, The University of Tokyo

*E-mail: yo.kentei@jaxa.jp

References

[1] J. Yu *et al.*: Chem. Mater. **18** (2006) 2169.
[2] *J. Yu, S. Kohara, K. Itoh, S. Nozawa, S. Miyoshi, Y. Arai, A. Masuno, H. Taniguchi, M. Itoh, M. Takata, T. Fukunaga, S. Koshihara, Y. Kuroiwa and S. Yoda: Chem. Mater.* ***21*** *(2009) 259.*
[3] F. Farges *et al.*: Phys. Rev. B **56** (1997) 1809.
[4] L. Cormier *et al.*: J. Phys.: Condens. Matter **9** (1997) 10129.
[5] P. Vashishta *et al.*: Phys. Rev. Lett. **62** (1989) 1651.
[6] S. Kohara and K. Suzuya: J. Phys.: Condens. Matter **17** (2005) S77.

A Novel Form of Topologically Ordered Amorphous Silica obtained from Collapsed Silicalite at High Pressure

Pressure-induced amorphization of open-structured solids provides a distinct way to synthesize amorphous materials with respect to glass formation by standard temperature quenching of liquids. This opens the route to prepare new amorphous forms with different entropies and intermediate range structures along with novel physical and mechanical properties (i.e. lower fragility etc.) [1]. Aluminosilicate and siliceous zeolites, built up of corner-sharing $Si(Al)O_4$ tetrahedra, are examples of such low-density, porous, open-structured materials, which undergo pressure-induced amorphization. The large volume collapse during the amorphization of these materials may be of considerable interest for new applications in shock wave absorption [2]. The present study focuses on the determination of the structure of the new form of amorphous silica obtained from the pressure-induced amorphization of the essentially pure SiO_2 zeolite, silicalite-1-F by Reverse Monte Carlo (RMC) refinement of total X-ray scattering data.

Calcined silicalite-1-F (SOMEZ, France) was compressed to 20 GPa in a Walker-type multi-anvil apparatus in order to prepare the amorphous form [3]. High energy total X-ray scattering data from the recovered amorphous sample (Fig. 1), were obtained using the two axis diffractometer and 61.6 keV X-rays at beamline **BL04B2** [4] and correspond to a characteristic broad-featured pattern of an amorphous material. The pair distribution function was obtained in the form of the total correlation function $T(r)$ (Fig. 2) by direct Fourier transformation of the total scattering data. Based on these data, the Si-O bond length of 1.62 Å is only slightly greater than that of normal silica glass [5]. It can be noted that in amorphous silicalite-1-F, the Si-Si correlation is very broad and is characterized by a double peak. This is an indication of strong local distortions of the intertetrahedral Si-O-Si bond angles.

RMC modeling was used to determine the structure of amorphous silicalite-1-F (Fig. 3). The starting RMC model was obtained by progressively reducing the volume of a 2×2×4 orthorhombic supercell of the silicalite structure while randomly moving atoms to maintain local tetrahedral geometry and network topology. Once the model had attained the measured pressure amorphized sample density (model size 35.344 × 34.726 × 46.244 $Å^3$), the model was further refined using RMC protocols by minimizing the difference between the $S(Q)$ calculated from the model and the experimental $S(Q)$ (Fig. 1). The model $S(Q)$ shows no Bragg peaks with no long-range oscillations in the partial radial distribution functions, $g_{ij}(r)$ [3], showing that the model is truly amorphous, despite originating from the low-pressure crystal structure.

It can be seen from the RMC models that the amorphization and the attendant loss of periodicity is linked to the collapse of the pores in the silicalite structure, which occurs through large random local changes in Si-O-Si bond angles based on the strong broadening of the Si-Si correlation. The strong reduction in Si-Si-Si and Si-O-Si bond angles with respect to silica glass [3,5] and the presence of a double peak in the Si-Si correlation (Fig. 2) are indicative of highly strained configurations on different length scales, respectively; in the ring edges and locally in the Si-O-Si angles around the oxygen atoms. This intertetrahedral Si-O-Si angle distribution in amorphized silicalite-1-F is centered around 125° rather than 145-150° and is much broader than in silica glass [3,5].

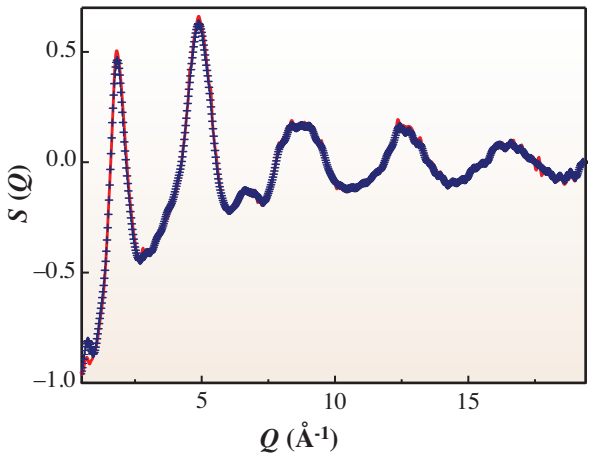

Fig. 1. X-ray total structure factor $S(Q)$ of pressure-amorphized silicalite-1-F (+) and calculated $S(Q)$ from the RMC refined model (red solid line).

There are small voids corresponding in particular to the collapsed 5, 6 and 10 membered rings (MRs) of the initial crystalline structure. The present experimental results and RMC model indicate that the amorphization can take place while still retaining remnant periodicity and without a major change in ring statistics. The ring statistics in pressure-amorphized silicalite-1-F found in Fig. 3 can be explained by an extraordinary "topologically ordered" structure (i.e. still retaining the initial chemical bonds and connectivity); amorphous materials usually exhibit "topologically disordered" structures, in which ring statistics are very broad and very different from the corresponding crystal phase. Inspection of the silica glass model (Fig. 3) shows that voids are also present, but distributed in a random manner, more a characteristic of a quenched liquid.

In conclusion, the present results based on the total X-ray scattering study of a novel form of silica recovered from high-pressure conditions emphasizes the difference between the structural topology of amorphous silica obtained by temperature-induced vitrification and that obtained by pressure-induced amorphization of a crystalline material, the siliceous zeolite silicalite-1-F. The latter is shown to retain the basic topology (i.e. chemical bonds and connectivity) of the initial crystalline phase, but with strong geometrical distortions. The same process in more complex aluminosilicate zeolites will, in addition, also conserve the chemical order of the crystal leading to an amorphous material, which is topologically and chemically ordered. This opens the route to prepare new amorphous materials with different intermediate-range structures, a lower entropy with respect to a standard glass, distinct physical and mechanical properties, eventually approaching those of an "ordered" or "perfect" glass. The structural collapse, in particular around the empty pores, in this material leads to a high degree of densification providing a mechanism for shock wave absorption.

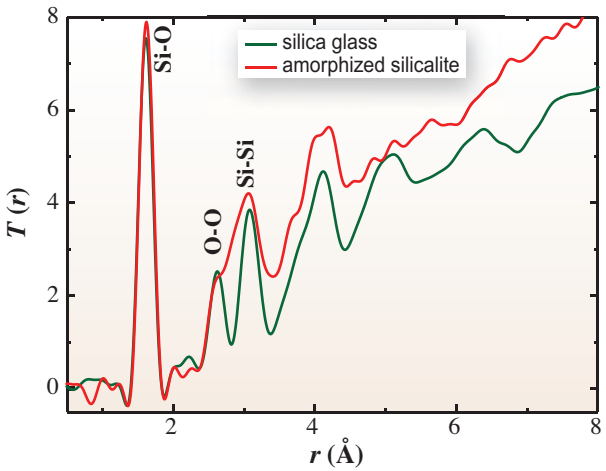

Fig. 2. Total correlation functions $T(r)$ of pressure-amorphized silicalite and silica glass.

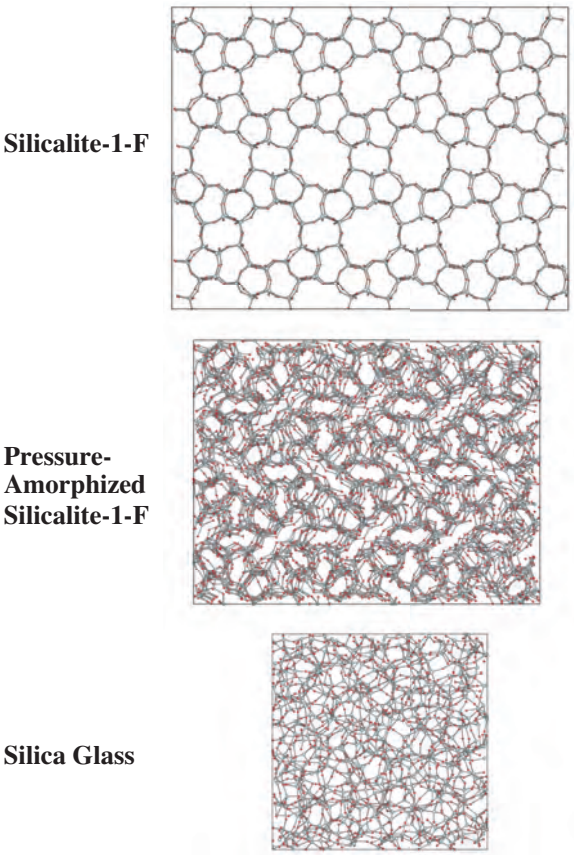

Fig. 3. The structure of silicalite-1-F projected along the [010] direction and RMC models of pressure amorphized silicalite-1-F and silica glass [5].

J. Haines[a,*], C. Levelut[b], A. Isambert[c], P. Hébert[c] and D. A. Keen[d]

[a] Institut Charles Gerhardt Montpellier, C2M, Université Montpellier II, France
[b] Laboratoire des Colloïdes, Verres et Nanomatériaux, Université Montpellier II, France
[c] CEA, DAM Le Ripault, France
[d] ISIS Facility, Rutherford Appleton Laboratory, United Kingdom

E-mail: jhaines@lpmc.univ-montp2.fr

References

[1] G.N. Greaves & S. Sen: Adv. in Phys. **56** (2007) 1.
[2] A. Isambert *et al.*: J. Mater. Chem. **18** (2008) 5746.
[3] *J. Haines, C. Levelut, A. Isambert, P. Hébert, S. Kohara, D.A. Keen, T. Hammouda and D. Andrault: J. Am. Chem. Soc.* ***131*** *(2009) 12333.*
[4] S. Kohara *et al.*: J. Phys.: Cond. Matter **19** (2007) 506101.
[5] M.G. Tucker *et al.*: J. Phys.: Cond. Matter **17** (2005) S67.

EARTH & PLANETARY

Synchrotron-based research in the field of Earth and planetary sciences, including mineral physics, geology, geochemistry, and astronomy, is one of the rapidly growing sectors of science conducted at synchrotron sources. Its applications have led to major advances in the frontier of Earth and planetary sciences. Constant challenges to develop and upgrade instrumentations and techniques, on the basis of the high-flux and low-emittance X-ray beam, have allowed researchers to analyze various materials in a wide variety of environments, that is, high-pressure and high-temperature or micro- to nanosize. In this chapter, we would like to introduce five research highlights in the categories of Earth and planetary sciences.

In situ X-ray diffraction observation of materials under the high-pressure and high-temperature conditions corresponding to the center of the Earth (~360 GPa and ~6000 K) is definitely one of the goals in the high-pressure research program at SPring-8. The first paper is the most up-to-date work on the Earth' s core materials. Kuwayama *et al*. conducted high-pressure/temperature experiments on iron and iron-nickel alloys using a laser-heated diamond anvil cell at up to 301 GPa and 2000 K, the Earth' s core conditions that had never been experimentally generated before. His observations suggested that the hcp phase is stable even under the Earth' s inner-core conditions. Murakami *et al*. report high-pressure Brillouin scattering spectroscopy on MgO in combination with the synchrotron X-ray diffraction method in the pressure range of the Earth's upper mantle to the lowermost mantle. Their results show that the shear velocity profile can reproduce the 1-D global seismic model of the lower mantle remarkably well using a model composed of ~92 vol% Mg-silicate perovskite phase and ~8 vol% MgO.

SCIENCE

Tange *et al*. developed the technique of high-pressure generation using a Kawai-type multi-anvil high-pressure apparatus, one of the large-volume presses, with sintered diamond anvils, and extended achievable high pressure of up to 80 GPa. By the new technique, they also determined the accurate phase relation and Fe-Mg partitioning in the system of MgO-FeO-SiO_2 in the middle part of the Earth's lower mantle. Kogiso *et al*. presented the microbeam X-ray fluorescence analysis of platinum-group elements in the natural peridotite that is dominant in the lower crust and abundant in the uppermost mantle. Measurements of the platinum-group element concentrations in microphases of the sample are challenging because of the extremely small amount analysis. The further development of the X-ray analytical technique will lead to the improvement of the accuracy of the analyzing system. Ogasaka *et al*. demonstrated the method for the calibration and development of new instruments for a hard X-ray telescope operated in space. Only hard X-ray synchrotron radiation allows us to conduct performance tests on the multilayer hard X-ray mirrors and to evaluate the performance as onboard equipment of a hard X-ray telescope.

Yasuo Ohishi

"Ookinkeigiku" - *Coreopsis or Tickseed*

Phase Relations of Iron-Nickel Alloys at Multimegabar Pressure: A Study of the Earth's Inner Core Material

Iron is believed to be the major component of the Earth's core because it is the most abundant element that satisfies the seismologically observed densities. On the basis of cosmochemical models and the studies of iron meteorites, it is generally accepted that the Earth's core also contains substantial amounts of nickel. The high-pressure behavior of iron-nickel alloys is, therefore, essential for interpreting the seismic observations and understanding the nature of the Earth's core.

The phase relation of iron at relatively low pressure has been well established. α–Fe with body-centered cubic (*bcc*) structure is stable at ambient condition. It transforms to γ-Fe with face-centered cubic (*fcc*) structure with increasing temperature and to ε-Fe with hexagonal close-packed (*hcp*) structure above ~10 GPa at 300 K. Static compression experiments revealed that the *hcp*-Fe phase is stable at least to 300 GPa at room temperature. In contrast, the phase relation and crystal structure of iron at high pressure and temperature (*P-T*) are still highly controversial. Although many crystal structures including *hcp*, *fcc*, *bcc*, *dhcp*, and orthorhombic have been proposed as the candidate structure of iron under the Earth's core conditions, it is a matter of extensive debate. The effect of nickel on the phase relation of iron at high pressure is also not clear.

To achieve extremely high *P-T* conditions found in the Earth's core is a major experimental challenge. The high-temperature experiments on iron and iron-nickel alloys at multi-megabar pressure range have still been limited. In particular, the data on iron around 300 GPa that is close to the inner core pressure are available only up to 1350 K [1]. The Fe-Ni alloy was studied up to 255 GPa at room temperature [2] and only to 225 GPa at high temperatures [3]. Note that it is difficult to study the solid-state iron at the inner core pressure by a shock compression method, because the Hugoniot intersects its melting curve at about 250 GPa. Is the β-phase of iron with *dhcp* or orthorhombic structure stable at high *P-T*? How does nickel affect the phase relation of iron? To determine the stable phase relations of iron-nickel alloys at high pressure and high temperature, we conducted laser-heated DAC (LHDAC) experiments on iron and iron-nickel alloys up to 301 GPa and 2000 K.

We have examined six different compositions of iron and iron-nickel alloys: pure Fe, Fe-18.4 wt% Ni, Fe-24.9 wt% Ni, Fe-29.8 wt% Ni, Fe-35.7 wt% Ni, and Fe-50.0 wt% Ni. The chemical compositions and homogeneities of these alloys were examined using a JEOL JXA-8800 electron microprobe. High-pressure conditions were generated using a symmetric DAC with flat 300 μm culet diamonds for pressures below 90 GPa. We used beveled diamond anvils with 150 and 90 μm culet for pressures up to 180 GPa and 60 μm culet for pressures above 180 GPa. The samples were loaded into a hole drilled in a pre-indented rhenium gasket, together with thermal insulation layers of MgO. In some runs on pure iron, SiO_2 was used as a pressure medium. After compression to a pressure of interest at room temperature, the sample was heated by a focused TEM_{01}*-mode Nd:yttrium-lithium-fluoride (YLF) laser by double-side heating technique, which minimizes the axial temperature gradient in the sample. High-

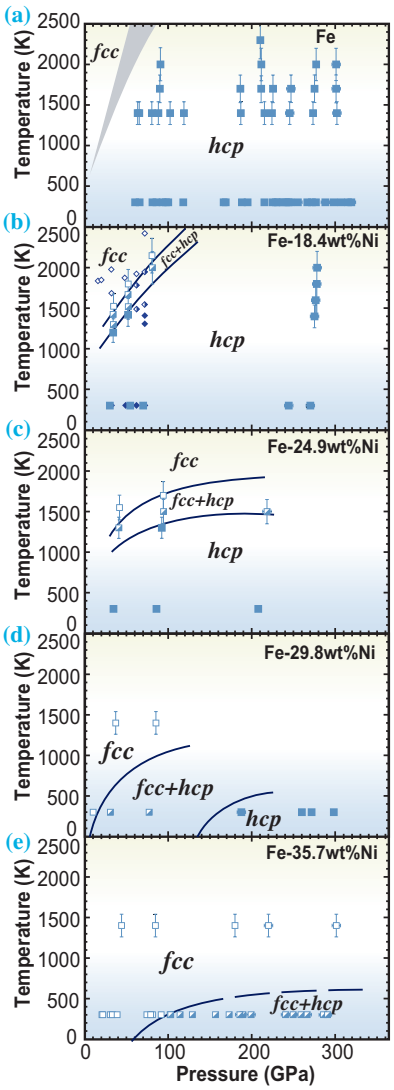

Fig. 1. Phase relations of iron and iron-nickel alloys [4]. Squares: this study; diamonds: previous results for Fe-20 wt.% Ni by Mao *et al.* [6].

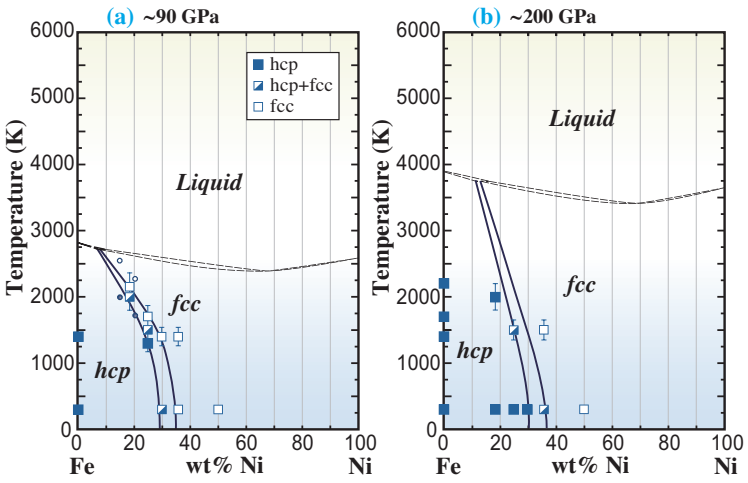

Fig. 2. T-x phase diagrams of iron-nickel alloy at **(a)** around 90 GPa and **(b)** 200 GPa [4].

pressure XRD measurements were performed using synchrotron radiation at beamline **BL10XU**. Angle-dispersive XRD patterns were obtained on an imaging plate (Rigaku R-AXIS IV) and X-ray charge-coupled device (CCD) (Bruker APEX).

Experimental results on iron and iron-nickel alloys are summarized in Fig. 1. *In situ* XRD measurements demonstrate the wide stability of *hcp*-iron up to 300 GPa and 2000 K without phase transition to *dhcp*, orthorhombic, or *bcc* phases. Our results also showed that the incorporation of nickel significantly expands the stability field of the *fcc* phase. Figure 2 shows the temperature-composition (*T*-*x*) phase diagrams of the iron-nickel binary system at around 90 and 200 GPa. In this figure, the composition of the *fcc*-*hcp*-liquid triple point is important, considering the crystalline phase at the inner core-outer core boundary (ICB). For example, if the nickel content in the outer core is lower than that of the *fcc*-*hcp*-liquid triple point, the *hcp* phase crystallizes during the inner core crystallization (Fig. 3(a)). In contrast, if the nickel content in the outer core is larger than that of the triple point, the *fcc* phase should crystallize at the ICB (Fig. 3(b)). Furthermore, the *fcc* phase may transform to an *hcp* structure at the deep inner core with Earth's secular cooling (Fig. 3(c)). According to our results, the *fcc*-*hcp*-liquid triple point is located at about 8% Ni at 90 GPa and 12% Ni at about 200 GPa. The nickel content in the Earth's core is unclear, but most of the literature suggested 5 to 10% Ni on the basis of the chondritic Earth model [5]. If this is true, the *hcp* phase should crystallize at the ICB.

Although realizing the *P*-*T* conditions of the center of the Earth (~360 GPa, ~6000 K) in the laboratory requires further technical developments, the novel LH-DAC technology will open up new windows to explore this region of the Earth and deep interiors of other planets.

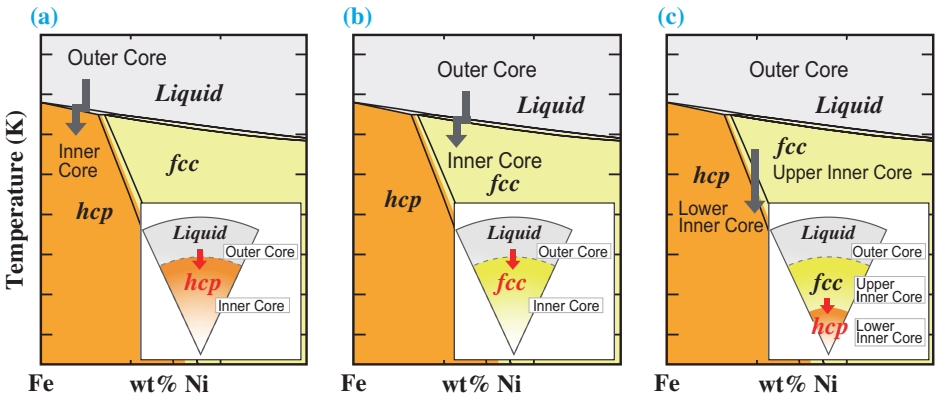

Fig. 3. Schematic phase diagrams of iron-nickel system at the pressure of the inner core boundary. **(a)** If the Ni content in the outer core is less than that of the *fcc*-*hcp*-liquid triple point, the inner core could be composed of the *hcp* phase. **(b)** If the nickel content in the outer core is larger than that of the triple point, the *fcc* phase should first be crystallized at the inner core boundary. **(c)** The *fcc* phase may transform to the *hcp* structure with secular cooling. Insets, schematic images of the Earth's inner core structure.

Yasuhiro Kuwayama[a,b,c]

[a] Geodynamics Research Center, Ehime University
[b] Department of Earth and Planetary Sciences, Tokyo Institute of Technology
[c] Institute for Research on Earth Evolution, Japan Agency for Marine-Earth Science and Technology (JAMSTEC)

E-mail: kuwayama@sci.ehime-u.ac.jp

References

[1] L.S. Dubrovinsky *et al.*: Phys. Rev. Lett. **84** (2000) 1720.
[2] H.K. Mao *et al.*: J. Geophys. Res. **95** (1990) 21737.
[3] L. Dubrovinsky *et al.*: Science **316** (2007) 1880.
[4] *Y. Kuwayama, K. Hirose, N. Sata and Y. Ohishi: Earth Planet. Sci. Lett.* ***273*** *(2008) 309.*
[5] W.F. McDonough: Treatise on Geochemistry, Elsevier, Amsterdam, vol. 2, (2004) 547.
[6] W.L. Mao *et al.*: Phys. Earth Planet. Inter. **155** (2006) 146.

Elasticity of MgO to 130 GPa: Implications for Lower Mantle Mineralogy

The average composition and structure of the Earth's deep mantle can be approached by comparing the observed seismic velocities with appropriate laboratory data collected for candidate minerals under relevant pressure and temperature conditions. It is widely believed that the Earth's lower mantle is primarily composed of silicate perovskite (Pv) and ferropericlase (Fp). Precise knowledge of the elastic properties of $MgSiO_3$ perovskite and MgO periclase, major end-members of constituent mineral phases of the lower mantle, under high-pressure condition is therefore crucial for constructing the accurate mineralogical model of the Earth's lower mantle. However, only few experimental acoustic measurements exist under lower mantle pressure condition. Recent technical advances in high-pressure Brillouin spectroscopic measurements using diamond anvil cell apparatus extended significantly the upper pressure limit for acoustic measurements. It is now possible to measure the aggregate shear wave velocity profiles of both $MgSiO_3$ perovskite and post-perovskite phases up to a pressure of 172 GPa [1,2]. Available experimental data for MgO from the direct sound wave velocity measurements under the lower mantle pressure regime are, however, still limited to a maximum pressure of 55 GPa on a single crystal [3]. Owing to the lack of acoustic data on MgO under the whole pressure range of the lower mantle, the pressure dependence of elastic velocities or moduli has thus far been poorly constrained. In this report, we show the results of elastic wave velocity measurements on MgO collected by Brillouin spectroscopy in a diamond anvil cell (DAC) in conjunction with synchrotron X-ray diffraction technique throughout the entire lower mantle pressure regime approaching 130 GPa.

High-pressure Brillouin scattering measurements of sound velocities in a diamond anvil cell were conducted using the newly developed acoustic measurement system, recently installed at **BL10XU** [4]. Six separate series of high-pressure Brillouin scattering experiments on polycrystalline MgO were performed using a symmetric-type diamond anvil cell. In all the experiments, we collected Brillouin spectra on the polycrystalline MgO, sandwiched with pressure medium of NaCl, at eighteen pressures from 14 to 128 GPa with simultaneous angle-dispersive X-ray diffraction measurements for phase identification and pressure determination. A representative Brillouin spectrum at the high-pressure condition is shown in Fig. 1. Figure 2 shows the pressure dependence of the aggregate shear velocities (V_S) for the MgO. Our new results on high-pressure elasticity of MgO have shown that the aggregate shear wave velocity and shear moduli at ambient pressure are highly consistent with earlier studies. However, the pressure derivative of the shear modulus/velocity (G'_0) of MgO is distinctly lower than that of previous lower-pressure experiments.

The large pressure range over which the aggregate shear wave velocity measurements of MgO periclase were performed in this study [5] thus allows us to put tighter constraints on mineralogical models of the Earth's lower mantle. On the basis of our new results, we have calculated the V_S profile appropriate for an adiabatic lower mantle geotherm in the three-component system MgO-SiO_2-FeO in the same manner as in Ref. [1]. The calculated V_S profiles for Pv [1] and Fp under the lower mantle condition are shown in Fig. 3, along with the 1-D global seismic lower mantle model (PREM). By applying the fairly low G'_0 of MgO determined in this study, the V_S profile of Fp remarkably ascents gently with pressure, as shown in Fig. 3. The PREM profile in the lower mantle is then best fitted within ±0.14% on average for V_S using a model with X_{Pv} = 0.92 (red line in Fig. 3). Given that the best fit profile using the previously reported higher G'_0 value (=2.2) of MgO resulted in X_{Pv} =0.90 (dotted line in Fig. 3), the best fit velocity-depth profile calculated in this study using the lower G'_0 value of MgO requires the more silicate perovskite component in the lower mantle constituents than

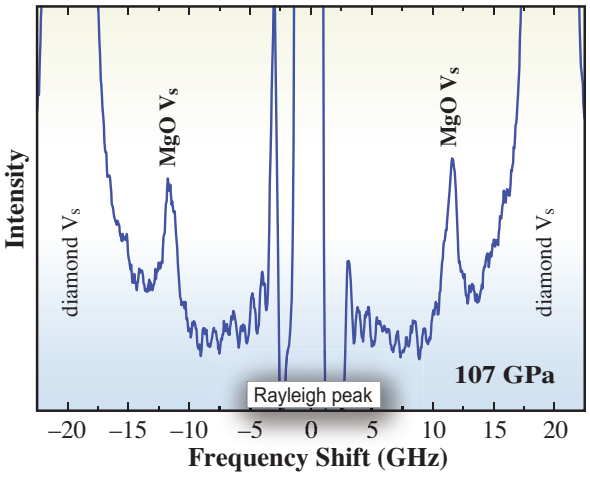

Fig. 1. Representative high-pressure Brillouin spectrum at 107 GPa. V_S, shear acoustic mode of the Brillouin shift.

previously considered, owing to the relatively moderate incline of the shear velocities of ferropericlase with depth.

According to the lower mantle model by applying the previous low-pressure experimental results on G'_0 of both $MgSiO_3$ perovskite and MgO, a superadiabatic geotherm and/or non-uniform bulk composition with depth in the lower mantle should be required in order to meet the global seismic model. Our result, however, strongly supports that the shear velocity profile can remarkably well reproduce the 1-D global seismic model with simple assumptions of an adiabatic geotherm and uniform composition model within the lower mantle. The shear velocity profile calculated from the pyrolitic mantle model with X_{Pv} of 0.80 is also shown in Fig. 3 (green line) for comparison. This profile is ~1.9% lower than that of the PREM model on average throughout the pressure range of the lower mantle, which is clearly incompatible with PREM. Although further experimental explorations particularly on thermoelastic parameters will be required for more strict constraints, our new results strongly offer the possibility that the lower mantle is predominantly composed of Mg-silicate perovskite phase (~92 vol%), and the bulk composition of the lower mantle could be close to chondritic rather than pyrolitic composition.

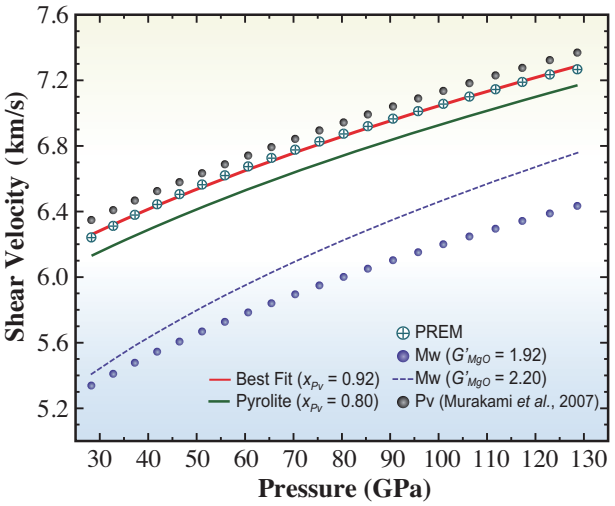

Fig. 3. Calculated shear wave velocity profiles of Fp and Pv as a function of pressure along the representative mantle geotherm, along with the PREM lower mantle seismic model. Blue circles, Fp with X_{Mg} of 0.79; black circles, Pv with X_{Mg} of 0.94 [1]; white circles with cross, PREM. The red line indicates the best fit profile to PREM (X_{Pv} = 0.92). The shear wave velocity profile of the simplified pyrolite model (X_{Pv} = 0.80) is also indicated by the green line. The dotted line shows the profile of Fp calculated from G'_0 = 2.20 of MgO for comparison.

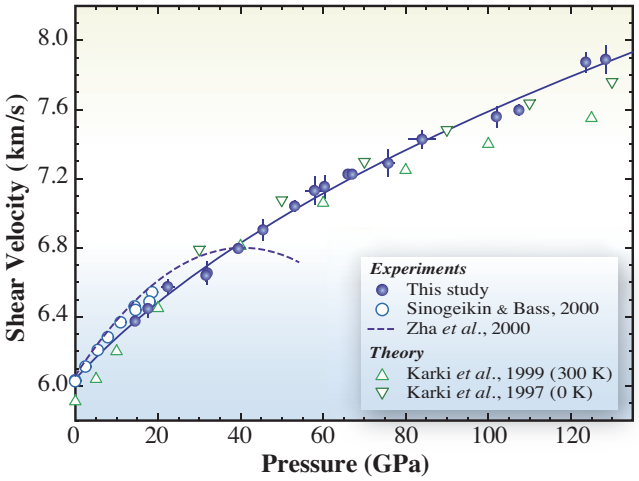

Fig. 2. Shear acoustic wave velocities of MgO as a function of pressure at 300 K (black circles). Third-order Eulerian finite strain fit is indicated by the black line. Open circles and dotted line indicate previous experimental results obtained by Brillouin scattering measurements. Open upward- and downward-pointing triangles indicate the results obtained by computational calculations using first principles at 0 K and 300 K.

Motohiko Murakami

Department of Earth and Planetary Materials Science, Tohoku University

E-mail: motohiko@m.tains.tohoku.ac.jp

References

[1] M. Murakami *et al.*: Earth Planet. Sci. Lett. **259** (2007) 18.
[2] M. Murakami *et al.*: Earth Planet. Sci. Lett. **256** (2007) 47.
[3] C-S. Zha *et al.*: Proc. Natl. Acad. Sci. USA **97** (2000) 13494.
[4] M. Murakami *et al.*: Phys. Earth Planet. Inter. **174** (2009) 282.
[5] *M. Murakami, Y. Ohishi, N. Hirao and K. Hirose: Earth Planet. Sci. Lett.* ***277*** *(2009) 123.*

Mineralogy of the Lower Mantle Investigated Using Sintered Diamond Multianvil Apparatus

The Kawai-type, in other words, 6-8 double-staged, multianvil apparatus (KMA) is one of the most popular experimental devices, which can reproduce high-pressure and high-temperature conditions relevant to the Earth's deep interior. KMA has the advantage of generating stable high *P-T* conditions with high reproducibility and large sample volume. Because of these characteristics, KMA has played an important role in the high-pressure Earth sciences, particularly in understanding the mineralogy of the upper mantle, mantle transition zone, and uppermost lower mantle (e.g., Ref. [1]). However, generally, pressures available in KMA are limited to ~30 GPa owing to the limitation in the hardness of the tungsten carbide (WC) used as second-stage anvils. The second-stage anvils are one of the most important parts in KMA, which concentrate the large press load (up to ~15 MN in the case of KMAs installed at **BL04B1**) generated by a hydraulic power unit into a sample put into the center of the apparatus.

In order to overcome this limitation in the pressure generation range of KMA, experimental techniques using sintered diamond (SD) as the material of second-stage anvils have been developed in Japan. The experimental techniques using SD anvils in KMA allowed studies to be carried out beyond the limit of ~30 GPa, but pressures have been limited to 40 GPa using conventional high-pressure cell assemblies optimized for experiments with WC anvils. This limitation in pressure generation using SD anvils has been overcome by changing the materials used for the gaskets and pressure medium, and the pressure range has since been expanded to 60 GPa. Recently, after further testing the materials for the pressure medium and anvils while optimizing the high-pressure cell assembly, the pressure range has been expanded to 80 GPa (Fig. 1) [2]. This pressure value corresponds to ~1900 km depth in the Earth's interior, and now, we can investigate the mineralogy of the lower mantle, which is found from 660 to 2900 km depth in the Earth, with the broad pressure range using KMA. In the next section, we introduce recent results obtained using the SDMA techniques.

As mentioned above, current high-pressure techniques using SDMA allow us to achieve pressures found in the middle part of the Earth's lower mantle. The Earth's lower mantle contains more than half the mass of the planet, and the system MgO-FeO-SiO_2 is fundamental to our understanding of its constituents and dynamics because the total amounts of MgO, FeO, and SiO_2 make up more than 90 wt% of the bulk silicate Earth. As a result, the phase relations in the system MgO-FeO-SiO_2 have been extensively investigated using high-pressure and high-temperature techniques (e.g., Ref. [3]). We performed a series of high *P-T* experiments in the system MgO-FeO-SiO_2 under deep lower mantle conditions for the first time using KMA [4]. Phase relations in the system MgO-FeO-SiO_2 were investigated between 22 and 47 GPa at 1500 and 2000°C using SDMA to clarify *P-T* effects on the phase relations. A $(Mg_{0.5},Fe_{0.5})SiO_3$ clinopyroxene synthesized at 1 atm and 1250°C under a controlled oxygen fugacity was used as the starting material. After the high *P-T* experiments, the recovered samples were analyzed with an electron microprobe and by analytic transmission electron microscopy and X-ray diffraction measurements using synchrotron radiation at **BL10XU** to determine the phases present in the sample and its chemical composition.

After the analyses of the recovered samples, it was confirmed that the three phases of $(Mg,Fe)SiO_3$ perovskite (Pv), (Mg,Fe)O magnesiowüstite (Mw), and stishovite (St) coexisted in all the run products. Since each sample is in a three-component system, the coexistence of three phases (Pv + Mw + St) at a given pressure and temperature indicates that Pv and Mw have univariant compositions assuming chemical equilibrium. The univariant compositions of Pv and Mw were determined as functions of pressure and temperature (Fig. 2). The pressure dependence of the phase relations can be seen easily in a pseudobinary phase diagram in the $MgSiO_3$-$FeSiO_3$ system (Fig. 3(a)). The univariant composition of Pv is also the maximum iron content of this phase at a given

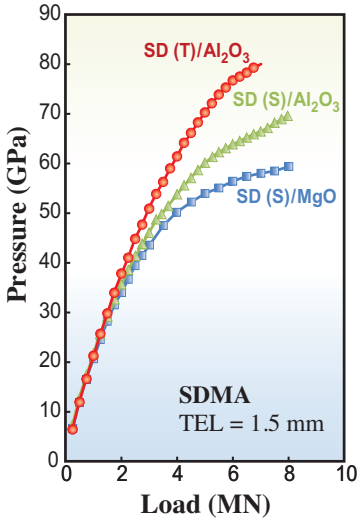

Fig. 1. Pressures generated using SDMA. Two kinds of sintered diamond, Al_2O_3 and MgO ceramics, were tested as the anvil and pressure medium, respectively.

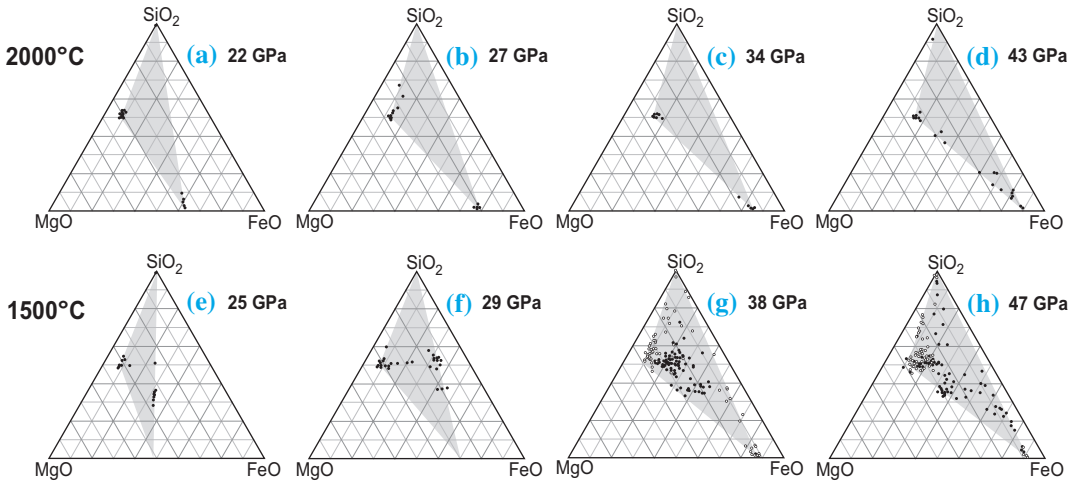

Fig. 2. Results of chemical analyses plotted on ternary diagrams. Samples were synthesized at 22–43 GPa and 2000°C **(a–d)**, and at 25–47 GPa and 1500°C **(e–h)**. Solid symbols show the measured compositions using EPMA. ATEM analyses were carried out in the case of **(g)** and **(h)**, and the results are shown as open symbols. Gray areas show univariant triangles indicating the coexistence of Pv, Mw, and St.

P-T condition, and the maximum iron solubility in Pv gradually increases with increasing pressure and temperature to be more than 30 mol% at 2000°C and pressures above 40 GPa. In addition to the pressure effect in the maximum iron solubility in Pv, a significant pressure effect was observed in the composition of Mw. The iron content of Mw dramatically increases from 50 to greater than 90 mol% with increasing pressure. As a result of this iron enrichment in the univariant composition of Mw, a significant pressure effect was found in Fe-Mg partitioning between Pv and Mw at pressures between 22 and 35 GPa, and the Fe-Mg distribution coefficients between Pv and Mw, $K_D = (X^{Pv}_{Fe}/X^{Pv}_{Mg})/(X^{Mw}_{Fe}/X^{Mw}_{Mg})$, decrease to less than 0.05 (Fig. 3). This significant pressure effect in Fe-Mg partitioning is expected to cause a strong concentration of ferrous iron in Mw with increasing depth in the lower mantle. The presence of highly iron-rich Mw would have some influence on deep mantle properties such as electric conductivity and viscosity.

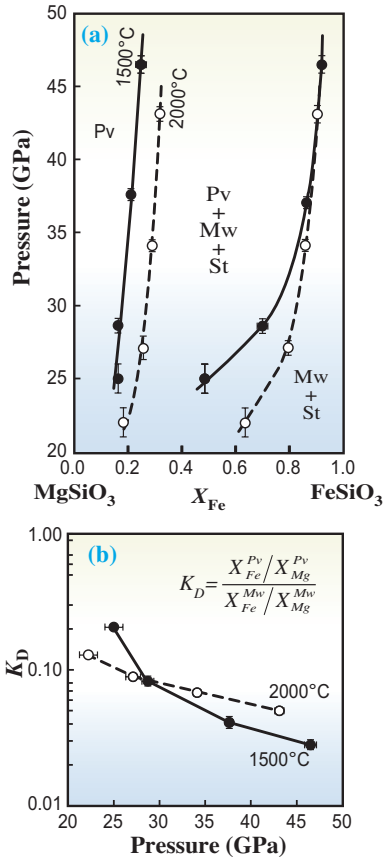

Fig. 3. **(a)** Univariant compositions of Pv and Mw, and corresponding phase boundaries in the $MgSiO_3$-$FeSiO_3$ pseudobinary system. **(b)** Fe-Mg distribution coefficients between Pv and Mw as a function of pressure. Solid circles and solid lines, 1500°C; open circles and broken lines, 2000°C in each diagram.

As briefly introduced here, the experimental technique using SDMA is a powerful tool to investigate phase equilibria under *P-T* conditions of the Earth's lower mantle. Therefore, it is expected that further systematic studies using SDMA will improve our understanding of lower mantle mineralogy.

Yoshinori Tange

Geodynamics Research Center, Ehime University

E-mail: tan@sci.ehime-u.ac.jp

References

[1] T. Irifune *et al.*: Nature **451** (2008) 814.
[2] Y. Tange *et al.*: High Pressure Res. **28** (2008) 245.
[3] H.-K. Mao *et al.*: Science **278** (1997) 2098.
[4] *Y. Tange, E. Takahashi, Y. Nishihara, K. Funakoshi and N. Sata: J. Geophys. Res.* ***114*** *(2009) B02214.*

Nondestructive Search for Micrometer-Scale Platinum-Group Minerals in Mantle Peridotite with Microbeam X-Ray Fluorescence Analysis

Because of their strong siderophile (iron-loving) character, platinum-group elements (PGEs: Ru, Rh, Pd, Os, Ir, and Pt) are highly concentrated in metallic phases in the Earth's interior and meteorites, but are scarcely distributed in silicate phases. For example, the Earth's silicate mantle contains PGE only on the order of 1 ppb [1]. Thanks to such sparseness, the PGE abundances in the Earth's mantle are sensitive to chemical processes that involve metallic phases, such as core-mantle segregation in the early Earth, late-stage meteorite bombardment (so-called late veneer), and core-mantle chemical interactions during the Earth's history. In other words, PGEs in the mantle are useful tracers for understanding the chemical evolution of the Earth's interior.

A critical point in discussing the chemical evolution of the Earth's interior using PGEs is that their distributions in the mantle are not well identified, and therefore, the behavior of PGE during differentiation processes (e.g., partial melting) in the mantle is unclear. Recent PGE analyses using laser-ablation inductively coupled plasma mass spectrometry (LA-ICP-MS) revealed that PGEs in mantle peridotite are highly concentrated in base-metal sulfides (i.e., Fe-Ni-Cu sulfides). On the other hand, discrete platinum-group minerals (PGMs), such as Pt-Ir-Os alloys and Ru-Os sulfides, have been detected in peridotite by scanning electron microprobe (SEM) and LA-ICP-MS analyses. These observations suggest that base-metal sulfides and/or PGMs dominate and control the PGE budget in the mantle. However, PGE concentrations in base-metal sulfides are strongly variable (<1 ppm to several tens ppm) even within single hand specimens [2], while the modal abundances of PGMs are difficult to determine because PGMs in mantle peridotite are generally extremely small (<<10 μm). Thus, it is still unclear to what extent PGEs in the mantle are hosted by base-metal sulfides and PGMs in the mantle.

In this study, we tried to reveal how abundantly and pervasively PGMs exist in mantle peridotite using X-ray fluorescence analysis combined with the microbeam technique (micro-XRF) at SPring-8. The extremely high brilliance of synchrotron radiation X-ray enables the X-ray beam to penetrate a rock sample up to several thousands μm depths, which is much greater than penetration depths of other nondestructive analytical methods (cf., SEM, a few μm; proton microprobe, a few tens μm). In addition, the high directionality of the synchrotron radiation

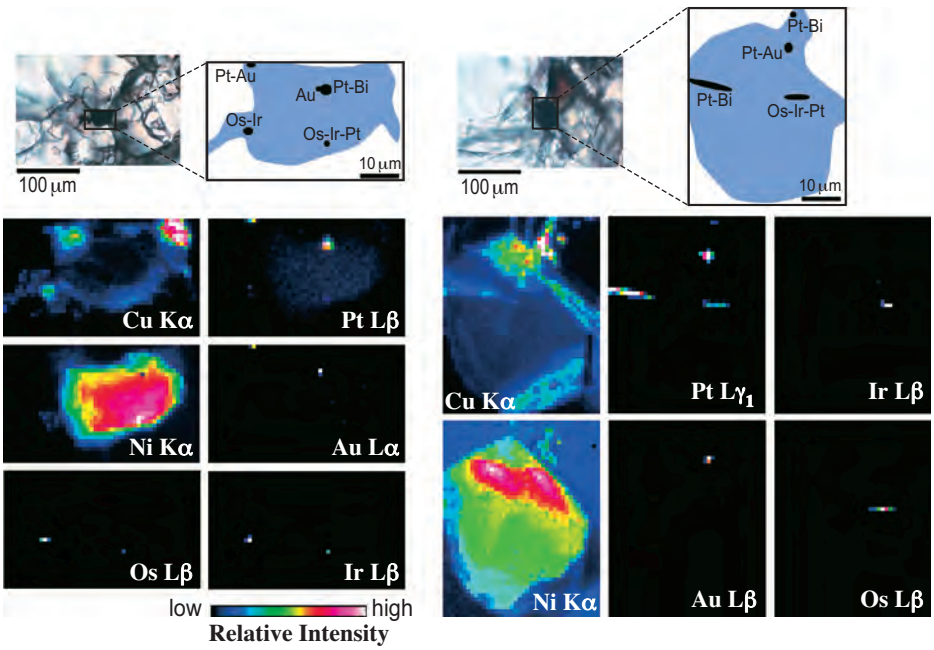

Fig. 1. Distribution maps of Ni, Cu, Au, and PGE in the Fe-Ni-Cu sulfides that include PGE microphases. Colors indicate relative intensities of the fluorescent X-ray lines of each element, which reflect the concentration and thickness distribution of the element. The pixel size of the element maps is 1.0 μm × 1.0 μm (= step size of scan). The locations and element combinations of the PGE microphases are shown as filled ovals in the schematic illustrations. Modified after Ref. [3].

X-ray is suitable for making a sub-micrometer spot size, which is comparable to that of SEM and much smaller than that of LA-ICP-MS analysis. These features enable us to conduct highly efficient "see-through" searches for minerals throughout thick rock samples on a sub-micrometer scale. Using this technique, we were able to find micrometer-scale PGM from the interior of a peridotite sample much more efficiently than with conventional analytical techniques [3].

We analyzed a spinel lherzolite from the Horoman peridotite complex, Japan, at beamlines **BL20XU** and **BL47XU**. The sample consists of a typical depleted lherzolite mineral assemblage with accessory Fe-Ni-Cu sulfides and other opaque minerals. A 150-μm-thick thin section was used for the analysis. For spot analyses, we used an incident beam of 15 keV or 113 keV cut with a slit into 20 μm × 20 μm to 40 μm × 40 μm spot size. For microbeam scanning, we used a 15-keV beam focused with a Fresnel zone plate to 1.0 μm width and 0.65 μm length. The photon fluxes (photons/s) are ~2×10^{10} for the 15-keV broad beam, ~1×10^{7} for the 113-keV broad beam, and 1–2×10^{10} for the 15-keV microbeam.

We first conducted spot analyses of the Fe-Ni-Cu sulfide and spinel grains in the sample with a broad beam. Among the 16 Fe-Ni-Cu sulfides and 8 spinel grains analyzed, we detected emission lines of PGE from two Fe-Ni-Cu sulfides. We then conducted a two-dimensional scan of these two sulfide grains with a 15-keV microbeam, and revealed that PGEs were concentrated in several grains of micrometer-scale phases in each sulfide (Fig. 1). The size of the PGE microphases ranges from ~1 to 10 μm in maximum dimension. Combinations of elements detected in the microphases are Os-Ir, Os-Ir-Pt, Pt-Au, Pt-Bi, and Au (Fig. 2). Some of the element combinations (Pt-Au, Ir-Os, and Ru-Os-Ir) are rare in PGM found in peridotite samples, although all the combinations were reported from ore deposit samples.

The total amounts of PGE in the microphases that we found are estimated to be roughly on the order of 100 pg, assuming that the thicknesses of the microphases are comparable to their minimum dimensions in the two-dimensional map (Fig. 1). This corresponds to ~10% of the PGE budget in the thin section, but this value cannot be applicable to other portions of the sample because of the strong heterogeneity of the PGE microphase distribution. A further increase in the efficiency of this method is necessary for a more accurate estimation of the PGE budget in peridotite samples.

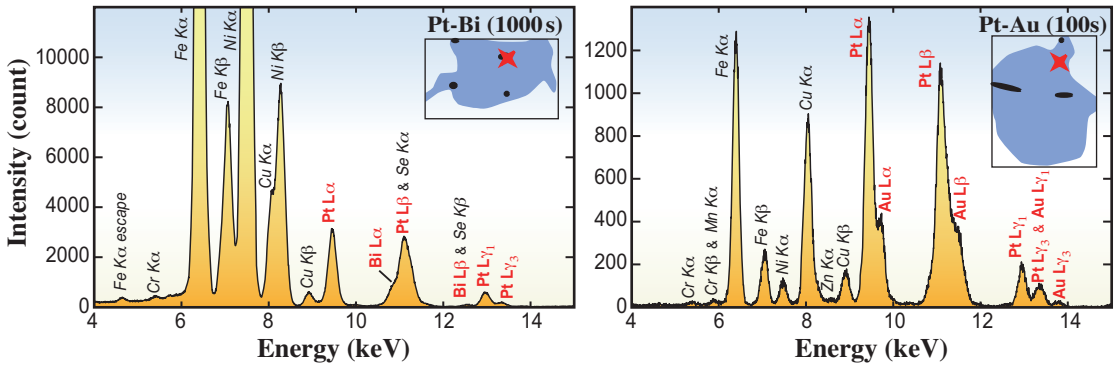

Fig. 2. Examples of fluorescent X-ray spectra of the PGE microphases. Fluorescent X-ray lines from the PGE microphases are labeled with red letters, and those from the host Fe-Ni-Cu sulfides and surrounding silicate minerals are with black letters. The locations of the microphases are shown as red stars in the insets. The acquisition times are shown in each panel. Modified after Ref. [3].

Tetsu Kogiso[a,*], Katsuhiko Suzuki[b] and Toshihiro Suzuki[b]

[a] Graduate School of Human and Environmental Studies, Kyoto University
[b] Institute for Research on Earth Evolution, Japan Agency for Marine-Earth Science and Technology

*E-mail: kogiso@gaia.h.kyoto-u.ac.jp

References

[1] H. Becker *et al.*: Geochim. Cosmochim. Acta **70** (2006) 4528.
[2] O. Alard *et al.*: Nature **407** (2000) 891.
[3] *T. Kogiso, K. Suzuki, T. Suzuki, K. Shinotsuka, K. Uesugi, A. Takeuchi and Y. Suzuki: Geochem. Geophys. Geosyst.* ***9*** *(2008) Q03018, doi: 10.1029/2007GC001888.*

Characterization of a Hard X-Ray Telescope

As in all physical experiments, instrument calibration has a crucial importance in astronomy. Especially in space astronomy, instruments are aboard orbiting satellites to avoid an atmospheric extinction of radiation from celestial objects. Therefore, instruments must be calibrated accurately and precisely before launch. This is because, obviously, there is very little chance to calibrate and tune instruments after they are launched into space. This research aims to develop a calibration technology for a newly developed astronomical instrument, hard X-ray focusing mirrors, which is only possible at a large synchrotron facility, SPring-8. The major part of this article is described in detail by Ogasaka *et al.* [1].

The recent progress in X-ray optics technology has realized the "hard X-ray focusing telescope," which utilizes reflective optics to focus X-rays above 10 keV. At such high energy, an effective optics is difficult to construct with ordinary total external reflection mirrors. Instead, multilayer mirrors are used, which utilize Bragg's reflection by the artificially layered structure of heavy (reflecting) and light (spacer) materials. Figure 1 shows a picture of the hard X-ray mirror developed for the balloon-borne observation experiment called SUMIT. The SUMIT hard X-ray mirror consists of 199 pairs of ultra-thin (0.2 mm thickness) Wolter-I optics, whose surfaces are coated with depth-graded Pt/C multilayers. Its energy bandpath reaches 80 keV, about an order-of-magnitude improvement compared with previous mirrors.

The multilayer hard X-ray mirror is considered a promising technology for future X-ray astronomical research. To fully utilize its new performances, however, the mirror must be calibrated before launch, primarily, to characterize its performance and, secondarily, to construct response matrices that are crucially important for data analysis. To perform a comprehensive characterization of hard X-ray mirrors, an experiment setup has been established at **BL20B2**, one of the medium-length beamlines at SPring-8. The advantages of the experiment at BL20B2 are high intensity of the X-ray beam and large distance to the X-ray source. As the separation between the X-ray source and sample to be measured increases, the beam divergence decreases, but the beam intensity decreases as well. At a synchrotron facility such as SPring-8, however, the source intensity is high enough to compensate it.

Fig. 1. Hard X-ray mirror on board SUMIT balloon experiment. 199 pairs of conically approximated Wolter-I optics are nested coaxially. Aperture diameter, mirror length, and focal length are 40 cm, 26 cm, and 8 m, respectively.

The experiment first took place in 2003, when the hard X-ray mirror for the US-Japan collaborative balloon experiment InFOCuS was tested. Since then, the experiment setup and measurement technologies have been upgraded through calibration of InFOCuS and the Japan-Brazil collaboration balloon experiment SUMIT. Initial results of these experiments are summarized in Ref. [1].

At BL20B2, we are now able to measure key parameters such as effective area, which is crucial to derive the X-ray flux of the observed object, and a point spread function (PSF), which is an intrinsic image blur of the optics and is relevant to analyze the spatial structure of the objects. Figure 2 shows a picture of the InFOCuS X-ray mirror placed at hutch 2 of BL20B2 and an example of a focused image (PSF) measured. In addition, the focusing characteristics of individual reflectors are also evaluated by restricting the area of X-ray illumination. Such measurements are considered as a "diagnostics" to understand the source of the image blur and decrease in effective area, and are only possible using a bright synchrotron light source.

One of the outputs from the experiment is the establishment of an "X-ray optical tuning" method. By this method, we can reduce the image blur by iteratively tuning the optics by looking at the focused image. When the X-ray mirror is assembled, there still are errors in the mechanical positions of reflectors owing to the limited accuracy of machining and assembling. Such uncertainties, on the order of a few to a few tens of μm, cause image blur, so they need to be corrected. They are measureable by analyzing an error in the focused image. We have established a method to derive mechanical error from the focused image and to correct it. Details of the optical tuning are described by Ogasaka *et al.* [2] and references therein.

Figure 3 explains how the optical tuning is performed. In this case, positional errors of radial support bars are corrected. Such errors cause off-roundness in the focused image and change in the

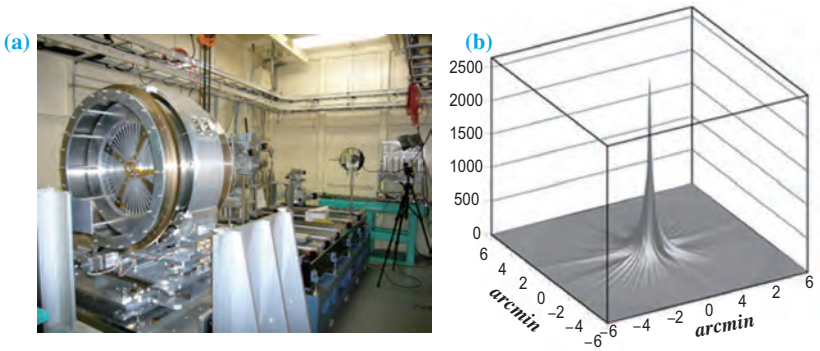

Fig. 2. **(a)** Photograph of InFOCuS hard X-ray mirror mounted on the 5-axis sample positioning stage placed at hutch 2 of BL20B2. **(b)** Example of a measured focused image of InFOCuS mirror. Data was taken at 30 keV. The half power diameter of the image is about 2 arcmin.

focal length. We derive the amount of adjustment to correct them through the image analysis, and then apply the adjustment. Figure 4 shows focused images of the SUMIT hard X-ray mirror measured at 30 keV, before and after the optical tuning. It took us several iterations before obtaining the final result. The image quality was improved from 2.4 to 2.0 arcmin (HPD: half power diameter). In terms of off-roundness, the error was reduced from 1.4 to 0.3 arcmin (HPD equivalent), which means that the off-roundness was almost completely eliminated. A more qualitative discussion is found in Ref. [2]. The optical tuning requires a rapid measurement of the focused image. In our case, it takes only about 4 h for one iteration (measurement and tuning), while it has been almost a day or even more without bright synchrotron light.

Japan's X-ray astronomy community is currently developing the next generation X-ray observatory ASTRO-H. It is a national mission initiated by JAXA and is scheduled for launch in FY2013 [3]. ASTRO-H will have two multilayer hard X-ray telescope systems to carry out new astrophysical research such as exploration of hidden black holes at the core of galaxies or study of the particle acceleration mechanism in the universe. The ground calibration of ASTRO-H hard X-ray mirrors will take place at BL20B2.

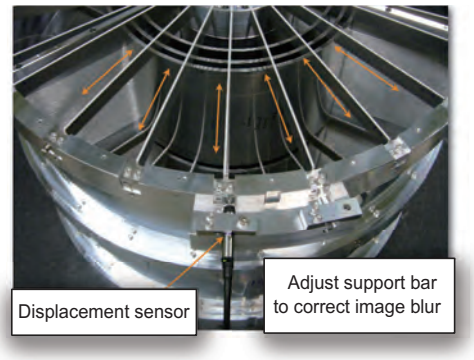

Fig. 3. Hard X-ray mirror under optical tuning. In this case, the positions of radial support bars are tuned. A displacement sensor is attached at the outer end of the radial bar to measure the adjusted amount.

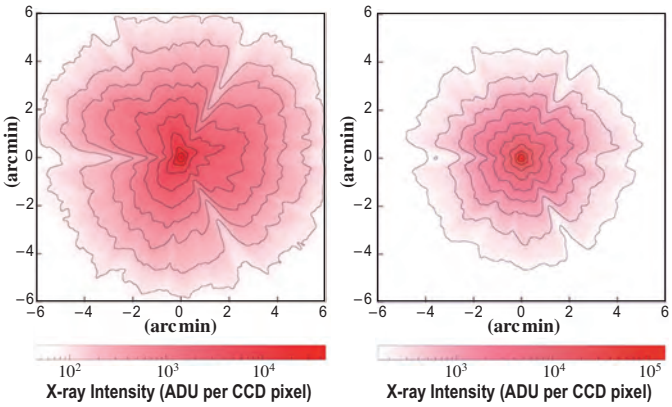

Fig. 4. Focused image of a hard X-ray mirror measured at 30 keV. The gray scale shows focused intensity on a logarithmic scale between 0.25 and 100% peak intensity. The contour interval is logarithmically constant over the same range. The left panel shows the image taken before the tuning, whereas the right panel shows that taken after the tuning. The off-roundness error was reduced from 1.4 to 0.3 arcmin, and the image HPD was from 2.4 to 2.0 arcmin.

Yasushi Ogasaka

Japan Science and Technology Agency

E-mail: ogasaka@u.phys.nagoya-u.ac.jp

References

[1] *Y. Ogasaka, K. Tamura, R. Shibata, A. Furuzawa, T. Miyazawa, K. Shimoda, Y. Fukaya, T. Iwahara, T. Nakamura, M. Naitou, Y. Kanou, N. Sasaki, D. Ueno, T. Okajima, E. Miyata, N. Tawa, K. Mukai, K. Ikegami, M. Aono, K. Uesugi, Y. Suzuki, S. Takeuchi, T. Futamura, R. Takahashi, M. Sakashita, C. Sakai, M. Nonoyama, N. Yamada, K. Onishi, T. Miyauchi, Y. Maeda, S. Okada, P. Serlemitsos, Y. Soong, K.-W. Chan, S. Rohrbach, F. Berendse, J. Tueller, H. Tsunemi, H. Kunieda and K. Yamashita: Jpn. J. Appl. Phys.* ***47*** *(2008) 5743.*
[2] Y. Ogasaka *et al.*: Proc. SPIE **7011** 70110P-1.
[3] http://astro-h.isas.jaxa.jp/

Environmental

"Momiji" - *Japanese maple*

SCIENCE

Environmental science encompasses various research fields, such as environmental problems, geochemistry and environmental enhancement using new techniques or functional materials. X-ray analytical methods using synchrotron radiation, such as X-ray absorption fine structure (XAFS) and X-ray diffraction (XRD), are powerful tools for the speciation of environmental samples, since, in many cases, they are very dilute, small in quantity, or spatially and chemically-inhomogeneous. Recently, newly developed techniques, such as *in situ* micro-XAFS methods, have further accelerated studies of environmental samples from their speciation to the elucidation of the mechanisms behind various environmental phenomenon, such as formation, accumulation, pollution, and leaching.

Topics selected in this section relate to health hazards and environmental protection. The first two topics concern harmful elements and compounds from artificial products. Takahashi *et al*. studied the leaching of Sb, a harmful element, from PET bottles produced in China and Japan into beverages by clarifying the chemical state of Sb in PET by XAFS. They showed that the degradation of PET itself is more important in Sb leaching rather than the chemical state of Sb in PET bottles.

In the second topic, Takaoka *et al*. studied the formation mechanism of toxic chlorinated aromatic compounds (aromatic-Cls) in waste incinerators during thermal processes by specifying the atomic speciation of copper in fly ash using XAFS and XRD. They found the direct chlorination of carbon by copper to be the key reaction in the creation of the aromatic-Cls, and then suggested that the mechanical or chemical elimination of the inflow of copper to thermal facility may inhibit the creation of aromatic-Cls.

In the last topic, Mitsunobu *et al*. studied the interaction of Sb with an abiotic contaminant reducer in an aquatic environment, Green Rust compounds (GR), by XAFS. They showed that the adsorption of Sb to GR with the formation of an inner-sphere complex stabilized the interaction between GR and Sb.

Tomoya Uruga

Speciation of Antimony in PET Bottles Produced in Japan and China by X-Ray Absorption Fine Structure Spectroscopy

Antimony (Sb) has been frequently used as a catalyst of polycondensation reaction to produce polyethylene terephthalate (PET). As a result, Sb is incorporated into some PET bottles used for beverages at concentrations of 100 to 300 mg/kg. Considering its high toxicity [1], the possible leaching of Sb into beverages is of great concern, which has motivated various studies of Sb content in PET bottles and Sb leaching into beverages [1]. In addition, the effects of pH, water temperature, elapsed time, and other factors on Sb leaching have also been examined [1,2]. In addition, the effect of beverage type in PET bottles has been studied especially in terms of the complexation effect of Sb with ligands in the liquid (such as citrus juice or acetic acid) that may enhance Sb leaching. However, there have been no studies dealing with the direct characterization of Sb species in PET so far, such as the oxidation state and local structural environment around Sb, which can be associated with its leaching into the liquid, as seen from the Sb behavior in the natural environment [3]. Since Sb is initially added as Sb_2O_3 in the production of PET, the possible oxidation of Sb(III) should be verified considering that the leaching behavior of Sb may depend on its oxidation state.

Considering the relatively scarce knowledge of the chemical state of Sb in PET, this study employed X-ray absorption fine structure (XAFS) to obtain Sb atomic scale information [4]. XAFS spectroscopy consisting of X-ray absorption near-edge structure (XANES) and extended X-ray absorption fine structure (EXAFS) give independent information such as the oxidation state and local structure of Sb (= coordination number and bond lengths to neighboring atoms), respectively. Although XAFS has been employed in various environmental studies [3,5], its application to the speciation of Sb in PET has not yet been reported. Thus, PET bottles collected in China and Japan have been used for XAFS measurement. In addition, leaching experiments have been done to investigate the possible relationship between the difference in the chemical state of Sb in PET and Sb leachability in water.

Prior to XAFS, Sb concentration has been determined in 105 and 72 brands of PET bottles sold in Japan and China, respectively. A relatively high content of Sb (170 – 220 mg/kg) has been reported for PET bottles in Japan; this has not been documented for those in China. It was also found that 30.5% and 100% of Japanese and Chinese PET bottles, respectively, contained more than 10 mg/kg of Sb (Fig. 1(a)). Generally, PET bottles can be classified into five to six types depending on their use: (A) bottles for aseptic cold filling mainly used for noncarbonated cold drinks; (B) pressure-tight bottles for carbonated drinks; (C) heat-resistant and pressure-tight bottles for semi-sparkling drinks; (D) heat-resistant bottles for hot filling like those hot tea; and (E) bottles for freezing. When the results were confined to Japanese PET bottles, it was found that most of the PET bottles categorized into types A and B contained Sb at more than 150 mg/kg (Fig. 1(b)). In addition, about half of the type C bottles also contained large amounts of Sb.

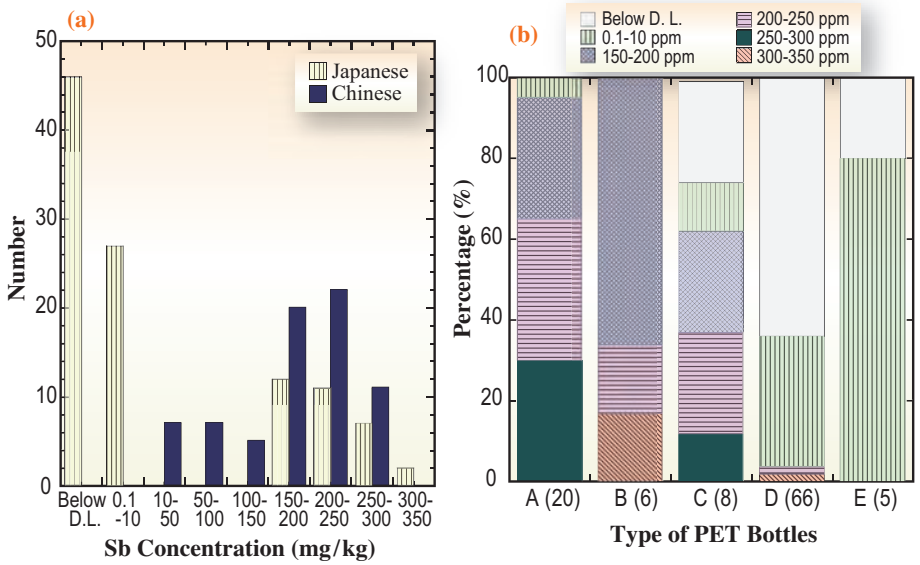

Fig. 1. **(a)** Concentrations of Sb in PET bottles sold in Japan and China. **(b)** Concentrations of Sb in PET bottles in Japan for various uses. (A) bottles for aseptic cold filling normally used for noncarbonated cold drinks; (B) pressure-tight bottles for carbonated drinks; (C) heat resistant and pressure tight bottles for semi-sparkling drinks; (D) heat resistant bottles for hot filling such as those for hot tea; and (E) bottles for freezer. Numbers in parentheses indicate the number of samples for each type. D.L. means detection limit.

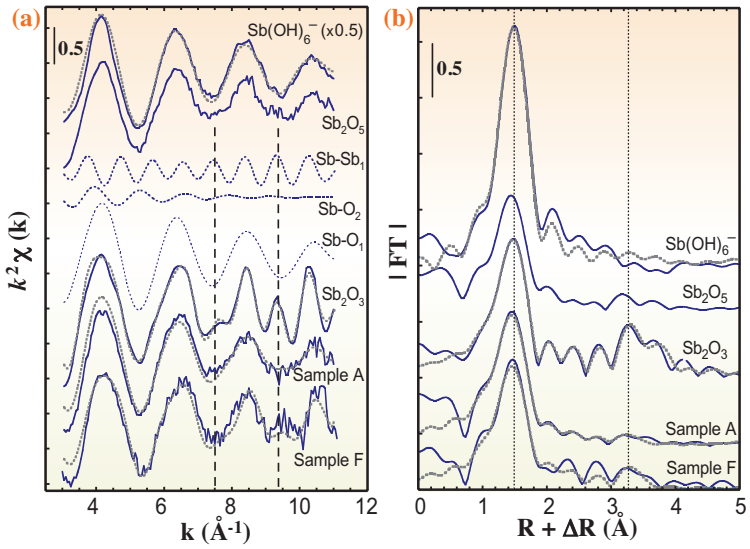

Fig. 2. EXAFS spectra at Sb *K*-edge for Sb in PET samples (A and F) in k space (**a**) and R space (**b**). Gray curves indicate the simulation results. Contributions of Sb-O_1, Sb-O_2, and Sb-Sb_1 in the spectrum of Sb_2O_3 in k space were also indicated.

The oxidation state and coordination environment of Sb incorporated into the PET bottles were estimated by XAFS at the Sb *K*-edge at beamlines **BL01B1** and **BL37XU**. Results of the EXAFS of Sb in PET bottles were interpreted by assuming that the nearest-neighbor atom of Sb is either carbon or oxygen (Fig. 2). On the basis of the possible bond lengths of Sb-O and Sb-C, it was shown that the first neighboring atom of Sb in PET was estimated to be oxygen with a coordination number of about three. In addition, the contribution of Sb to Sb shells was discounted in the EXAFS, showing that Sb was not present as Sb_2O_3 in PET, although Sb was initially added as Sb_2O_3 in PET production. This information is consistent with the coordination environment estimated from the polycondensation reaction catalyzed by Sb, where Sb can be present as either Sb glycolate or Sb glycolate binding to the end group of the PET polymer.

Antimony *K*-edge XANES showed that the Sb(III) initially added as Sb_2O_3 into PET was partially oxidized, and, that the Sb(V) fractions reached approximately 50% in some samples (Fig. 3). However, the oxidation state and coordination environment of Sb in PET had no relationship with the concentration of Sb that leached into water from PET. This conclusion is supported by Westerhoff *et al.* [2] who showed the effects of pH, temperature, and sunlight on Sb leaching. First, the acidification did not increase the Sb concentration in their study. If the Sb release is a function of inorganic Sb(III) fraction that has lower solubility at higher pH, then Sb leaching can be a function of pH, which is not the case for Sb leaching in PET [2]. On the other hand, higher temperature and sunlight enhanced the release of Sb. It is most likely that temperature and sunlight can facilitate the degradation of PET itself. Based on this information coupled with the speciation of Sb in PET observed in this study [4], the degradation of PET itself is more important for Sb leaching rather than Sb speciation in PET bottles.

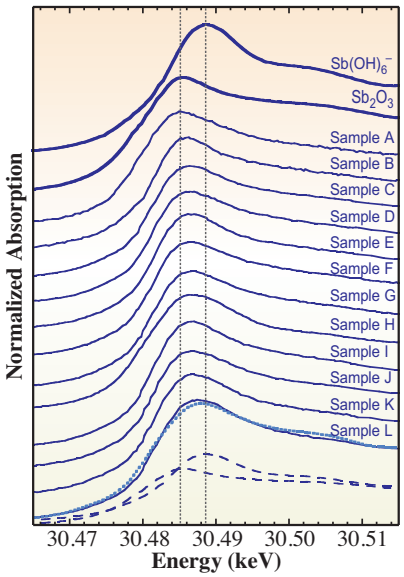

Fig. 3. XANES spectra at Sb *K*-edge for Sb in various PET samples (A – L) with those for Sb_2O_3 and $Sb(OH)_6^-$. The presence of both Sb(III) and Sb(V) at various Sb(III)/Sb(V) ratios is suggested. The simulation result is shown for Sample L with the contributions of Sb(III) and Sb(V) indicated by the broken curves.

Yoshio Takahashi

Department of Earth and Planetary Systems Science, Hiroshima University

E-mail: ytakaha@hiroshima-u.ac.jp

References

[1] W. Shotyk and M. Krachler: Environ. Sci. Technol. **41** (2007) 1560.
[2] P. Westerhoff *et al.*: Water Res. **42** (2008) 551.
[3] S. Mitsunobu *et al.*: Environ. Sci. Technol. **40** (2006) 7270.
[4] *Y. Takahashi, K. Sakuma, T. Itai, G. Zheng and S. Mitsunobu: Environ. Sci. Technol. **42** (2008) 9045.*
[5] Y. Takahashi *et al.*: Environ. Sci. Technol. **38** (2004) 1038.

Synchrotron X-Ray Spectroscopic Evidence of Dioxin Formation Mechanism in Solid Waste Incinerator – Direct Chlorination of Carbon by Copper Chloride –

Thermal processes are a major anthropogenic source of chlorinated aromatic compounds (aromatic-Cls, see I in Fig. 1 or Fig. 2) such as dioxins and PCBs. Many of them are toxic to both humans and wildlife. Therefore, understanding the mechanisms of the formation of aromatic-Cls in solid waste incinerators is necessary in order to control the emission of aromatic-Cls. Ash collected from the postcombustion zone, called fly ash, has high concentrations of aromatic-Cls. Unburned carbon and chlorine sources in fly ash and surrounding oxygen are essential factors for aromatic-Cl formation. In addition, trace metal compounds in fly ash promote aromatic-Cl formation. Copper in particular has a strong potential, and its chlorination mechanism has been proposed by various researchers. However, limited experimental data to support the predicted behavior of copper at the atomic level have been acquired. Although X-ray absorption spectroscopy has recently been used to monitor the redox change of copper in fly ash upon heating [1], the atomic environment of copper has not yet been clarified fully and little direct evidence exists to clarify the formation mechanism of aromatic-Cls with copper at the atomic level and to describe the chlorination mechanism in detail. In this work [2], we determine the behavior of copper in fly ash.

To examine the behavior of copper, we prepared a model fly ash (MFA) consisting of a mixture of copper(II) chloride dihydrate ($CuCl_2 \cdot 2H_2O$), activated carbon (AC), and boron nitride (BN) containing 1.9% Cu, 2.0% Cl, 5.0% AC; the remaining 91.1% was almost entirely BN. After the MFA was ground, 200 mg was pressed into a disk. Cu *K*-edge XAFS was performed at beamline **BL01B1**. The MFA disk was heated in a T-type cell [1] for *in situ* experiment. The temperature of the sample was increased gradually from room temperature to 400°C. A 10% O_2 (90% N_2) gas simulating the condition of the postcombustion zone was introduced from the inlet of the T-type cell at 50 mL/min and exhausted from the outlet. The energy area from 8730 to 9820 eV of Cu *K*-edge extended X-ray absorption fine structure (EXAFS) could be measured within 2.5 min by a quick scan mode. The EXAFS spectra of a MFA disk were collected in the transmission mode with a Si(111) monochromator. The chemical forms in the MFA were determined by powder X-ray diffraction analysis using synchrotron radiation (SR-XRD) at beamline **BL02B2**. The MFA was packed in a quartz capillary column and sealed.

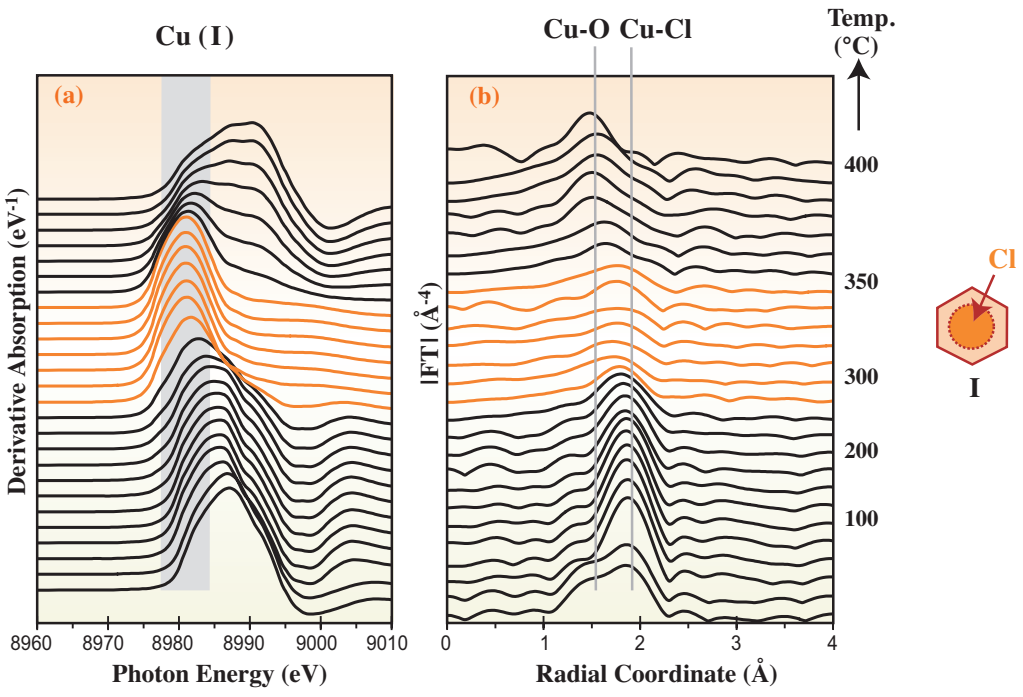

Fig. 1. Derivative Cu-K XANES spectra (a) and Fourier-transformed spectra (b) at each temperature during heating MFA. Maximum amounts of chlorinated aromatic compounds (I) were generated at 300-350°C.

We placed the capillary in the Debye-Scherrer camera for SR-XRD measurement. The capillary was heated using N_2 gas from room temperature to 400°C, and SR-XRD patterns were recorded.

Dynamic changes in the forms of copper in the MFA were clearly observed by X-ray absorption and diffraction analysis using synchrotron radiation (Figs. 1 and 2). The difference in copper form was caused by the reduction of copper near 300°C and the maintenance of its chemical form even at around 350°C as follows: The energy point of the first maximum in the derivative of the Cu *K*-edge XANES spectrum (called the "edge") can provide information on the redox state of copper (Fig. 1(a)) [3]. The edge position changed to 8981.0 eV around 300°C, and the valence of copper was shown to be lower than that of Cu(II) by comparing the edges of reference materials. Therefore, copper was reduced from Cu(II) to Cu(I) or Cu(0). The coordination number of the first shell of Cu-Cl decreased by 1.5±0.3 between 310 and 350°C with half of the $CuCl_2$ form at 100°C, and the atomic distance was shortened by 2.19±0.02 Å compared with that in $CuCl_2$ at 100°C, according to analysis of the EXAFS spectra (Fig. 1(b)). On the basis of the SR-XRD pattern, CuCl was clearly identified from 275 to 350°C (Fig. 2). We conclude that most $CuCl_2$ within the carbon matrix dechlorinated to CuCl at around 300°C and maintained this state up to about 350°C. The C-Cl bond was derived from the dechlorination of copper because the only chlorination source in the MFA was copper(II) chloride, i.e., the direct chlorination of carbon by copper occurred and the aromatic-Cl concentration reaches its maximum in the fly ash. Eliminating the inflow of copper to thermal facilities or chemically inhibiting copper at the atomic level might decrease the creation of aromatic-Cls by thermal processes and thus have beneficial effects on the environment and human health.

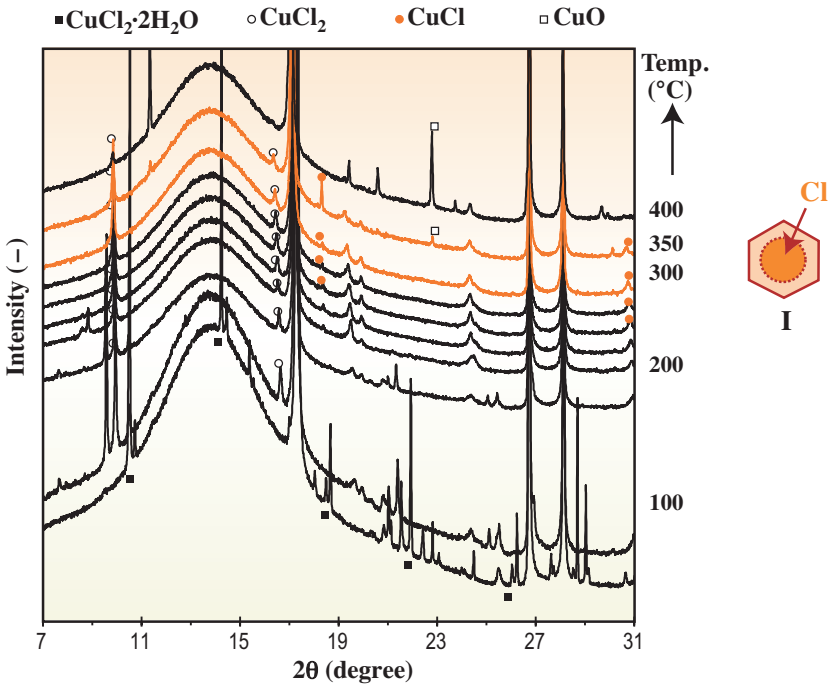

Fig. 2. SR-XRD patterns at each temperature during heating of MFA. Maximum amounts of chlorinated aromatic compounds (I) were generated at 300-350°C.

Masaki Takaoka* and Takashi Fujimori

Department of Urban and Environmental Engineering, Kyoto University

*E-mail: takaoka@environ.mbox.media.kyoto-u.ac.jp

References

[1] M. Takaoka *et al.*: Environ. Sci. Technol. **39** (2005) 5878.
[2] *T. Fujimori and M. Takaoka: Environ. Sci. Technol.* ***43*** *(2009) 2241.*
[3] T. Fujimori *et al.*: X-ray Spectrom. **37** (2008) 210.

Antimony Interaction with an Abiotic Reducer in Aquatic Environment: Green Rust Compounds

Antimony (Sb) is toxic and its compounds are considered pollutants of priority interest by the United States Environmental Protection Agency and European Union. Sb belongs to group 15 of the periodic table and can exist in multiple oxidation states. The Sb oxidation states frequently observed in the natural environment are Sb(III) and Sb(V). The characteristics of Sb in the environment such as solubility and sorption behavior on natural solids depend on its oxidation state. Moreover, the toxicity of Sb also depends on its oxidation states; Sb(III) compounds have 10 times higher acute toxicity than Sb(V) [1]. Thus, it is essential to determine the oxidation state of Sb in environmental samples to estimate and evaluate its fate. Recently, Sb compounds has been widely used (100 000 tons annually worldwide) for many industrial materials (e.g., flame retardants and catalysts for plastic production, fining agents for glassware, and pigments in paints). However, the geochemical and environmental behaviors of Sb in natural soils and sediments remain largely unknown.

Fe(II)-Fe(III) layered double hydroxides, called green rust (GR), have a brucite-like structure (Fig. 1), which also alternated with interlayer anions (e.g., SO_4^{2-}, CO_3^{2-} and Cl^-) and water molecules [2]. GR compounds are formed by a number of abiotic and biotic processes under circumneutral to alkaline conditions in a suboxic environment (Fe(II)/Fe(III) transition zone). Recently, in samples taken from hydromorphic soil and groundwater, GR has been identified as a natural mineral [3]. A number of studies of GR interaction with inorganic and organic contaminants have shown that GR can reduce many contaminants including chromate, selenate, uranyl, nitrate, and halogenated ethanes (e.g., [4]). Owing to its high reactivity and rapid reduction rate, GR has been newly considered as a remarkable solid in nature. GR may affect the fate and transport of environmental toxins including Sb. To our knowledge, there have been no studies yet of the interaction of Sb with GR, and little is known about the sorption mechanism and reduction potential of any GRs for Sb. Thus, the objectives of the present study are to investigate the interaction of Sb with GR using a atomic-scale speciation method, XAFS. On the other hand, GR is a "metastable" mineral that gradually transforms to other Fe hydroxides such as magnetite (Fe_2O_3) and lepidocrocite (γ-FeOOH). Moreover, the presence of some anions in GR kinetically slows down the rate of transformation, indicating that GR is stabilized by anions. Since Sb(V) dominantly occurs as a monovalent hydroxide anion, $Sb(OH)^V{}_6^-$, at pH > 2.5, Sb(V) may have a similar special effect on other anions. Therefore, we also investigate the stabilization effect of Sb on GR transformation.

We studied the interaction of Sb with GR by batch sorption experiment with various initial concentrations of Sb(V). The GR for the experiment was synthesized by the air oxidation of ferrous sulfate solution at neutral pH. The batch experiment was carried out in an anoxic glovebox purged with N_2 gas. After shaking for 24 h at 25°C at pHs of 8.0±0.2, solid samples were collected

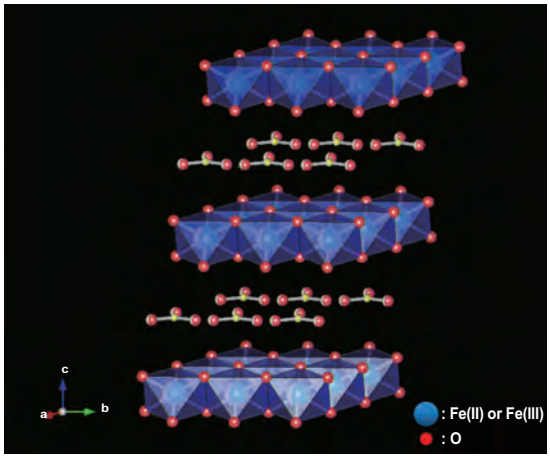

Fig. 1. Structure of green rust. Sulfate, carbonate, and chloride anions generally alternate in the interlayer.

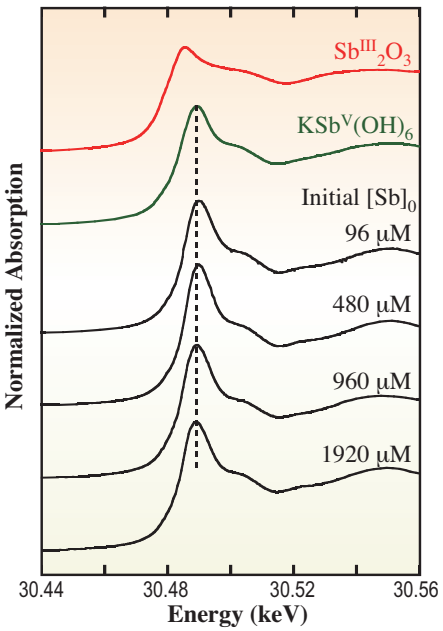

Fig. 2. Normalized Sb *K*-edge XANES spectra of the reference materials (Sb_2O_3 and $KSb(OH)_6$) and collected solids in which Sb is adsorbed at various initial concentrations. A dotted line is drawn to indicate the absorption maximum of Sb(V), $KSb(OH)_6$.

by filtration for further analyses. Antimony and iron (Fe) *K*-edge XAFS spectra were measured at beamline **BL01B1** in the fluorescence mode to determine the oxidation states of Sb and Fe, surface complexes of Sb on the solids, and mineral species of the solids.

The normalized Sb *K*-edge XANES profiles (Fig. 2) show that the adsorption edge of the solid samples were similar to that of $KSb^{V}(OH)_6^-$, indicating that Sb in the samples was predominantly Sb(V). This suggests that GR does not work as a strong reductant in the natural environment. The local structure of Sb in solids was examined by EXAFS to obtain information on the surface complexes of Sb adsorbed on GR. In the Fourier transformation (FT, Fig. 3), two backscattering peaks were consistently observed at 1.5 and 2.8 Å (phase-shift-uncorrected), respectively, at all initial Sb concentration. The simulation results showed that the first peak in FT was due to the Sb-O coordination (coordination number, nearly 6; bond distance, 1.98 Å). The second peak was fitted with one Fe atom at a distance of 3.07 Å. These findings clearly indicates that Sb(V) is adsorbed on GR with an edge-sharing inner-sphere complex. In addition to the speciation of sorbed species, the mineral phase in the Sb(V)-GR system was also characterized using Fe *K*-edge XANES (Fig. 4). A simulation of Fe XANES using reference materials was conducted to determine the GR abundance in the solid samples. Sulfate GR is transformed into $Fe(OH)_2$ and magnetite even under an anoxic condition for a relatively short time. At all initial Sb concentrations, the abundance of GR was significantly larger than that of the control (=system without Sb(V)). Moreover, the GR abundance increased with increasing initial Sb concentration. Therefore, these findings suggest that Sb has a stabilizing effect on GR transformation and that the stability of GR depends on the Sb concentration in the range used in the present study. The present study first demonstrates that GR can be stabilized in the presence of Sb. A similar effect on GR has been reported in other oxyanions (i.e., phosphate, arsenate, and silicate) adsorbed to GR with the formation of an inner-sphere complex. Thus, it is suggested that the inner-sphere complex of Sb in GR (confirmed by EXAFS analysis) strongly contributes to the stabilization of "metastable" GR by Sb [5].

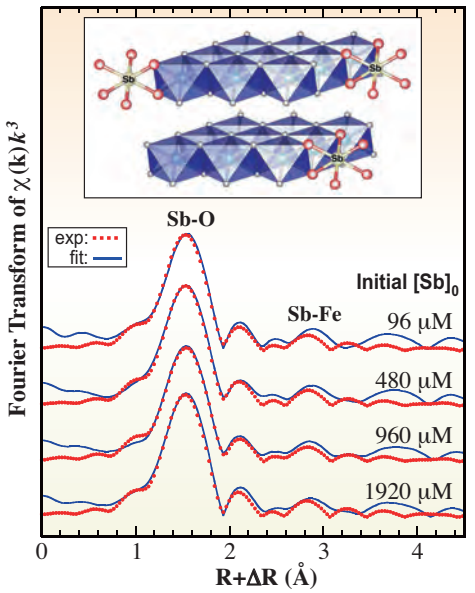

Fig. 3. Fourier-transformed EXAFS spectra of solid samples collected in Sb(V)-GR system (lower) and schematic figure of binding structure of Sb in GR proposed on the basis of results of EXAFS analysis (upper).

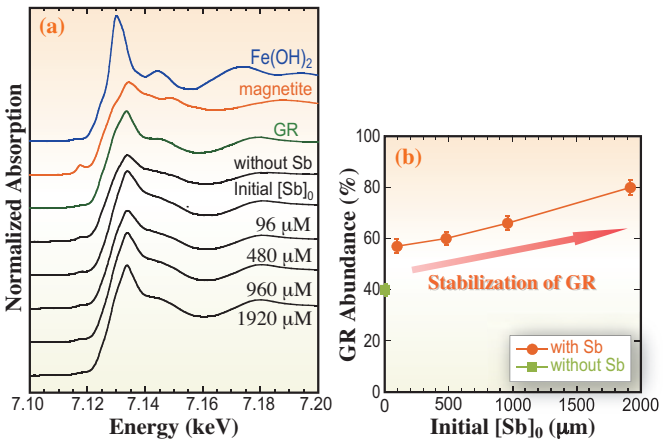

Fig. 4. **(a)** Normalized Fe *K*-edge XANES spectra of the reference materials, collected solids in Sb-GR systems, and control (system without Sb). **(b)** GR abundances of collected solids from Sb-GR system and control samples obtained by simulation of Fe *K*-edge XANES.

Satoshi Mitsunobu[a,*] and Yoshio Takahashi[b]

[a] Institute for Environmental Sciences, University of Shizuoka,
[b] Department of Earth and Planetary Systems Science, Hiroshima University

*E-mail: mitunobu@u-shizuoka-ken.ac.jp

References

[1] M. Krachler *et al.*: Trends Anal. Chem. **13** (2001) 79.
[2] G. W. Brindley *et al.*: Nature **263** (1976) 353.
[3] B. C. Christiansen *et al.*: Environ. Sci. Technol. **43** (2009) 3436.
[4] S. C. B. Myneni *et al.*: Science **278** (1997) 1106.
[5] *S. Mitsunobu, Y. Takahashi, Y. Sakai, and K. Inumaru: Environ. Sci. Technol.* ***43*** *(2009) 318.*

Industrial


"Tanpopo" - *Dandelion*

Recently, SPring-8 has had a good track record in developing industrial applications in various fields, such as electronics, materials, energy, chemical and environment-related companies, that is, in 2008, nearly 300 research proposals were accepted from industries and SPring-8 was used by nearly 190 companies. This means that the utilization of SPring-8 has already become common in a wide range of industrial fields. The most important factor contributing to our success in attracting a wide range of industries is the implementation of various utilization propulsion programs at public beamlines, which have been continuously improved. From 2007, JASRI implemented a new utilization propulsion program at public beamlines: the Priority Research Proposal (priority field: industrial application). In this program, for example, applications can be submitted 4 times a year for the use of the three public beamlines dedicated to industrial research in order to match research development cycles.

In the present issue, eight topics chosen to represent the outstanding work carried out in Industrial Applications. Although most users of industrial applications had previously belonged to the field of electronics, many researchers from other industrial fields, such as those involving metals, ceramics, concrete materials, fuel cells, hydrogen storage materials, polymers, cosmetics, hair care, and foods are now joining SPring-8. The topical experiments introduced here were performed using the following techniques: X-ray reflectivity (XRR; BL46XU and BL24XU),

APPLICATIONS

grazing-incidence X-ray diffraction (GIXD; BL46XU, BL19B2, and BL13XU), powder X-ray diffraction (BL19B2), microbeam X-ray diffraction (BL40XU), dispersive XAFS (BL14B1 and BL28B2), and nano-XAS photoemission electron microscopy (PEEM; BL17SU).

Two excellent studies from next-generation Si LSI fields were selected this year as research frontiers of 2009: the depth distribution of acid generators in chemically amplified resists and the strain effect on the oxidation kinetics at the interface between dense and thin interfacial transition layers using XRR. Also, three studies from electronic device fields were selected. GIXD was applied to understand the alignment mechanism of liquid crystal on alignment film and the organic semiconducting ultrathin film crystal structure. The voltage-induced nonvolatile resistance switching mechanism was investigated by nano-XAS PEEM. The number of studies in the catalysis field is now increasing because of growing concern on global environmental problems. One of the topics is a catalytic reaction study on Pd particles using dispersive XAFS. The last two topics are related to food, clothing and housing: the formation mechanism of tobermorite under a hydrothermal reaction atmosphere, investigated using *in situ* X-ray diffraction (XRD) and tooth enamel microstructural evaluation using microbeam XRD.

Yoshio Watanabe


"Mokusyungiku" - *Marguerite*


"Dokudami" - *Houttuynia*

X-Ray Reflectivity Study on Depth Profile of Acid Generator Distribution in Chemically Amplified Resists

In the last half-century, integrated circuits have decreased in size at a remarkable speed with the progress in fabrication techniques. Their critical dimensions are still continuing to decrease in size. 22 nm patterns with line width roughness smaller than 2.2 nm are expected within 5 years. The exposure source for this sub-30 nm dimension is predicted to be extreme ultraviolet (EUV) radiation, where chemically amplified resists will be used to meet the sensitivity requirement for the mass production of semiconductor devices (Fig. 1). Chemically amplified resists, which consist of an acid generator and an acid-reactive polymer, utilize acid catalytic reactions for sensitivity enhancement. With the reduction in lateral dimension, the resist thickness has also been reduced and is projected to be 35 – 65 nm at the 22 nm node, according to the International Technology Roadmap for Semiconductors published by the Semiconductor Industry Association.

Below 100 nm thickness, the effects of resist interfaces become increasingly important. Surface effects such as acid generator segregation, T-top shape caused by an insoluble surface layer, and film loss during development have been reported. In addition to these factors common to deep UV (DUV), EUV, and electron beam (EB) resists, a strong absorption has to be taken into account in EUV resists. The absorption coefficient of typical polymers for EUV resists is approximately 4 μm^{-1}, which is 4 times higher than those of DUV resists and higher beyond comparison than those of EB resists. In addition, the enhancement of resist absorption has been proposed for the efficient use of the EUV energy. Therefore, the side wall profiles of patterned resists are a significant concern for EUV resists, which are affected by the depth profile of acid generator distribution.

In EUV resists for 22 nm patterning and below, a high concentration of acid generators is required [1]. When EUV photons enter resist materials, molecules are ionized and photoelectrons are emitted. The photoelectrons further induce ionization and generate secondary electrons. These secondary electrons sensitize acid generators. To suppress resolution blur caused by the secondary electron migration, the increase in the acid generator concentration is effective up to 30 wt%. In the development of EUV resists, the trade-off relationships among resolution, line edge roughness (LER), and sensitivity are the most serious problems. The enhancement of pattern formation efficiency is an essential solution to the trade-off problem. The increase in the acid generator concentration is also an effective method for enhancing the pattern formation efficiency. However, the increase in the acid generator concentration is likely to degrade the uniformity of acid distribution. Thus, the depth profile of acid generator distribution is an important issue for the development of EUV resists. The depth profile has been investigated by time-of-flight secondary ion mass spectrometry (TOF-SIMS) [2]. However, the depth resolution of TOF-SIMS is inadequate for its application to resist thicknesses corresponding to next-generation lithography. In this study, we have investigated the depth distribution of acid generators using X-ray reflectivity measurements [3-5].

Partially protected poly(4-hydroxystyrene) (PHS) was used as a model polymer of chemically amplified EUV resists. A tert-butyl (tBu) group was chosen as a protecting group to prevent the deprotection of the

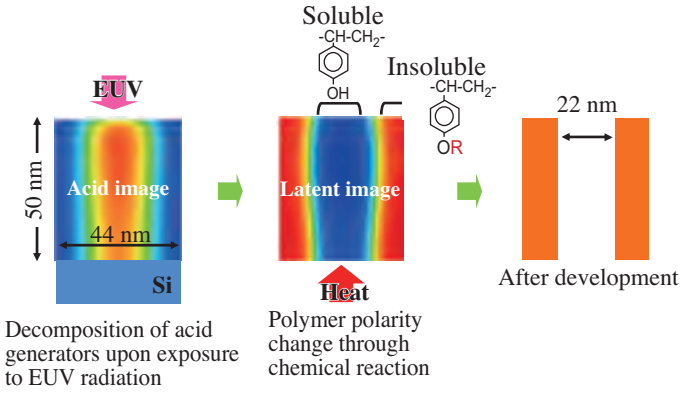

Fig. 1. 22 nm lithography for mass production of semiconductor devices (chemically amplified resist).

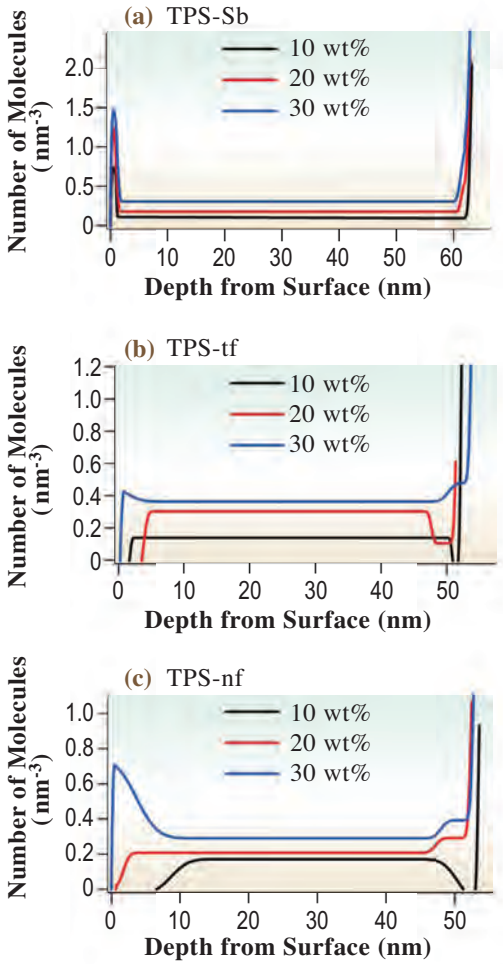

Fig. 2. Concentration profiles (molecule nm^{-3}) of **(a)** TPS-Sb, **(b)** TPS-tf, and **(c)** TPS-nf for 0, 10, 20, and 30 wt% concentrations in tBu-PHS films plotted *versus* distance from film surface.

polymer protecting group during X-ray exposure. 35% of the hydroxyl group was protected. Tryphenylsulfonium nonaflate (TPS-nf), triphenylsulfonium triflate (TPS-tf), and triphenylsulfonium hexafluoroantimonate (TPS-Sb) were used as acid generators. To obtain the density profiles of resist films, a monochrome X-ray from a synchrotron radiation source was irradiated at incidence angles of 0 to 4°. The experiment was performed at beamline **BL46XU**.

The depth profiles of the acid generator distribution reconstructed from the depth density profiles of resist films are shown in Fig. 2. In general, all three chemically amplified resist films showed a similar trend. As the acid generator concentration increased, the concentration at the interfacial areas increased. However, the details depended on the molecular structure of acid generators. The driving force for surface segregation is the difference in the interfacial tension between a small molecule and a polymer. Compounds with fluorinated groups generally give a low surface energy and preferentially segregate at interfaces. All the acid generators used in this experiment contain fluorine in their structures. Therefore, they all have a tendency to gather at the interfaces to lower the surface energy. However, tBu-PHS interacts with acid generators through hydrogen bonding. This strong ionic-dipole interaction between acid generators and the polar polymer tends to confine acid generators in the bulk of the film. Therefore, the depth distribution of acid generators is determined by the balance between the drive to reduce the surface energy by the segregation of fluorinated groups at the interfaces and ionic dipole interactions in the bulk of the film (Fig. 3).

The design of next-generation resist materials requires the control of the interaction between polymer and acid generators. SPring-8 is an effective tool for the analysis of state-of-the-art resist materials.

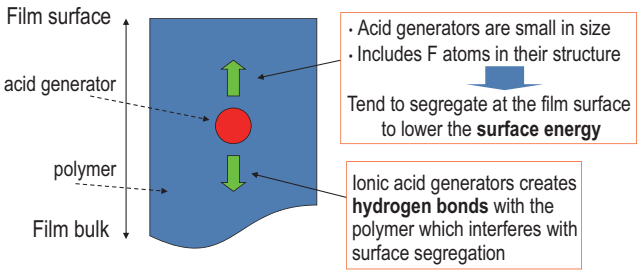

Fig. 3. Interaction of acid generators in chemically amplified resist films.

Takahiro Kozawa

The Institute of Scientific and Industrial Research, Osaka University

E-mail: kozawa@sanken.osaka-u.ac.jp

References

[1] T. Kozawa *et al.*: J. Appl. Phys. **103** (2008) 084306.
[2] T. Hirayama *et al.*: Jpn. J. Appl. Phys. **44** (2005) 5484.
[3] *T. Fukuyama, T. Kozawa, S. Tagawa, R. Takasu, H. Yukawa, M. Sato, J. Onodera, I. Hirosawa, T. Koganesawa and K. Horie: Appl. Phys. Express* ***1*** *(2008) 065004.*
[4] T. Fukuyama *et al.*: Jpn. J. Appl. Phys. **48** (2009) 06FC03.
[5] T. Fukuyama *et al.*: J. Photopolym. Sci. Technol. **22** (2009) 105.

Stability-Instability Transition of Reaction Fronts in Thermal Silicon Oxidation

Thermal silicon oxidation is important not only for the formation of gate dielectric oxide films on a silicon surface but also for size control of silicon nanostructures. Therefore, the modeling of oxidation kinetics has been extensively explored on planar silicon surfaces and at the interface between growing silicon oxide film and planar or nanoscale silicon surfaces. Thanks to recent *in situ* experiments and theoretical calculations, our understanding the silicon oxidation kinetics at the interface between thermal silicon oxide and Si(001) has progressed considerably [1,2]. For surface oxidation, the thermal oxidation can be categorized into two domains – active oxidation (etching) and passive oxidation (oxide growth) – depending on the oxygen pressure and oxidation temperature. However, the morphological stability of the growing interface, i.e., the reaction fronts in the growth regime, which governs the roughening at the interface, has not been well clarified yet. In this work, to reveal whether the interface stress affects the stability of oxidation fronts, we systematically explore the details of the roughening at the interfaces in thermal silicon oxide films on Si(001) as a function of oxidation temperature by combining atomic force microscopy (AFM) (destructive method) and synchrotron X-ray reflectivity measurements (XRR) (nondestructive method).

The B-doped Si(100) wafers were subjected to various annealing conditions in an Ar atmosphere containing a small constant fraction of O_2 gas (0.20 ± 0.01%). Morphologies at the interface were observed in air by tapping-mode AFM immediately after the removal of the as-grown silicon oxide layers. XRR measurements of the samples thermally oxidized in the furnace were performed using the z-axis goniometer at beamline **BL24XU** [3]. The 0.124 nm X-ray wavelength was used at the incident angle by varying the angle from 0.1 to 4.0°.

Figure 1 shows the temperature dependence of roughness at the interface between thermal SiO_2 grown in 0.2% O_2-Ar mixture for 2.5 h and the silicon substrates with miscut angles below 4°, obtained by AFM. The interface becomes rough owing to the formation of interfacial multiple step structures at oxidation temperature (T_{ox}) > 1150°C and has the maximum roughness at T_{ox} = 1250°C. The temperature-dependent roughening can therefore be categorized into three regions with respect to growth temperature: **(I)** $T_{ox} < 1150$°C, where roughness is constant; **(II)** $1150 < T_{ox} < 1250$°C, where roughness sharply increases as oxidation temperature increases and is maximum at 1250°C independent of miscut angles below 4°; and **(III)** $1250 < T_{ox} < 1380$°C, where interface roughness gradually decreases; that is, the roughened interface becomes smooth during the oxidation as the oxidation temperature increases. There is maximum roughness at around 1250°C, indicating that there are competing mechanisms causing the roughening and smoothening as discussed below.

To understand the mechanism of the temperature dependence underlying the interface roughening and smoothening, we performed XRR measurements on the samples with θ = 0.1° and analyzed the density and thickness of the oxide film and interface transition layers on the basis of a two-layer model. We plot the fitting parameters of the samples oxidized at different temperatures in Figs. 2(a) - 2(c). As seen in Fig. 2(a), $\sigma_{i\text{-}s}$ is constant in region **(I)**, but it becomes extremely rough from T_{ox} = 1150°C with the roughness reaching a maximum at T_{ox} = 1250°C in region **(II)**. It then gradually becomes smaller in region **(III)**. In contrast to $\sigma_{i\text{-}s}$, the surface roughness of the silicon oxide bulk film (σ_f), which has the largest roughness in the interfaces of the films at T_{ox} < 1250°C, becomes smaller in regions **(I)** and **(II)** with some modulations and behaves as $\sigma_{i\text{-}s}$ in region **(III)**. The $\sigma_{f\text{-}i}$, on the other hand, is almost constant in regions **(I)** and **(II)**, but the interface becomes slightly rough above 1250°C, and the roughness finally becomes the largest at 1380°C.

The density ratio between the interfacial transition layers and silicon oxide bulk film (d_i/d_f) , which is larger than unity, decreases from 1.12 to 1.05 between 1000 and 1380°C (Fig. 2(b)), while t_i gradually decreases as T_{ox} increases (Fig. 2(c)). This indicates that the planar density of the transition layers d_s, which is defined as

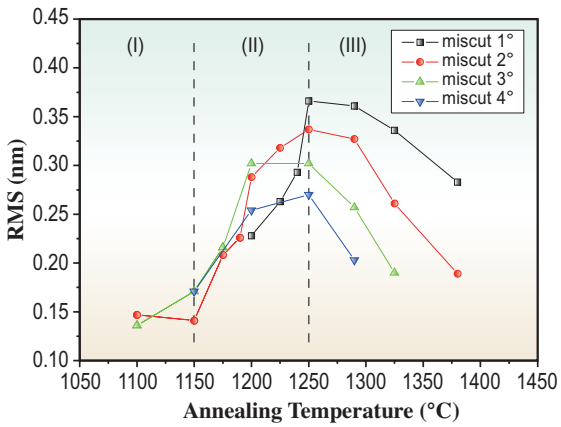

Fig. 1. Rms *vs* oxidation temperature. Samples miscut at several angles were thermally oxidized in the 0.2% oxygen-Ar mixture for 2.5 h. Three characteristic regions are labeled **(I)**, **(II)**, and **(III)** with respect to the oxidation temperature.

$d_i t_i$, becomes smaller with T_{ox}.

On the basis of the AFM and XRR results, the remarkable temperature dependence of oxidation kinetics at the SiO_2/Si(001) interface can be explained as follows: the decreasing in the density and thickness of the interfacial transition layers with increasing T_{ox} indicate that the stress generated by the high-temperature oxidation (>1100°C) is mainly relieved in the interfacial transition layers. The oxidation-induced stress at the interface therefore becomes smaller as T_{ox} increases. In region **(I)**, where the lateral diffusion of silicon species at the interface is negligibly small [2], the oxidation-induced stress between the silicon oxide bulk films and interfacial transition layers is balanced via the relaxation of stress in the transition layers, because $\sigma_{f\text{-}i}$ is almost constant in this region (Fig. 2(a)). The high degree of σ_f is indicative of the small degree of viscosity of the oxide film compared with that of the interfacial transition layers, although it becomes smaller with increasing T_{ox}. In region **(II)**, the lateral diffusion of silicon species becomes prominent at the SiO_x(i)-Si interface [2]. As a result, the strain induced by the oxidation is relieved through the dense and high-viscosity interfacial transition layers not only perpendicular to but also parallel to the SiO_x(i)-Si interface. In region **(III)**, the relaxation of the oxidation-induced stress in the silicon oxide bulk film possibly plays an important role in the decrease in $\sigma_{i\text{-}s}$. The σ_f and $\sigma_{i\text{-}s}$ become almost the same at T_{ox} = 1250°C and then coincidently become smaller with increasing T_{ox}, whereas $\sigma_{f\text{-}i}$ gradually increases in region **(III)** (Figs. 2(a) - 2(c)). The results indicate that the oxide film and interface transition layers act together at T_{ox} > 1250°C and imply that the oxidation-induced strain is homogeneously relaxed not only in the interfacial transition layers but also in the entire region of the silicon oxide bulk films by relaxation via viscosity flow in the silicon oxide bulk film with high-temperature annealing. This feature is consistent with the presence of the transition in the density of the interfacial transition layers at 1200°C (Fig. 2(b)). The homogeneous strain distribution in the silicon oxide bulk film via viscous flow causes the uniform reaction rate at the interface. This explains the onset of the smoothening of the SiO_x(i)-Si interface and the smoothening of the surface of silicon oxide bulk films.

In summary, we discovered a temperature-dependent morphological instability-stability transition at the SiO_2/Si(001) interface during thermal silicon oxidation above 1100°C in dilute oxygen atmosphere in a furnace. The transition implies a strain effect on the oxidation kinetics at the interface between the dense and thin interfacial transition layers and the substrate at T_{ox} > 1250°C.

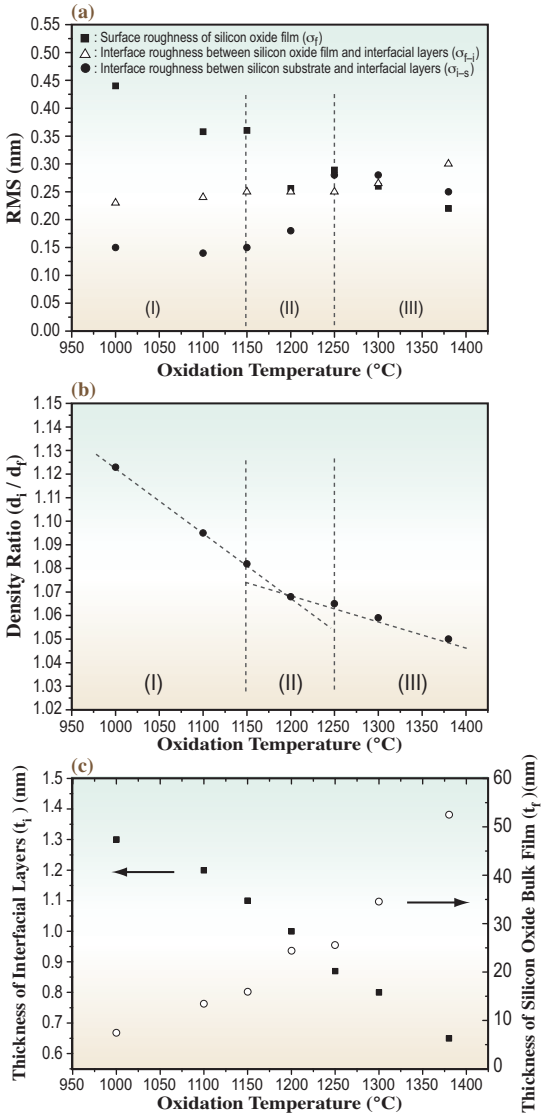

Fig. 2. Plots of best-fit parameters for XRR measurements on samples grown at oxidation temperatures between 1000 and 1380°C in the 0.2% O_2/Ar mixture. **(a)** Roughness at the surface (σ_f) and interfaces between silicon oxide bulk film and interfacial transition layers ($\sigma_{f\text{-}i}$) and between interfacial transition layers and silicon substrate ($\sigma_{i\text{-}s}$). **(b)** Density ratio between interfacial transition layers (d_i) and silicon oxide film (d_s). Dotted lines are two types of linear fittings. **(c)** Thicknesses of interfacial transition layers (t_i) and silicon oxide bulk films (t_f).

Hiroo Omi

NTT Basic Research Laboratories, NTT Corporation

E-mail: homi@will.brl.ntt.co.jp

References

[1] G. Grinstein *et al.*: Phys. Rev. Lett. **81** (1998) 2490.
[2] H. Omi *et al.*: Phy. Rev. Lett. **97** (2006) 016102.
[3] *H. Omi, H. Kageshima, T. Kawamura, M. Uematsu, Y. Kobayashi, S. Fujikawa, Y. Tsusaka, Y. Kagoshima and J. Matsui: Phys. Rev. B* ***79*** *(2009) 245319.*

Direct Observation of Reduced Path Formation in CuO-based Resistance-Switching Devices

The voltage-induced nonvolatile resistance switching (RS) phenomena observed in some oxide materials have recently attracted much attention as the basis for next-generation nonvolatile random access memory technology, called resistance random access memory (ReRAM). ReRAM has several advantages such as a simple structure consisting of metal/oxide/metal sandwich, a high-density integration, and a high operation speed [1]. However, the mechanism of RS has not been fully understood yet, and this has largely affected the future application potential of ReRAM. One of the most predominant models employed to explain the RS phenomena is the "conduction filament" model: conductive filamentary paths are generated by the application of voltage that induces the local reduction of oxides sandwiched between two electrodes. Therefore, a direct observation of the reduced path formation in ReRAM devices is the key to understanding the RS phenomena.

A photoemission electron microscope (PEEM) in combination with wavelength-tunable synchrotron radiation (SR) is a powerful tool for addressing this issue. The PEEM detects the lateral distribution of the photoelectron emission intensity as a function of the photon energy. Thus, the PEEM can be used to map the chemical states of constituent elements by X-ray absorption spectroscopy (XAS). In order to investigate the lateral chemical (oxidation/reduction) distributions in CuO-based ReRAM devices [2], we have performed the PEEM observation of planar-type Pt/CuO/Pt resistance-switching devices fabricated on SiO_2/Si substrates (Fig. 1). The XAS-PEEM measurements were performed using a high spatial resolution PEEM (ELMITEC LEEM III) installed at beamline **BL17SU** [3].

Figure 2(a) shows the reduced state map of Cu ions at the Pt/CuO/Pt device obtained from XAS-PEEM measurements. The bright regions in the map indicate the abundance of reduced components such as Cu_2O and/or Cu metal in the CuO matrix. It is clearly seen that the reduced regions vertically run from cathode to anode like a chain of islands, suggesting the formation of a reduction path due to the application of the voltage between the two electrodes. The reduction in chemical states in the filament path is also confirmed from the micro-XAS spectra, as shown in Fig. 2(b); a high degree of reduction from CuO to Cu_2O and/or Cu metal is clearly observed in the filament paths (Region I), while the original CuO components are dominant outside of the filament paths (Region II). Since the conductivity is strongly enhanced by the reduction of CuO [2], these results indicate that the reduction path formed in the CuO channel due to voltage application is responsible for the occurrence of the RS phenomena in Pt/CuO/Pt ReRAM devices. Furthermore, the present study demonstrates the usefulness of the microregion XAS measurements using PEEM for studying the chemical distribution in oxide devices and so on. We hope that this study promotes further XAS-PEEM works on the inhomogeneous chemical states in various types of ReRAM at SPring-8 in the near future.

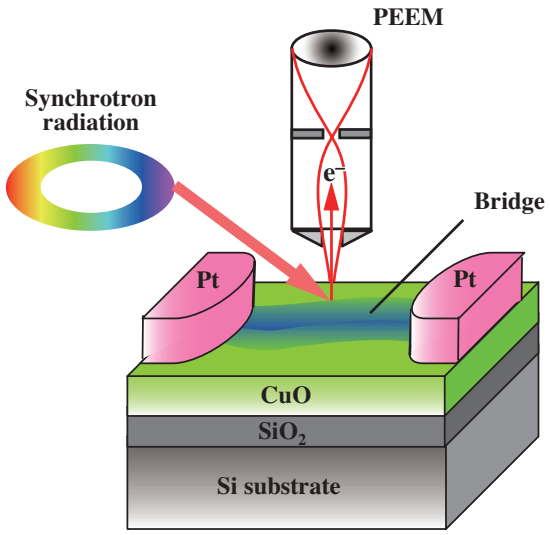

Fig. 1. Schematic illustration of PEEM measurements for Pt/CuO/Pt devices.

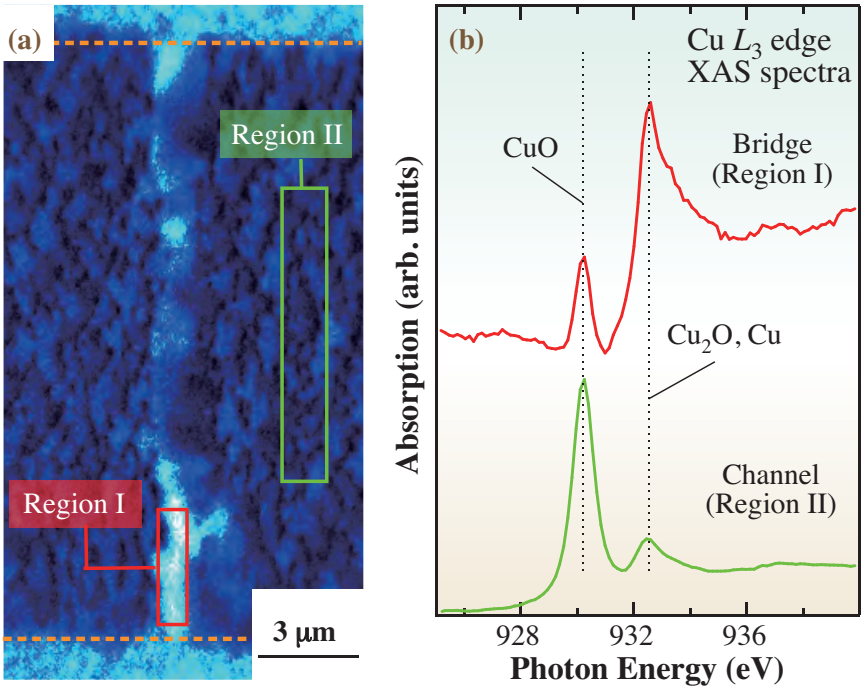

Fig. 2. **(a)** Chemical PEEM image of the planar-type Pt/CuO/Pt device after the application of voltage. The PEEM images were recorded at photon energies corresponding to the Cu L_3 absorption edge. **(b)** XAS spectra recorded in the filament path (Region I) and CuO channel (Region II) near the Cu L_3 absorption edge. These XAS spectra consist of two peaks, which are assigned to the CuO states at 930.3 eV and reduced states (Cu_2O and/or Cu metal) at 932.6 eV.

R. Yasuhara[a], H. Kumigashira[a,b,c,*] and M. Oshima[a,b,c]

[a] Dept. of Applied Chemistry, The University of Tokyo
[b] Core Research for Evolutional Science and Technology (CREST), Japan Science and Technology Agency
[c] Synchrotron Radiation Research Organization, The University of Tokyo

*E-mail: kumigashira@sr.t.u-tokyo.ac.jp

References

[1] I.G. Baek *et al.*: Tech. Dig. -Int. Electron Devices Meet. (2005) 750.
[2] K. Fujiwara *et al.*: Jpn. J. Appl. Phys. **47** (2008) 6266.
[3] *R. Yasuhara, K. Fujiwara, K. Horiba, H. Kumigashira, M. Kotsugi, M. Oshima and H. Takagi: Appl. Phys. Lett.* ***95*** *(2009) 012110.*

Characterization of Liquid Crystal Alignment on Rubbed Polyimide Film by Grazing-Incidence X-Ray Diffraction

The understanding of the alignment mechanism of liquid crystal (LC) on alignment film is of fundamental interest and of industrial importance in the manufacture of LC devices. Rubbed polyimide (PI) films have been used as liquid crystal alignment films in LC displays (LCDs). It is widely considered that molecules of liquid crystals are aligned by intermolecular interactions with PI molecules of rubbed films, and the characterization of polyimide molecular orientation is essential in the development and fabrication of LCDs. Until now, using grazing incidence X-ray diffraction (GIXD), which is a very powerful technique to characterize the molecular alignments of thin films, we have studied the effects of rubbing, washing and annealing on the surface structure of polyimide film [1].

In this study, we attempt to characterize the molecular alignment of a very thin liquid crystal layer (4 ~ 40 nm) formed on PI film to investigate the dependence of the molecular orientation of the LC film surface on the LC thickness to determine the interaction between LC and PI [2].

A nematic liquid crystal 4-pentyl-4-4biphenylcalbonitrile, denoted as 5CB, was used in this experiment. 5CB molecules are of rodlike shape and are aligned parallel to their molecular axes at room temperature. Poly (pyromellitic dianhydride oxydianiline), denoted as PMDA-ODA, was selected as the alignment PI film. A polyamic acid solution of PMDA-ODA was coated on Si substrates using a spinning coater. After pre-baking at 80°C for 5 min to dry the solvent, curing for imidization was performed at 250°C for 30 min. Then, PMDA-ODA films were rubbed under the condition that the insert depth of the fiber is 0.4 mm. The rotation and translation speeds of a rubbing roller were set at 300 rpm and 20 mm/s. The 5CB was evaporated executed under air atmosphere using an evaporation chamber. By heating the 5CBs at 100°C, the 5CBs are gradually evaporated onto the rubbed PMDA-ODA-coated substrate. The evaporation times were 5, 10, 20 and 40 min.

X-Ray reflectivity (XRR) and GIXD measurements were performed using the multi-axis diffractometer installed at beamline **BL19B2**. Scattered X-rays from samples were detected using a NaI scintillation counter through a Soller slit with a 0.089° divergent angle ("KeV" Co. Ltd.).

Figure 1 shows the observed X-ray reflectivity of the 5CB evaporated film onto the rubbed PMDA-ODA-coated substrate. The evaporation time was 10 min. The analysis was carried out by tuning both the mass density and thickness of the PMDA-ODA and 5CB film to fit the observed reflectivity. The estimated film thicknesses of the PMDA-ODA and 5CB film were 100.9 and 8.9 nm, respectively. A linear relationship between the film thickness of the 5CB and evaporation time was observed as shown in the inset of Fig. 1.

In-plane φ-2θz scans of the 5CB evaporated film of 38.4 nm thickness onto the rubbed PMDA-OAD film shown in Fig. 2(a) were obtained under the condition that the incident angle was set at 0.10°. Under this condition, we could obtain surface-sensitive information of the 5CB thin film. Blue and red solid circles indicate the observed in-plane φ-2θz profiles whose scattering vector is parallel and normal, respectively, to the rubbing direction. Strong and somewhat broad diffraction peaks were clearly observed at around 16.0°. These diffraction peaks mainly come from the intermolecular correlation perpendicular to the molecular axis of the 5CB (Fig.3). The surface sensitive peak of the 5CB layer was stronger in the normal to rubbing direction. This means that the 5CB molecules preferentially aligned in the rubbing direction.

Figure 2(b) shows Bragg d-spacings of the 5CB's broad diffraction peaks at around 16.0° estimated by profile fitting. In addition, Bragg spacings in the normal (blue star) and parallel (red star) directions corresponded to the PI chain, and that of the 5CB directly deposited on the Si substrate without the rubbed PMDA/ODA film (green star) is indicated in Fig. 2(b). The larger Bragg spacing of the 5CB in

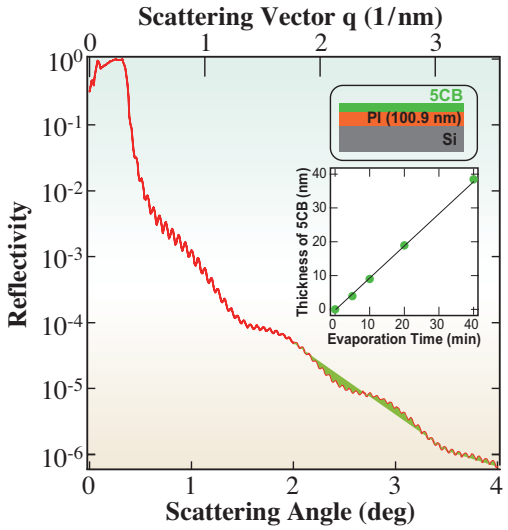

Fig. 1. Observed X-ray reflectivity of the 5CB film evaporated for 10 min onto the PMDA-ODA film. The inset shows the linear relationship between the 5CB film thickness and evaporation time.

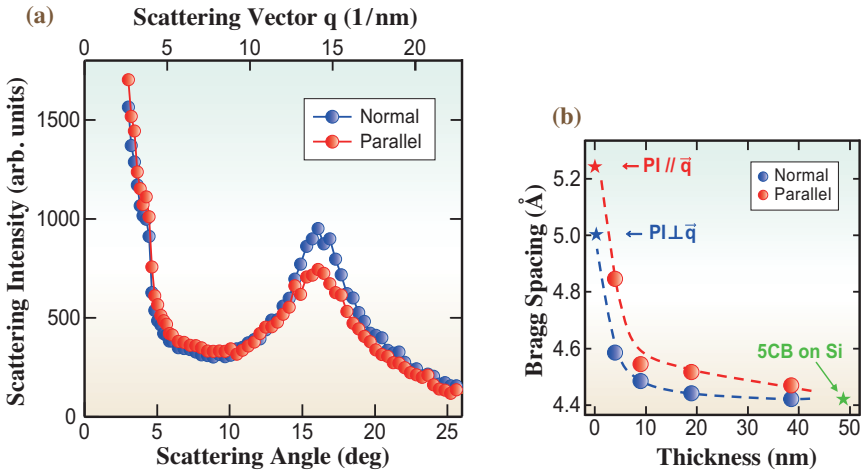

Fig. 2. **(a)** In-plane φ-2θz profiles of the 5CB evaporated film onto the rubbed PMDA-ODA film. **(b)** Estimated Bragg spacing of the 5CB's broad diffraction peaks.

the parallel direction can be explained by considering that 5CB molecules were strongly bounded by PI chains in the parallel direction with longer interchain spacings. The estimated Bragg spacings in both directions decrease with increasing 5CB film thickness, and seem to approach that of the 5CB film directly deposited on the Si substrate. In the 5CB films thinner than 10 nm, their estimated Bragg spacings seem to asymptotically increase to those of rubbed polyimide film in the parallel and normal directions with decreasing thickness of the 5CB film to zero. The behaviors of the 5CB films described above suggest that the 5CB molecules are strongly bounded by the rubbed polyimide film, and that the 5CB molecules have similar periodicity to the rubbed PI at the interface of PI. As the distance from the alignment film increases, the effect of the alignment film becomes weaker and the intermolecular spacing of the 5CB comes close to the intrinsic intermolecular spacing. It was also observed that the peak width at around 16° decreases with its thickness, which is considered to indicate the lower 5CB ordering near the rubbed polyimide film (Fig. 3).

In summary, we characterized the molecular distribution in a very thin liquid crystal layer evaporated onto rubbed polyimide film. The anisotropic distribution of liquid crystal molecules in the thin 5CB layer was successfully observed by GIXD. In the surface-sensitive in-plane diffraction, we found that the 5CB film thickness affects the Bragg spacing and ordering, which were estimated from the diffraction peak position and width. In the vicinity of the alignment film, the intermolecular spacing of the 5CB is expanded by the alignment film in the direction perpendicular to the molecular axis of the 5CB molecule. It was also proved that the 5CB is less ordered near the PI film. The intermolecular spacing of the 5CB becomes close to its intrinsic value as it recedes from the PI film.

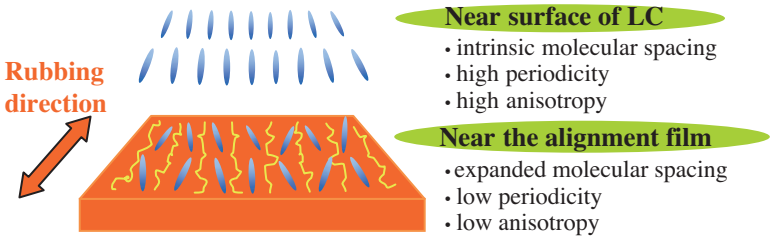

Fig. 3. Illustration of proposed model for the 5CB molecular alignment. The blue arrow indicates the intermolecular correlation perpendicular to the 5CB molecular axis.

Tomoyuki Koganezawa[a,*], Ichiro Hirosawa[a] and Hidenori Ishii[b]

[a] SPring-8 / JASRI
[b] Nissan Chemical Industries, Ltd.

*Email: koganeza@spring8.or.jp

References

[1] I. Hirosawa *et al.*: IEICE Trans. Electron **E92.C** (2009) 1376.
[2] *T. Koganezawa, I. Hirosawa, H. Ishii and T. Sakai: IEICE Trans. Electron. **E92.C** (2009) 1371.*

Precise Observation of Dynamic Structural Change of Pd Particles under CO/NO Catalytic Reaction Studied by Dispersive X-Ray Absorption Fine Structure

The metal particles used in the catalytic reaction are made fine in order to spread the surface area and increase the reaction space. However, it is expected that the nanometer-sized metal particles show the original catalytic reaction which is different from that for the larger particles. In recent studies, it has been revealed that the small particles show size dependent properties, that is, the lattice constant, oxidation process, shape of the particles, and so on. At this moment, we have to consider the fine particle itself as the independent research subject that includes the particle-support and particle-gas interactions, and the study of fine particles by the bulk and surface systems approach is insufficient.

Pd metal particles are used in automotive exhaust catalysts for the removal of CO, NO_x and hydrocarbons. Newton and coworkers pointed out that the Pd metal fine particles show a rapid change in the mean particle size during the catalytic reaction [1]. They used the X-ray absorption fine structure (XAFS) technique, which has the element-selective and local sensitive features, and therefore, has been frequently used for the study of the supported fine particles. In particular, the dispersive optical system that was used in the above study has some original features. The dispersive optical system enables us to observe XAFS spectra without mechanical movement [2]. Although this system has been mainly applied for the real-time-resolved observation of chemical reaction, the precise determination of XAFS parameters has also been accomplished. In this study, both advantages of dispersive XAFS, namely, fast and precise observations, were applied to the structure and shape changes of Pd metal fine particles [3]. *In situ* and real-time observations of the CO/NO catalytic reaction on the Pd/Al_2O_3 with 0.2 Hz rate resulted in the highly stable structural and electronic parameters.

The Pd *K*-edge XAFS spectra were measured at the bending magnet beamlines **BL14B1** and **BL28B2**. The main systems of optical equipment at both beamlines are similar and are displayed in Fig. 1. Dispersed X-rays were obtained from the curved crystal of the Si(422) reflection plane with the Laue configuration. From the curvature with a radius of 2000 mm, X-rays with an energy range of 800 eV were obtained. $Gd_2O_2S(Tb)$ was exposed to dispersed X-rays from the sample, and emitted lights were collected using a charge-coupled device (CCD) camera (12 bits). Powdered γ-Al_2O_3 was used in the impregnation with dilute aqueous palladium nitric acid, $Pd(NO_3)_2$. Following drying and calcination at 500°C, $Pd(4\ wt\%)/Al_2O_3$ sample was prepared. For the CO/NO catalytic reaction study, CO(9%)/He and NO(9%)/He were used. The gases were supplied at a flow rate of 50 cc/min. Spectra were measured at 0.2 Hz.

Figure 2 shows the extended X-ray absorption fine structure (EXAFS) functions of the Pd/Al_2O_3 during CO flow at 400°C for 1000 s. The gradual changes in the amplitude and wavelength are clearly recognized. A decrease in the amplitude means a decrease in the Pd-Pd coordination number (*CN*), and a shortening of the wavelength means an expansion of the Pd-Pd interatomic distance (*R*). It is noted that both changes in the amplitude and wavelength show very smooth shifts. Variations in the XAFS parameters during CO/NO successive flow for the Pd metal particles are shown in Fig. 3. From the analysis of Pd-Pd first shell in the metal state, *CN*, *R*, Debye-Waller factor (C_2) and edge shift were determined. It is understood that all the obtained XAFS parameters show high relative statistics, that is, 0.02 eV for the edge shift, 0.05 for the *CN* and 0.002 Å for the *R*.

For CO first flow, it is revealed that the enlargement of the *R* of 0.07 Å is brought about by CO. Some of the adsorbed CO are considered to dissociate on the surface of Pd particles, and the crystal lattice is expanded by atomic C that is absorbed into the interstitial position. The *CN* of the Pd-Pd shell gradually decreases at the same time scale as the increase in the *R*, which means that CO dissociative adsorption can induce the dispersion of Pd metal fine particles. After NO flow, the expanded lattice rapidly contracts with the recovery of the original values for the edge shift and *CN*, suggesting the removal of both the adsorbed CO and absorbed C. The edge shift denotes a gradual increase after CO removal by NO flow, which indicates that the surface of Pd particles is gradually oxidized by the dissociative

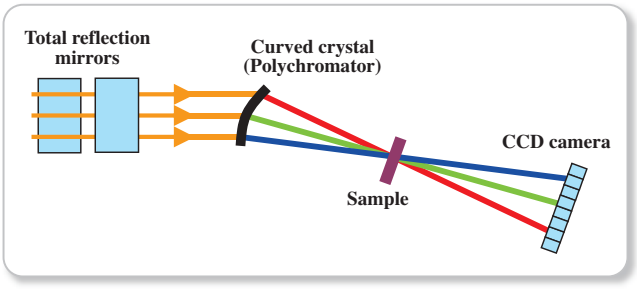

Fig. 1. Schematic of the dispersive XAFS observation.

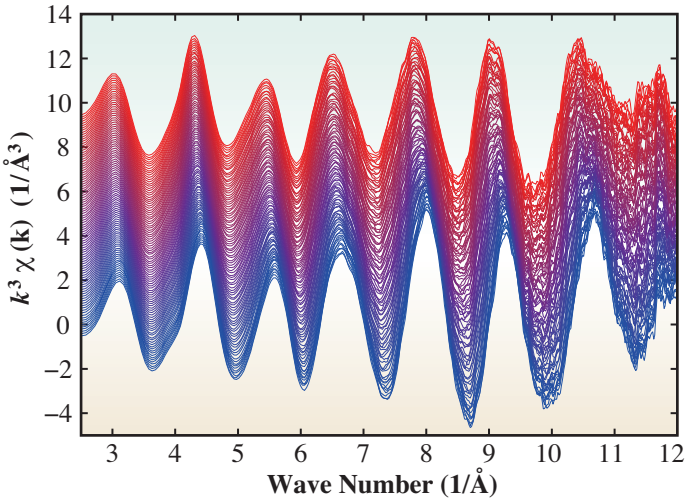

Fig. 2. 0.2 Hz observation of k^3-weighted EXAFS functions of the Pd/Al_2O_3 at 400°C during CO flow from 0 s (bottom) to 1000 s (top).

adsorption of NO. This surface-oxidized layer is smoothly removed by the next CO flow, which is confirmed from the abrupt changes in the edge shift and *CN*. As for the edge shift, a slight positive shift is also observed just after second CO flow. CO adsorption on the Pd oxidized layer may induce the charge transfer from Pd to CO. After the removal of the surface-oxidized layer, a gradual increase in the *R* is observed again. CO adsorption on the Pd surface is normally considered as the molecular adsorption at the C end. In this study, it has been revealed that the slow dissociative adsorption mode exists and causes the expansion of the Pd lattice and the dispersion of the Pd particles, which creates a new understanding of the CO/NO catalytic reaction. As for the surface-oxidized layer, the slow creation and rapid removal make the surface of the particles clean during the long catalytic reaction. The charge transfer just after the second CO flow implies the particular adsorption state and may be the key to the fast cleaning of the Pd surface oxide layer. It has been clearly demonstrated by *in situ* and real-time-resolved dispersive XAFS observation that several dynamic mechanisms such as contraction-expansion, aggregation-dispersion and oxidation-reduction changes are recognized in metal fine particles.

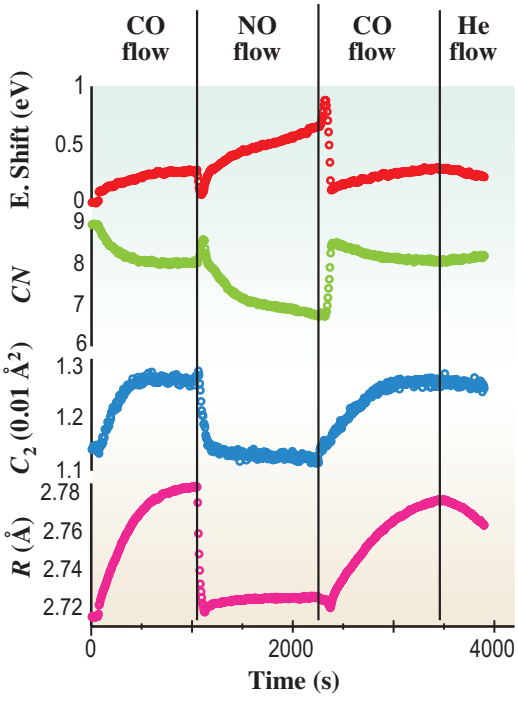

Fig. 3. Variations of XAFS parameters for the Pd-Pd shell of Pd/Al_2O_3 during CO/NO successive flow at 400°C.

Daiju Matsumura

SPring-8 / JAEA

E-mail: daiju@spring8.or.jp

References

[1] M.A. Newton *et al.*: Nature Materials **6** (2007) 528.
[2] T. Matsushita and R. P. Phizackerley: Jpn. J. Appl. Phys. **20** (1981) 2223.
[3] *D. Matsumura, Y. Okajima, Y. Nishihata, J. Mizuki, M. Taniguchi, M. Uenishi and H. Tanaka: J. Phys.: Conf. Ser.* ***190*** *(2009) 012154.*

Crystal Structure at the Initial Growth Stage of Organic Semiconducting Thin Films Studied by GIXD

Recently, organic semiconductors have attracted great attention because of their notable functions as materials used in organic electronic devices such as organic thin-film transistors (OTFTs), solar cells and organic light-emitting diodes (OLEDs). The organic devices have many advantages in terms of a low-cost, low-temperature process, compatibility with flexible substrates, and a large variety of composite materials. A number of novel organic semiconductors have been synthesized, and the performance has continuously progressed. Reported values of the carrier mobility in OTFTs exceed that in amorphous silicon, which is used as the material for TFTs in liquid crystal displays. However, the stability and uniformity of OTFTs require improvements. Control of the crystal growth of semiconducting molecules is an effective method to increase device performance and stability, because the physical properties of organic semiconductors show significant anisotropy. Furthermore, control of the crystallinity of the films is required to decrease their carrier scattering at grain boundaries. Therefore, investigation of the crystal structure of ultrathin films is demanded to improve device performance of OTFTs.

Distyryl-oligothiophenes, one of the organic semiconductors, have been used in OTFTs as a promising material. We have so far demonstrated that the OTFTs based on distyryl-oligothiophenes show remarkable stability in air [1-5], and the high field-effect mobility (up to 0.1 cm/Vs) was unchanged for more than 300 days. However, the details of the film structure have not been investigated. Because the charge carriers move on the interface between the organic semiconductor layer and dielectric surface in the OTFTs, the structure of organic semiconductors at the initial stage of crystal growth is important to understand its remarkable transport properties. In this study, the in-plane structures of ultrathin films based of distyryl-oligothiophenes (Fig. 1) on SiO_2 substrates were investigated by grazing incidence X-ray diffractometry (GIXD). The effects of film thickness and end-cap groups on the in-plane structure were examined.

Distyryl-oligothiophenes were synthesized and sublimated from a k-cell-type crucible onto SiO_2 substrates under a base pressure of 2×10^{-4} Pa. The film thicknesses were 0.2 to 100 nm and were monitored using a quartz crystal microbalance during the deposition process, and calibrated using cross-sectional height profiles, area and coverage of islands observed by atomic force microscopy (AFM) after deposition. Characterization of the films was carried out using multi axes X-ray diffractometer at beamlines **BL13XU** and **BL46XU**. In-plane diffractions were measured at grazing incidence condition.

Figure 2 shows AFM images of deposited films of distyryl-oligothiophenes. The size and number density of the islands changed with the nature of the end-cap groups. The number density of the islands increases with increasing volume of the end-cap group. This is due to the fact that the frequency of nucleation on the substrate depends on the surface energy of clusters, which decreases with the packing density of molecules in the crystals. The decrease in the number density of nuclei causes the increase in the grain size in thick films. The X-ray diffraction patterns in the conventional $\theta/2\theta$ mode of DS-4T, DFS-4T and Py-4T deposited on SiO_2 substrates with the film thickness of 100 nm show that the *ab*-planes of the grains orient parallel to the substrate surfaces. The obtained d_{001} spacings of DS-4T, DFS-4T and Py-4T were 2.802, 3.220 and 3.110 nm, respectively, which are comparable to their molecular lengths. Figure 3 shows the thickness dependence of the in-plane GIXD patterns of thin films of distyryl-oligothiophenes. Depending on the thickness, slight peak shifts are observed in 020 of DS-4T and 110 of DFS-4T. The peak shift of 020 of DS-4T is due to the occurrence of another polymorph with increasing thickness. As to the slight peak shift observed in 110 of DFS-4T, it could be due to changes in the molecular packing between ultrathin films and thicker ones.

From the GIXD data, it is clarified that the volume of end-cap groups causes the decrease in crystallinity in this series of compounds. This could be due to the decrease in the molecular interaction caused by the steric hindrance. Because a smaller molecular interaction results in a smaller surface energy of the

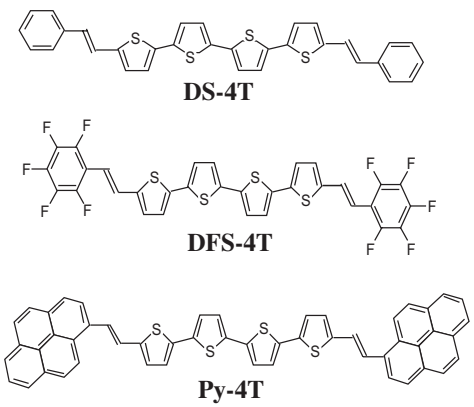

Fig.1. Molecular structures of end-capped oligothiophenes DS-4T, DFS-4T and Py-4T.

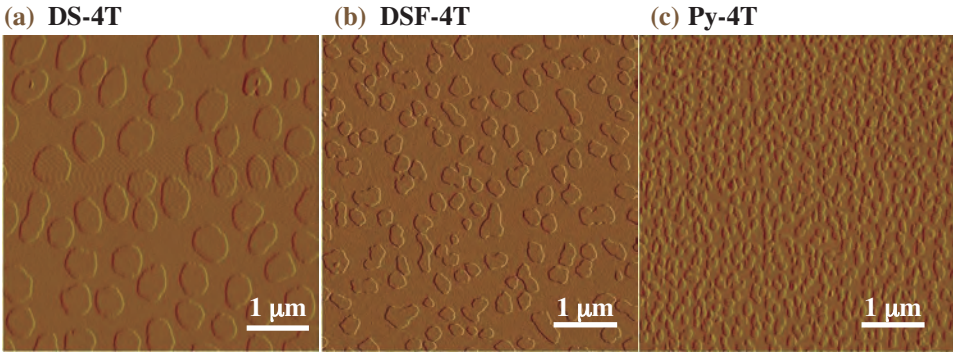

Fig. 2. AFM images of ultrathin films DS-4T, DFS-4T and Py-4T. The average thickness was 1 nm and the islands were composed of monolayers.

nuclei during the crystal growth, the difference in the number density of the island shown in Fig. 2 can be attributed to the difference in the molecular packing. This difference could be related to the transport properties in OTFTs. Since the π-orbital in the molecules extends to the *ab*-axis direction, the difference in the area of the *ab*-plane should be essential to the difference in the charge mobility among the derivatives. The area of the *ab*-plane of DS-4T is smaller than that of DFS-4T. Therefore, introducing end-cap groups with increasing volume into oligothiophene molecules seems to result in the decrease in grain size and the decrease in the conductivities in each grain.

The present results have proved that GIXD is an effective tool for characterizing the crystal structure of organic ultrathin films for OTFTs with the thickness covering 0.2 ~ 100 nm.

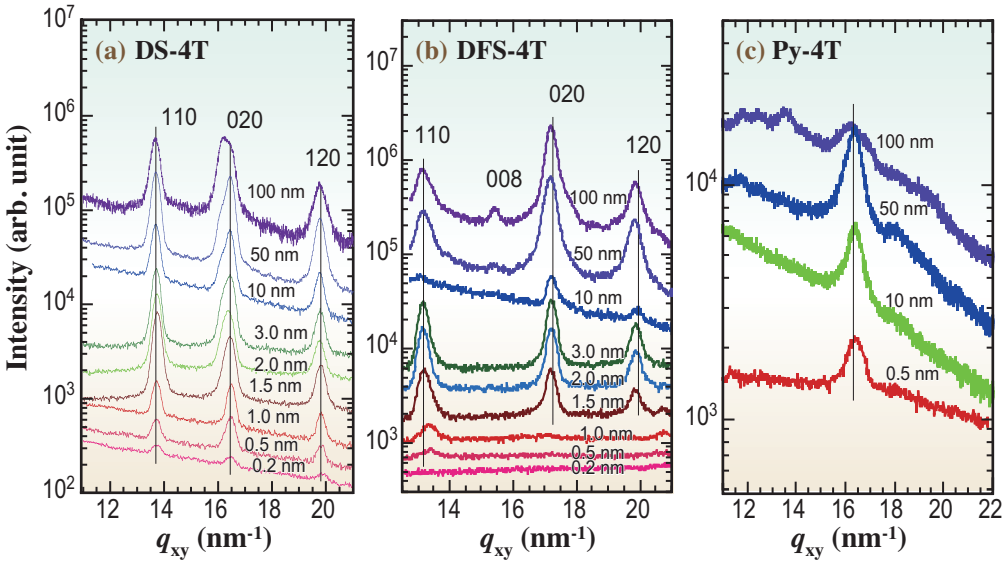

Fig. 3. Thickness dependence of in-plane GIXD patterns of DS-4T, DFS-4T and Py-4T films deposited on SiO_2.

Noriyuki Yoshimoto

Department of Materials Science and Engineering, Iwate University

E-mail: yoshimoto@iwate-u.ac.jp

References

[1] C. Videlot-Ackermann *et al.*: J. Am. Chem. Soc. **127** (2005) 16346.
[2] C. Videlot-Ackermann *et al.*: Organic Electronics **7** (2006) 465.
[3] Y. Didane *et al.*: J. Am. Chem. Soc. **103** (2008) 17681.
[4] N. Yoshimoto *et al.*: Cryst. Res. Tech. **42** (2007) 1228.
[5] *N. Yoshimoto, W.Y. Li, K. Omote, J. Ackermann, C. Videlot-Ackermann, H. Brisset and F. Fages: J. Phys.: Conf. Ser.* ***83*** *(2007) 012026.*

Formation of Autoclaved Aerated Concrete Studied by *In Situ* X-ray Diffraction under Hydrothermal Condition

Autoclaved aerated concrete (AAC) is a porous concrete material having the features of both lightweight (density of about 0.5 g/cm^3) and mechanical strength. Because of its porous structure, AAC also has superior properties in terms of high heat insulation and fire resistance. Therefore AAC has been one of the most industrially important building materials in the world. About 2.5 million m^3 of AAC is manufactured every year in Japan, and 18 million m^3 in Europe. Typically, AAC is produced by hydrothermal treatment of mixtures of quartz sand, lime, cement, gypsum and aluminum powder in a temperature range of 180 - 200°C. During the hydrothermal treatment, platy-shaped tobermorite crystals ($5CaO•6SiO_2•5H_2O$) are formed as a major component of AAC (Fig. 1). It is known that the crystallinity of tobermorite largely affects the physical properties of AAC.

The formation mechanism of tobermorite has not been understood thoroughly owing to the difficulty in investigating under the hydrothermal reaction atmosphere, i.e., an autoclave process. The conventional *ex situ* approach, conducted by terminating the reaction in the middle of the autoclave process, includes ambiguity caused by the temperature dependence of solubility, unfavorable reactions during the cooling process, a variation among different pieces used as samples at different reaction stages, and so on. Thus, *in situ* observation of the reaction has been highly desirable. We have developed a system for high-performance *in situ* transmission XRD under hydrothermal conditions, using high-energy X-rays in combination with an originally designed autoclave cell [1]. Here, we report phase transformations during the AAC formation process investigated by *in situ* XRD.

In situ XRD was carried out at **BL19B2** beamline, using an X-ray energy of 30 keV. A pre-cured mixture solid (quartz sand, lime, cement, gypsum and water), together with distilled water as a steam source, was set in the autoclave cell. The temperature was elevated from 100 to 190°C with a ramping rate of 1°C/min., then held at 190°C for 6 h. During this process, the XRD measurements were conducted at intervals of either 15 or 30 min.

Figure 2 shows a series of XRD patterns obtained during the autoclave process. Several constituents related to tobermorite formation are identified. The intensities of the major peaks are plotted in Fig. 3, together with the temperature and pressure inside the cell. Both the temperature and pressure were very stable throughout the experiment.

There are several advantages for an *in situ* experiment compared with *ex situ* approaches. One is the ability to detect a small change in the course of reaction. In this study, we were able to observe the intensity change of 'non-crystalline' calcium silicate hydrate (C-S-H), which is formed by a reaction of dissolved quartz with dissolved $Ca(OH)_2$, and well-known as a precursor of tobermorite [2]. Generally, with an *ex situ* type of experiment, it is difficult to determine the amount of non-crystalline materials during a reaction process because the intensity of the amorphous halo could be affected by the background intensity, which could vary among different pieces of the sample or by sample preparation. In an *in situ* experiment, however, the same portion of the sample is continuously measured throughout the experiment. This allows one to detect a slight change in the amorphous intensity. The intensity change at the C-S-H amorphous halo region (3.43 nm^{-1}) is plotted together in Fig. 3 (no background subtracted). The intensity reaches a maximum at around 150 min, which is the same time at which there is a drastic decrease in the amount of portlandite and the beginning of the tobermorite formation. Then, the intensity decreases as the formation of tobermorite proceeds.

Another advantage is the ability to investigate the reaction pathways directly. Two pathways of tobermorite formation are observed in this study. The first is a formation via non-crystalline C-S-H (formula (1)), as described above.

$$\underset{(xCaO•ySiO_2•zH_2O)}{\text{Non-crystalline C-S-H}} + \underset{(SiO_2)}{\text{Quartz}} \rightarrow \underset{(5CaO•6SiO_2•5H_2O)}{\text{Tobermorite}} \quad (1)$$

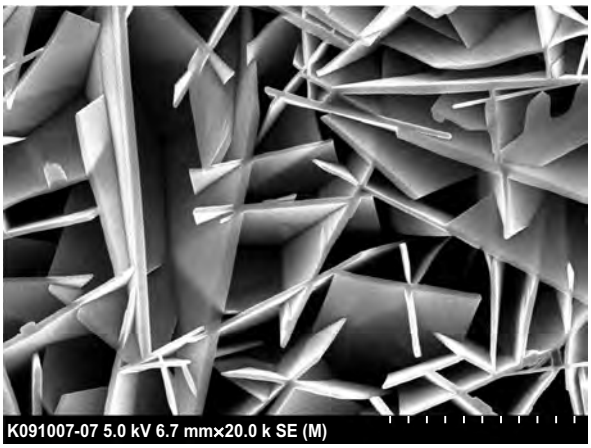

Fig. 1. SEM image of platy crystals of tobermorite. (Scale: one division corresponds to 0.2 μm.)

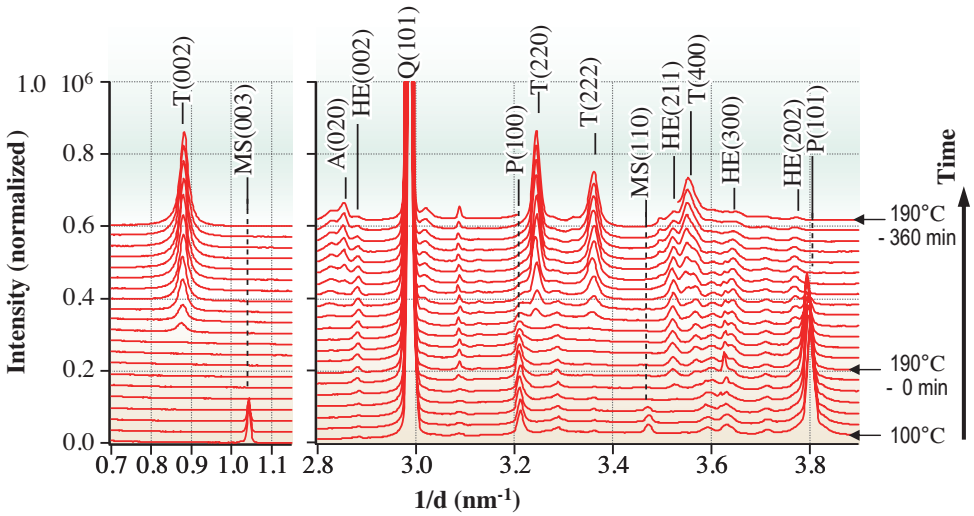

Fig. 2. Stack of *in situ* XRD patterns obtained during the autoclave process. The reaction under the autoclave proceeds from bottom to top. T: tobermorite, P: $Ca(OH)_2$, Q: quartz, MS: monosulfate-14, HE: hydroxylellestadite, A: anhydrite. [1]

The second pathway is that with hydroxylellestadite (HE : $Ca_{10}(SiO_4)_3(SO_4)_3(OH)_2$) as a calcium source. HE is an intermediate material formed with sulfur released from monosulfate-14 (MS: $Ca_4Al_2O_6(SO_4)\cdot 14H_2O$), as indicated in Fig. 3. In a model system using high-purity reagents, it has been reported that HE reacts with dissolved quartz to form tobermorite and anhydrite [3] (formula (2)).

$$\underset{(Ca_{10}(SiO_4)_3(SO_4)_3(OH)_2)}{\text{HE}} + \underset{(SiO_2)}{\text{Quartz}} \rightarrow \underset{(5CaO\cdot 6SiO_2\cdot 5H_2O)}{\text{Tobermorite}} + \underset{(CaSO_4)}{\text{Anhydrite}} \quad (2)$$

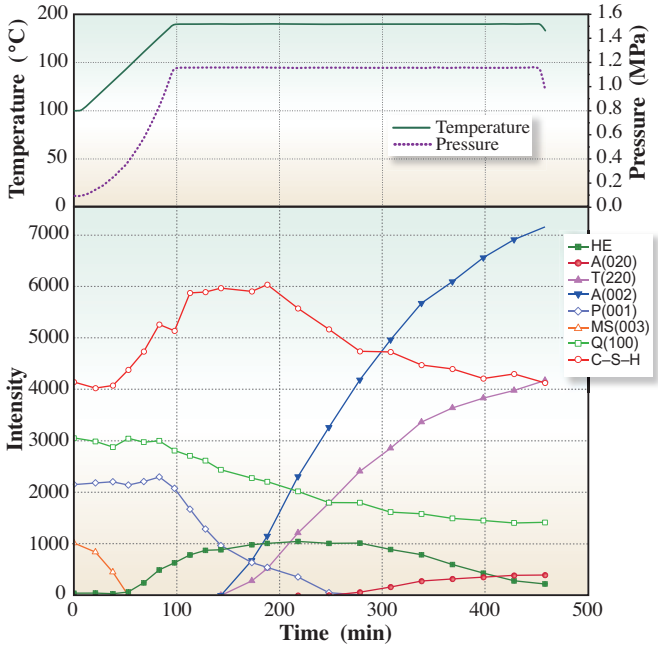

Fig. 3. Top: Time dependence of the temperature and the pressure inside the cell during the autoclave process. Bottom: Time dependence of the intensities of the major constituents during the autoclave process. [1]

Figure 3 shows the decrease in the amount of HE, and the increase in the amount of anhydrite occurs simultaneously. This is considered to be strong evidence of the occurrence of the tobermorite formation via HE in a real manufacturing process. It should be pointed out that the amount of non-crystalline C-S-H starts to decrease much earlier than that of HE, suggesting the difference in reactivity between these two intermediate materials.

The newly developed autoclave cell, combined with high-energy transmission XRD, can be used for *in situ* analyses of hydrothermal reactions. By using a CCD or a photon-counting pixel array detector, it is possible to conduct much faster measurements, which enables the discussion of the reaction kinetics.

Jun Kikuma

Analysis and Simulation Center,
Asahi-KASEI Corporation

E-mail: kikuma.jb@om.asahi-kasei.co.jp

References

[1] *J. Kikuma, M. Tsunashima, T. Ishikawa, S. Matsuno, A. Ogawa, K. Matsui and M. Sato: J. Synchrotron Rad.* ***16*** *(2009) 683.*
[2] H.F.W. Taylor, "Cement Chemistry", 2nd ed. London: Thomas Telford 1997.
[3] M. Sakiyama *et al.*: J. Soc. Inorganic Mat. Jpn. **7** (2000) 685.

Detection of Tooth Enamel Microstructural Transformations during De- and Re-mineralization in the Early Stage of Caries

Dental caries is one of the most common diseases in the world. In the aged society of Japan, preventing the loss of teeth by caries and periodontal disease is considered as a national health issue by the Ministry of Health, Labour and Welfare. Because the loss of teeth causes the insufficient chewing of food, caries threatens not only oral but also systemic health and decreases the quality of social life. Moreover, conserving healthy teeth is important to enjoy daily life with healthy eating, talking and smiling. Hence, preventing caries is important to live a long and healthy life. Since clinical efforts alone cannot eradicate caries, individual daily prevention efforts are important to conserve healthy teeth.

The development of dental caries is regarded as a chronic process that typically occurs over a period of several years. A tooth is covered with enamel, most of which consists of needle-shaped crystals of hydroxyapatite (HAp) that contain calcium and phosphate as the main component (Fig. 1). The acidogenic microorganisms ferment ingested carbohydrates and develop a dental plaque with a variety of organic acids excreted as metabolic by-products. These acids dissolve the subsurface enamel beneath the plaque (demineralization), while the surface of the enamel is conserved. At this early stage of caries, the demineralized enamel area is called a subsurface lesion, and is observed clinically as a white opaque spot. In such a stage, the subsurface lesion can be reversibly cured (remineralized) to a nearly sound state without surgical procedures [1].

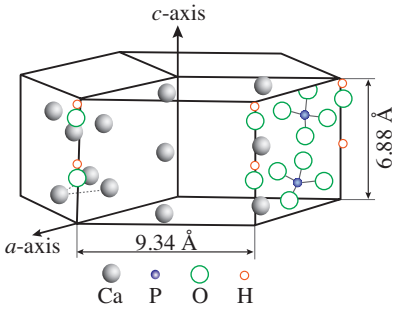

Fig. 1. Detailed crystal structure of hydroxyapatite.

In usual life, remineralization occurs between meals by salivary components such as calcium and phosphate. However, occasionally, the remineralization cannot overcome the demineralization, and the caries lesion gradually develops to irreversible stages. This process has been studied extensively by transversal microradiography (TMR) [2]. TMR provides the mineral distribution in the enamel at a micrometer order to a plano-parallel direction, and used as the gold-standard method for the analysis of demineralization and remineralization in dental science (Fig. 2). However, TMR cannot provide evidence on the distribution of HAp crystallites [2,3]. In fact, whether the restored subsurface is filled with HAp crystallites as in the sound enamel or with other forms of calcium-phosphate salts (e.g., octacalcium phosphate, amorphous calcium phosphate) cannot be determined by TMR.

We developed a new method of determining the

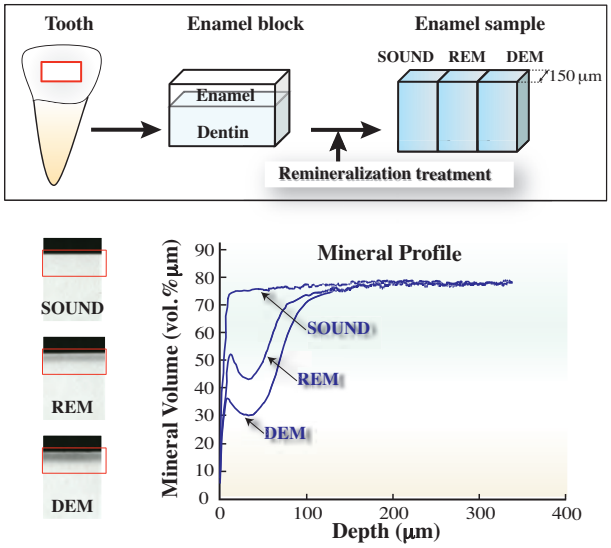

Fig. 2. Preparation of tooth enamel sample. Typical mineral distributions obtained by the transversal microradiography of tooth enamel after demineralization (DEM) and remineralization (REM) in comparison with the untreated enamel (SOUND).

HAp crystal content profile of the 200 μm subsurface area. X-ray diffraction is used to measure the local quantity of HAp crystals. Thin tooth sections containing sound and demineralized enamels were prepared and analyzed at beamline **BL40XU**. A 6 μm X-ray microbeam was produced with a pinhole. The distance from the sample to the detector was 150 mm for the wide-angle X-ray diffraction (WAXRD) and 3000 mm for the small-angle X-ray scattering (SAXS). The sample was moved at 5 μm step so that the X-ray beam scanned it from the surface to the base, and the WAXRD and SAXS images were simultaneously obtained at each position (Fig. 3). From the WAXRD image, the intensity of the arc corresponding to the diffraction from the (100) plane of HAp was integrated and plotted against the depth of the enamel to produce a HAp profile. As shown in Fig. 4, the intensity was decreased by the demineralization treatment, and the profile was essentially the same as that obtained by the TMR method. Moreover, because, apart from its intensity, the diffraction pattern was unchanged by demineralization treatment, the HAp crystallite structure is conserved in the demineralized enamel. The SAXS intensity represented the amount of voids in the enamel crystallites. It increased in the subsurface area where demineralization was observed in WAXRD and TMR, showing that the crystallites became thinner and voids were created between them. These results suggest that the size of the HAp crystallites is decreased by demineralization but their orientation is conserved [4]. This technique is expected to be useful for analyzing the demineralization and remineralization mechanisms of tooth enamel.

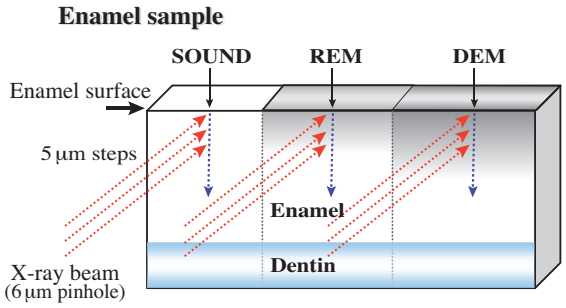

Fig. 3. Scheme of X-ray diffraction analysis of enamel samples.

It is anticipated that, if calcium is positively provided by the ingestion of calcium-rich foods under neutral condition, the calcium ions from foods and phosphate ions from saliva can facilitate the remineralization of the early caries [5]. We found that phosphoryl oligosaccharide of calcium (POs-Ca) provides "active" calcium ions to the subsurface lesion under neutral pH condition. It is soluble in saliva without forming precipitates with phosphate or carbonate ions and drastically promotes the remineralization [5]. In our latest study, we found that the remineralization with POs-Ca was actually "recrystallization": the regrown HAp crystallites were found by microbeam X-ray diffraction to have the same orientation as the original sound enamel. This demonstrates that POs-Ca can heal the lesion through the recrystallization of HAp crystallites in the enamel with regard to both volume and orientation.

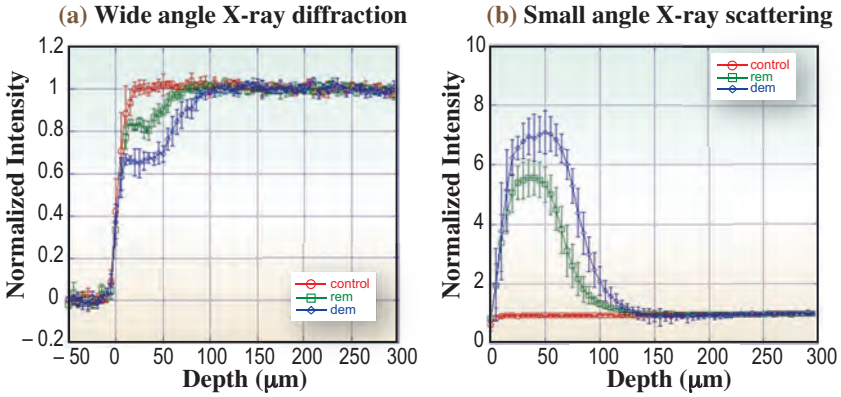

Fig. 4. Plots of X-ray diffraction intensities against depth of sound (control), remineralized zone (rem), and demineralized zone (dem) enamels. **(a)** Wide-angle X-ray diffraction. **(b)** Small-angle X-ray scattering.

Tomoko Tanaka*, Yoshinobu Terada and Hiroshi Kamasaka

Institute of Health Sciences, Ezaki Glico Co., Ltd.

*E-mail: tanaka-tomoko-2@glico.co.jp

References

[1] O.B. Dirks: J. Dent. Res. **45** (1966) 503.
[2] D. Angmar *et al.*: J. Ultrastructure Res. **8** (1963) 12.
[3] J.J. Damen *et al.*: Adv. Dent. Res. **11** (1997) 415.
[4] *N. Yagi, N. Ohta, T. Matsuo, T. Tanaka, Y. Terada, H. Kamasaka, K. To-o, T. Kometani and T. Kuriki: J. Synchrotron Rad.* ***16*** *(2009) 398.*
[5] H. Kamasaka *et al.*: Trends Glycosci. Glycosci. **15** (2003) 75.

Nuclear

PHYSICS

The linearly polarized photon beam is produced by backward Compton scattering of laser photons from 8 GeV electrons at BL33LEP. The current LEPS facility studies photoproduction of hadrons at forward angles, where the high linear polarization plays an essential role to decompose various reaction processes.

The beam polarization is high and can be changed easily by changing the laser polarization. The LEPS covers a photon energy region from 1.5 GeV to 2.9 GeV, which is suitable for studying the creation of excited baryons containing a strange quark or an anti-strange quark near the production thresholds. The production and decay properties of the excited hadrons shed light on their structure in terms of confined quarks.

The first topic we chose is the penta-quark Θ^+ photoproduction from a deuteron target. The aim of the study is to confirm the first evidence of Θ^+, which was reported in 2003 by the LEPS collaboration. The Fermi-motion corrected invariant mass of a neutron and K^+ clearly shows an evidence of Θ^+ with improved statistics.

The second topic we chose is the $\Lambda(1520)$ photoproduction from protons and deuterons. $\Lambda(1520)$ is an excited hyperon with a mass similar to that of Θ^+. A theoretical model on photoproductions of $\Lambda(1520)$ predicted that the main contribution for the production is a contact-term contribution associated with the t-channel K exchange process. The validity of the model was tested by measuring the cross sections and photon beam asymmetry simultaneously.

Takashi Nakano
Research Center for Nuclear Physics
Osaka University

Further Evidence for Θ^+ from LEPS

Since the LEPS collaboration reported the observation of a narrow baryon resonance-like structure in the nK^+ invariant mass spectrum produced in $\gamma n \rightarrow K^+K^-n$ reactions [1], a considerable number of experiments have been carried out to check the existence of the exotic baryon Θ^+, which is a genuine exotic baryon with the minimum quark configuration of $uudd\bar{s}$.

Although the LEPS result seemed to be supported by several experiments, many experiments at high energies, particularly collider experiments, yielded no positive evidence in the pK_s invariant mass distributions with a good mass resolution and high statistics. The experiment most relevant to the current study was also carried out by the CLAS collaboration [2]. The search was carried out by detecting all charged particles in the final state in $\gamma d \rightarrow K^-K^+n$ reactions. The neutron momentum was reconstructed by the missing momentum technique, and Θ^+ was searched in the nK^+ invariant mass distribution. No narrow peak was observed, and the upper limit (95% CL) for the elementary $\gamma n \rightarrow K^-\Theta^+$ reaction was found to be ~3 nb by using a phenomenological model based on $\Lambda(1520)$ production.

To shed light on the controversial situation, we studied the photoproduction of Θ^+ from a neutron by closely comparing it with the photoproduction of $\Lambda(1520)$ from a proton in a deuteron. Because the LEPS detector has a symmetric acceptance for positive and negative particles, a similar procedure can be applied to both analyses. The validity of corrections and event selection criteria can also be cross-checked. The analysis was performed using the data collected with the LEPS detector in 2002-2003 [3].

A photon beam in the energy range from 1.5 GeV to 2.4 GeV is produced at BL33LEP by Compton backscattering of laser photons from 8 GeV electrons in the storage ring with a typical beam intensity of 10^6 photons/s. The photons were alternatively injected into liquid deuterium (LD_2) or liquid hydrogen (LH_2) targets.

We analyze events of the type $\gamma d \rightarrow K^+K^-X$, where X denotes particles that were not required to be identified by the LEPS detector. Because the momenta of the target nucleons are not measured, the minimum momentum spectator approximation (MMSA) has been developed to obtain the invariant mass of pK^- or nK^+ pairs from $\gamma d \rightarrow K^+K^-pn$ reactions. The processes of interest are sequential processes of quasi-free productions of $\Lambda(1520)$ or Θ^+ and their decays, $\gamma p \rightarrow K^+ \Lambda(1520) \rightarrow K^+K^-p$ and $\gamma n \rightarrow K^-\Theta^+ \rightarrow K^-K^+n$.

The dominant contribution in the selected K^+K^-

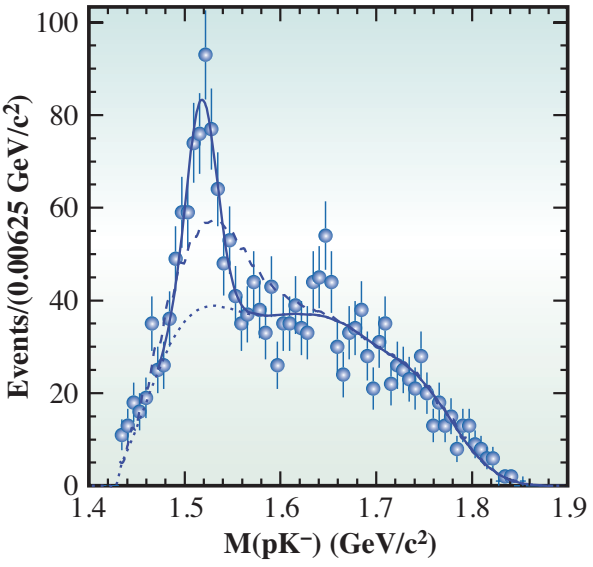

Fig. 1. $M(pK^-)$ distribution with a fit to the background spectrum only (dashed line) and with a Gaussian function (solid line). The dotted line is the background.

events is from φ decays, which are rejected by a cut on the KK invariant mass. Figure 1 shows the $M(pK^-)$ distribution, where the Λ(1520) contribution is clearly identified.

The $M(pK^+)$ distribution for the final candidate events is shown in Fig. 2. There is a narrow peak structure near 1.52-1.53 GeV/c^2. The distribution is fitted to the RMM spectra with and without a Gaussian peak with the estimated width of 11 MeV/c^2 to represent the Θ^+ signals. The statistical significance is 5.2σ, and the differential cross section for the $\gamma n \rightarrow K^-\Theta^+$ reaction is estimated to be 12 ± 2 nb/sr in the LEPS angular range.

There is a contradiction between the upper limit given by CLAS [2] and the differential cross section given here. However, there are differences between the CLAS and the LEPS measurements. If Θ^+ is mainly produced at forward angles, it is possible that CLAS would not see the K^- associated with Θ^+ production because the most forward angle for K^- detection is about 20 degrees in the CLAS measurement, whereas most of the LEPS acceptance is within 20 degrees. In the near future, LEPS will analyze data with a larger acceptance using a time-projection chamber for large angles to provide the Θ^+ angular distribution.

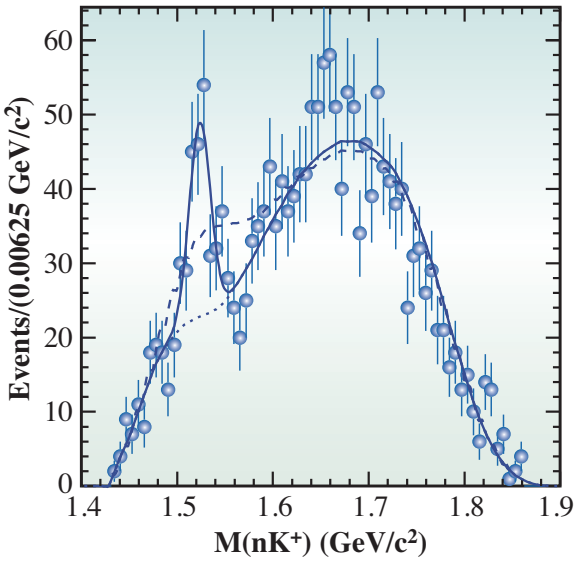

Fig. 2. $M(pK^+)$ distribution with a fit to the background spectrum only (dashed line) and with a Gaussian function (solid line). The dotted line is the background.

Takashi Nakano for LEPS Collaboration

Research Center for Nuclear Physics (RCNP),
Osaka University

E-mail: nakano@rcnp.osaka-u.ac.jp

References

[1] T. Nakano *et al.*: Phys. Rev. Lett. **91** (2003) 012002.
[2] B. McKinnon *et al.*: Phys. Rev. Lett. **96** (2006) 212001.
[3] *T. Nakano, N. Muramatsu, D.S. Ahn, J.K. Ahn, H. Akimune, Y. Asano, W.C. Chang, S. Daté , H. Ejiri, H. Fujimura, M. Fujiwara, S. Fukui, H. Hasegawa, K. Hicks, K. Hori, T. Hotta, K. Imai, T. Ishikawa, T. Iwata, Y. Kato, H. Kawai, Z.Y. Kim, K. Kino, H. Kohri, N. Kumagai, S. Makino, T. Matsuda, N. Matsuoka, T. Matsumura, T. Mibe, M. Miyabe, Y. Miyachi, M. Niiyama, M. Nomachi, Y. Ohashi, H. Ohkuma, T. Ooba, D.S. Oshuev, C. Rangacharyulu, A. Sakaguchi, P.M. Shagin, Y. Shiino, A. Shimizu, H. Shimizu, Y. Sugaya, M. Sumihama, Y. Toi, H. Toyokawa, A. Wakai, C.W. Wang, S.C. Wang, K. Yonehara, T. Yorita, M. Yoshimura, M. Yosoi and R.G. T. Zegers: Phys. Rev. C **79** (2009) 025210.*

Near-Threshold Photoproduction of Λ(1520) from Protons and Deuterons [1]

Λ(1520) is an excited state of baryon resonance composed of up, down, and strange quarks in naive quark models. Its mass and spin have been experimentally determined to be 1519.5 MeV/c^2 and 3/2, respectively. Recently, the study of Λ(1520) has received much attention as a reference state of possible exotic hadrons. For example, the hypothetical pentaquark state Θ^+ ($uudd\bar{s}$) has a similar mass (1530 MeV/c^2) with an opposite strangeness, and it has been observed only in the near-threshold photoproduction from neutrons [2] but not from protons. Theoretically this difference can be explained by the dominant contribution of the contact-term diagram, which is necessary to conserve gauge invariance with t-channel *K*-meson exchange [3]. This theoretical framework also predicts that the near-threshold photoproduction of Λ(1520) from neutrons is much smaller than that from protons. Nevertheless, there are no experimental results of Λ(1520) photoproduction from protons at the near-threshold energies nor from neutrons in any energy region. Another exotic hadron candidate, which has a mass close to Λ(1520), is Λ(1405). This state is considered to be degenerated with Λ(1520) in naive quark models, but their mass difference is larger than that expected from spin-orbit force. Therefore, the importance of the meson-baryon correlation inside Λ(1405) has been intensively discussed. The hadron structure of Λ(1520) is also interesting as a reference state, and it can be studied by the access through the $K^*N\Lambda(1520)$ coupling in photoproduction experiments.

The LEPS collaboration has collected data to investigate Λ(1520) with a linearly polarized photon beam produced at **BL33LEP** by backward Compton scattering of an Ar laser (7 W, ~351 nm) from 8 GeV electrons. Photons in the energy range of 1.5-2.4 GeV were tagged by detecting recoil electrons, and liquid hydrogen (LH_2) or deuterium (LD_2) targets were alternatively exposed to the photon beam at an intensity of ~10^6/s. The integrated numbers of tagged photons reached ~2.8×10^{12} for the LH_2 runs and ~4.6×10^{12} for the LD_2 runs in the years 2002-2003. Charged particles produced at the targets were detected and momentum-analyzed using the LEPS forward spectrometer, which consisted of a silicon vertex detector, three drift chambers and a dipole magnet (0.7 Tesla). Those charged particles were identified by measuring their time-of-flight at a plastic scintillator wall 4 m downstream of the target. We detected two charged particles in the final state of the $\gamma p \rightarrow K^+\Lambda(1520) \rightarrow K^+K^-p$ or $\gamma n \rightarrow K^0\Lambda(1520) \rightarrow K^0K^-p$ reaction. When K^+K^- or K^+p pairs were detected at the forward spectrometer, the backward photoproduction of Λ(1520) at the γp center-of-mass system was kinematically accepted and Λ(1520) was identified in the K^+ missing mass spectrum assuming the proton mass for the target. (See Figs. 1(a) and 1(b).) In contrast, the forward photoproduction of Λ(1520) at the γp or γn center-of-mass system was covered by detecting a K^-p pair at the forward spectrometer, and Λ(1520) was identified in the K^-p invariant mass spectrum, as shown in Figs. 1(c) and 1(d).

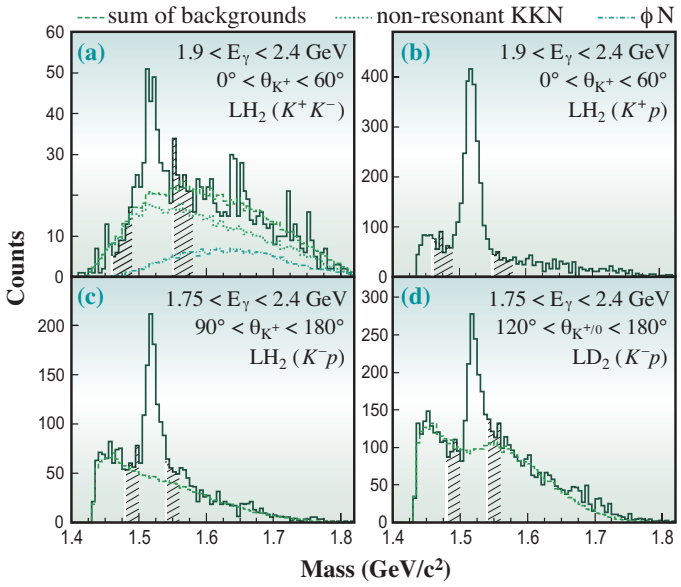

Fig. 1. Panels **(a)** and **(b)** show K^+ missing mass spectra for the LH_2 runs in the K^+K^- and K^+p detection modes, respectively. Panels **(c)** and **(d)** show K^-p invariant mass spectra in the K^-p detection mode for the LH_2 and LD_2 runs, respectively.

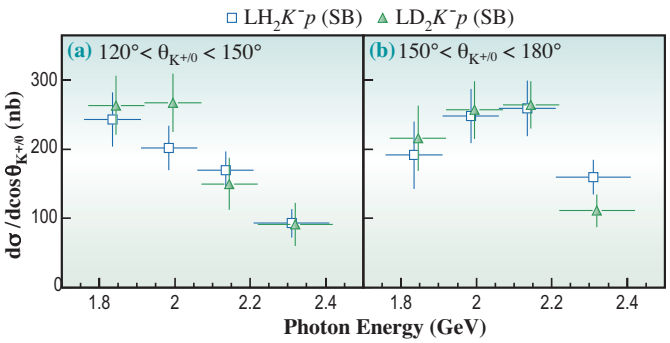

Fig. 2. Differential cross sections of the Λ(1520) photoproduction from protons (□) and deuterons (▲) in the two backward $K^{+/0}$ angular regions.

Figure 2 shows differential cross sections of the forward Λ(1520) photoproduction from protons and deuterons, measured in the K^-p detection mode. The cross sections from deuterons were comparable to those from protons, although the number of nucleons was twofold. Their ratio was measured to be 1.02±0.11 in the range of $1.75<E_\gamma<2.4$ GeV and $120°<\theta_{K^{+/0}}<180°$. The Λ(1520) photoproduction from neutrons was therefore found to be suppressed, as predicted by the theory advocating the importance of contact-term diagram. Figure 3(a) shows differential cross sections of the reaction $\gamma p \rightarrow K^+\Lambda(1520)$, measured in 30° bins of K^+ angle, using all the detection modes. The cross sections at the forward K^+ angles were more than three times larger than those at the backward K^+ angles, and this behavior was consistent with the theoretical prediction based on the dominant contribution of the contact term and K exchange, as shown by the dashed and dotted lines corresponding to E_γ=1.85 and 2.35 GeV, respectively. The cross sections measured at forward K^+ angles were lower than the theoretical predictions calculated on the basis of the old high energy measurement by the LAMP2 Collaboration. (See Fig. 3(b).) The present result suggests new information for theoretical models, including the rescaling with a new cut-off parameter, as done in Fig. 3(a). We also measured the degrees of asymmetry in the $\Lambda(1520)\rightarrow K^-p$ decay angular distribution at the t-channel helicity frame of rest Λ(1520) and in the azimuthal angle distribution of the Λ(1520) production plane relative to the polarization vector of the photon beam. In particular, the latter asymmetry, called photon beam asymmetry (Σ), is sensitive to the strength of the $K^*N\Lambda(1520)$ coupling constant. We found this asymmetry to be close to zero (Σ=-0.01±0.07), and the $K^*N\Lambda(1520)$ coupling constant was therefore small. Although the present measurement is not precise enough to discuss the hadron structure of Λ(1520), our observation suggests that the t-channel K^* exchange contribution is small in Λ(1520) photoproduction. This result is consistent with the theory emphasizing the dominance of contact-term contribution.

In summary, we studied the Λ (1520) photoproduction from protons and deuterons by detecting two charged particles in three different ways that were complementary to each other in acceptance. The present analyses were the first ever measurements near the threshold energy and with a neutron target. The measured differential cross sections and photon beam asymmetry suggested that the contact-term contribution associated with t-channel K exchange is important in Λ(1520) photoproduction and that the $K^*N\Lambda(1520)$ coupling constant is relatively small.

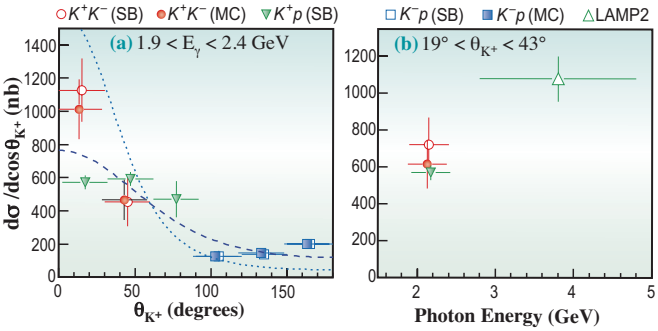

Fig. 3. **(a)** Differential cross sections from protons, measured by three different detection modes. Background spectra under the Λ(1520) resonance peak were subtracted by the two methods using sidebands (SB) and Monte Carlo simulations (MC). **(b)** Differential cross sections of the $\gamma p \rightarrow K^+\Lambda(1520)$ reaction at forward K^+ angles, measured by this work and the LAMP2 Collaboration.

Norihito Muramatsu for the LEPS Collaboration

Research Center for Nuclear Physics (RCNP),
Osaka University

E-mail: mura@rcnp.osaka-u.ac.jp

References

[1] *N. Muramatsu, J.Y. Chen, W.C. Chang, D.S. Ahn, J.K. Ahn, H. Akimune, Y. Asano, S. Date´ , H. Ejiri, H. Fujimura, M. Fujiwara, S. Fukui, S. Hasegawa, K. Hicks, K. Horie, T. Hotta, K. Imai, T. Ishikawa, T. Iwata, Y. Kato, H. Kawai, K. Kino, H. Kohri, N. Kumagai, S. Makino, T. Matsuda, T. Matsumura, N. Matsuoka, T. Mibe, M. Miyabe, M. Miyachi, T. Nakano, M. Niiyama, M. Nomachi, Y. Ohashi, H. Ohkuma, T. Ooba, D. S. Oshuev, C. Rangacharyulu, A. Sakaguchi, P.M. Shagin, Y. Shiino, H. Shimizu, Y. Sugaya, M. Sumihama, Y. Toi, H. Toyokawa, A. Wakai, C.W. Wang, S.C. Wang, K. Yonehara, T. Yorita, M. Yoshimura, M. Yosoi, and R.G.T. Zegers: Phys. Rev. Lett.* ***103*** *(2009) 012001.*
[2] T. Nakano *et al.*: Phys. Rev. C **79** (2009) 025210.
[3] S.-I. Nam *et al.*: Phys. Rev. D **71** (2005) 114012.

Accelerators & Beamlines Frontiers

Beam Performance

Developments and Upgrades of Storage Ring and Booster Synchrotron

Improvement of the Coupling Correction

The vertical beam spread is one of the most important parameters for the high brilliance storage ring, which is represented by the coupling ratio of the horizontal and vertical beam emittances. The coupling between the horizontal and vertical betatron oscillations and the vertical dispersion with the energy spread generate the vertical beam spread, so that they should be corrected. The latter has been corrected since 1999, and the former since 2007, both of which are controlled using skew quadrupole magnets [1-3].

The betatron coupling has an effect on the beam through the resonance of the beam motion. The coupling has sum and difference resonances that form the lattice on the tune map, as shown in Fig. 1. In the early stage of the coupling correction, only the nearest neighbor resonance ($\nu_x - \nu_y = 22$) to the operation point (40.15, 18.35) was corrected. At present, to improve the correction, four resonances surrounding the operation point are corrected.

From the perturbation theory of the betatron motion with the single resonance approximation [4,5], it is implied that the vertical beam size is proportional to the strength of the coupling resonance. Hence, the strengths of the skew quadrupole magnets for the coupling correction are determined so as to give the minimum vertical beam size. Resonance modes are orthogonal to each other, so that they are corrected independently by the appropriate combination of skew quadrupole magnets. Moreover, although the strength of the coupling resonance is a complex value and has two degrees of freedom, it is corrected independently with a sufficient number of skew quadrupole magnets. The tuning process of the coupling correction is shown in Fig. 2. The fitting curves obtained with the quadratic approximations represent the changes in the vertical beam size with respect to the strengths of the coupling resonances in terms of the skew quadrupole magnets. The light blue crossing symbols joined by the straight lines represent the minimum vertical beam size in each tuning process of the coupling resonances. The more the modes of the coupling resonances are corrected, the smaller the vertical beam size becomes.

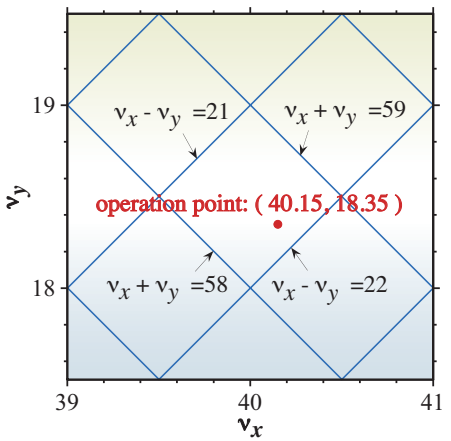

Fig. 1. Coupling resonances around the operation point in the SPring-8 storage ring.

In tuning of the emittance coupling, the vertical dispersion correction is performed after the betatron coupling resonance correction. This is because the former correction can be performed without exciting the coupling resonances. As a result of these corrections, we achieve the emittance coupling ratio of 0.2%.

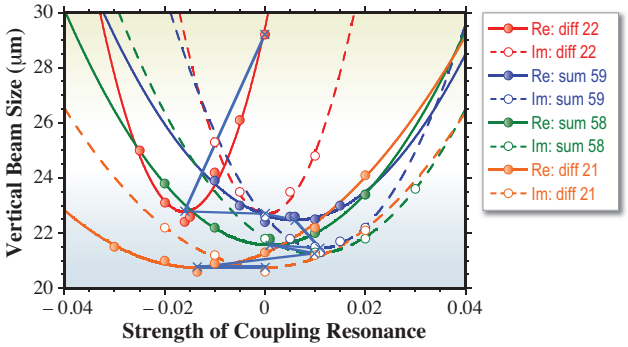

Fig. 2. Tuning of the coupling correction.

Lattice Modification for Installing Small-Gap Undulators in the Long Straight Section

There are four magnet-free long straight sections of about 30 m in the SPring-8 storage ring. In two of these sections, a 25-m-long undulator (BL19LXU) and a series of figure-8 undulators (BL07LSU) have already been installed. In addition, a set of short-period undulators with a narrow gap is planned to be installed in one of the remaining long straight sections to build a high performance beamline for inelastic X-ray scattering (BL43LXU). To obtain sufficient photon flux and brilliance over a desired energy range, it is necessary to make the minimum undulator gap as small as possible.

To this end, we designed a new lattice (Fig. 3)

in which one of the long straight sections is divided into three sub-sections for installing three 5-m-long undulators and the rest of the ring is kept unchanged. Additional quadrupole magnets will be installed between the sub-sections to lower the vertical betatron function, and hence, allow smaller undulator gaps. The vertical betatron function takes the minimum value of 5.0 m at the middle of each sub-section, and the allowable minimum gap of undulators is 5.2 mm that is obtained by scaling the currently allowed minimum gap at other straight sections.

In the new lattice, however, the symmetry of the ring is lowered, and in general, in such a ring with low symmetry, it becomes difficult to maintain a sufficient dynamic aperture for on- and off-momentum electrons. If the dynamic aperture shrinks, the injection efficiency and beam lifetime are largely affected. To avoid this and keep the dynamic aperture large, we extended the method of "quasi-transparent matching of sextupole fields" [6] by incorporating the concept of "counter-sextupoles" [7] and applied it. With this new technique, we could recover the dynamic aperture even after breaking the lattice symmetry as shown in Fig. 4: we kept the betatron phase condition for transparent matching of optics, carried out local chromaticity correction for off-momentum electrons and reduced the dominant effect of nonlinear kicks using sextupole magnets in the matching section. Commissioning of the new beamline is planned in the second half of 2011, and accelerator components (magnets, vacuum chambers, girders, new power supplies, etc.) will be rearranged and settled in accordance with the schedule.

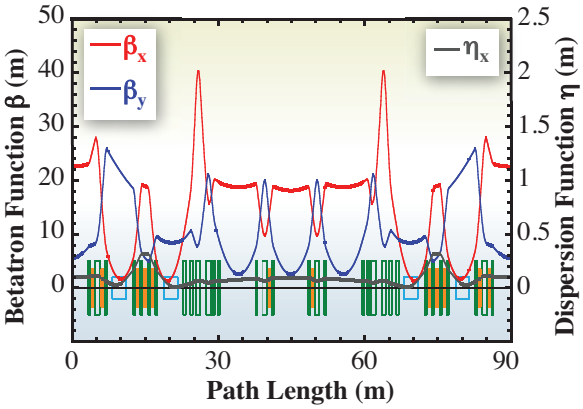

Fig. 3. Newly designed lattice functions for the modified long straight section for BL43LXU. The horizontal betatron function (β_x), vertical betatron function (β_y), and horizontal dispersion function (η_x) are shown. Also shown in the figure is the magnet arrangement (blue: bending magnets, green: quadrupole magnets, orange: sextupole magnets).

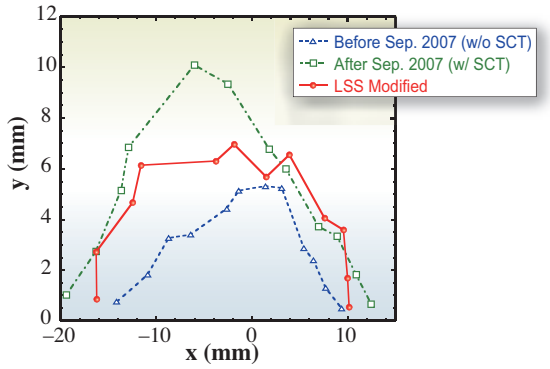

Fig. 4. Comparison of dynamic aperture simulations. The dashed line (blue) is for the ring without counter-sextupole magnets before September 2007, the dot-dashed line (green) is for the ring with counter-sextupole magnets after September 2007, and the solid line (red) is for the ring with a locally modified long straight section as shown in Fig. 3.

Suppression of Stored Beam Oscillation at Injection

In top-up operation, it is important that frequent beam injections should not affect the stored beam. At the time of beam injection, a pulsed bump orbit is made using four bump magnets. This bump orbit is not closed perfectly, and as a result, the horizontal oscillation of a stored beam is excited. To stabilize the photon beam axis during injection, we have been trying to suppress the oscillation amplitude by improving the bump magnet design, reducing the effect due to the nonlinearity of sextupole magnets, tuning circuits of bump magnet power supplies, introducing a pulsed corrector magnet, etc. With these improvements, the amplitude of residual oscillation in the horizontal direction has now been suppressed well. However, a relatively large oscillation amplitude of about 0.4 mm in RMS remains at the timing of firing bump magnets, which is caused by the non-similarity of the temporal shape of the magnetic field.

From 2007, to suppress this residual oscillation at the timing of firing bump magnets, we started to test a newly developed fast kicker magnet system. We checked its performance with a beam and improved the power supply. A newly developed fast pulsed power supply can generate a current of about 200 A, corresponding to the magnetic field of 4.61 mT, with a pulse width of 1.0 μs. Although this pulse width is slightly broader than required, the kick performance is enough for suppressing the residual oscillation. We then optimized the timing and kick angle to generate the most effective counter kick, and the result is shown in Fig. 5. As seen from the figure, we could suppress the horizontal beam oscillation by about

60% using the kicker magnet system. In the future, we will improve the kicker performance and try to suppress the residual oscillation further.

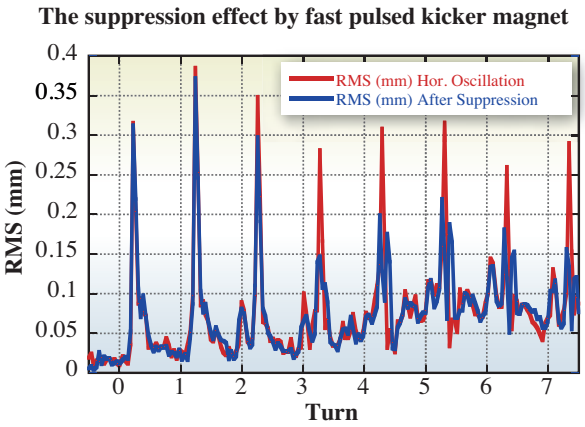

Fig. 5. Suppression of the horizontal beam oscillation using the fast pulsed kicker system. The RMS oscillation amplitude is plotted as a function of the timing (4.8 μs per turn) after the bump firing.

Development of Fast Pulsed Kicker Magnet System

A fast pulsed kicker magnet system can be used to give a vertical kick to the electron bunch and induce the head-tail oscillation for generating short pulsed X-rays [8]. We started developing this system in 2007. The main subject in this development is how to generate large currents with a narrow pulse width using a compact kicker magnet system. The specifications typically required for this system are as follows: current of more than 500 A corresponding to a magnetic field of about 8 mT, pulse width of less than 1 μs, and magnet length of about 0.3 m or shorter.

In constructing the system, we adopted the following as a guiding principle: firstly, we use an air-core type magnet with one-turn coils to lower the inductance as much as possible for fast pulse generation; secondly, we put a power supply system as close as possible to the kicker magnet for the same reason; finally, we separate the driving power supply system from the main high voltage system and put it close to the magnet. Hence, we needed to develop a new compact driving power supply system that should be comparable to the existing 500-A-class large power supply system.

A key technology for this development is the use of a power MOSFET as a switching device. The size of this device is about 2 cm × 2 cm, while the performance is almost the same as that of the IGBT, whose size is larger than that of the MOSFET by a factor of about 20. Using this device, we made the

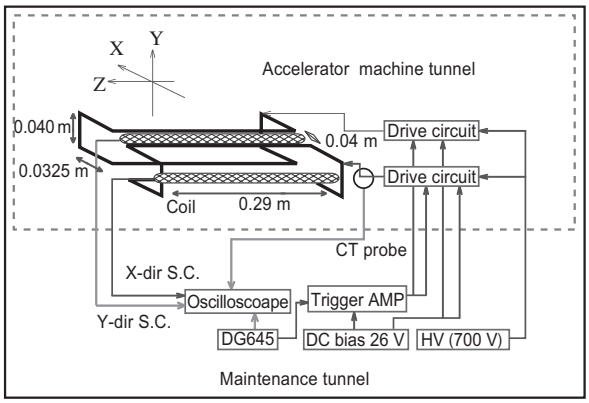

Fig. 6. Schematic of the kicker magnet system (vertical kicker case as an example). A driving circuit is connected to the high voltage power supply and delay generator DG645, and one circuit supplies current to one coil.

first test system and succeeded in generating 157 A/coil with 2.5 μs pulse width. In 2009, we started developing the second test power supply system and have recently succeeded in generating 270 A/coil with 1.0 μs pulse width. The conceptual design of our compact driving circuit is as follows: a high voltage (max. 900 V) is supplied from the external power supply system, the circuit is turned on by a TTL pulse signal of a trigger amplifier, and the resonant circuit is switched on by four MOSFETs connected in parallel. Figure 6 shows the schematic of the fast pulsed kicker magnet system. The kicker magnet is installed on the ceramic vacuum chamber so as to increase the penetrability of the magnetic field and decrease the eddy current effect and inductance. Figure 7 shows the cross-sectional structure of the kicker magnet and the actually installed kicker magnet system in the storage ring in the case of the vertical kicker. We will continue the development to increase the current up to 500 A and to realize a shorter pulse width of less than 1.0 μs. Results of the application of the fast kicker system can be found in Ref. [9] and elsewhere in this report.

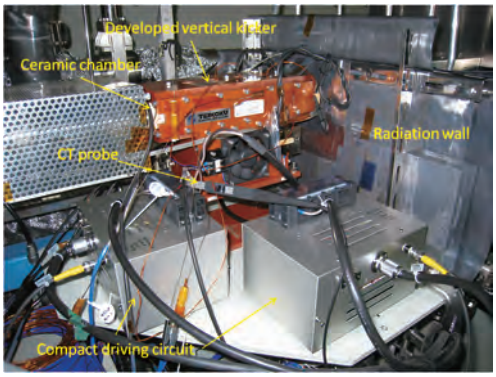

Fig. 7. Photograph of the vertical kicker magnet system installed in the storage ring.

Development of Bunch-by-Bunch Feedback System

The beam instabilities limit the average and bunch current in the SPring-8 storage ring. To overcome these instabilities, digital bunch-by-bunch feedback (BBF) systems were developed and in operation in the storage ring. The BBF is used to detect the position signal of each bunch from a beam position monitor (BPM), calculates the required amount of kick digitally, and drives kickers with bunch-by-bunch bases.

The hybrid filling composed of 10 mA/bunch singlet bunches and a train of bunches with 0.05 mA/bunch has a great advantage to fulfill simultaneously the requirements of both users of high current singlet bunches and of the average current. To achieve such filling, the BBF needs to suppress simultaneously the single-bunch mode-coupling instabilities of the singlet bunches and the coupled-bunch instabilities of the train of bunches. However, the contrast of the bunch current of those bunches is too high for usual BBF systems to control both high and low current bunches without any external devices.

To overcome this problem, we are developing the bunch current sensitive automatic attenuator (BSAT) shown in Fig. 8. The BSAT detects the bunch current and controls the variable attenuators to reduce the level of the BPM position signal of high current bunches to equalize the level of the position signal. Such device is already in operation for the bunch current ratio of six but is insufficient for the high ratio in such hybrid filling. The bench test of the attenuators was performed and satisfactory results in the attenuation and timing performance were obtained. The FPGA program that converts the feedback processor to the controller of the BSAT is under development.

To achieve such hybrid filling, we also need to increase the horizontal kick using the feedback kicker. The horizontal oscillation of the beam is excited by the injection bump formation, and a large kick is necessary to suppress the strong single-bunch instabilities under such large oscillation amplitude. To increase the horizontal kick, we installed the newly developed high efficiency horizontal kicker and confirmed its high efficiency with the beam test, and the kick is increased by a factor of 1.5. The high efficiency kicker also has a vertical kicker inside and its kick is two times more than those of the previous vertical kickers. With this, we could enhance the vertical feedback and could reduce the vertical chromaticity from six to two suppressing the strong beam instabilities in such low chromaticity. This reduction of the chromaticity increased the injection efficiency from ~85% to ~93%, or the beam loss is reduced to half.

In the booster synchrotron, the continuous vertical tune measurement is desired for the stable operation of the bunch purification system based on the RFKO method. However, the usual tune measurement method is not so fast for such application, and thus, we developed a new type of tune measurement system with the feedback shown in Fig. 9. During 100 ms after the injection, this system excites the beam with a positive feedback controlled using the SPring-8 digital

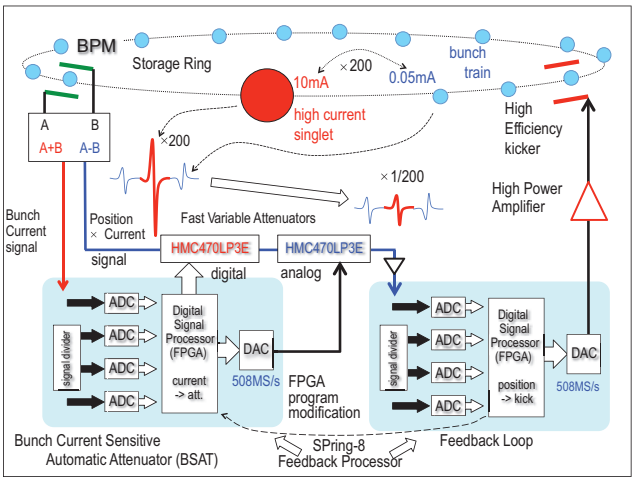

Fig. 8. Bunch current sensitive automatic attenuator (BSAT). The sum signal (A+B) of BPM electrodes (A,B), which is proportional to the bunch current, is detected using a processor based on the SPring-8 feedback processor whose FPGA program is modified for this purpose. The processor calculates the required attenuation and sets variable attenuators (HMC470LP3E and HMC470LP3E). The position signal pulses (A-B) of the bunches are attenuated as its bunch current, and then sent to the feedback processor.

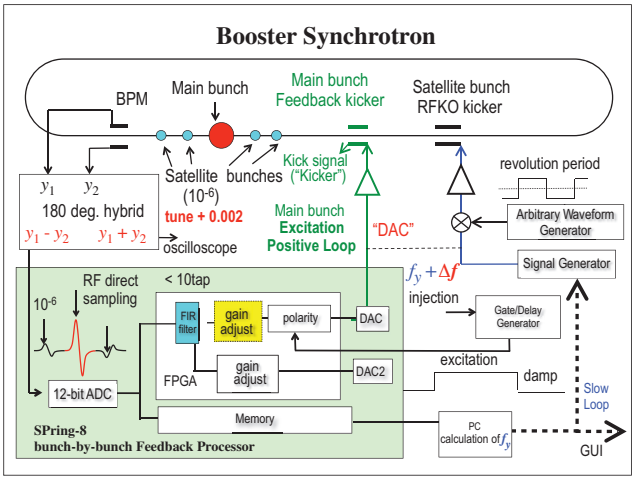

Fig. 9. Continuous tune measurement system for the booster synchrotron of SPring-8. The positive feedback loop by the feedback processor excites the vertical motion of the beam, and the vertical position data is stored in the memory of the processor. These data are sent to a PC to calculate the tune. After the measurement, the polarity of the feedback is inverted and the beam motion is damped. The control of the RFKO frequency (slow loop) based on the measured tune is not yet completed.

feedback processor, and the position data is stored in the memory of the processor for the analysis to find the tune. The beam test of this system was successfully performed.

Improvement of Beam Loss Monitor

By detecting a beam loss in the SPring-8 storage ring, manifesting its mechanism, and handling it, we can suppress irradiation-induced damage to accelerator components and avoid accidents such as vacuum leakage caused by the meltdown of a vacuum chamber [10] and demagnetization of permanent magnets of in-vacuum insertion devices (IDs) [11].

For this purpose, a noise-compensation-type beam loss monitoring system with PIN photodiodes has been developed since Oct. 2008 [12] and installed at characteristic points in the tunnel of the storage ring, such as the injection point, beam dump point, bending magnet of the cell-2 (c2-B2), entrance of the 25-m-long in-vacuum undulator (ID19), the minimum gap height of which is 12 mm, and chamber for the irradiation experiment (SS48).

In Sep. 2009, a common trigger system was introduced to the beam loss monitoring system and additional beam loss detectors were installed. Then, a beam loss distribution around the storage ring has been observed at all times during the user operation. Figure 10 shows the distribution of the beam loss signal on the nominal beam dump and on the beam abort observed from Oct. 28 to Nov. 15. The maximum value of 1.2 V in Fig. 10 indicates the saturation of the signal from the amplifier circuit for the beam loss monitor.

In the case of the nominal beam dump, the largest loss monitor signal is observed around the injection section (i.e., the injection point, dump point, and c2-B2), where a pulsed local bump orbit in the vertical direction is made for slowly scraping the electron beam on the timing of the nominal beam dump. The loss monitor signal is also observed at the out-vacuum IDs (ID05, ID07, and ID08) but not at the in-vacuum IDs (ID09, ID10, ID19, and ID20). It is considered that the secondary particles generated on the nominal beam dump are distributed around the injection section and at the out-vacuum IDs in the storage ring. The beam loss signal at the out-vacuum IDs seems to be related to a trajectory of the electron beam being distorted by the sextupole magnets in the vertical local bump orbit during the nominal beam dump. The mechanism why the beam loss is induced at the out-vacuum IDs on the nominal dump is now under investigation.

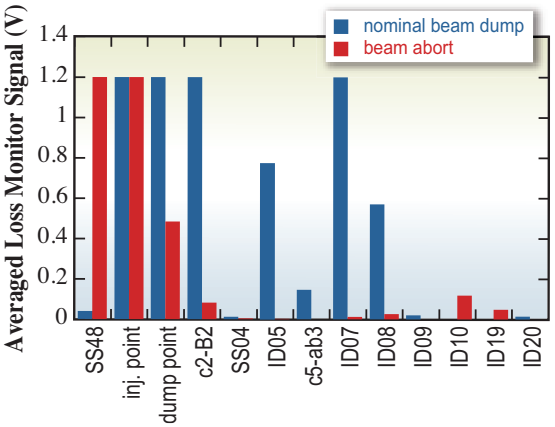

Fig. 10. Distribution of beam loss signal on nominal beam dump and beam abort.

In the case of the beam abort, at which the RF accelerating power is suddenly turned off, the beam loss signal is localized at the SS48 and injection point. The signal is not observed at the positions of the IDs. It seems that the chambers at the SS48 and injection point play a key role as the beam scraper. This result is well explained by the tracking simulation using CETRA code (see Fig. 11).

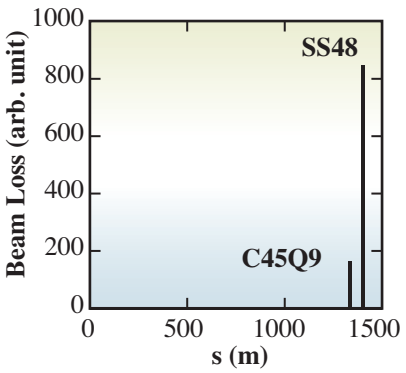

Fig. 11. Tracking result for the case of "beam abort" by CETRA.

Development of Accelerator Diagnostics Beamlines

Beam emittance is one of the most important characteristics of a synchrotron light source. Beam tests of generating short X-ray pulses have been carried out at SPring-8 by decreasing the momentum compaction factor α of the storage ring optics [13]. Operating the ring with optics of lower a value is controversial as it deteriorates the beam emittance.

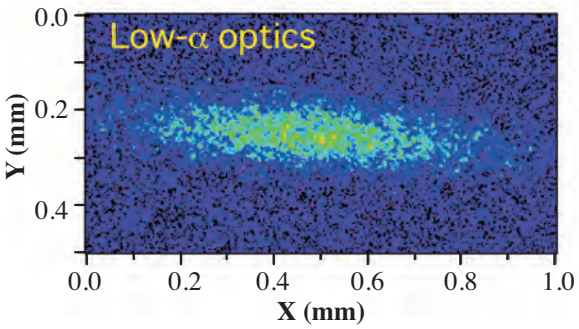

Fig. 12. An example of the beam profile observed with the XBI in the test of low-α operation. The horizontal beam size (s) was 216 mm, and the emittance deduced from the measured beam size was 25 nm·rad, consistent with the designed value of the optics.

Therefore, emittance diagnostics are crucial for tests of low-α operation. Figure 12 shows an example of the beam profile observed with the X-ray beam imager [14] implemented at the diagnostics beamline I (BL38B2). The emittance deduced from the measured beam size was consistent with the designed value, and it was confirmed that the emittance was properly controlled as designed in the tests of low-α operation.

We have plans to develop a diagnostics system of emittance and energy spread of the electron beam by measuring the energy spectrum and angular divergence of the higher harmonics of the ID at the diagnostics beamline II (BL05SS). Since the error magnetic fields reduce the spectral photon flux of higher harmonics, we have elaborated on tuning the magnetic field before installing of the ID. The well-corrected fundamental phase error of the magnetic field has led us to detect clear peaks of higher harmonics in the observed energy spectrum of the ID.

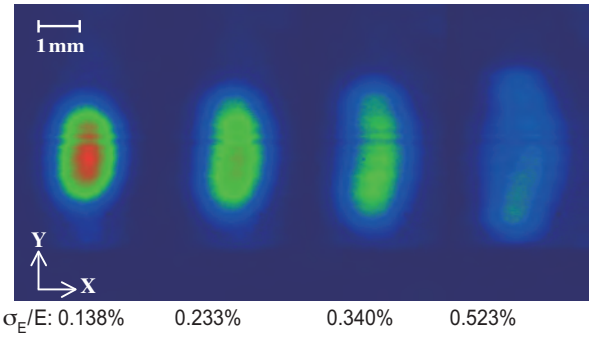

Fig. 13. Observed spatial profiles of the 19th harmonics of the ID at the monochromatic photon energy of 8.3 keV, while modulating the RF phase of the electron beam at the synchrotron frequency of 2.2 kHz. The horizontal angular aperture was limited by the front-end slit at 4 μrad. The values of the effective energy spread shown at the bottom were deduced by observing simultaneously temporal bunch oscillations with a visible light streak camera at the diagnostics beamline I.

The performance of the ID yielding clear higher harmonics peaks has encouraged us to apply it to the energy-spread diagnostics by observing a spatial profile in the vertical of the higher harmonics and to develop a fast turn-by-turn diagnostics system. Before developing the fast system, by observing the 19th harmonics of the ID, we confirmed experimentally that the vertical angular divergence of the higher harmonics has enough sensitivity to the beam energy spread. Figure 13 shows that the observed vertical profiles have larger widths for larger effective energy spread, which was increased by exciting the energy oscillation by modulating the RF phase at the synchrotron frequency.

We have been investigating the characteristics of an X-ray streak camera (X-SC) at the diagnostics beamline II to apply it to the diagnostics of short X-ray pulses generated by decreasing the momentum compaction factor α or by other methods. The temporal resolution of an X-SC is generally dominated by the effect of the energy spread of electrons emitted by the input photocathode. To evaluate it quantitatively, we analyzed the temporal spreads of single X-ray photons, which are the shortest X-ray pulses, on the X-SC image. Beam tests to generate short X-ray pulses are in progress at SPring-8 by slitting X-rays from an electron bunch tilted by a vertical single kick under nonzero chromaticity [8]. Figure 14 shows an example of an X-SC image of short X-ray pulses thus obtained after a half period of synchrotron oscillation from the single kick. The pulse length of 7.4 ps (FWHM) obtained with the kick is about six times shorter than that without the kick [9].

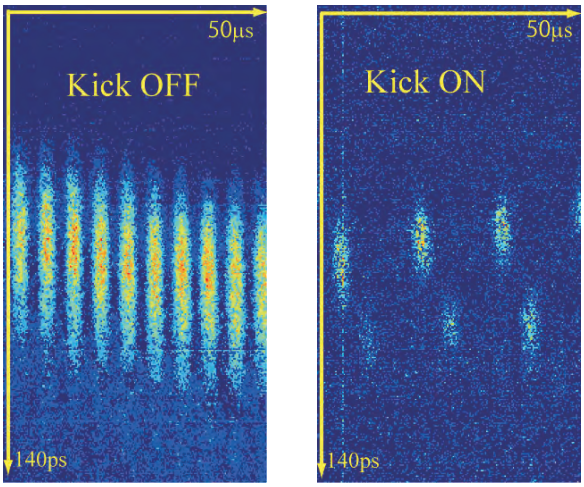

Fig. 14. X-SC image of X-ray pulse with/without a single vertical kick under nonzero vertical chromaticity. The X-SC was operated in the dual-time scan mode, and the horizontal scan separates the pulses from consecutive turns of the stored single bunch.

Investigation of Heating Problem of Gate Valves in the Storage Ring

The SPring-8 storage ring is running with various types of operation mode. Initially, the operation modes were restricted by beam instabilities; however, the limitation was overcome by introducing a bunch-by-bunch feedback system. Now, heat load for finger-type RF shields in gate valves is the major issue behind the restriction. More specifically, the temperatures inside the gate valves are controlled at less than 100°C, taking into account the creep rupture of beryllium-copper (BeCu) of the shields. However, we investigated more precisely the heat mechanism of the gate valves for future upgrades, such as bunch current increase, short pulse beam operation, and so on.

For starters, we assembled a BeCu RF shield with a silver plate, which has high electric conductivity, to suppress heat generation at the RF shield. We installed the gate valve with the silver plated RF shield the storage ring, and measured the temperatures at the RF shield and around it. However, there was no particular change in the temperatures with or without the silver plate on the shield, thus, any effects of the silver plate could not be recognized. This result was quite tricky, and the properties of thermal transfer in the gate valve should be figured out.

Therefore, we performed a bench test to investigate whether the heat load at the RF shield is released around the shield or not. Figure 15 shows a cross section of the gate valve (valve opened). The gate valve has two ICF152 flanges (1) on both sides. Stainless steel parts (2) are fixed with screws on each flange. A BeCu RF shield (3) is fixed between two stainless steel parts ((4) and (5)). In the case of "valve opened", (5) is pressed against (2) by a cam mechanism. There, we suspected that the thermal contact resistance between (2) and (5) is not good. To investigate this issue, we performed the following steps.

First, we mounted a heater on one flange (1) from outside and heated (2) at around 55°C, while keeping (2) and (5) separated. Next, we started to measure temperature changes on (2) and (4) in contact with (2) and (5).

Figure 16 shows measured correlations (marked as black) between time and temperatures on (2) and (4). The thermal contact resistance was calculated as 31.3 K/W. On the other hand, the thermal conductivity of (2) and (4) is 1.9 K/W in the thermal resistance and that the thermal contact resistance is clearly high. Considering the opposite, we concluded that the heat load at the RF shield could not be released enough to surrounding parts and this caused a temperature rise at the RF shield. Furthermore, we improved the gate valve to obtain better contact between (2) and (5), and followed the same test described above (Fig. 16 marked as red). The thermal contact resistance was extracted as 0.9 to 1.4, which is crucially improved by a factor of 1/20 compared with the prior result. In addition, we installed the gate valve, which has improved the contact between (2) and (5), and the maximum temperature rise at the RF shield could be suppressed by 10°C.

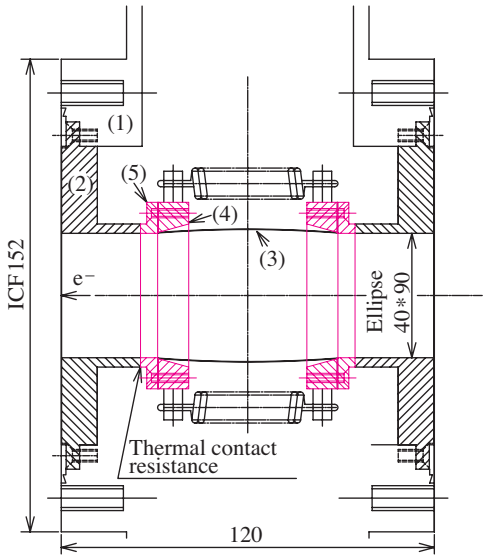

Fig. 15. Cross section of the gate valve (valve opened).

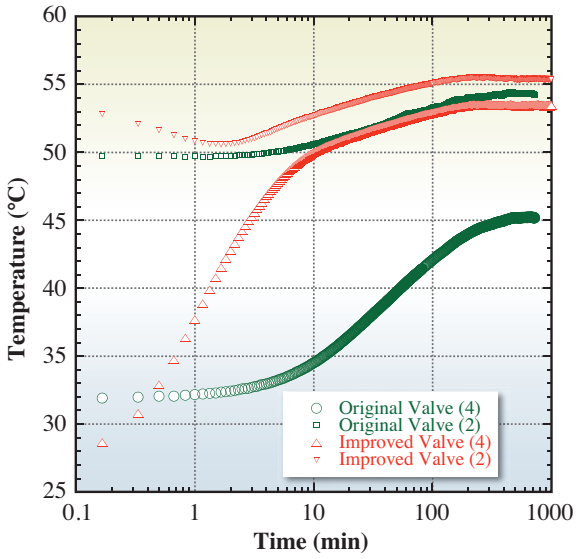

Fig. 16. Measured correlations between time and temperatures on (2) and (4) since the (2) and (5) contact.

Development of an Aluminum Flange with an Electron Beam Modified Seal Edge

Many aluminum (A2219-T852) flanges, which have a knife-edge seal, have been used at the SPring-8 storage ring. Since the flange material is A2219-T852 and ion plated, its delivery time is longer than that of the general-purpose one. Therefore, we investigated the possibility of introducing an aluminum flange that has an electron beam modified (EBM) knife-edge seal. We adopted A5052 as the base material for the EBM flange. Oxygen-free copper is melted in the seal part with the EB welding, and finally, the seal is formed with machining.

We performed an endurance test that consists of 10 times of flange fastening and 3 times of baking (150°C/1 h) for an ICF375 EBM flange prototype. After the endurance test, there was no leak of more than 1×10^{-11} Pa m^3/s and no degradation in the seal edge profile measured using a projector.

Furthermore, component analysis was carried out and the mechanical strength and creep rupture stress were investigated, particularly for the EBM part. It is found that the reformed part has a copper content of ~20 wt% and shows dendritic cells. Its hardness of ~180 Hv is higher than that of the original flange (~130 Hv). On the other hand, the mechanical strength (Table 1) and creep rupture stress (Fig. 17) of the EBM flange are higher than those of the original one in general. However, the elongation of the EBM flange is small, which is similar to that of cast metals.

We confirmed that the EBM flange has sufficient mechanical strength as the original flange at this stage. We plan further investigations on the tolerance to scratch and corrosion and so on.

Table 1. Mechanical properties of A5052-EBM and A2219-T852 at room temperature and 150°C

	Temperature	0.2% proof stress (N/mm^2)	Tensile strength (N/mm^2)	Elongation (%)
A5052-EBM	RT	352	470	0.7
A2219-T852	RT	339	439	8.7
A5052-EBM	150°C	307	444	1.3
A2219-T852	150°C	301	339	18.0

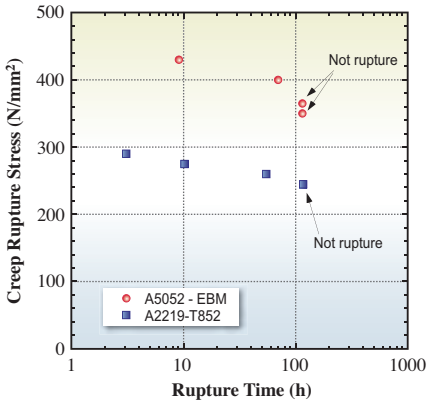

Fig. 17. Measured correlations of creep rupture stress and rupture time of A5052-EBM and A2219-T852 at 150°C.

Research and Development of Femtosecond Pulse X-ray Generation

The generation of an X-ray with an energy of 10.7 keV and a pulse width of 600 fs in two standard deviations can be achieved if we install superconducting crab cavities and a minipole undulator in one of the long straight sections of the SPring-8 storage ring. The flashing repetition of such an X-ray is the same as that of the preexisting synchrotron radiation, or that of the electron bunches circulating around the ring. This feature complements the low repetition of the X-FEL, which has extraordinarily high temporal intensities. This method, in addition, can supply a femtosecond X-ray without causing any disturbance to users on the other beamlines. Its principle of generation [15], performance expected with design parameters [16], and R&D issues such as a high power phase shifter [17] have been described in previous reports.

Now, our technical goal is in sight. Although our plan is not scheduled, it can be pictured more realistically. A layout was drawn to ensure that we could install all the necessary equipment in the building or in the limited open space between the ring and side of the mountain, sitting at the center of the storage ring. Although some existing cooling towers required transfer, we found it possible to construct buildings for a liquid-helium refrigerator and an RF power source (Fig. 18). We also can place four waveguides, four cryostats each with a crab cavity, one liquid helium transfer line, and one gas return line

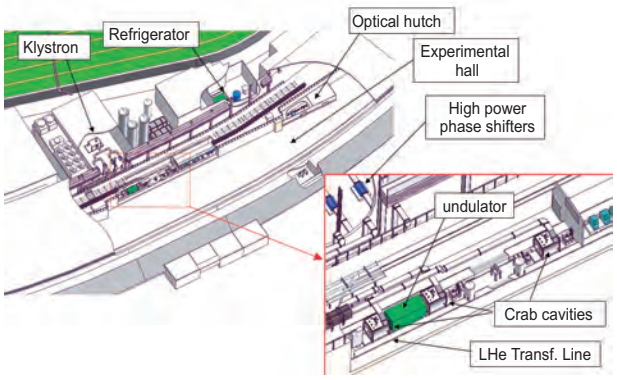

Fig. 18. Layout of the short-pulse X-ray generation system.

in the storage ring tunnel. We chose the route of the waveguides leading from the RF source to the cavities, taking both the phase stability and radiation shielding into account. In the case of a gas leak, the relevant area is partitioned off with bulkheads as a safety measure against oxygen deficiency.

High Power Test of the RF Cavity Dedicated to the Coupler Conditioning

We use 32 single-cell RF cavities in the storage ring and eight 5-cell RF cavities in the booster synchrotron. The resonant frequency of all the cavities is 508.58 MHz. To feed an RF power into the cavities, we used a rectangular-to-coaxial transducing RF input coupler [18]. Since the rated RF power of the 5-cell cavity is 300 kW, we subjected the coupler to a high-power test and conditioned it up to 300 kW before installation in the cavities.

In order to carry out the conditioning efficiently, we developed a compact RF cavity dedicated to the conditioning by referring to the one used in KEK [19]. The cavity has a diameter of 146 mm, a length of 130 mm, and a stub with a diameter of 70 mm and a length of 105 mm. Two couplers facing each other are connected to the cavity and couple to rotational magnetic fields around the stub tightly. An RF power is fed into the cavity through the upstream coupler and extracted from the cavity through the downstream coupler. About 1.7% of the feeding RF power dissipates over the inner surface of the cavity assembly. In order to efficiently remove the heat from the cavity body and prevent the destruction by heat stress, we made the body using OFHC copper and provided it with 13 cooling channels.

The resonant frequency of the cavity assembly inevitably changes because of errors in the measurement for fabricating or assembling. Therefore, we attached a frequency tuner to the cavity. Thus, the VSWR of the cavity assembly is kept less than 1.1 at 508.58 MHz.

We tested the fabricated cavity and conditioned the input couplers. Figure 19 shows the cavity assembly in the RF test stand. The vacuum pressure in the assembly became temporarily worse at about 10^{-2} Pa, but improved to 2×10^{-4} Pa during the conditioning in 20 h. The leakage X-ray from the inside of the cavity was small and we could carry out the high-power test without X-ray shields. Results showed that, we could successfully and stably transmit a rated RF power of 300 kW through the input couplers without damage to the couplers or the cavity.

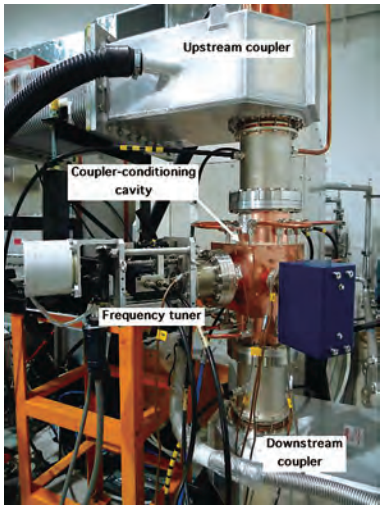

Fig. 19. Cavity assembly in the RF test stand of the SPring-8.

Improvement of RF Tuner Controller of Booster Synchrotron

The booster synchrotron of SPring-8 has 8 RF cavities that are named RF1Cav1···RF1Cav4, RF2Cav1···RF2Cav4, and each cavity consists of 5 cells independently equipped with a tuner controller. These years, it has been observed that the RF reflection occasionally became so large that the interlock system forced the RF supply to turn off. There are a couple of possibilities for the reflection. One is that a discharge occurs somewhere inside, and the other is that a tuner controller, which presumably works as a feedback system for a phase drift, happens to move in an opposite direction.

To solve the above problem, we carefully observed what was happening. For this purpose, we set up a data logger in the low level RF room so that RF phases and reflections at 8 cavities were recorded whenever the above problem occurs. The data logger was triggered by the so-called RF switch that is supposed to turn off when the large RF reflection triggered the interlock system. After observing such an event 16 times, it turned out that twice out of 16 times, the tuner controller moved in the opposite direction, which shifted the RF phase by 16 degrees in 900 ms (Fig. 20(a)). The RF reflection was linearly becoming larger by about 0.5 [arb. unit] in 900 ms, which eventually triggered the RF switch off. In the meantime, the phase drifted by as much as 14 degrees, whereas the tuner controller did not feedback the drift. We attribute it to the malfunction of the tuner controller. The other 14 cases appeared to be caused by discharge somewhere inside, since a

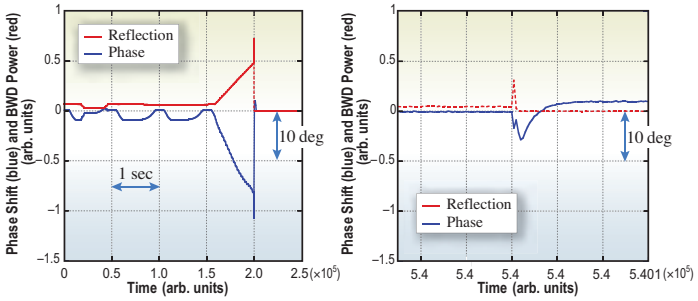

Fig. 20. Two examples of RF reflection and phase measurement.

large RF reflection occurred within a single sampling of the data logger with the sampling rate of 50 kS/s (Fig. 20(b)). Note that the time (horizontal) scales of the two figures are different.

Next, we developed a PLC-based tuner controller. The new controller has several new features, yet is fully compatible with existing apparatus. One of the biggest advantages of the new controller is that by taking advantage of the flexibility of PLC, the relative positions of 5 tuner controllers for each cell in a cavity can be kept constant. The function prevents the 5 tuners from becoming off balance, which that could induce a large RF reflection. Another feature is the availability of the FL-Net connection. In the future, all the connections between VME and PLC will be carried out via the FL-Net. The newly developed tuner controller was at first tested at the RF test stand, where we debugged the PLC logic by operating the controller manually and also remotely. For instance, we remotely operated the tuner controller using our PC to check if the remote commands properly operated the controller. After fixing all the recognized errors at the test stand, the tuner controller was moved to the booster synchrotron and connected to the RF2Cav4 tuner of the booster.

Now, as per November 19, 2009, the booster is running under normal user operation after we reinstalled the new tuner controller to RF2Cav4 in the first week of November, and no problem has been found since then. We made 8 more controllers and replaced all the existing tuner controllers with new ones in the winter of FY 2009. Even if unexpected errors showed up later, we were able to fix them by modifying the PLC software, which is also one of the advantages of PLC-based devices. We will keep watching if the number RF switch off due to the large reflection will be reduced or not.

Power Saving Operation for the SPring-8 Booster Synchrotron

During the top-up operation of the SPring-8 storage ring, the booster synchrotron ejects the beam only when the stored current becomes less than 99.5 mA. The interval of the beam ejection is usually about 20 s. We tested the intermittent excitation of the booster magnets to reduce the power consumption. The magnets stand with DC corresponding to 1 GeV during no beam, and operates 1-8 GeV pattern excitation during beam ejection.

Switching from the continuous to the intermittent operation of the magnet system changes the thermal loading of the equipment and the excitation current. As a result, the betatron tune shifts from the optimum value for the RFKO and it increases the bunch impurity of isolated bunches. Therefore, the intermittent operation was introduced only for a multi-bunch filling pattern without the necessity of bunch purity so far.

We improved a machine cooling system of the utility facility so that the temperature of the main cooling water to be stabilized is constant for both the continuous and intermittent operations. Figure 21 shows a block diagram of the machine cooling system. The temperature control for the main cooling water is performed by adjusting the subsidiary cooling water flow in a heat exchanger. To form the highly purified bunches by the RFKO, the vertical tune-shift should be converged within ±0.002. The improvement of the machine cooling system suppresses the tune-shift to less than 0.0015 between the continuous and intermittent operations. Therefore, the intermittent operation becomes applicable to the filling pattern with several isolated bunches. The results of electrical energy measurement of the magnet system are about 1500 kWh for the continuous operation and about 300 kWh for the intermittent operation. It can be expected

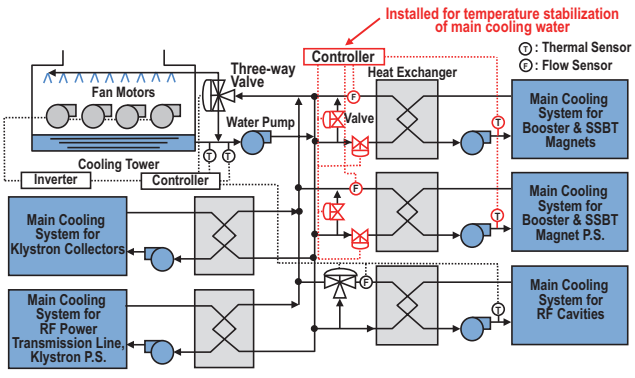

Fig. 21. Block diagram of the machine cooling system of the booster.

that the power consumption of the magnet system of the booster decreases to 1/5 in the top-up operation.

Development of Low Dark Current Accelerating Structure

For several-bunch operation of SPring-8, a very low impurity of bunch filling is required. A major source of the impurity originates from dark currents of an injector linac. An RF knockout system in a booster synchrotron is effectively operated to lower the impurity; however, lower dark currents of the linac are preferable. Thus, we are developing a new accelerating structure to reduce the dark currents emitted from the structure surface. Applied improvements are a new single-feed waveguide coupler and an ellipsoidal cross section of the disk iris. A design view of the structure is shown in Fig. 22.

The source points of the dark current locate near the disk iris where the electric field is concentrated. To moderate this concentration, the shape of the iris cross section was modified from a quasi-circle to an ellipse. The field strength was evaluated using a simulation code, CST Microwave Studio. The maximum field strength is minimized at where the major radius of the ellipse is approximately 4 mm. As a result, the maximum field strength was reduced to 87% of the original shape. The electric-field strength distributions in an original structure and a new one are shown in Fig. 23. Since the field-emitted currents are estimated to be roughly proportional to the electric field to the 16th power, the dark current emitted from the iris will be reduced by an order of magnitude.

In the waveguide coupler, an E-plane of the waveguide is attached to the disk-loaded structure, and the concentration of the surface current becomes smaller than that of a conventional H-field coupler. This feature reduces the pulse heating damage of the structure surface and leads to the reduction of the dark currents.

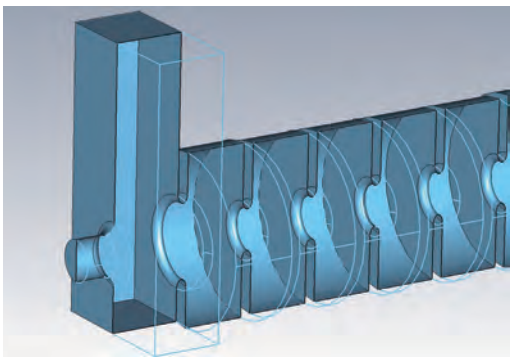

Fig. 22. Design view around the coupler cell of a low dark current accelerating structure.

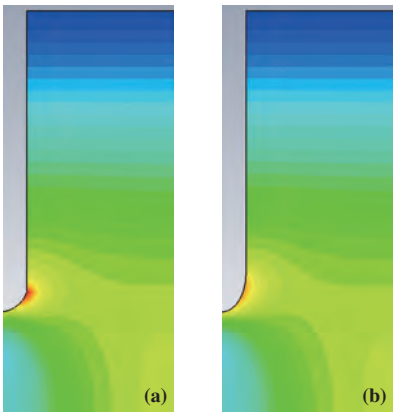

Fig. 23. Electric field strength distribution near the disk-iris. **(a)** existing structure, **(b)** new structure.

After the RF design, a 1-meter-long structure was fabricated as shown in Fig. 24. The main parameters are shown in Table 2. The cavity cells were finished using a diamond turning machine and bonded together by vacuum brazing. We plan a high power test of this structure in 2010.

Fig. 24. Low dark current accelerating structure after brazing.

Table 2. Parameters of low dark current accelerating structure

Frequency	2856 MHz
Phase shift / cell	2π/3 constant impedance
Coupler type	Waveguide coupler
Iris diameter (2a)	20 mm
Coupler iris diameter	36.4 mm
Disk thickness	5 mm
Iris shape (cross section)	Ellipse
(Major / minor radius)	(4.0 mm / 2.5 mm)
Group velocity v_g/c	0.01
Total length	1050 mm
Filling time	302 ns
VSWR	1.1

Developments and Upgrades of Linac

Laser Driven RF Signal Generation for Photocathode RF Gun

Precise synchronization between an RF signal and a laser pulse is essential for the pump-and-prove experiments using photocathode RF guns. The electron beam bunch lengths of less than hundreds femtoseconds have recently been utilized, and thus, the RF and laser synchronization has to be controlled so that its timing jitter becomes less than 100 fs. For this purpose, we developed an amplitude-stabilized RF signal generator driven by laser pulses generated by laser oscillator [20].

Circuit

The laser oscillator is simply synchronized with a 2856 MHz reference oscillator at the frequency of 89.25 MHz, 1/32 of 2856 MHz, by applying a PLL technique, as shown in the upper block of Fig. 25. The laser oscillator with a piezo-controlled mirror works as a voltage controlled oscillator in the PLL feedback. The measured timing jitters between the laser pulses and reference RF waves were 300-400 fs with this PLL feedback system. For further high-precision synchronization, we developed a laser-driven RF regeneration as follows.

A fast photodiode detects the 89.25 MHz laser pulses and generates electric pulses of the same frequency, as shown at the upper left of the bottom block in Fig. 25. The next stage circuit filters the pulse signal and picks up only the 2856 MHz waves from among the higher harmonics. Thus, the RF signal of 2856 MHz can be regenerated from the 89.25 MHz laser pulses.

To reduce the RF variation caused by the laser power fluctuation, we designed an amplitude-stabilized RF generator employing the following two key components: a limiter amplifier (GigOptix, iT3011E) stabilizes the RF signals from the photodiode, and a comb generator (Herotec, Inc., GC100) produces narrow pulses with a fast rise-time resulting in intense higher harmonics. The following cavity type BPF passes only the 32nd harmonics, 2856 MHz.

Performance

The output power variation of the amplitude-stabilized RF generator was kept within 1.5% when the 89.25 MHz pulse signal varied in the power range of 10 dB. The short-term (<1 min) amplitude stability for the stabilized RF generator was decreased to 0.20% (RMS), while that for the unstabilized one was 0.27% (RMS). According to these results, we have confirmed that the amplitude stabilization effectively worked against not only the long-term drift, but the short-term fluctuation of the laser power.

The short-term (< 1 s) jitter was about 160 fs for the stabilized RF generator, which is almost the minimum resolution of the measurement system, while that of the unstabilized one was about 270 fs. This result shows that the stabilized generator has an advantage in the timing synchronization compared with the unstabilized one.

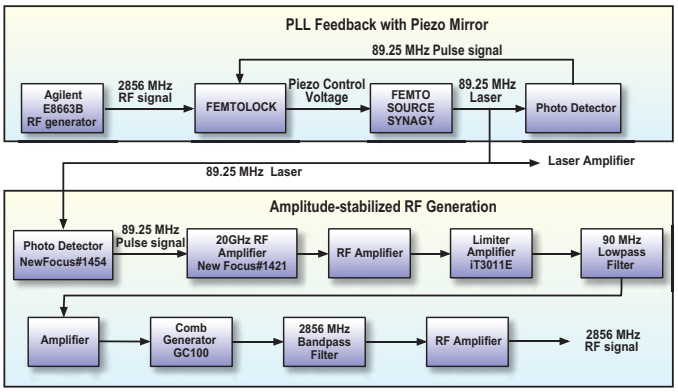

Fig. 25. Block diagram of amplitude-stabilized laser-driven rf generator.

Haruo Ohkuma*, Hiroto Yonehara and Hirofumi Hanaki

SPring-8/JASRI

*E-mail: ohkuma@spring8.or.jp

References

[1] M. Takao *et al.*: Proc. 4th Annual Meeting of Particle Accelerator Society of Japan, 2007, p.622.
[2] SPring-8 Annual Report 2006, p.19 (in Japanese).
[3] M. Masaki *et al.*: Proc. EPAC2008, p.3035.
[4] G. Guignard: Phys. Rev. **E51** (19995) 6104.
[5] M. Takao: Phys. Rev. STAB **9** (2006) 084002.
[6] H. Tanaka *et al.*: Proc. EPAC2000, p.1086.
[7] K. Soutome *et al.*: Proc. EPAC2008, p.3149.
[8] W. Guo *et al.*: Phys. Rev. STAB **10** (2007) 020701.
[9] C. Mitsuda *et al.*: Proc. SRI09 – in press.
[10] M. Shoji *et al.*: Vacuum **84** (2009) 738.
[11] T. Bizen: Nucl. Instrum. Meth. A **574** (2006) 401.
[12] Y. Shimosaki *et al.*: Proc. EPAC2008.
[13] SPring-8 Research Frontiers 2008, p.176.
[14] S. Takano *et al.*: Nucl. Instrum. Meth. A **556** (2006) 357.
[15] SPring-8 Research Frontiers 2006, p.183.
[16] SPring-8 Research Frontiers 2007, p.195.
[17] SPring-8 Research Frontiers 2008, p.184.
[18] M. Akemoto: Proc. PAC1991, p.1037.
[19] F. Naito *et al.*: Proc. APAC1998, p.776.
[20] H. Dewa *et al.*: Proc. FEL2009, Liverpool, p.678.

New Apparatus & Upgrades

A Beamline Dedicated to Soft Matter Research has been Now Launched at BL03XU

The "Frontier Soft Matter Beamline (FSBL)" constructed by the Advanced Softmaterial Beamline Consortium consisting of 19 research groups from both commercial corporations and universities was launched at **BL03XU** on February 4, 2010. FSBL will open the door to new activities aiming to further advance polymer science and develop soft matter/new polymeric materials by fully utilizing the sophisticated light source capabilities of SPring-8. It is the first full-fledged strategic concept in the world that promotes the collaborative use of a radiation facility among a government, businesses, and universities

FSBL is equipped with X-ray diffraction/scattering measurement systems that can be used for high-speed simultaneous measurements of the hierarchical structures of bulk and thin-film samples of soft matter at a scale of several nanometers to several hundred nanometers. This beamline employs the standard SPring-8 in-vacuum undulator (magnet material: NdFeB, periodic length: 32 mm, number of periods: 140, total length: 4.5 m, available energy: 5 keV ~ 18 keV) as the light source and the cryogenic-cooling double-crystal monochromator. Rh- and Pt-coated mirrors (horizontal and vertical) are used to focus and eliminate the higher harmonics of the undulator beam. The performance of the X-ray at the sample position is presented in Table 1.

The experimental hutches consist of the first and second hutches as presented in Fig. 1. The first hutch incorporates a measurement system that can be used to carry out grazing-incidence wide-angle X-ray diffraction (GIWAXD) measurements and also grazingincidence small-angle X-ray scattering (GISAXS) measurements when an X-ray is directly injected very close to the surface of a sample using a thin-film goniometer (horizontal placement type), time-resolved measurements with both GIWAXD and GISAXS, simultaneous measurements, and X-ray reflectometry. It is the only measurement system in Japan that can be used to unravel the dynamic structures of thin organic/polymer films and surfaces/interfaces in various external environments. It is expected to greatly contribute to improving the performance of polymeric materials/soft matter for use in a wide variety of fields (e.g., electronic devices, batteries/cells, adhesives/coating, printing, and biomaterials) and products such as organic ELs, organic FETs, organic memory, organic fuel cells, and organic solar cell materials. The second hutch incorporates a system that can be used to carry out small-angle X-ray scattering (SAXS) measurements, wide-angle X-ray diffraction (WAXD) measurements, and simultaneous time-resolved measurements that combine SAXS/WAXD and various other different measurements (Fig. 2). If necessary, a kinematic mount can installed in the first hutch at the space of 3 m length × 3 m width × 4 m height, which enables to observe in situ structural changes in real processing such as fiber spinning and film drawing. We are planning to install even more advanced optical and measurement systems to observe time-fluctuation in structure and nano- or meso-structures.

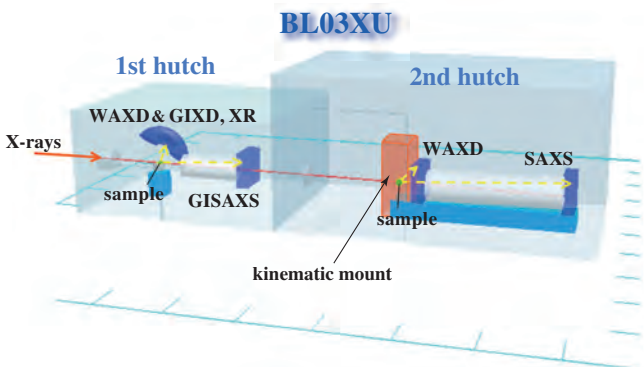

Fig. 1. Outline of the experimental hutches.

The first test measurement was carried out using one of the ultrafine prototype vinylon fibers produced in the early stage (around 1955) of its commercialization. Vinylon was the first synthetic polymer fiber entirely produced in Japan. The newly constructed beamline can be used to instantly produce pictures of fibers and "nano-filaments." Figure 3(b) shows an X-ray scattering image visualized on a two-dimensional digital detector after irradiating it with X-rays for no more than 20 s. As can be seen in the figure, the image is very sharply defined. The image clearly reveals very weak scattering at an extremely small scattering angle, and thus also revealing that the fiber has an orderly structure with a microcrystalline region formed by polymer molecules and a noncrystalline (amorphous) region (similar to irregular glass structure) alternating at 18.5 nanometer intervals. The sharp clear X-ray scattering pattern provided in Figure 3(c) (fiber diffraction pattern) reveals that it has a molecular orientation where the polymer chains in the microcrystal

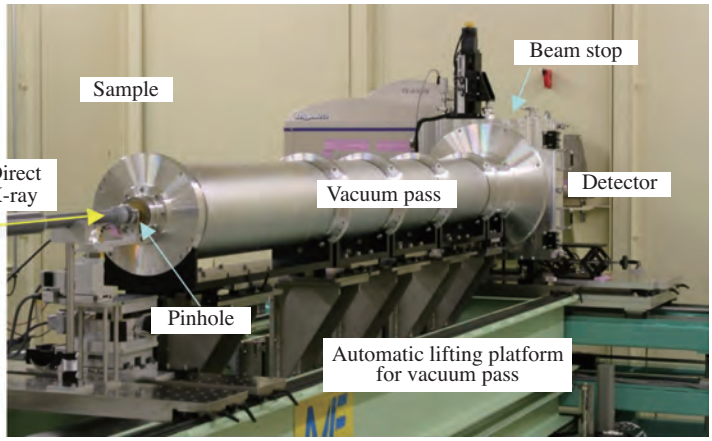

Fig. 2. SAXS measurement in the second experimental hutch (length of vacuum path: 3 m).

have been arranged in the axial direction of the fiber at amicroscopic level of accuracy. Japanese vinylon was manufactured half a century ago and demonstrated, at the molecular level, the high level of technology used to produce polymer fibers in those days.

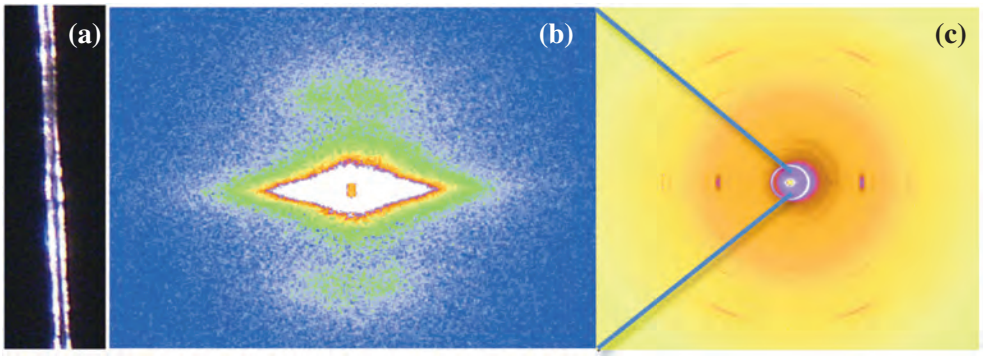

Fig 3. SAXS **(b)** and WAXD **(c)** patterns of a single vinylon fiber **(a)** approx. 15 μm in diameter.
Measurement conditions -- wavelength: 0.1 nm; vacuum path length: (b) 3 m and (c) 30 cm; detector: (b) Image Intensifier +CCD detector (ORCA R2) (Hamamatsu Photonics K.K.) and (c) Imaging Plate system (R-AXIS VII) (Rigaku Corporation); sample: vinylon prototype manufactured in late 1950s to early 1960s, contributed (loaned) to the Institute for Chemical Research of Kyoto University (Prof. Toshiji Kanaya) by a descendant (member of the Takatsuki-kai group) of Professor Ichiro Sakurada, Kyoto University who succeeded in synthesizing vinylon for the first time in Japan. (b) shows the scattering pattern that was revealed by measuring it at a favorable angle and resolution around the center of (c).

Table 1. X-ray performance of BL03XU

Energy range	6 to 35 keV (2.0 to 0.36 Å)
Energy resolution	$\Delta E/E < 10^{-4}$
Photon flux	$> 10^{13}$ (without slits)
Beam size	170 μm (H) × 80 μm (V)

Advanced Softmaterial Beamline Consortium

E-mail: fsbl@spring8.or.jp

19 Research Members

Corporate members:
Asahi Kasei Corporation, Kwansei Gakuin University, Canon Inc., Kuraray Co., Ltd., Showa Denko K. K., Sumitomo Chemical Co., Ltd., Sumitomo Rubber Industries, Ltd., Sumitomo Bakelite Co., Ltd., Denso Corporation, Toyobo Co., Ltd., Toray Industries, Inc., Nitto Denko Corporation, Bridgestone Corporation, Mitsui Chemicals, Inc., Mitsubishi Chemical Corporation, Mitsubishi Rayon Co., Ltd., Yokohama Rubber Co., Ltd., Teijin Limited, and DIC Corporation

Academic members:
Kyushu University, the University of Kitakyushu, Kyoto Institute of Technology, University of Kyoto, Tokyo Metropolitan University, Stony Brook University, Tokyo Polytechnic University, Tokyo University of Agriculture and Technology, the University of Tokyo, Toyota Technological Institute, Nagoya Institute of Technology, Hiroshima University, Mie University, and Yamagata University

The University of Tokyo Soft X-Ray Materials Science Beamline

The University of Tokyo Synchrotron Radiation Research Organization (UT-SRRO) has constructed a new soft X-ray undulator beamline for materials science, "University-of-Tokyo Synchrotron Radiation (SR) Outstation" at beamline **BL07LSU**, in collaboration with RIKEN and JASRI. Eight figure-8-type undulators consisting of four horizontally polarized undulators and four vertically polarized ones are installed in a 30-m-long straight section of SPring-8. The undulator can provide us with polarization-controlled soft X-rays (SX) in the photon energy range from 250 eV to 2 keV. By adopting seven electromagnetic phase shifters between horizontally and vertically polarized undulators, we are able to switch between right- and left-circular polarizations of undulator light faster than 10 Hz. The optics of the beamline consists of a pre-focusing mirror (M0), a Monk-Gillieson type varied line spacing plane grating monochromator (VLS-PGM), and a post-focusing mirror (M2). By using two gratings (G600 and G1200), the energy resolution better than 10,000 can be achieved with the photon flux of 10^{12} photons/s and with the beam spot size of less than 10 μm.

The schematic of the beamline is shown in Fig. 1. At this beamline, three main experiments began to be performed from autumn in 2009. The first project (Fig. 2(a)) is 3DnanoESCA, where the electronic structures of the sample irradiated by about 50-nm-size SX beam can be investigated by angle-resolved photoemission. The pin-point in-depth profiles of the electronic structure can be obtained for LSIs, quantum dots, magnetic patterned media, environmental catalysts and other nano-fabricated materials. The second one is soft X-ray emission spectroscopy (Fig. 2(b)) for biomaterials and operating polymer electrolyte fuel cells, where a submicron beam is incident on liquid/solid interfaces. The third project is time-resolved photoemission spectroscopy (Fig. 2(c)). The apparatus was equipped with an angle-resolved time-of-flight (ARToF) electron energy analyzer, where pump-probe experiments with the combination of fs laser and SR for the studies of photoinduced phase

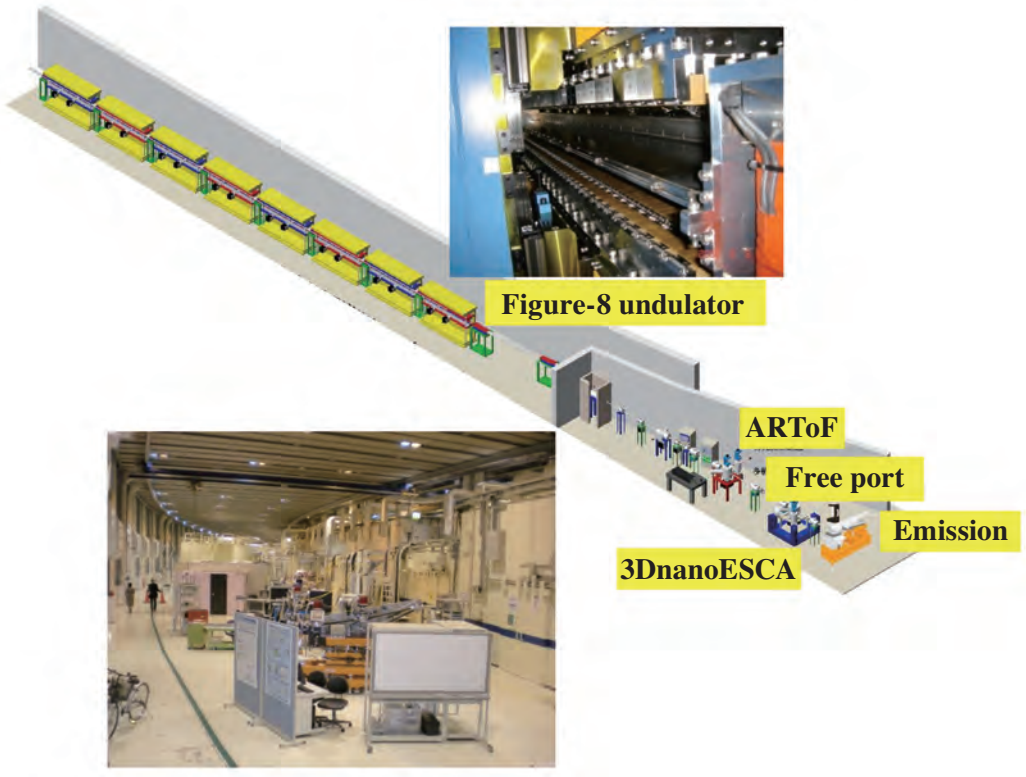

Fig. 1. Schematic of the University-of-Tokyo Materials Science SR Outstation with eight figure-8-type undulators.

transitions and photocatalytic reactions can be performed. The three experimental apparatuses have been fully opened for collaborative. In addition, the beamline has a free port for users who bring their own experimental apparatuses, such as those for stereoscopic photoelectron microscopy and soft X-ray microscopy using the coherence of undulator light. All the beamtimes should be allocated on the basis of a review by the Proposal Assessment Committee of UT-SRRO.

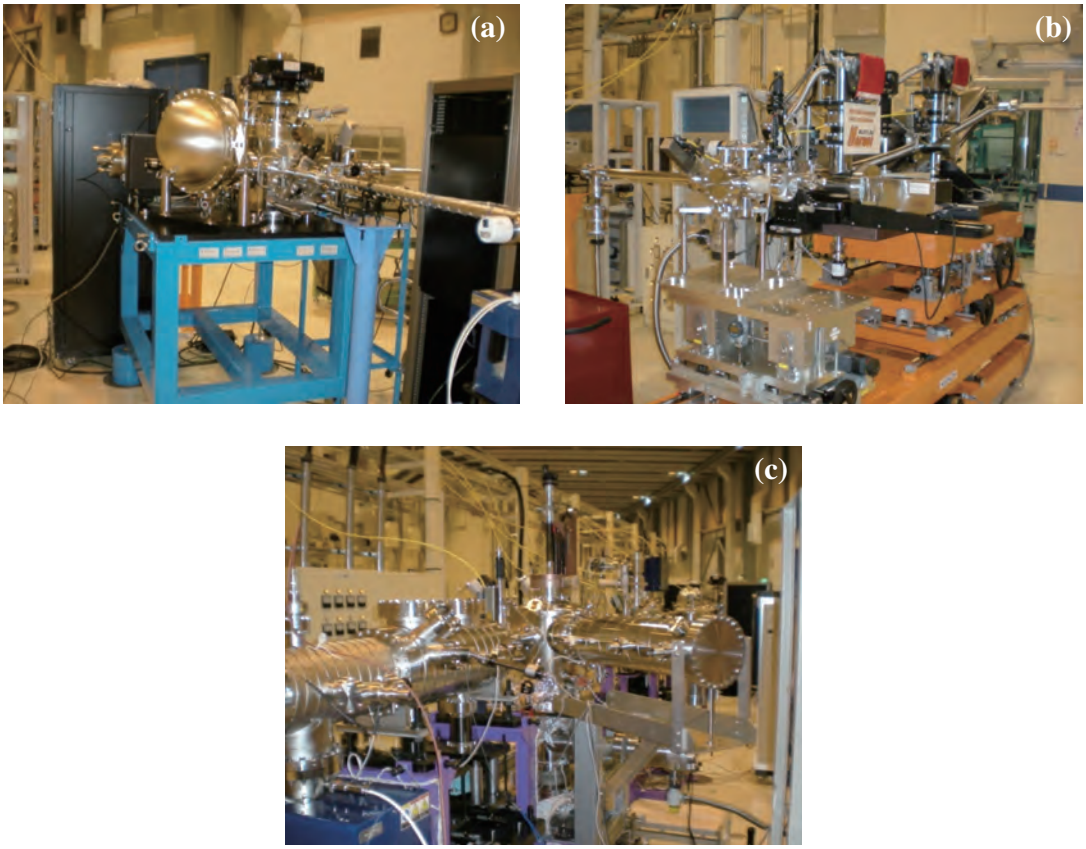

Fig. 2. **(a)** 3DnanoESCA. Electronic structures of the sample within an area of 50 nm can be investigated by angle-resolved photoemission. **(b)** Soft X-ray emission spectroscopy apparatus for biomaterials and operating polymer electrolyte fuel cells. **(c)** Time-resolved photoemission spectroscopy apparatus equipped with an angle-resolved time-of-flight (ARToF) electron energy analyzer.

Masaharu Oshima* and Akito Kakizaki

Synchrotron Radiation Research Organization,
The University of Tokyo

*E-mail: oshima@sr.t.u-tokyo.ac.jp

New Microbeam Beamline Dedicated to Protein Microcrystallography

Protein crystallography is one of the powerful tools for determining protein structure using crystal and X-ray. Proteins substantially important in biological research, such as membrane proteins and protein complexes, are often difficult to grow as single crystals with a size larger than 10 microns. Structure determination using such microcrystals was not achievable with the existing SR beamline because the diffraction signals from microcrystals are quite weak. At SPring-8, a new beamline **BL32XU** is under construction for the Targeted Proteins Research Program promoted by MEXT of Japan. The beamline is designed to provide a stabilized and brilliant microbeam to collect high-quality data from microcrystals by enhancing the diffraction signal from a crystal, and also by reducing background scattering (Fig. 1).

The source of the beamline is a hybrid in-vacuum undulator whose periodic length is 2.6 cm with the number of periods of 173. A liquid-nitrogen-cooled double-crystal monochromator equipped with Si(111) crystals covers the required energy range of 8 – 20 keV. The high precision monochromator has been specially designed on the basis of the SPring-8 standard one. The monochromatized beam is focused with K-B mirrors with a large reduction ratio of about 26 for the vertical direction, and 40 for the horizontal direction. The focusing mirror surfaces are fabricated with atomic level accuracy by Elastic Emission Machinery (EEM) technique.

We have observed the first beam on October 3, 2009, and have been conducting beamline commissioning. At the end of November 2009, we achieved a focused beam with a size of 0.9 × 0.9 μm^2 with photon flux of 6 × 10^{10} photons/s. Using the focused beam, diffraction data from some small protein crystals were successfully collected (Fig. 2).

Beamline BL32XU will overcome difficulties in data collection from protein microcrystals and open a new door for protein crystallography.

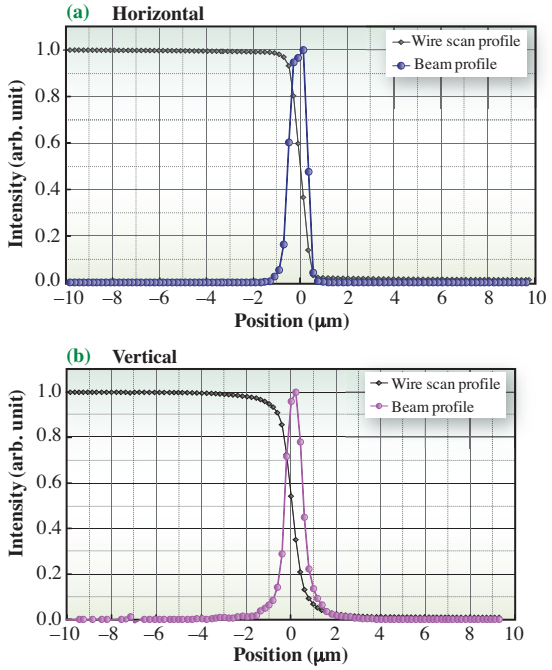

Fig. 2. **(a)** Horizontal and **(b)** vertical beam profiles with each raw wire scan profile. In both directions, FWHM of the focused beam corresponds to 0.9 μm.

Kunio Hirata*, Yoshiaki Kawano and Masaki Yamamoto

SPring-8 / RIKEN

*E-mail: hirata@spring8.or.jp

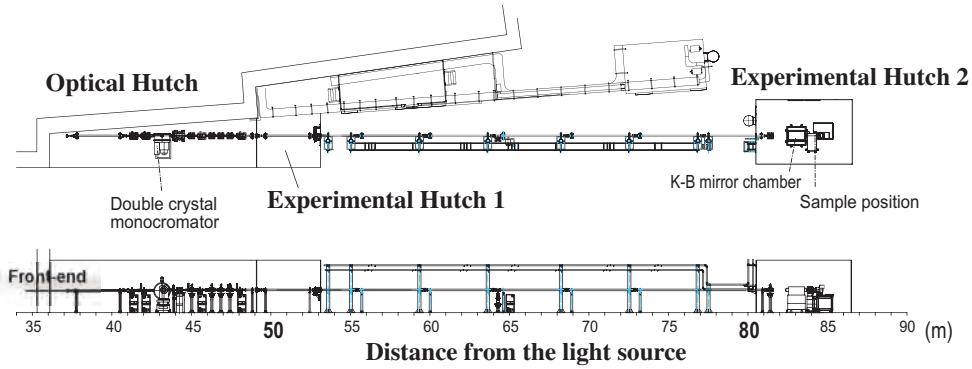

Fig. 1. Engineering drawing of beamline BL32XU.

TOYOTA Beamline BL33XU

TOYOTA beamline **BL33XU** has been designed and constructed especially for the observation of chemical reaction dynamically through XAFS technique. It will be very useful for research on catalysts, secondary batteries and fuel cells, which are very important technological targets for a sustainable future. The first X-ray beam was introduced in the optics hutch of BL33XU on April 3, 2009. In May, we finished the installation of optical components. The expected performance was confirmed before the long summer shutdown period. Since October, we have been using this XAFS beamline as an analytical tool, and at the same time, developing a super quick-XAFS system simultaneously.

BL33XU is a 120-m-long beamline, which has an experimental station outside of the storage ring building (Fig. 1). The light source is the SPring-8 standard in-vacuum undulator, especially equipped with a tapering mechanism, which broadens the undulator spectrum for XAFS measurement and is used for the first time at SPring-8. The SPring-8 standard components are used at the front-end. Two 1-m-long total-reflection mirrors are placed in the optics hutch in the parallel setting. By using these mirrors, the X-ray beam is deflected in the horizontal direction and extracted parallel to the incident beam. The glancing angle is fixed at 1.5 mrad, reflecting X-rays less than 45 keV. The second mirror is equipped with a bending mechanism that can focus the beam horizontally. The X-ray beam is transported through a vacuum duct toward the experimental hutches outside the storage ring building. As a monochromator, we adopted a new type called compact monochromator with a channel-cut Si single crystal driven by a servo motor. We use tandemly arranged two compact monochromators alternatively. Si 111 reflection covers the energy range between 4.0 and 28.2 keV, and Si 220 reflection covers the energy range between 6.5 and 46.0 keV. The compact monochromators are cooled by circulating liquid nitrogen. Although the beam position changes slightly during energy scan, this enables us to scan energy very quickly. The tapered undulator and this monochromator allow us to obtain a XAFS spectrum very quickly. Figure 2 shows our result of obtained with the super quick-XAFS system. So far, we can obtain one XAFS spectrum at 25 msec. After the monochromator, a pair of 700-mm-long total-reflection mirrors is installed in order to reduce higher order X-rays and focus vertically. X-ray beam is then introduced in the 2nd experimental hutch where the XAFS experiment is performed.

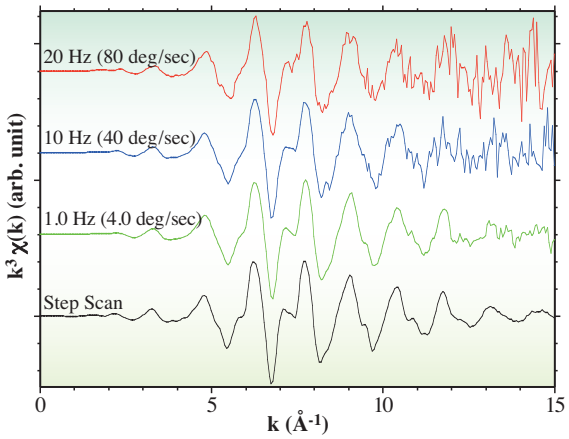

Fig. 2. Super quick-XAFS spectra.

In the 2nd experimental hutch we have a high speed gas reaction analysis system, which consists of: (i) three independent gas supply lines, (ii) a high speed gas switching and mixing apparatus, and (iii) a mass spectrometer with a sampling rate of 50 msec. For this system, a gas cylinder cabinet is embedded in the wall of the experimental station.

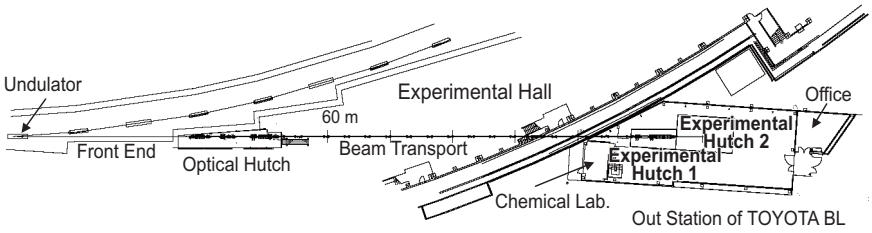

Fig. 1. TOYOTA beamline BL33XU.

Yoshiharu Hirose

Analysis & Evaluation Division,
TOYOTA Central R&D Labs., Inc.

E-mail: e0432@mosk.tytlabs.co.jp

Development of the High-Throughput and High-Accuracy Measurement System for Powder Diffraction

An automatic measurement system for powder diffraction experiments with synchrotron radiation has been developed to achieve both high throughput and high accuracy at the powder diffraction beamline **BL02B2** [1]. The system mainly consists of three parts: an automatic sample changer, an image analyzer for automatic sample position alignment, and an online X-ray CCD detector. These three parts have been successfully synchronized with an original control program written using *LabVIEW*. With this system, the time taken except for X-ray exposure was decreased from several tens of minutes to one minute and the sample position accuracy was improved from several tens of microns to one micron.

The standard procedures of powder diffraction experiments at BL02B2 are as follows.

1. Sample set
2. Sample position alignment
3. Imaging plate set
4. X-ray exposure
5. Imaging plate removal and readout

Here, we describe the concepts of the automatic sample changer and image analyzer, which automate procedure Nos.1 and 2, respectively.

We first had two different ideas for the arrangement of an automatic sample changer. One is to install a sample changer in the existing diffractometer. The other is to develop a sample changer apart from the diffractometer. In the end, we adopted the latter idea, because a thin-film form with reflection geometry as well as capillary form with transmission geometry can be available by utilizing sufficient space. In the latter case, however, the easy and fast setup of the sample changer to the diffractometer was required. Therefore, fine alignment using the stepping motors follows rough alignment using the manual handles. By taking advantage of the two-step alignment, the setup can be completed within 5 min. In the automatic sample changer, a dedicated sample stage was used. Although four axes are usually required, the sample stage is equipped with only two axes to reduce the time for sample position alignment. In order to enable the sample position alignment using only two axes, the design of the sample holder is very important. We used a stainless holder with a sufficiently long groove, which can keep a capillary straight. In addition, a circular sample holder is available for reflection geometry.

Sample position alignment was performed by manually moving the four axes of the goniometer head through the microscope. To achieve automatic sample position alignment, the image analyzer system was introduced. The system can recognize the sample image through the dedicated CCD with one micron resolution. We developed a program to identify the sample edge by differentiating the grayscale and move the sample to the beam center using two axes of the sample stage. Figure 1 shows photographs of the automatic sample changer and a schematic of the automatic sample position alignment.

The system allows us to collect 36 data continuously and automatically. If the X-ray exposure time is sufficiently short, the system acts as a very powerful tool for powder diffraction experiments. The basic design can also be applied to other experiments at synchrotron radiation facilities. Improvements in sample position accuracy and reproducibility by automation contribute to materials science research as well as analytical research.

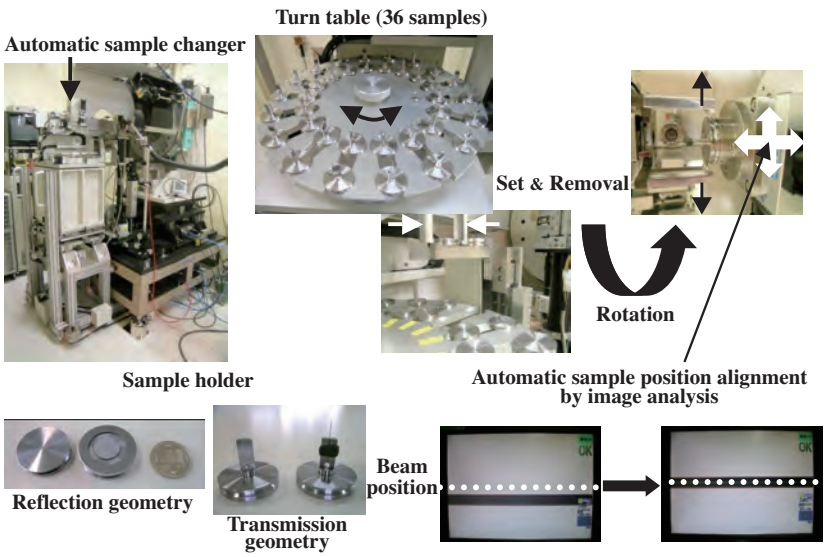

Fig. 1. Automatic sample changer and automatic sample alignment system installed at BL02B2.

Kenichi Kato

SPring-8 / RIKEN

E-mail: katok@spring8.or.jp

References

[1] *K. Kato, M. Takata and T. Ishikawa: Advances in X-ray Analysis* ***51*** *(2008) 36.*

Development of a Differential Pumping System of Soft X-Ray Beamline for Windowless Experiments under Normal Atmospheric Conditions

In synchrotron radiation facilities, thin metal and polymer films are usually used as a vacuum window to separate the ultra-high vacuum of the storage ring or the optics chamber from the high-pressure environment of the experimental apparatus. A beryllium (Be) window is often used as a standard vacuum window owing to its high optical transmission of the X-ray beam. However, Be windows absorb low energy photons, and cannot be used for a soft X-ray beamline. Instead, the standard procedure in a soft X-ray beamline is to install all the equipment necessary for experiments inside the high-vacuum chamber. This method can have drawbacks as well. On one hand, the high-vacuum chamber produces an ideally clean environment. On the other hand, technologically significant phenomena take place under higher-pressure regions (1~760 mbar). Recently, the demands to study samples under a high-pressure environment have been increasing in the soft X-ray region. For example, several groups have attempted to obtain photoemission data at pressures of up to 100 mbar by separating the sample region from the beamline with a vacuum window [1]. The vacuum windows used in the soft X-ray regions need to be ultra-thin to transmit the photons to the sample region. However, thin films are fragile and have difficulty withstanding a high pressure difference. Furthermore, organic contamination of the vacuum window reduces the photon intensity in the absorption edges of the light elements. In order to overcome these complications, the development of a windowless method must be investigated. A windowless connection between a high-vacuum beamline and a high-pressure sample chamber would provide an opportunity that opens new scientific possibilities in soft X-ray sciences.

One approach to overcoming the window problem is to use a differential pump [2]. In a differential pump, the conductance between two vacuum chambers is limited by an open aperture or pipes. It allows photons of all energy ranges to pass freely along a line of the light path between the two different pressure regions. A challenge of the present investigation is to create a windowless connection between an experimental chamber filled by 1 atm helium (He) and the high-vacuum beamline. Since soft X-rays below 1.5 keV are fairly absorbed in atmospheric air, a He path was used instead of an air path. While He gas has a higher transmission than air in the soft X-ray region owing to its smaller atomic number, it is more difficult to evacuate He using vacuum pumps. In this study, a differential pumping system was developed for use with windowless soft X-ray experiments under normal atmospheric conditions. The performance of the differential pump was evaluated by connecting it to both atmospheric air and helium environments. The transmission of soft X-rays was measured under the condition of atmospheric helium to demonstrate the performance of the apparatus.

Figure 1 shows a photograph of the present differential pumping system. The details of the system were described in a recent report [3]. The apparatus consists of an aperture-based four-stage differential pump, which was designed on the basis of a simple

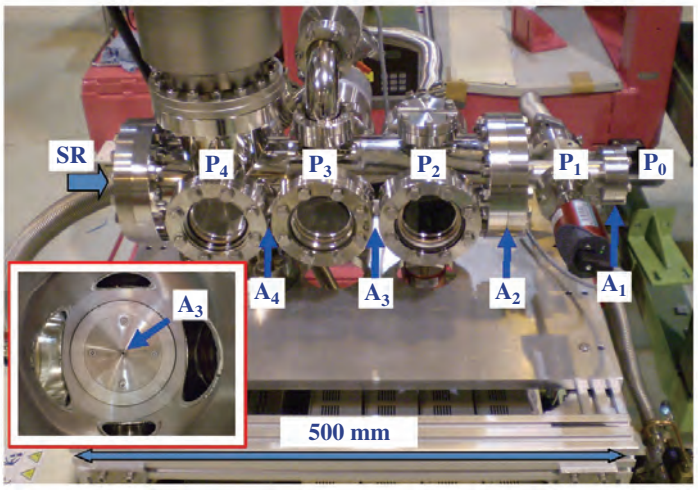

Fig. 1. Photograph of the fabricated differential pumping system. A_x (x = 0 - 4) is the location of each conductance-limiting aperture, and P_x (x = 0 - 4) is the pressure at each differential pumping stage. Inset is a photograph of the aperture installed between the third and fourth stages at **BL27SU**.

model calculation. The design has relatively short conductance-limiting components that allow easy installation and alignment of the system on the synchrotron beamline. The total length of the system is about 500 mm, which is significantly shorter than those of other similar systems previously reported [2].

Figure 2 shows the pressure distribution curves obtained from the simulation and the test measurement of the system. The pressure P_0 in the sample region is 1×10^5 Pa (=1 atm). When P_0 is the atmospheric air, the pressure at the uppermost stage (P^4) is 8.5×10^{-5} Pa. The present apparatus achieved differential pressures of about 9 orders of magnitude less than the atmospheric pressure of air. The next challenge was to connect the experimental chamber filled with 1 atm of helium gas to the high-vacuum beamline in the windowless system. The pressure of the P_4 section increased by a factor of about 40, compared with the P_4 value for air. The pressure deteriorated for mainly two reasons [3]. The first reason is that a gas mass increases the gas flow, as was the case with helium. The second reason is that the turbomolecular pumps had lower pumping speeds with helium than with air, and the lower speeds reduced the pumps' performance. Although the performance of the system degraded by about one order of magnitude when using helium, the observed P_4 value (3.3×10^{-3} Pa) is sufficient to connect this system to the beamline. The present system provides excellent isolation between the atmospheric pressure of the sample environment and the high-vacuum of the beamline across the short distance.

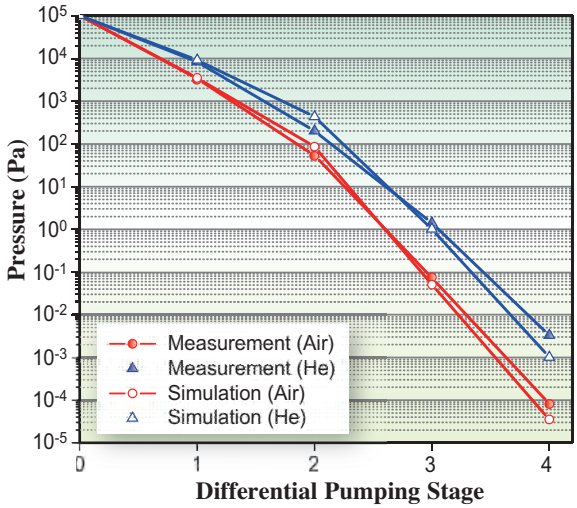

Fig. 2. Performance measurement of the present differential pumping system. The pressure distribution curves were measured for the atmospheric pressures of air (solid circles) and helium (solid triangles). The calculated pressure for the optimized design is also indicated for air (empty circles) and helium (empty triangles).

Figure 3 shows the transmission curves of soft X-rays under atmospheric helium. The experimentally determined transmission curves are nearly identical to the simulated ones. The transmission at 550 eV (the oxygen *K*-edge region) measured at 10 mm downstream of the first aperture is about 85%. When the photon flight path in the atmospheric pressure region is expanded to 50 mm, more than 70% of the incident photons are transmitted to the detector. Although the transmission is decreased in the low photon energy region, about 60% of the incident photons are transmitted to the detector at 350 eV. The fabricated differential pump was a success: low energy soft X-ray photons passed through the atmospheric pressure environment.

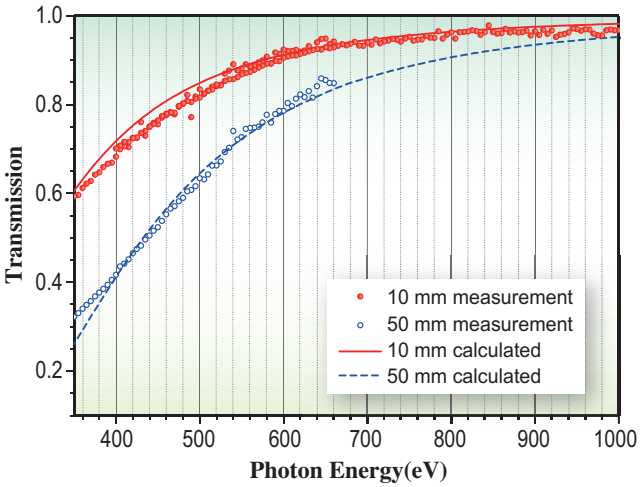

Fig. 3. Experimental and calculated transmission curves of soft X-ray photons obtained under helium-path conditions. The experimental transmission curves were measured at the helium-path lengths of 10 mm (solid circles) and 50 mm (empty circles). The solid (10 mm) and dashed (50 mm) lines indicate the simulated transmission curves of the fabricated differential pumping system.

Yusuke Tamenori

SPring-8 /JASRI

E-mail: tamenori@spring8.or.jp

References

[1] D.F. Ogletree *et al.*: Rev. Sci. Instrum. **73** (2002) 3872.
[2] T.Gog *et al.*: J. Synchrotron Rad. **14** (2007) 339.
[3] *Y. Tamenori: J. Synchrotron Rad. **17** (2010) 243.*

Facility Status

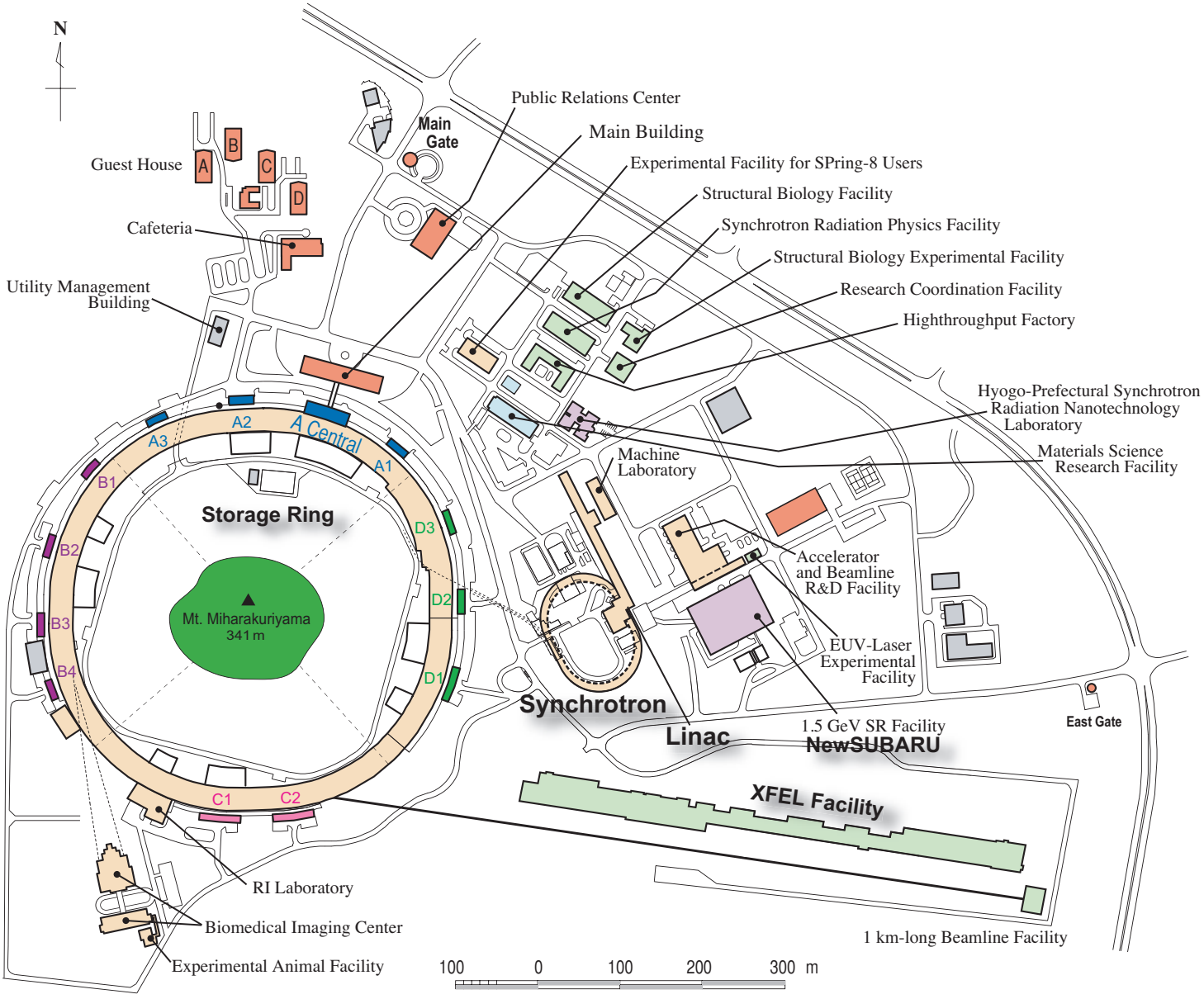

I. Introduction

In 2009, there were two remarkable events that occurred at SPring-8. The first event is that the total number of SPring-8 users visits reached 100,000. The second event is the budgets cuts proposed by Japanese Revitalization Unit. These two contrasting events imply that the importance of SPring-8 has been very clear to researchers, but not so to the public.

It was on June 5, 2009, that the number of total user visits to SPring-8 has reached 100,000. This record demonstrates that SPring-8 has continuously and successfully kept providing researchers with an advanced research platform to pioneer their scientific activities. Materials, life, and environmental sciences are forming the core areas of the academic activities, while the applications towards industrial products, cultural heritages, and forensic cases are exploring the application areas of synchrotron radiation science and technology.

Among the various scientific events held in 2009, the 1st Japan-United Kingdom Joint Workshop on Synchrotron Radiation Industrial Applications was held in Kobe, August 2009. The workshop was organized in celebration of the 150th anniversary of the Anglo-Japanese Treaty of Amity and Commerce concluded in 1858. SPring-8 and Diamond Light Source were selected as the representative facilities for Japan and the UK, respectively, because of a MoU concluded between them. Having the pleasure of the company of people from MEXT and the UK embassy, the delegations from SPring-8 and Diamond Light Source reported the current status and discussed the prospects of industrial applications in each facility.

Another important scientific event that deserved to be emphasized was the first SPring-8 Conference held in Tokyo, September 2009. Previously, the SPring-8 Symposium and SPring-8 Industrial Application Symposium were almost independently organized to report and discuss the outcomes from academia and industrial domains, respectively. To cross-fertilize both regions by directly exchanging information, these two major symposia were held at the same venue and the same period this year, and was called SPring-8 Conference. Having the pleasure of the company of people from MEXT, the 1st SPring-8 Conference was successfully held with more than 400 participants.

Additionally, another milestone activity was the 1st symposium on the SPring-8 Upgrade Plan held in Tokyo, June 2009. The SPring-8 Upgrade Plan with 2019 set as the target year is aimed at further developing and improving not only the accelerator complex and its beamlines but also its effective utilization, and has been examined by a working group comprising the scientists and engineers of RIKEN and JASRI who will lead the next generation. That was the first time that the SPring-8 upgrade plan was revealed to the outside, and it attracted much attention from many users and companies. The working group concluded that the plan should be developed through extensive discussions to meet the needs of the SR research community.

The construction of a new contract beamline of Kyoto University called Advanced Basic Science for Battery Innovation (BL28XU) was approved October 2009. This new beamline will be constructed to promote research and development on an advanced method that can make the *in situ* dynamic atomic-level observation of the structures and basic reaction mechanisms of batteries possible. It must contribute greatly to the rapid progress in high-performance batteries, and lead to the development of electric vehicles for wide spread use. This new beamline will be commissioned in 2011.

On the 30th of November 2009, the Government Revitalization Unit approved the recommendation made by its working group, which stated that the SPring-8 budget request should be reduced by between 1/3 and 1/2 for fiscal 2010. Since it was clear that SPring-8 would not be able to provide X-ray beams to its users with such drastic budgets cuts, the SPring-8 users as well as the international synchrotron radiation community petitioned the Government Revitalization Unit to reverse its decision. After high-level deliberations, the Cabinet decided on December 25 to appropriate 8.49 billion JPY, 170 million JPY down from the previous year, to facility operation and maintenance, with which SPring-8 should be able to ensure the same level of operation hours as currently exist.

II. Machine Operation

The operation statistics since the facility was opened to users are shown in Fig. 1. In 2009, the total operation time of the accelerator complex was 5025.9 hours. The operation time of the storage ring was 4990.4 hours, of which 79.5% (3967.9 hours) was made available for SR experiments. The down time resulting from failure accounted for 0.87% (34.4 hours) of user time; in 2009, no great loss of user time exceeding several hours occurred. Since 2004, there has been no injection time because top-up injection was introduced. Concerning user service operation, a high availability (ratio of net user time to planned user time), e.g., 99.0%, was achieved in 2009. The total tuning and study time of 1023.6 hours was used for machine tuning, for the study of the linac, booster synchrotron and storage ring, and also for beamline tuning and study.

Operations in three different filling modes were provided for the following user time: 14.3% in the multi-bunch mode, 40.2% in the several bunch mode, such as the 203-bunch mode (203 equally spaced bunches), and 45.5% in the hybrid filling mode, such as a 1/14-partially filled multi-bunch with 12-isolated bunches. In 2009, the several bunch mode was the dominant filling mode. In particular, the 203-bunch mode reached 23.9% of the total user time. For the hybrid filling mode, 1.0 mA, 1.4 mA, 1.6 mA, or 3.0 mA is stored in each isolated bunch. An isolated bunch impurity lower than 10^{-10} is routinely maintained in the top-up operation. Table I shows a summary of the useful beam parameters of the storage ring. Table II shows a summary of the beam filling patterns.

Table I. Beam parameters of SPring-8 storage ring

Energy [GeV]	8
Number of buckets	2436
Tunes (ν_x / ν_y)	40.15 / 18.35
Current [mA]:	
single bunch	12
multi bunch	100
Bunch length (σ) [psec]	13
Horizontal emittance [nm·rad]	3.4 *
Vertical emittance [pm·rad]	6.8 *
Coupling [%]	0.2
RF Voltage [MV]	16
Momentum acceptance [%]	±3 (±240 MeV)
Beam size [μm]: (σ_x / σ_y)* [μm]	
Long ID section	294 / 10
ID section	301 / 6
BM section	107 / 13
Beam divergence [μrad]: (σ_x' / σ_y')* [μrad]	
Long ID section	13 / 0.7
ID section	12 / 1.1
BM section	56 / 0.6
Operatinal chromaticities: (ξ_x / ξ_y)	+2 / +6 **
Lifetime [h] :	
100 mA (multi-bunch)	~200
1 mA (single bunch)	~20
Horizontal dispersion [m]:	
Long ID section	0.103
ID section	0.107
BM section	0.032
Fast orbit stability (0.1 – 200 Hz) [μm]:	
horizontal (rms)	~4
vertical (rms)	~1

* Assuming 0.2% coupling for "Low Emittance Optics"
** With bunch-by-bunch feedback

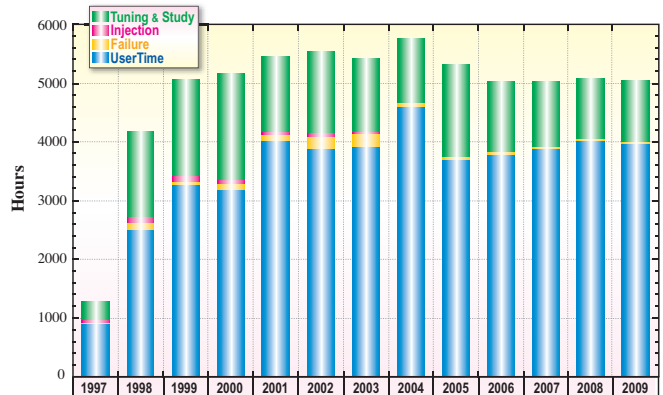

	1997	1998	1999	2000	2001	2002	2003	2004	2005	2006	2007	2008	2009
Accelerator Operation Time	1286.0	4189.6	5051.6	5167.5	5456.1	5542.9	5419.5	5759.2	5317.1	5026.2	5027.9	5078.5	5025.9
Storage Ring Operation Time	1270.6	4135.4	4863.9	4972.9	5340.6	5484.1	5328.5	5736.7	4781.3	5008.5	5019.2	5063.4	4990.4
Tuning & Study (Acc. & BL)	304	1457.6	1624.2	1815	1276.5	1394.9	1245.8	1085.9	1559.2	1193.6	1100.3	1010	1023.6
Injection	50	110	95.2	70.4	59.3	60.8	39.2	0	0	0	0	0	0
Failure	26	110	57.2	88.7	87.1	190.5	208.5	82.4	59.7	42.5	27.6	30.7	34.4
User Time	906	2512	3275	3193.4	4033.2	3896.7	3926	4590.9	3698.2	3790.1	3900	4037.8	3967.9
Planned Time	984	2712	3432	3352	4176	4152	4176	4680	3762	3840	3936	4080	4008
Availability (%)	97.2	96.7	98.2	97.4	98	95.3	95	98.1	98.3	98.7	99.1	99	99

Fig. 1. Operation statistics since the facility became available to users.

Table II. Filling patterns

	bunch current (mA)	life time (h)
Multi-bunch (160 bunch-train × 12)	0.05	~ 200
203 bunches	0.5	25 ~ 30
11 bunch-train × 29	0.3	35 ~ 50
1/7 - filling + 5 single bunches	3.0 (single)	18 ~ 25
1/14 - filling + 12 single bunches	1.6 (single)	18 ~ 25
2/29 - filling + 26 single bunches	1.4 (single)	18 ~ 25
4/58 - filling + 53 single bunches	1.0 (single)	18 ~ 25

III. Beamlines

The SPring-8 storage ring can accommodate up to 62 beamlines: 34 insertion devices, 4 long undulators, and 24 bending magnets. At the time of writing, 53 beamlines are in operation, covering a wide variety of research fields of synchrotron radiation science and technology. The beamlines are classified into the following four types.

(1) Public Beamlines
(2) Contract Beamlines
(3) RIKEN Beamlines
(4) Accelerator Diagnostics Beamlines

There are now 26 public beamlines in full operation. The beamlines, that are proposed and constructed by external organizations, such as universities, research institutes, and private companies, are called contract beamlines and are exclusively used by the contractors for their own research purposes. At present, 17 contract beamlines are in operation. The contract beamlines include NSRRC BM (BL12B2) and NSRRC ID (BL12XU) beamlines, which were contracted by the National Synchrotron Radiation Research Center in Taiwan. These are the first contract beamlines installed at SPring-8 by a foreign organization. Currently, a new contract beamline called Advanced Basic Science for Battery Innovation (BL28XU) is under construction. The beamlines constructed by RIKEN are called RIKEN beamlines and are used for RIKEN's own research activities. RIKEN is now operating eight RIKEN beamlines and is constructing a new beamline called RIKEN Quantum Nano Dynamics (BL43LXU). In addition, two accelerator diagnostics beamlines are in operation.

To display the beamline portfolio of SPring-8, the beamline map is shown in Fig. 2 together with the beamline classification. The research field of each beamline is presented in Table III.

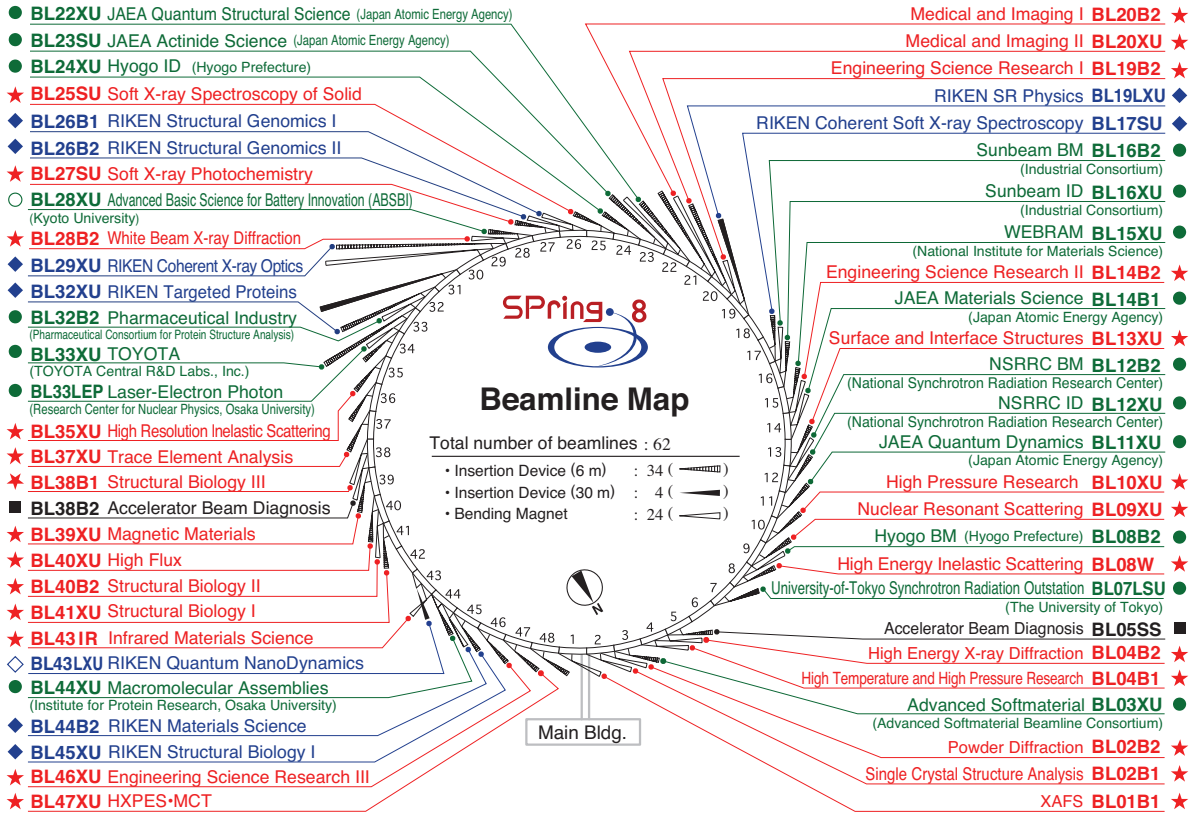

Fig. 2. Beamline map.

Table III. List of beamlines

BL #	Beamline Name	(Public Use)	Areas of Research
★ Public Beamlines			
BL01B1	XAFS	(Oct. 1997)	XAFS in wide energy region (3.8 to 113 keV). XAFS of dilute systems and thin films. Quick XAFS with a time resolution of seconds to as tenth seconds.
BL02B1	Single Crystal Structure Analysis	(Oct. 1997)	Precise crystal structure analysis using high resolution data of single crystal (X-ray energy: 5 - 115 keV). Magnetic resonant X-ray scattering.
BL02B2	Powder Diffraction	(Sep. 1999)	Accurate structure analysis of crystalline materials using powder diffraction data by Rietveld refinements and maximum entropy method (MEM).
BL04B1	High Temperature and High Pressure Research	(Oct. 1997)	Mineral physics at high temperature and high pressure. Energy-dispersive X-ray diffraction and X-ray radiography using the large-volume press.
BL04B2	High Energy X-ray Diffraction	(Sep. 1999)	Structural analysis of glass, liquid, and amorphous materials. X-ray diffraction under ultra high-pressure.
BL08W	High Energy Inelastic Scattering	(Oct. 1997)	Magnetic Compton scattering. High-resolution Compton scattering. High-energy Bragg scattering. High-energy fluorescent X-ray analysis.
BL09XU	Nuclear Resonant Scattering	(Oct. 1997)	Lattice dynamics using nuclear inelastic scattering. Time domain Mössbauer spectroscopy, especially under the extreme conditions. Coherent X-ray optics using nuclear resonant scattering. Nuclear excitation by electron transition (NEET).
BL10XU	High Pressure Research	(Oct. 1997)	Structure analysis and phase transitions under ultra high pressure (DAC experiment). Earth and planetary science.
BL13XU	Surface and Interface Structures	(Sep. 2001)	Atomic-scale structural analysis of ultra-thin films, nanostructures and surfaces of crystalline materials in air or in vacuum by combination methods of surface X-ray diffraction, microbeam diffraction, and time-resolved diffraction.
BL14B2	Engineering Science Research II	(Sep. 2007)	XAFS in wide energy region (3.8 to 72 keV). XAFS of dilute systems and thin films.
BL19B2	Engineering Science Research I	(Nov. 2001)	Residual stress measurement. Structural analysis of thin film, surface, interface. Powder diffraction. X-ray imaging, X-ray topography. Ultra-small angle X-ray scattering.
BL20XU	Medical and Imaging II	(Sep. 2001)	Microimaging. Hard X-ray microbeam/scanning microscopy, imaging microscopy, microtomography, phase-contrast microtomography with Bonse-Hart interferometer, X-ray holography, coherent X-ray optics, and other experiments on X-ray optics and developments of optical elements. Medical application. Microangiography, refraction-enhanced imaging, radiation therapy, phase-contrast CT using interferometer. Ultra-small angle scattering.
BL20B2	Medical and Imaging I	(Sep. 1999)	Medical research mainly involves microradiography, microtomography and refraction-contrast imaging on biological specimens and small animals. Imaging techniques involve the evaluation and development of various kinds of optical elements for novel imaging techniques.
BL25SU	Soft X-ray Spectroscopy of Solid	(Apr. 1998)	Observation of electronic structures by photoemission spectroscopy (PES). Observation of electronic band structures by angle resolved photoemission spectroscopy (ARPES). Magnetic state study by magnetic circular dichroism (MCD) of soft X-ray absorption. Element-specific magnetization curve measurements by MCD analysis of atomic arrangements by photoelectron diffraction (PED). Observation of magnetic domains by photoelectron emission microscope (PEEM).
BL27SU	Soft X-ray Photochemistry	(May 1998)	Industrial research of functional material. Atomic and molecular spectroscopy by high resolution electron spectroscopy. Surface analysis and solid state physics.
BL28B2	White Beam X-ray Diffraction	(Sep. 1999)	White X-ray diffraction and topography. Time-resolved energy-dispersive XAFS (DXAFS) for studies of chemical and/or physical reaction process. Biomedical imaging and radiation biology studies.
BL35XU	High Resolution Inelastic Scattering	(Sep. 2001)	Material dynamics on ~meV energy scales using inelastic X-ray scattering (IXS) and nuclear resonant scattering (NRS).
BL37XU	Trace Element Analysis	(Nov. 2002)	X-ray microbeam spectrochemical analysis. Ultra trace element analysis. High energy X-ray fluorescence analysis.
BL38B1	Structural Biology III	(Oct. 2000)	Structural biology. Macromolecular crystallography. Automatic data collection.
BL39XU	Magnetic Materials	(Oct. 1997)	X-ray magnetic circular dichroism (XMCD) spectroscopy and element-specific magnetometry under multiple-extreme conditions. Micro-XMCD. X-ray emission spectroscopy. Resonant X-ray magnetic scattering.
BL40XU	High Flux	(Apr. 2000)	Time-resolved diffraction and scattering experiments. Microbeam X-ray diffraction experiments. Quick XAFS.
BL40B2	Structural Biology II	(Sep. 1999)	Noncrystalline small and wide angle X-ray scattering.
BL41XU	Structural Biology I	(Oct. 1997)	Structural biology. Macromolecular crystallography. Ultra-high resolution structural analysis.
BL43IR	Infrared Materials Science	(Apr. 2000)	Infrared microspectroscopy. Magneto-optical spectroscopy.
BL46XU	Engineering Science Research III	(Nov. 2000)	Structural characterization of thin films by X-ray diffraction and X-ray reflectivity measurement. Residual stress measurement. Time resolved X-ray diffraction measurement. Hard X-ray photoemission spectroscopy.
BL47XU	HXRES·MCT	(Oct. 1997)	Hard X-ray photoelectron spectroscopy. Projection type microtomography. Imaging type microtomography. Hard X-ray microbeam/scanning microscopy.

BL #	Beamline Name	(First Beam)	Areas of Research
	● Contract Beamlines		
BL03XU	**Advanced Softmaterial** (Advanced Softmaterial Beamline Consortium)	(Nov. 2009)	Structural characterization of softmaterials using small- and wide-angle X-ray scattering. Grazing-incidence small- and wide-angle X-ray scattering for thin films. X-ray diffraction and reflectivity measurements for softmaterials.
BL07LSU	**University-of-Tokyo Synchrotron Radiation Outstation** (The University of Tokyo)	(Oct.2009)	Time-resolved soft X-ray spectroscopy, nano-beam photoemission spectroscopy, ultra high-resolution soft X-ray emission spectroscopy, and any methods requiring the highly brilliant soft X-ray beam.
BL08B2	**Hyogo BM** (Hyogo Prefecture)	(Jun. 2005)	XAFS in a wide energy region. Small angle X-ray scattering for structural analyses of polymer and nanocomposite materials. X-ray topography. Imaging. Powder diffraction with a high angular resolution.
BL24XU	**Hyogo ID** (Hyogo Prefecture)	(May. 1998)	Structure analysis of small bio-crystals for industry. Surface/interface analysis for industry by fluorescent X-ray analysis, strain measurements and grazing incidence X-ray diffraction. Microbeam formation studies for materials and life sciences.
BL12XU	**NSRRC ID** (National Synchrotron Rad. Res. Center, Taiwan)	(Dec. 2001)	High resolution non-resonant or resonant inelastic X-ray scattering. High resolution near-edge X-ray Raman scattering. Phase transitions under high-pressure, low and high temperatures. High-resolution X-ray absorption and emission spectroscopy. X-ray physics and optics.
BL12B2	**NSRRC BM** (National Synchrotron Rad. Res. Center, Taiwan)	(Oct. 2000)	X-ray absorption spectroscopy. Powder X-ray diffraction. High resolution X-ray scattering. Protein crystallography.
BL15XU	**WEBRAM** (National Institute for Materials Science)	(Jan. 2000)	Hard X-ray photoelectron spectroscopy. Highly precise X-ray powder diffraction
BL16XU	**Sunbeam ID** (Industrial Consortium)	(Oct. 1998)	Characterization of thin films for ULSI and magnetic devices, catalysts, functional materials, and structural materials by X-ray diffraction, fluorescence X-ray analysis, X-ray magnetic circular dichroism, and imaging with X-ray microbeam.
BL16B2	**Sunbeam BM** (Industrial Consortium)	(Oct. 1998)	Characterization of industrial materials by X-ray absorption fine structure measurements, X-ray diffraction and other methods.
BL32B2	**Pharmaceutical Industry** (Pharmaceutical Consortium for Protein Structure Analysis)	(Apr. 2002)	Protein structure analysis for structure-based drug design: Design and optimization of new leading compounds based on pharmacodynamic action mechanism elucidated at the molecular level which obtained from a detailed interaction analysis of receptor-drug complexes.
BL33XU	**TOYOTA** (TOYOTA Central R&D Labs., Inc.)	(Apr. 2009)	Time-resolved XAFS. Characterization of industrial materials, such as catalysts, secondary batteries, fuel cells.
BL33LEP	**Laser-Electron Photon** (RCNP, Osaka University)	(Jun. 1999)	Meson photoproduction from nucleon and nucleus. Photoexcitation of hyperons, nucleon resonances, and other exotic states. Photonuclear reactions. Beam diagnoses. Test and calibration of detectors with GeV photon beam.
BL44XU	**Macromolecular Assemblies** (IPR, Osaka University)	(May 1999)	Crystal structure analysis of biological macromolecular assemblies (e.g. membrane complexes, protein complexes, protein-nucleic acid complexes, and viruses).
BL11XU	**JAEA Quantum Dynamics**	(Oct. 1998)	Nuclear scattering. Surface and interface structure analysis with MBE. Inelastic X-ray scattering. XAFS.
BL14B1	**JAEA Materials Science**	(Dec. 1997)	Materials science under high-temperature. *In situ* study on catalysis using dispersive XAFS. X-ray diffraction for structure physics.
BL22XU	**JAEA Quantum Structural Science**	(May 2002)	Materials science under high-pressure. Resonant X-ray scattering. Speckle scattering. Residual stress/strain distribution analysis.
BL23SU	**JAEA Actinide Science**	(Feb. 1998)	Surface chemistry with supersonic molecular beam. Biophysical spectroscopy. Photoelectron spectroscopy. Magnetic circular dichroism.
	◆ RIKEN Beamlines		
BL17SU	**RIKEN Coherent Soft X-ray Spectroscopy**	(Sep. 2003)	High resolution photoemission spectroscopy. Soft X-ray emission spectroscopy for liquid and biological samples. Soft X-ray diffraction spectroscopy. Surface science.
BL19LXU	**RIKEN SR Physics**	(Oct. 2000)	SR science with highly brilliant X-ray beam.
BL26B1	**RIKEN Structural Genomics I**	(Apr. 2002)	Structural genomics research based on single crystal X-ray diffraction.
BL26B2	**RIKEN Structural Genomics II**	(Apr. 2002)	Structural genomics research based on single crystal X-ray diffraction.
BL29XU	**RIKEN Coherent X-ray Optics**	(Dec. 1998)	X-ray optics, especially coherent X-ray optics.
BL32XU	**RIKEN Targeted Proteins**	(Oct. 2009)	Protein micro-crystallography.
BL44B2	**RIKEN Materials Science**	(Feb. 1998)	Structural materials science research using powder X-ray diffraction
BL45XU	**RIKEN Structural Biology I**	(Jul. 1997)	Time-resolved and static structures of non-crystalline biological materials using small-angle scattering and diffraction techniques.
	■ Accelerator Diagnostics Beamlines		
BL05SS	**Accelerator Beam Diagnosis**	(Mar. 2004)	Accelerator beam diagnosis. R&D of accelerator components. Production of MeV γ-ray photons.
BL38B2	**Accelerator Beam Diagnosis**	(Sep. 1999)	Accelerator beam diagnosis. R&D of accelerator components.

IV. User Program and Statistics

IV-1. Program Overview

JASRI calls for public use proposals twice a year. The submitted proposals are reviewed by the Proposal Review Committee (PRC). As for General Proposals, 659 proposals out of 1163 submitted proposals were approved in the research term 2008B, and 654 out of 979 proposals were approved in 2009A. Since the start of the Long-term Program in 2000B, 24 Long-term Proposals have been implemented. Two new proposals were approved in 2009A, and 8 and 9 proposals were carried out in 2008B and 2009A, respectively. In 2008B and 2009A, Nanotechnology Support Proposals, Industrial Application Proposals, Medical Bio Trial Use Proposals and Medical Bio EX Proposals were called for as Priority Field Proposals. Out of 314 submitted proposals, 166 proposals were approved in 2008B, and 172 out of 254 proposals were approved in 2009A. The proposal statistics are shown in Table IV for the period from 1997B to 2009A; Power User Proposals and JASRI Proposals are excluded. During the period from 2003B to 2009A, 17 user groups were designated as Power User groups (PUs), which include six PUs active in 2009A. To date, a total of 2763 shifts have been used by PUs, of which 537 shifts were spent from 2008B to 2009A.

SPring-8 consistently provided 1,879 hours of user beamtime in 2008B and 1,927 hours in 2009A. Since the start of operation in 1997, SPring-8 has succeeded in providing users with a total beamtime of 44,925 hours. In 2008B, 889 experiments were conducted by 5,955 users at public and contract beamlines, and 907 experiments by 6,001 users in 2009A. From the start of operation in 1997 to 2009A, a total of 15,347 experiments were conducted by 103,286 users. It was on the 5th of June 2009 that the total number of user visits to SPring-8 reached 100,000.

The beamtime available to the users, the number of experiments conducted, and the number of user visits at the public and contract beamlines are summarized in Table V and in Fig. 3.

Figure 4 shows the breakdown of the approved proposals sorted by user affiliation and of the number of experiments conducted at the public and contract beamlines from 1997B to 2009A. The percentages of experiments conducted by users from abroad were 5.7% in 2008B and 6.1% in 2009A.

Since SPring-8 is a public facility widely open not only to academia but also to industrial sectors, JASRI established the Industrial Application Division in 2005. The division's coordinators specializing in the fields of SR industrial applications are available for consultation with new users. Currently, Industrial Application Proposals account for approximately 20% of the total number of proposals conducted at the public beamlines. From 2007B, SPring-8 has introduced the SPring-8 Measurement Service, in which the personnel of the Industrial Application Division can carry out XAFS measurements on behalf of users at BL14B2. SPring-8 has expanded the measurement service to Mail-in Protein Crystallography Data Collection at BL38B1 and powder X-ray diffraction at BL19B2 since 2009B.

Table IV. Numbers of submitted proposals and approved proposals in each research term

Research Term	Beamtime available to users at each beamline	Submission deadline	Number of submitted proposals	Number of approved proposals
1997B: 1997.10 - 1998.03	168	1997.1.10	198	134
1998A: 1998.04 - 1998.10	204	1998.1.6	305	229
1999A: 1998.11 - 1999.06	250	1998.7.12	392	258
1999B: 1999.09 - 1999.12	140	1999.6.19	431	246
2000A: 2000.02 - 2000.06	204	1999.10.16	424	326
2000B: 2000.10 - 2001.01	156	2000.6.17	582	380
2001A: 2001.02 - 2001.06	238	2000.10.21	502	409
2001B: 2001.09 - 2002.02	190	2001.5.26	619	457
2002A: 2002.02 - 2002.07	226	2001.10.27	643	520
2002B: 2002.09 - 2003.02	190	2002.6.3	751	472
2003A: 2003.02 - 2003.07	228	2002.10.28	733	563
2003B: 2003.09 - 2004.02	202	2003.6.16	938	621
2004A: 2004.02 - 2004.07	211	2003.11.4	772	595
2004B: 2004.09 - 2004.12	203	2004.6.9	886	562
2005A: 2005.04 - 2005.08	188	2005.1.5	878	547
2005B: 2005.09 - 2005.12	182	2005.6.7	973	624
2006A: 2006.03 - 2006.07	220	2005.11.15	916	699
2006B: 2006.09 - 2006.12	159	2006.5.25	867	555
2007A: 2007.03 - 2007.07	246	2006.11.16	1099	761
2007B: 2007.09 - 2008.02	216	2007.6.7	1007	721
2008A: 2008.04 - 2008.07	225	2007.12.13	1009	749
2008B: 2008.10 - 2009.03	189	2008.6.26	1163	659
2009A: 2009.04 - 2009.07	195	2009.12.11	979	654

Table V. SPring-8 user operation results

Research Term	User Time (hours)	Public BL		Contract BL	
		Experiments	Users	Experiments	Users
1997B: 1997.10 - 1998.03	1,286	94	681	–	–
1998A: 1998.04 - 1998.10	1,702	234	1,252	7	–
1999A: 1998.11 - 1999.06	2,585	274	1,542	33	467
1999B: 1999.09 - 1999.12	1,371	242	1,631	65	427
2000A: 2000.02 - 2000.06	2,051	365	2,486	100	794
2000B: 2000.10 - 2001.01	1,522	383	2,370	88	620
2001A: 2001.02 - 2001.06	2,313	474	2,915	102	766
2001B: 2001.09 - 2002.02	1,867	488	3,277	114	977
2002A: 2002.02 - 2002.07	2,093	545	3,246	110	1,043
2002B: 2002.09 - 2003.02	1,867	540	3,508	142	1,046
2003A: 2003.02 - 2003.07	2,246	634	3,777	164	1,347
2003B: 2003.09 - 2004.02	1,844	549	3,428	154	1,264
2004A: 2004.02 - 2004.07	2,095	569	3,756	161	1,269
2004B: 2004.09 - 2004.12	1,971	555	3,546	146	1,154
2005A: 2005.04 - 2005.08	1,880	560	3,741	146	1,185
2005B: 2005.09 - 2005.12	1,818	620	4,032	187	1,379
2006A: 2006.03 - 2006.07	2,202	724	4,809	226	1,831
2006B: 2006.09 - 2006.12	1,587	550	3,513	199	1,487
2007A: 2007.03 - 2007.07	2,448	781	4,999	260	2,282
2007B: 2007.09 - 2008.02	2,140	739	4,814	226	1,938
2008A: 2008.04 - 2008.07	2,231	769	4,840	232	1,891
2008B: 2008.10 - 2009.03	1,879	672	4,325	217	1,630
2009A: 2009.04 - 2009.07	1,927	669	4,240	238	1,761
	44,925	12,030	76,728	3,317	26,558

Note: The numbers of long-term proposals are counted by beamline, that is, if two beamlines were used for one experiment, those are counted as two experiments.

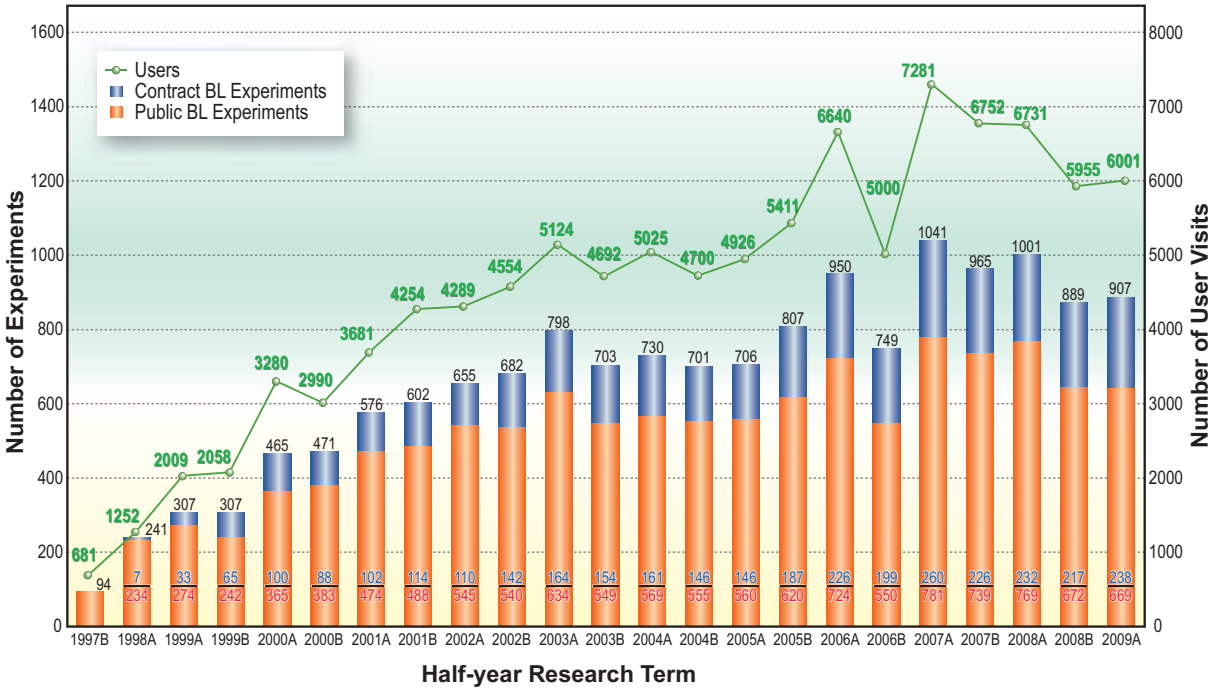

Fig. 3. Numbers of user visits and conducted experiments.

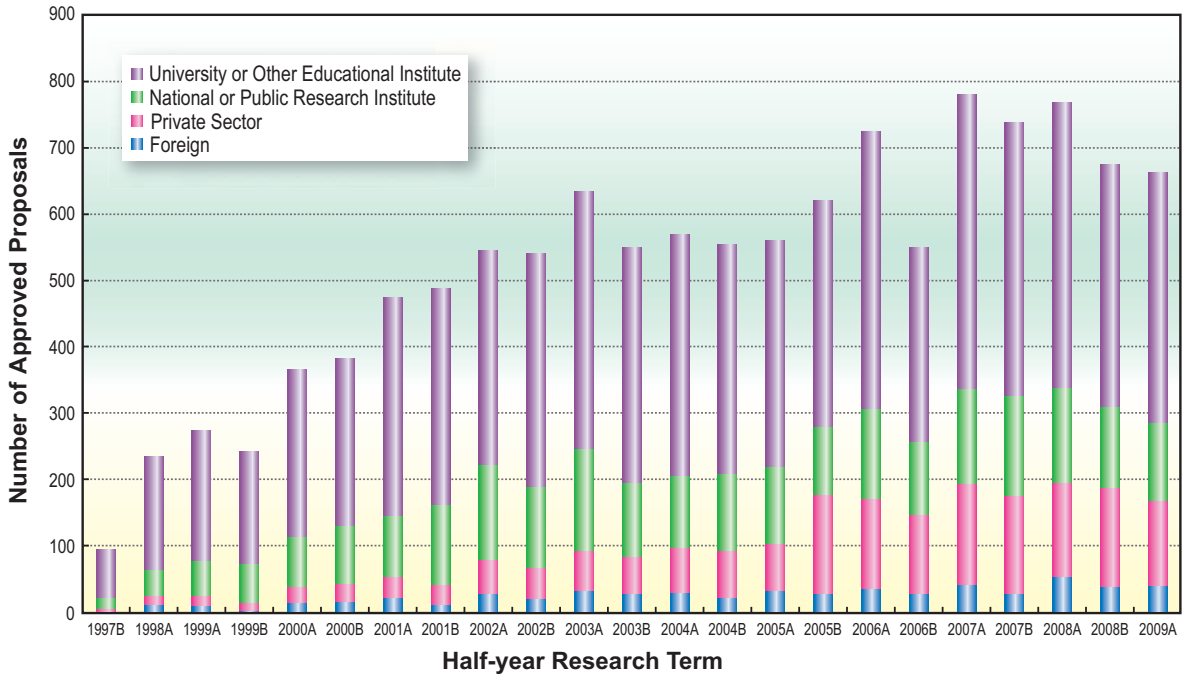

Fig. 4. Number of approved proposals by affiliation of applicants (public beamlines).

IV-2. Types of Research
(Proprietary Research and Non-Proprietary Research)

With respect to the handling of research results obtained by using SPring-8, there are two types of research at SPring-8, namely, proprietary research and non-proprietary research. For research to be considered non-proprietary, users must submit the SPring-8 Experiment Report within 60 days of the completion of each experiment to make the results available to the public. Users can use beamlines free of charge if their research is non-proprietary. As for proprietary research, the research proposals are reviewed only from the viewpoint of feasibility, safety, sociality, and ethics. In this type of research, users are charged a beamtime fee of 480,000 yen/shift based on cost recovery for SPring-8 beamline operation. In return, SPring-8 Experiment Reports need not be submitted.

IV-3. Types of Proposals

A. General Research Program

(i) General Proposal

JASRI calls for General Proposals twice a year. Once approved, the validity of each proposal is six months. Up to 10% of the total beamtime is allocated to proprietary proposals.

(ii) Long-term Proposal

Beamtime is reserved for Long-term Proposals for three years in order to promote research expected (a) to produce outstanding results in the field of science and technology, (b) to establish a new research field or experimental method, and (c) to significantly improve industrial base technology by fully utilizing the characteristics of SPring-8. The call for Long-term Proposals and the review process take place twice a year prior to those for General Proposals. For this type of proposal, proprietary research is not available. The review process consists of two steps: application forms are reviewed initially and applicants who meet certain criteria will proceed to the interview.

(iii) Urgent Proposal

This system is designed for users with urgent needs to conduct experiments of great scientific significance. The PRC reviews the submitted proposals on a rolling basis and promptly determines whether to approve or reject them.

(iv) Budding Researchers Support Proposal

The Budding Researchers Support Program is intended to encourage doctoral students with an exploratory and original research proposal or research theme that is expected to contribute to the development of synchrotron radiation research. Under this program, successful applicants will be provided with domestic travel and lodging expenses. At the time of the experiment at SPring-8, applicants must be doctoral students who show initiative, can work independently, and are self-reliant when conducting research at SPring-8. All applicants are required to obtain permission to apply from their Ph.D. adviser, who must be included as a project team member.

(v) Non-proprietary Grant-aided Proposal

The Non-proprietary Grant-aided Program is intended for research proposals that have been reviewed and approved for a large research grant available in Japan. Under this program, the proposals are exempt from a scientific review process, and only the feasibility and safety of the experiment are considered. These proposals are given priority consideration for up to 5% of the entire user beamtime and 20% of the user beamtime for each beamline. However, users are required to pay a program fee of 131,000 yen/shift.

(vi) Time-designated Proposal

The time-designated use is intended for users wishing to conduct proprietary research in a particular time period. Submitted proposals are promptly reviewed through a simplified process. Users are charged a beamtime fee of 720,000 yen/shift for proprietary use (incl. 50% premium).

(vii) SPring-8 Measurement Service

The staff of JASRI perform measurements on behalf of users, and users can choose whether to come to SPring-8 and be present during the measurements or to simply send their samples to SPring-8. The service is intended to provide convenience for companies and research institutes that find it difficult to retain specialized staff and to accommodate the need for quick access. Application for the service is considered a proprietary proposal and is subject to the proprietary beamtime and user fees applicable to Time-designated Proposals (calculated in two-hour increments).

B. Priority Research Program

The Priority Research Program is categorized into the following two types: the priority field type and the priority user type. For the priority field type, JASRI designates research fields of strategic importance.

For the priority user type, eligible candidates, who are highly familiar with the public beamlines and their methodological approaches, and who are expected to deepen the academic fields of SR science and technology, are designated as power users. JASRI has been providing active support for this program to produce a number of high-quality results.

B-1) Priority Field Type

Currently, the following three types of research are designated under the priority field type:

(i) Nanotechnology Support Proposal (period of designation: FY2007-FY2011)

On the basis of the achievements gained through the Nanotechnology Support Project (a national project from FY2002 to FY2006), the research field of nanotechnology and nanomaterials has been designated as the priority field. The purpose of this system is to support research in the field of nanotechnology and nanomaterials for innovation creation in 5-10 years time.

(ii) Industrial Application Proposal (period of designation: FY2007-FY2011)

This field is aimed at promoting the expansion of industrial application fields by attracting new users, developing a basic technology through the industry academia-government cooperation, and promoting projects whose achievements contribute to companies and society. JASRI provides intensive support in the categories of "new users," "new area," "industrial base consortium," and "advanced technology development." To meet the needs of industrial users, JASRI calls for Industrial Application Proposals four times a year for the three public beamlines (BL14B2, BL19B2 and BL46XU) dedicated to industrial applications.

(iii) Medical Bio Trial Use Proposal and Medical Bio EX Proposal (period of designation: FY2006-FY2009)

Aiming at establishing new experimental methods in the medical bio field, there are two types of proposal in this field: Medical Bio Trial Use Proposal and Medical Bio EX Proposal. The Medical Bio Trial Use Proposal is intended for the promotion of beamline use by new users, who seek to develop and establish a new approach to solving problems at the forefront of medical biology research. The Medical Bio EX Proposal, which is an expanded and developed form of the Medical Bio Trial Use Proposal, is designed for research aimed at discovering the causes of major diseases and to develop their diagnostic and treatment methods. This program was successfully finished at the end of FY2009.

B-2) Priority User Type

(i) Power User Proposal

Power User Proposals are non-proprietary proposals designed for designated power user groups (PUs) to produce outstanding results in the field of pioneering use of SR using up to 20% of the beamtime allocated to beamlines accepting PUs. The power user designation period is five years. PUs are subject to an interim review of research achievements, equipment development, and user support by the Power User Review Committee at the end of the third year to determine whether to continue or discontinue the power user status. When the designation period is completed, a post implementation review is conducted by the Committee. JASRI invites applications for power user positions once a year, which takes place before the proposal calls for research term A.

IV-4. Beamtime Allocation

The beamtime allocation of public beamlines is arranged in such that more than 50% of the total beamtime is allocated to public use proposals (proposals that are submitted in response to calls for proposals and approved by the PRC), while up to 20% is allocated to JASRI's own research proposals. The remaining beamtime is used for seminars, trainings, setup/removal and adjustment of equipment for user experiments, and proposals with special needs and requirements (Urgent, Time-designated, and Power User Proposals). The conceptual scheme of the beamtime allocation at the public beamlines is shown in Fig. 5.

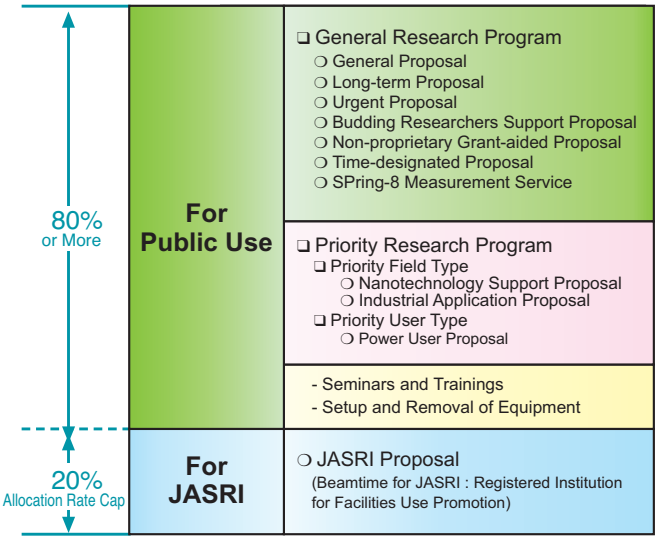

Fig. 5. Conceptual scheme of beamtime allocation at public beamlines.

IV-5. Research Outcome

When users conduct non-proprietary experiments, they are required to submit the SPring-8 Experiment Report to JASRI within 60 days of the completion of their experiments. When the research results obtained through the use of SPring-8 are published in academic journals and other publications, the project leaders are requested to report to JASRI. As of March 2010, the number of registered refereed papers is 5,327, out of which 4,245 papers resulted from the use of public beamlines, 868 papers from that of contract beamlines, 733 papers from that of RIKEN beamlines, and 353 papers from hardware/software R&D. The papers resulting from the use of two or more beamlines are counted at each beamline. Figure 6 shows the annual statistics of refereed papers.

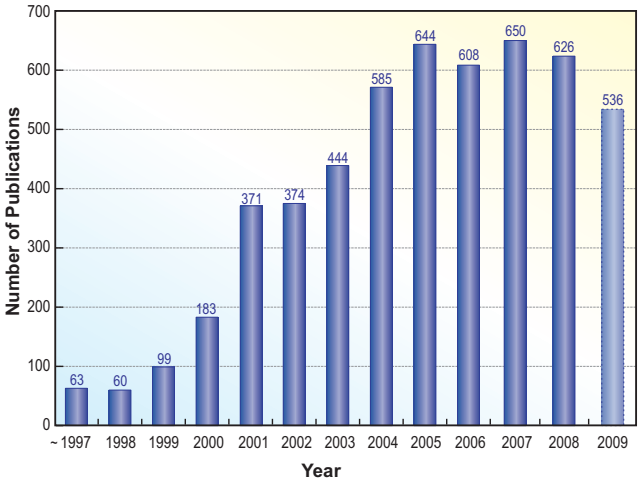

Fig. 6. Number of refereed publications as of March 2010.

V. Budget and Personnel

Since the start of operation in 1997, SPring-8 had been jointly managed by RIKEN, JAERI (JAEA, as it is known today), and JASRI. Since JAERI withdrew from the management of SPring-8 on September 30, 2005, SPring-8 has been administered by RIKEN and JASRI in a collaborative manner.

Figure 7 shows the annual budget allocated to the operation, maintenance, and promotion of the use of SPring-8 from FY1997 to date. The budget for FY2009 is 8.66 billion yen. The total number of staff members of JASRI, RIKEN and XFEL Project is 1,315 as of October 2009, as shown in Fig. 8.

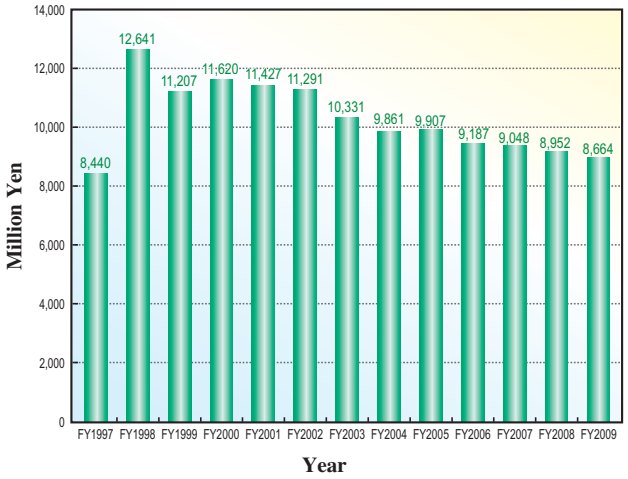

Fig. 7. SPring-8 budget.

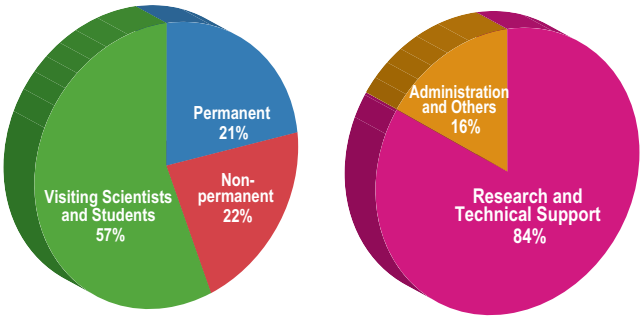

	by Type			by Field	
	Permanent	Non-permanent	Visiting Scientists and Students	Research and Technical Support	Administration and Others
JASRI	233	151	158	392	150
RIKEN	54	87	513	603	47
XFEL	1	52	96	128	14

Including double counts.

Fig. 8. Personnel at SPring-8: JASRI, RIKEN and XFEL (FY2009).

VI. Research Complex

The facilities of SPring-8, XFEL and NewSUBARU form a center of excellence at the SPring-8 campus, where JASRI, public beamline users, contractors of contract beamlines, RIKEN, and the University of Hyogo work in close cooperation to form a research complex by playing their own roles to deliver high-quality results in the field of synchrotron radiation science and technology. Figure 9 shows the SPring-8 research complex and the operation and management of each research facility. The organizational charts of RIKEN and JASRI, which form the kernel of this research complex, are shown in Fig. 10 and Fig. 11, respectively.

Fig. 9. SPring-8 research complex.

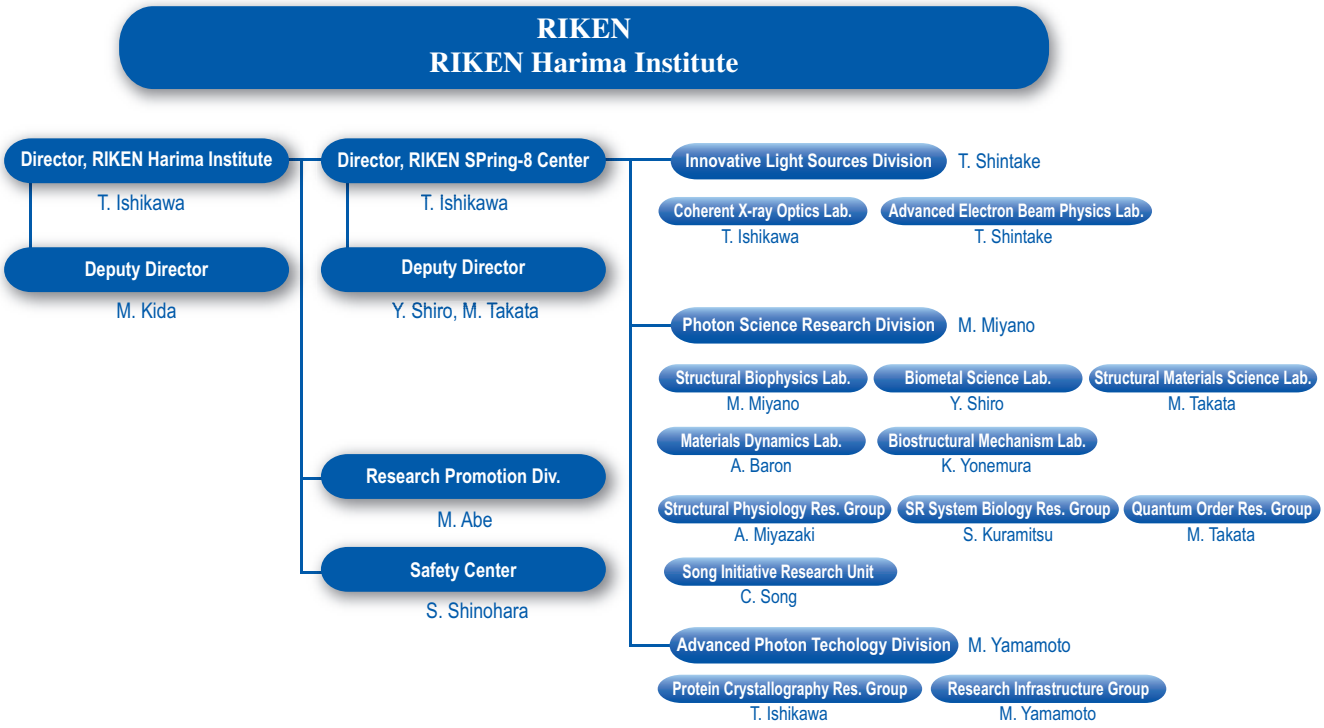

Fig. 10. RIKEN Harima chart as of April 2010.

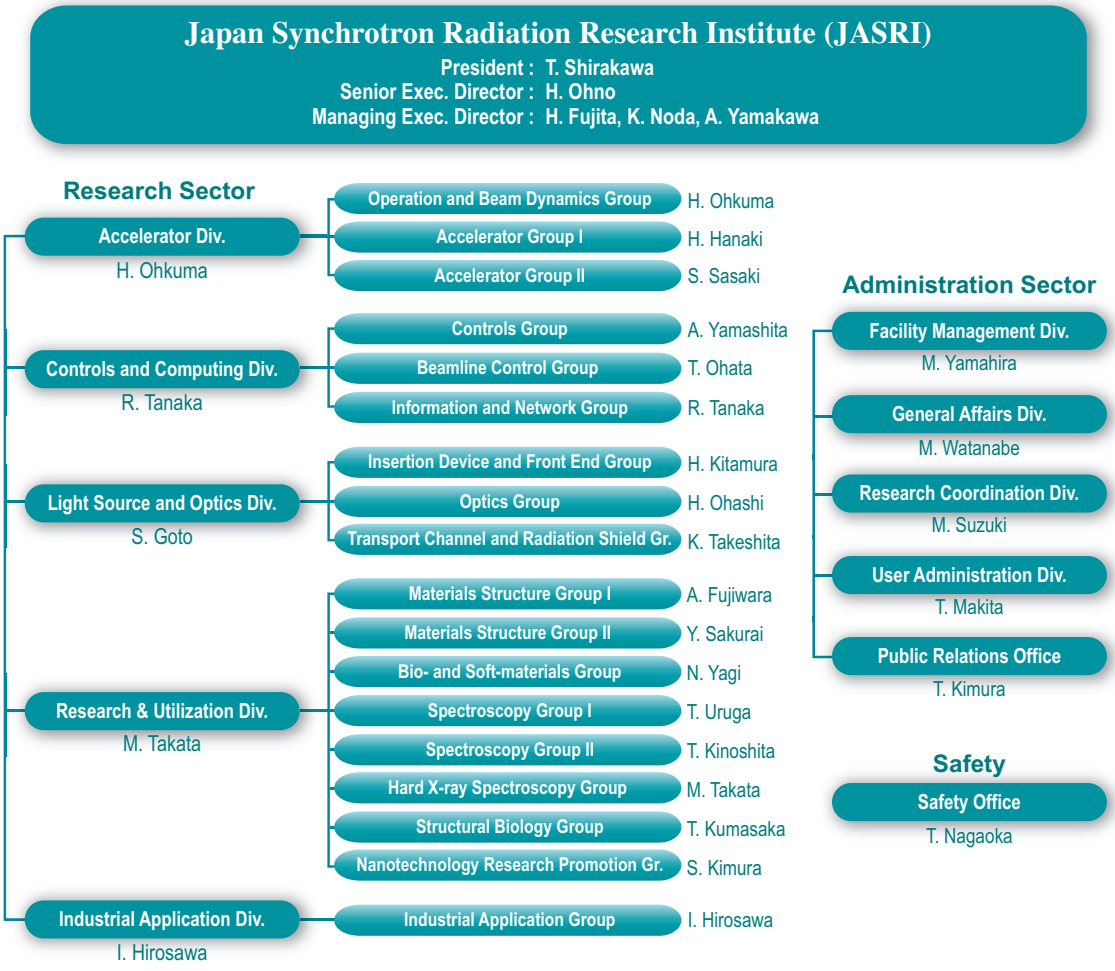

Fig. 11. JASRI chart as of April 2010.

VII. Users Societies, Conferences and Other Activities

Users Society

In May 1988, the User Group for Advanced X-ray Source was organized by potential users, aiming at discussing the research plan and the user policy. On the basis of the achievements of this group, the **SPring-8 Users Society** was established in May 1993 to promote and advance the research activities of users, and it made a substantial contribution to the construction of SPring-8. The current goal is to support the upgrade of the storage ring and individual beamlines, and to promote the utilization of SPring-8. At present, 35 scientific research groups and nine commissions of the Society are active in scientific contributions to develop research activities and in information exchange between staffs members and users. The development of synchrotron radiation science for the next ten years from now has been discussed by these research groups, and the report entitled "Future Prospects for Scientific Activities at SPring-8" has been published in March 2009. The number of active members in the Society is 1,267 as of December 31, 2009.

The **Industrial Users Society of SPring-8** was established by the members of various companies in September 1990 to promote the use of SPring-8 and to dedicate in the development of the SPring-8 user program. Several research groups focused on various fields of applications have been organized; at present, nine are active. The main purpose of the society is not only to provide information on the trends of the synchrotron radiation facilities in Japan and abroad, and their latest research achievements, but also to enhance communication among the industrial sector, JASRI, and MEXT. As a result, the percentage of industrial applications has increased to 20% in terms of the number of proposals approved. The Society consists of 68 companies and one organization as of December 31, 2009.

In 2009, the annual meetings of the two societies were jointly held for the first time, as the 1st SPring-8 Conference. Previously, these meetings were almost independently organized to report and discuss the outcomes from academia and industrial domains, respectively. The first joint conference was successfully held that made it possible to cross-fertilize both regions by directly exchanging information.

Users Meeting

The meeting for users jointly organized by the SPring-8 Users Society and/or the Industrial User Society of SPring-8, and JASRI and RIKEN is listed below.

- The 1st SPring-8 Conference
  September 3-4, 2009 - Tokyo Station Conference, Tokyo

Conferences and Workshops

The conferences and workshops organized, sponsored, or hosted by JASRI, RIKEN or both in 2009 are listed below.

22th Annual Meeting of Japanese Society for Synchrotron Radiation Research
January 9-12, 2009 - The University of Tokyo Hongo Campus, Tokyo

The Report Meeting of SPring-8 Priority Nanotechnology Support Program FY2008
March 12, 2009 - Public Relations Center, SPring-8

The Annual Meeting of SPring-8 Priority Nanotechnology Support Program FY2008
May 8, 2009 - National Institute for Materials Science Sengen Site, Ibaraki

The 1st Symposium on SPring-8 Upgrade Plan
June 19, 2009 - Tokyo Station Conference, Tokyo

The 8th Annual Meeting of Structural-Biological Whole Cell Project of *Thermus thermophilus* HB8
August 21-23, 2009 - Public Relations Center, SPring-8

The 2nd Workshop on the SPring-8 Budding Researchers Support Program
September 1, 2009 - Campus Innovation Centre, Tokyo

International Workshop on X-ray Mirror Design, Fabrication, and Metrology (IWXM)
September 22-24, 2009 - Osaka University Suita Campus, Osaka

The 12th International Conference on Accelerator and Large Experimental Physics Control Systems (ICALEPCS 2009)
October 12-16, 2009 - Kobe International Conference Center (KICC), Kobe

Synchrotron Radiation Industrial Applications Seminar –SPring-8 / Photon Factory Collaboration–
October 30, 2009 - Tsukuba International Congress Centre, Ibaraki

The 5th XFEL Symposium
November 27, 2009 - Shinagawa Intercity Hall, Tokyo

Other Activities

The 17th SPring-8 Open House
April 26, 2009

The 9th SPring-8 Summer School 2009
July 10-13, 2009 - Kamitsubo Hall, SPring-8

The 3rd AOFSRR Summer School - Cheiron School 2009
November 2- 11, 2009 - Public Relations Center, SPring-8

Project XFEL

The year 2009 should be a memorable one for photon-related scientists and engineers since the first X-ray Free Electron Laser in the hard X-ray region using Self-Amplified Spontaneous Emission (SASE) scheme was observed at the Linac Coherent Light Source (LCLS) at the SLAC National Accelerator Laboratory in the U.S. The initial user operation in the softer X-ray region has demonstrated extraordinary potentials of SASE-FEL, and at the same time, has shown very small opportunity with only one XFEL line in the world. The world community is eagerly waiting for us to appear on the stage. The operational stability achieved at the LCLS supports our conclusion from the operational experience of SPring-8 Compact SASE Source (SCSS) that SASE sources are, in principle, stable, contrary to the various experiences at the FLASH-FEL at Hamburg.

Our five-year project of XFEL construction that started in 2006 has reached the middle of the second half. Buildings for accelerator and undulators were completed at the end of the previous fiscal year. Accelerator assembly and undulator alignment are moving ahead at a fast pace, together with the construction of the experimental building as well as the electron beam transport to the SPring-8 booster synchrotron. Everything is on, or a little ahead of, schedule as of February 2010 so that we are able to complete all the hardware assembly before autumn, make RF aging within the calendar year, and start electron beam tuning in January 2011. Meanwhile, many users have been enjoying the stable operation of SCSS of around 60 nm wavelength, which has enormously contributed to the development of many components of the 8 GeV XFEL.

In addition, the XFEL and SPring-8 photon beam colliding facility was approved, enabling a novel scheme of pump-probe experiments that use the XFEL light as a pump and SPring-8 synchrotron X-rays as a probe. This new possibility will enhance the synergy between SPring-8 and XFEL, in addition to the electron beam injection capability from XFEL linac to the SPring-8 storage ring.

We would like to encourage and invite completely new ideas to use the unique capability of our XFEL, which is located closely to the world's brightest synchrotron radiation source, SPring-8.

Tetsuya Ishikawa

SPRING-8 COMPACT SASE SOURCE PROJECT
SCSS
SPRING-8
COMPACT
SASE
SOURCE

Progress of the XFEL Project

1. Status of XFEL Construction

A five-year construction project for an 8-GeV XFEL facility, which was started in FY2006 as one of the Key National Technologies for Japan, has been going well in FY2009, the fourth year of construction. This progress in four years promises the start of beam commissioning by the end of FY 2010.

The manufacture of all the components is in progress so as to start full power rf aging at the beginning of October 2010. Installation and alignment of system components were started in the undulator hall, klystron gallery, and accelerator tunnel except for the injector section.

The manufacture of the S-band and C-band rf acceleration systems was completed in FY2009. Ninety percent of accelerating tubes were installed in the accelerator tunnel with rf waveguides connected, as shown in Fig. 1. Half the number of rf sources, each of which is composed of a modulator, a klystron, and a charging power supply, were installed in the klystron gallery, as shown in Fig. 2. Prior to the installation, high power performance was tested for all the rf sources. Figure 3 shows a typical measurement data to assure the required performance.

Low level rf (LLRF) and timing systems driving and controlling rf high power equipment were tested using a full set of the C-band acceleration system. The achieved results confirmed the sufficient performance

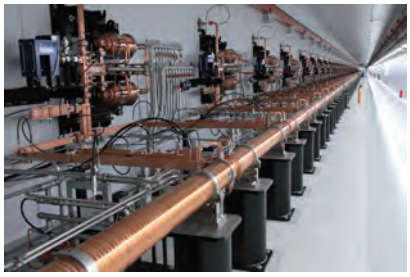

Fig. 1. C-band acceleration units installed in the accelerator building.

Fig. 2. Oil tank of the compact C-band oil-field modulator (left middle) and the racks to contain LLRF and timing systems in the klystron gallery.

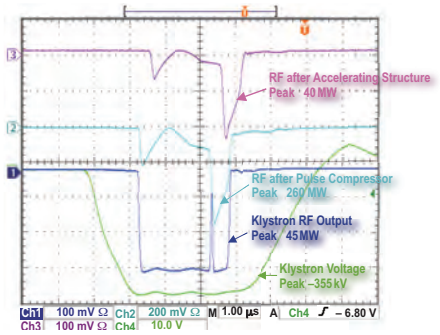

Fig. 3. Typical waveforms of the high power C-band rf components measured in the test bunker.

of the systems. Figure 4 shows the obtained ambient temperature stability in the water-cooled rack, which is critically important for stabilizing the rf system. Installation and parameter tuning of the LLRF and timing systems are on schedule.

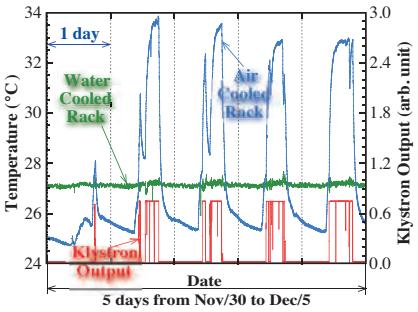

Fig. 4. Ambient temperature stabilities in the water-cooled rack and air-cooled rack together with the klystron output driven by the stable LLRF and timing systems contained in the water-cooled rack.

The manufacture of in-vacuum undulators progresses on schedule so as to install all the undulators until the middle of September 2010. Six undulators were installed and aligned to the specified positions along the BL3 line with a precision of 100 μm. Figure 5 shows the six installed in-vacuum undulators in the undulator hall.

The manufacture of magnets and their power supplies was completed. Installation and alignment of the magnets were also finished in the accelerator tunnel except for the injector part, together with those of beam position monitors (BPMs). Installation of the magnet power supplies in the gallery is scheduled in July 2010.

Seventy percent of the vacuum system composed of chambers, gages, bellows, pumps and so on was manufactured and installed in the accelerator tunnel. A vacuum leak test was also performed, showing the

Fig. 5. Six in-vacuum undulators installed in the undulator hall.

effectiveness of the newly developed flange system [1] because no leakage was detected.

For the photon beamline, detailed design works and the fabrication of key components, which include mirrors, an ultrahigh-vacuum (UHV) compatible double-crystal monochromator, front-end system, interlock system, and experimental hutches, were carried out. In particular, the performance of new monochromator mechanics, which aims to control and stabilize the angular position of crystals on the order of sub-microradian under UHV condition, has been studied. R&D on XFEL diagnostics have been advanced. For monitoring the total intensity and center of mass of XFEL radiation, a thin-foil scattering monitor has been studied at beamline BL29XU. For a profile monitor under high-intensity field, a fluorescence property from a CVD diamond has been examined. The development and evaluation of a thin-silicon crystal for the XFEL beam splitter have been carried out.

In the XFEL experiments, X-ray two-dimensional (2D) detectors and their data acquisition (DAQ) systems are to be developed on top of the existing standard beamline control system. As the standard X-ray 2D detector of the facility, multiport CCD detector development was launched in March 2009. The design of the chip layout, control and readout electronics, as well as the detector mechanics, was completed this year. The mass production of the sensor chips is under way, and the assembly of the first detector system is in progress. The DAQ system to store and monitor the data stream up to 4 Gbps consists of the DAQ front-end, 10 G network, high-performance high-reliability storage, and software to control the equipment. The performance evaluation for all the components to be installed in June 2010 has been completed. The detailed technical design of the control software has been completed and its implementation has been started.

In FY2009, the construction of the XFEL beam transport tunnel building and XFEL experimental facility has progressed. The transport tunnel building adopted a cast-in-place concrete pile method to support piles of 1000 mm ϕ firmly on the rock bed to suppress building deformation. The building frame was made with radiation-shielding concrete, the thickness of which is 1.1 m at the floor, wall, and ceiling in order to achieve the required shield performance. Completion of the beam transport tunnel building is scheduled in March 2010.

The experimental facility adopted a trussed girder structure to provide a pillar less wide space as an experimental hall. As foundation, spread foundation directly set on the rock bed was used in order to achieve the required stability without ground sinkage and sufficiently small ground vibration. The experimental facility will be completed in May 2010.

2. Operation Status of the SCSS Test Accelerator

After the proof-of-principle experiment showing that an FEL system based on the SCSS concept can generate a high-performance SASE FEL, the test accelerator has been improved aiming at ideal FEL operation. Despite the day-by-day operation, the continuous power saturation of a SASE FEL has been routinely obtained over wavelengths from 50 to 60 nm. In FY2009 (9 months from April to December), the total beam time is 1393 h (139 days) and 49% or 684 h (77 days) was provided to user experiments. The downtime rate for the user beam time was 4%. The regular beam time in a day is currently 9 h from 10:00 a.m. to 7:00 p.m.

Our present efforts are categorized into the following four parts: (I) R&D on beam feedback for stabilizing a SASE FEL, (II) development of key optical components for EUV-FEL utilization, (III) R&D on a seeded FEL with temporal coherence, and (IV) summary of user experimental programs.

(I) Beam feedback development: In order to stabilize the FEL position at the experimental hutch, a simple two-stage orbit feedback correction has been introduced in the undulator section. Here, the horizontal and vertical positions are corrected first at the entrance of the undulator section using the upstream single steering magnets. The angle errors are then corrected in both planes using the single-steering magnets just downstream of the BPM used in the first stage to minimize the displacements over the undulator section. The correction is currently performed with a cycle of 0.2 Hz using the orbit estimated by averaging 45 shot-by-shot data [2]. By this correction, the horizontal and vertical orbit drifts have been reduced to 6.4 and 2.3 μm, respectively. Figure 6 shows the vertical orbit drifts between the two undulators over 2 hours with

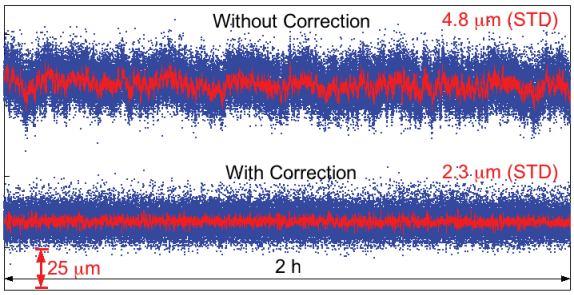

Fig. 6. Vertical orbit drifts over 2 h with and without the correction. The blue dots and red lines represent the shot-by-shot data and moving-averaged orbit with the 45 data. The measurement position is the middle of the undulator section.

and without the correction.

The XFEL at SPring-8 has a multiple-stage bunch compression system composed of one velocity bunching and three magnetic-bunching processes. To achieve the stable SASE FEL, local beam feedback loops fixing the beam current distribution at the exit of each bunching process are crucial as demonstrated at LCLS. Key points in the development are a feedback model for the velocity bunching and the separation between the velocity bunching and the first magnetic bunching. To test the feedback model for the velocity bunching and stabilize SASE intensity further in the SCSS test accelerator, a simple feedback loop has been introduced, in which an energy variation of the magnetic chicane is returned to a phase of the 238 MHz SHB [3]. Here, it is assumed that a voltage drift of the electron gun mainly causes the energy variation in such day-by-day operation. Figure 7 shows the SASE intensity and beam energy variations at the magnetic chicane with and without the correction. It is found that the energy-correlated SASE intensity variation is suppressed to some extent by the

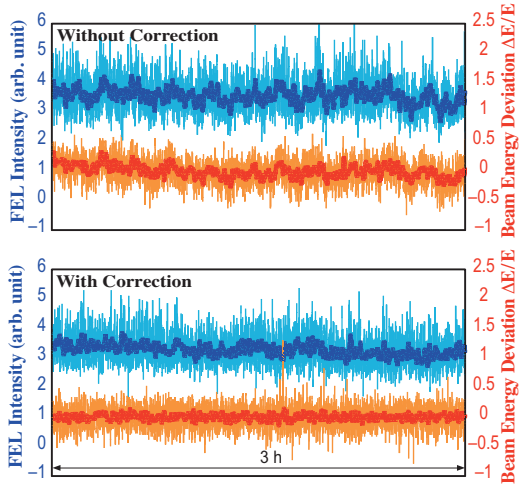

Fig. 7. Shot-by-shot SASE intensity and beam energy variations at the magnetic chicane over 3 h with and without the feedback correction. The blue and red bold lines represent the moving-averaged variables with 20 shot-by-shot data.

correction. To complete the two-stage feedback loops for stabilizing the beam current distribution, a beam arrival timing detection system and an intensity detection system of THz coherent SR (CSR) are under development. Figure 8 shows the firstly observed THz CSR signal measured using a pyroelectric detector.

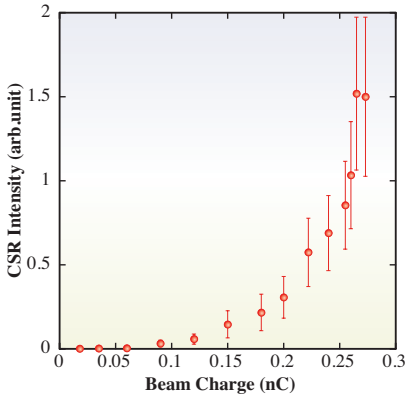

Fig. 8. THz CSR signals measured using a pyroelectric detector at the magnetic chicane just before the undulator section.

(II) Development of key optical components for EUV-FEL utilization: We have installed a focusing optical system at branch E of the EUV-FEL beamline in the experimental facility. The beamline has no stationary endstation in the experimental facility to conduct different scientific experiments by users. The focusing system was designed to be able to conveniently connect different endstations as follows: a working distance of 1 m from the center of the last mirror to the focusing point, the exit beam lying on the horizontal plane of the incident beam, the focusing point near the unfocusing beam, which passes through the focusing system without reflection, and the focused spot size below 30 μm diameter. To satisfy the above requirements, the focusing system consists of a pair of elliptical and cylindrical mirrors.

The profile of the focused beam was measured using a scanning pinhole with a diameter of 10 μm, as shown in Fig. 9. The focused spot size was 22 μm (V) × 26 μm (H) (FWHM), which was obtained by a deconvolution of the measured spot size with the diameter of the pinhole. Since the pulse energy of the focused beam using a cryogenic radiometer was 10 μJ, the beam power density was estimated to be ~20 TW/cm^2 as a pulse duration of 100 fs.

(III) R&D on a seeded FEL with temporal coherence: An amplifying process based on the self-amplified spontaneous emission (SASE) scheme, which is the most popular technique in the single-pass FEL methods, produces a spiky longitudinal profile at each shot owing to its limited temporal coherence. A full

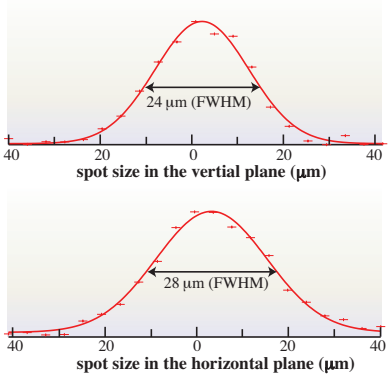

Fig. 9. Focused spot size measured using a scanning pinhole.

coherent FEL can be realized by injecting coherent light produced by an external seeding source to undulators. High order harmonics (HH), which are generated from rare gas targets interacted with intense femtosecond near-infrared laser pulses, is one of the most suitable seeding sources in the EUV region because of its excellent coherence and sufficient power (Fig. 10(a)).

The seeded FEL had been realized with 160 nm wavelength in 2002 [4]. For injection with shorter wavelength, about 10 nJ HH power is required in an undulator from the numerical simulations. A high power Ti:sapphire laser system, which produces 0.2 J and 150 fs pulses at 30 Hz repetition rate, has been developed for high-order harmonic generation. Figure 10(b) illustrates the schematic diagram of the seeded FEL. The HH from a Xe gas cell is directed to the undulators from the magnetic chicane of the SCSS test accelerator. The seeded FEL will operate with 50-60 nm wavelength for user experiment in 2010.

(IV) Summary of user experimental programs: During 2009, the EUV-FEL experimental facility has accommodated about 100 scientists representing 19 scientific groups not only from Japan but worldwide, such as Germany and Italy. The research using EUV-FEL is carried out in a large variety of disciplines, including technical research preparatory for XFEL

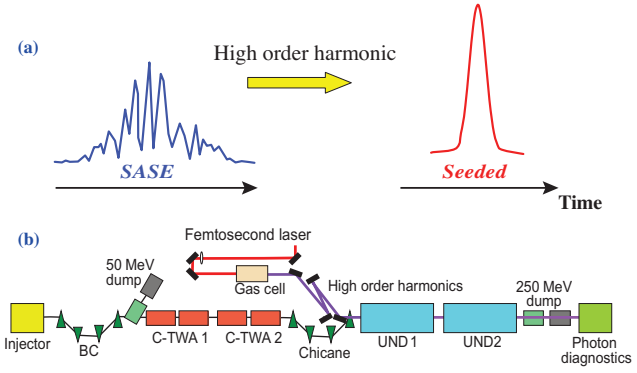

Fig. 10. **(a)** Temporal profiles of SASE and seeded FEL. **(b)** Schematic of seeded FEL.

experiments, atomic and molecular physics, coherent diffraction imaging methods, materials science such as advanced scintillators, and nonlinear X-ray devices. The number of publications from the users of EUV-FEL in FY2009 was nine papers [i-ix].

Here, we show one of the specially chosen research highlights. The group of H. Yoneda has observed a strong nonlinear absorption of Sn film at a wavelength of 61 nm from EUV-FEL [iii]. The transmission of the film is dramatically changed at a threshold energy of 6 J/cm^2, as shown in Fig. 11. This can be applied to new photonic devices for the EUV region, such as for spatial model cleaning and ultra-pulse slicing to the short-duration pulse generation.

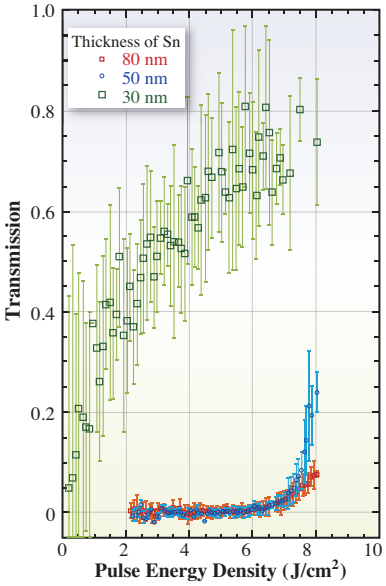

Fig. 11. Nonlinear response of transmission of the EUV-FEL.

SPring-8 Joint-Project for XFEL

E-mail: Project-XFEL@riken.jp

References

[1] T. Bizen: Proc. 11th European Particle Accel. Conf., Genoa, June, (2008) 1404.
[2] S. Tanaka *et al.*: 5th Annual Meeting of Particle Accelerator Society of Japan, JAEA, Tokai-mura, Japan, 2009.
[3] Y. Tajiri *et al.*: 5th Annual Meeting of Particle Accelerator Society of Japan, JAEA, Tokai-mura, Japan, 2009.
[4] G. Lambert *et al.*: Nature Physics **4** (2008) 296.

Publication list from the users:

[i] T. Shimizu *et al.*: Rev. Sci. Instrum. (2010) - in press.
[ii] Y. Inubushi *et al.*: Rev. Sci. Instrum. **81** (2010) 036101.
[iii] H. Yoneda *et al.*: Opt. Express **17** (2009) 23443.
[iv] M. Kato *et al.*: Nucl. Instrum. and Meth. A **612** (2009) 209.
[v] K. Motomura *et al.*: J. Phys. B: At. Mol. Opt. Phys. **42** (2009) 221003.
[vi] H. Fukuzawa *et al.*: J. Phys. B: At. Mol. Opt. Phys. **42** (2009) 181001.
[vii] K. Motomura *et al.*: Nucl. Instrum. Meth. Phys. Res. A **606** (2009) 770.
[viii] X.-J. Liu *et al.*: Rev. Sci. Instrum. **80** (2009) 053105.
[ix] H. Iwayama *et al.*: J. Phys. B: At. Mol. Opt. Phys. **42** (2009) 134019.

NewSUBARU

A 1.5 GeV synchrotron radiation ring named NewSUBARU is the main facility of the Laboratory of Advanced Science and Technology for Industry (LASTI) at the University of Hyogo. NewSUBARU is at the site of SPring-8 and can provide light beams from IR to soft X-ray. We have achieved storing 500 mA at 1 GeV and 200 mA at 1.5 GeV. At present, NewSUBARU has six bending section beamlines (BL-2, BL-3, BL-5, BL-6, BL-10, and BL-11), a short undulator beamline (BL-7), a long undulator beamline (BL-9), and an optical-klystron beamline (BL-1), as shown in Fig. 1.

Topics of the NewSUBARU research activities for this year are as follows. First is the basic characteristic research of NewSUBARU electron storage ring and gamma ray generation by laser Compton backscattering. The second is extreme ultraviolet (EUV) activities involving a microscope, using EUV beam splitters, pattern replications using EUV interference lithography, and the development of EUV resist with low line edge roughness (LER). Beamline BL09C was branched from beamline BL09B for use in EUV interference lithography for the evaluation of the exposure characteristics of EUV resist. Third is micro- and nanodevices such as high-density cell culture using micro 3D scaffold and X-ray grating for X-ray phase grating. Fourth is on the characterization of various materials such as DLC, Au-$SrTiO_3$, Zn-Al alloys, and TiO_2. Furthermore, the performance of the material analysis beamline BL5 for industrial purpose was evaluated by NEXAFS spectra measurements using the standard samples of graphite and BN.

Most of our research activities are conducted in collaboration with industries, government research institutes, and other universities. We will continue to respond to the community's demand by offering new science and technologies.

Shinji Matsui
Director of LASTI, University of Hyogo

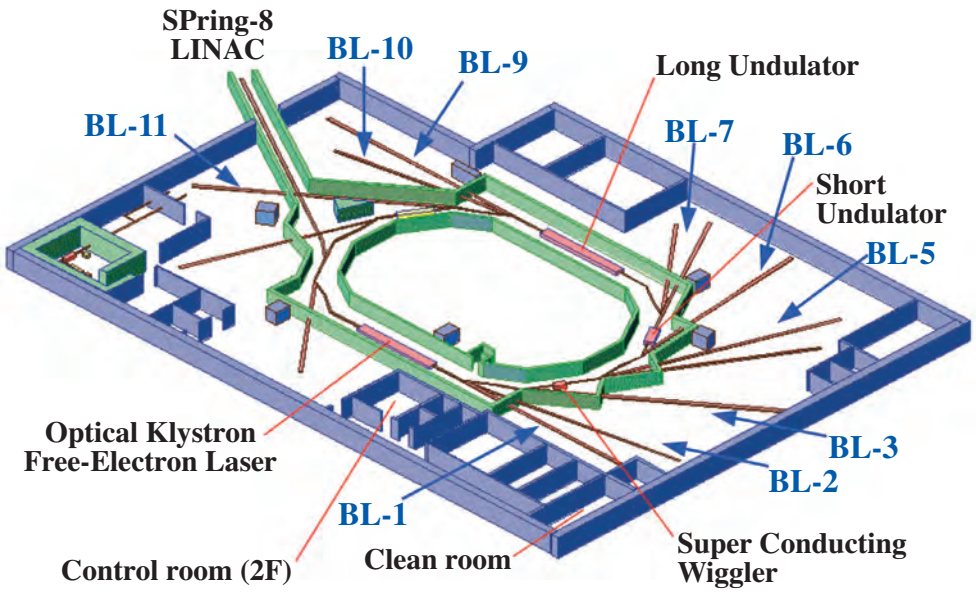

Fig. 1. Beamline arrangement in NewSUBARU.

EUV Interference Lithography at BL9 Beamline in NewSUBARU

Extreme ultraviolet lithography (EUVL) [1] is a most promising lithographic technology for next-generation lithography of the 32 nm node around 2013. EUV resist development is one of the critical issues related to the use of EUVL technology in the high volume manufacturing (HVM) of semiconductor devices. According to the International Technology Roadmap for Semiconductor (ITRS) [2], the pattern resolution, exposure sensitivity, and line width roughness (LWR) of EUV resists are the significant factors to the fabrication of the electric devices such as Microprocessing Unit (MPU), Ferroelectric Random Access Memory (FRAM), Static Random Access Memory (SRAM), and Dynamic Random Access Memory (DRAM). To maintain the lithographic throughput in HVM, the resist exposure sensitivity has to be high. In addition, to maintain the function of electric devices, the line edge width of resists should be very small. For example, according to the ITRS, 1.2 nm (3σ) of LWR for 22-nm-half-pitch (HP) node and 0.6 nm (3σ) of LWR for 11-nm-HP node are required. Thus, the fluctuation of the resist pattern width has to be maintained at 1/10 of the molecular size of the resist. Therefore, the paradigm shift of the resist material is required.

Up to now, the full field exposure tool such as α-demo tool is used to evaluate the EUV resist for the 32-nm-HP node. Since the imaging resolution of these tools is limited to 25 nm, the exposure tool should have an imaging resolution of 22 nm and below. Thus, the EUV interference lithography tool was constructed at BL9 beamline in NewSUBARU [3]. The light source of this beamline is a 10.8-m-long undulator (LU) [4]. The synchrotron radiation flux created from LU is approximately 1,000 times larger than that from the bending magnet. In addition, LU light has excellent spatial and time coherences.

Figure 1 shows the principle of EUV interference lithography (EUV-IL). In the EUV-IL, the dual beam interference system is used [4]. Transparent grating has two windows. From each grating, EUV incident light is diffracted into –1st, 0th, and +1st orders. Then, double periodic interference fringes are created at the intersection point of the –1st-order diffraction light from one grating and +1st-order diffraction light from another grating. The diffraction condition of each grating can be expressed as $m\lambda = d(\sin\theta_f - \sin\theta_i)$, where m, d, θ_f, and θ_i are number of diffraction order, pitch size of grating pattern, angle of transmitted light, and angle of incident light, respectively. In addition, the pitch size of interference fringes p is expressed as $p = \lambda/(2\sin\theta)$, where θ is half of the angle between the propagation directions of the two beams of the –1st and +1st diffraction orders. Considering normal incident light, the incident light angle may be expressed as $\theta_i = 0$. Then, the pitch size of interference fringes p is expressed as $p = d/2$. Thus, half-size of the grating pattern size can be replicated in a wafer. In EUV-IL, the distance of two windows has to be smaller than the coherence length. In addition, if the grating pitch pattern d becomes smaller, the diffraction angle θ_f of –1st and 1st diffraction orders becomes larger. Then, if the distance of the two windows of a transmission grating is constant, the distance between a grating and a wafer becomes smaller. Thus, a large spatial coherence length is required to achieve the practical distance between a grating and a wafer for imaging a resist pattern on a wafer.

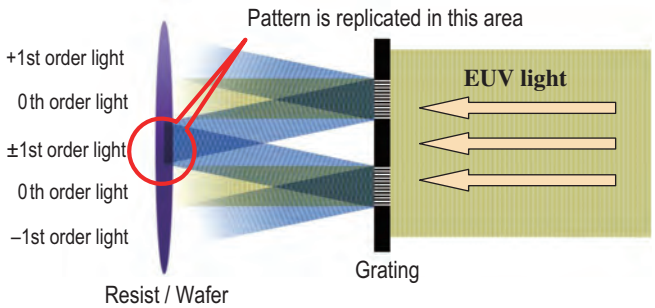

Fig. 1. Schematic of BL9 beamline and exposure chamber.

Figures 2(a) and 2(b) show the photographs of BL9 beamline and exposure chamber for EUV-IL, respectively. The LU source spectrum with the peak in a specific wavelength can be obtained by tuning a gap between the upside and downside of undulator magnets. The brilliance of EUV light of an undulator as a source is approximately 50,000 times higher than that of a bending magnet as a source. Figure 2 shows that the EUV light was focused on a pinhole using an optical component. At the pinhole position the beam is focused at a size of 10 μm in the y-direction. The distance from the pinhole to a resist is maintained to be approximately 3.3 m. Since high wavelength range larger than 20 nm is removed using a 0.2-μm-thick zirconium (Zr) filter, the light is monochromated to be a wavelength of 13.4 nm on a resist sample.

The spatial coherence of light source measurement can be determined via Young's double-slit experiment. It was confirmed that the spatial coherences using a 25 μm slit and a 10 μm slit are 544 and 1173 μm at the transmission grating position, respectively. Therefore, since a large spatial coherence length

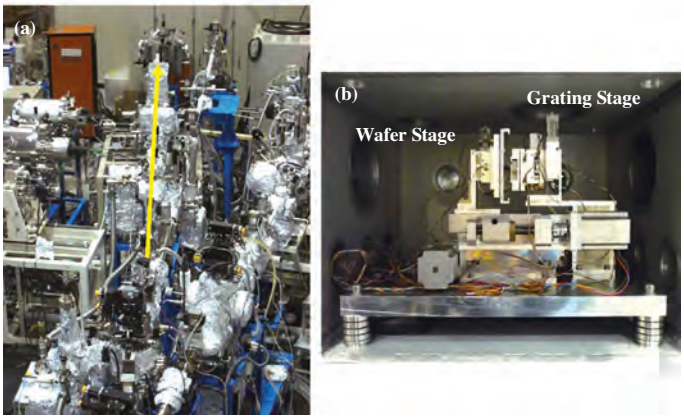

Fig. 2. Principle of EUV interference lithography.

was obtained using these optical elements, and by enlarging the distance between a grating and a wafer, the design and fabrication process of the transmission grating could be carried out effectively.

By using the 100-nm-pitch transmission grating, a 25-nm-HP resist pattern was replicated by EUV-IL. A wafer stage and a grating stage were installed in the EUV-IL exposure chamber. The wafer stage consists of *x*-, *y*-, and *z*-stages and a tilt stage, and the grating stage consists of *x*- and *y*-stages and a tilt stage. By using these stages, light axis adjustment was carried out. Figure 3 shows a photograph of a replicated ZEP520A resist pattern of 25 nm HP, which was observed using a critical-dimension scanning microscope (CD-SEM, S8840, Hitachi). In the near future, various types of chemically amplified resist will be evaluated. In addition, in a future study, we will attempt to replicate a 20-nm-HP resist pattern and below. By using a two-dimensional transmission grating, as shown in Fig. 4(a), with a four-beam diffraction, a dot or hole pattern can be replicated. In this case, by grating a 50-nm-HP dot pattern, a 35-nm-HP dot resist pattern was replicated, as shown in Fig. 4(b). The resist was ZEP520A. The resist thickness was 50 nm.

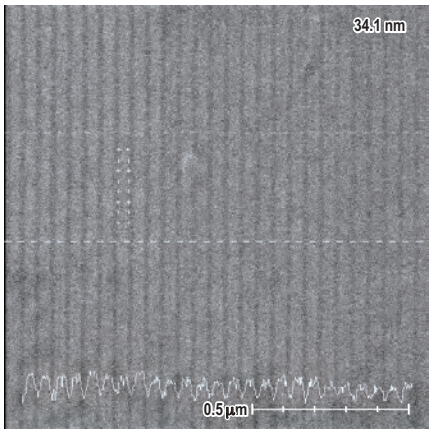

Fig. 3. SEM image of replicated resist pattern of 25 nm HP.

For the replication of a 20 nm L/S resist pattern and below by EUV-IL, we developed a fabrication process that is suitable for a transmission grating pattern of a 40 nm L/S and below. Employing a hard-mask process using a silicon dioxide (SiO_2) layer on a tantalum-nitride (TaN) layer in the fabrication of two-window transmission grating, we succeeded in achieving a fivefold higher dry-etch selectivity than that obtained by a non hard-mask process. As a result, we confirmed applicability of the 40-nm-HP grating.

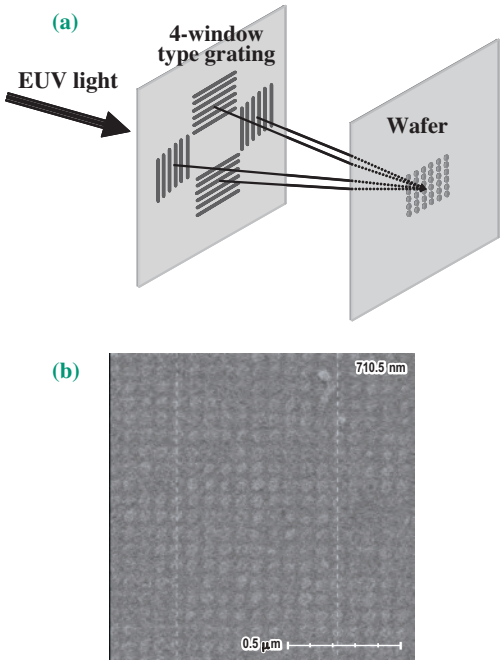

Fig. 4. **(a)** Configuration of two-dimensional transmission grating and **(b)** SEM image of replicated resist pattern of 35-nm-HP dot resist pattern.

Takeo Watanabe* and Hiroo Kinoshita

LASTI, University of Hyogo

*E-mail: takeo@lasti.u-hyogo.ac.jp

References

[1] H. Kinoshita *et al.*: J. Vac. Sci. Technol. B **7** (1989) 1648.
[2] International Technology Roadmap for Semiconductors, 2006, Update edition.
[3] *Y. Fukushima, N. Sakagami, T. Kimura, Y. Kamaji, T. Iguchi, Y. Yamaguchi, M. Tada, T. Harada, T. Watanabe, and H. Kinoshita, to be published in Jpn. J. Appl. Phys. (2010).*
[4] S. Hashimoto *et al.*: Trans. Mat. Res. Soc. Jpn. **26** (2001) 783.

Editor
Seishi Kikuta
SPring-8 / JASRI

Editing & Layout
Marcia M. Obuti-Daté
SPring-8 / JASRI

Printing
Hato Printing Co., Ltd.

J A S R I
Library and Information
Users Administration Division

1-1-1 Kouto, Sayo-cho, Sayo-gun
Hyogo 679-5198 • JAPAN
Tel. +81-(0)791 58-2797 Fax. +81-(0)791 58-1869

frontiers@spring8.or.jp
http://www.spring8.or.jp/

July 2010

Japan Synchrotron Radiation Research Institute
1-1-1 Kouto, Sayo-cho, Sayo-gun, Hyogo 679-5198 JAPAN
http://www.spring8.or.jp